

Multivariate Time Series for the Analysis of Land Surface Dynamics

Evaluating Trends and Drivers of Land Surface Variables for the Indo-Gangetic River Basins

Dissertation zur Erlangung der Doktorwürde der
Philosophischen Fakultät der
Julius-Maximilians-Universität Würzburg

vorgelegt von
Soner Üreyen

März 2022



Julius-Maximilians-
**UNIVERSITÄT
WÜRZBURG**



This document is licensed under the Creative Commons Attribution-NonCommercial-NoDerivatives 4.0 International License (CC BY-NC-ND 4.0):
<http://creativecommons.org/licenses/by-nc-nd/4.0> This CC license does not apply to third party material (attributed to another source) in this publication.

Titelbild:

Im Hintergrund zeigt ein MODIS Satellitenbild einen Ausschnitt der Indus-Ganges Ebene in Schwarzweiß-Farben. Die MODIS Szene ist überlagert mit langjährigen Kompositen des DLR Global SnowPack, DLR Global WaterPack, JRC Global Surface Water Layer und MODIS NDVI Datensatzes (von links nach rechts).

Eingereicht am: 23.03.2022

Von: Soner Üreyen

Ort: Lehrstuhl für Fernerkundung der Julius-Maximilians-Universität Würzburg,
in Kooperation mit dem Deutschen Fernerkundungsdatenzentrum (DFD) des
Deutschen Zentrums für Luft- und Raumfahrt (DLR)

Erstbetreuerin: Prof. Dr. Claudia Künzer, Universität Würzburg

Zweitbetreuer: Prof. Dr. Heiko Paeth, Universität Würzburg

This dissertation was prepared at the department “Land Surface Dynamics” of the German Remote Sensing Data Center (DFD), Earth Observation Center (EOC), German Aerospace Center (DLR), Oberpfaffenhofen, Germany.



*“All truths are easy to understand once they are discovered,
the point is to discover them.”*

– Galileo Galilei

Acknowledgement

First and foremost, I wish to express my deepest sense of gratitude to my primary mentor and supervisor Prof. Dr. Claudia Kuenzer, for giving me the opportunity to pursue my PhD studies and the freedom to explore my ideas. With her valuable experience on remote sensing time series and her clear guidance, she supervised me through the entire process of my dissertation. I am very thankful for her ongoing academic and moral support through these years and for the time she spent with me in numerous constructive and long discussions.

Further, I would like to thank my mentors Prof. Dr. Heiko Paeth (University of Wuerzburg) and Prof. Dr. Natascha Oppelt (University of Kiel), for agreeing to supervise this thesis and their supportive feedback.

Also, I would like to greatly thank my team leaders Dr. Felix Bachofer and Juliane Huth for their continuous support and helpful discussions in all respects. Additional thanks go to Felix for his valuable contributions and comments on my studies.

It has been a great pleasure to pursue my PhD thesis at the German Remote Sensing Data Center (DFD) of the German Aerospace Center (DLR), not only because of the countless scientific opportunities, but to a large extent also because of the great team at the Land Surface Dynamics department and highly competent colleagues, many of whom have greatly enriched my journey at DLR so far. Here, special thanks go to Mariel Dirscherl, Igor Klein, and Dr. Celia Baumhoer for proofreading and providing me with valuable comments on my studies and thesis. In addition, I would like to thank Dr. Mattia Marconcini, Igor Klein, Dr. Andreas Dietz, and Dr. Sebastian Rößler for providing me with relevant time series data. Also, I would like to thank Daniela Palacios-Lopez, Julian Zeidler and my former colleagues Aiyim Orynbaikyzy, Dr. Ya-Lun Tsai, and Dr. Zhongyang Hu with whom I spent many lunch breaks, coffee breaks, or walks (and online talks during the global pandemic). Additional thanks also go to my further fellow PhD students Thorsten Hoeser, Chaonan Ji, Jonas Koehler, and Sophie Reiner mann for being an extremely open-minded and supportive group.

Finally, deep appreciations also go to my parents and sister, for their ongoing support considering all aspects.

English Abstract

The investigation of the Earth system and interplays between its components is of utmost importance to enhance the understanding of the impacts of global climate change on the Earth's land surface. In this context, Earth observation (EO) provides valuable long-term records covering an abundance of land surface variables and, thus, allowing for large-scale analyses to quantify and analyze land surface dynamics across various Earth system components. In view of this, the geographical entity of river basins was identified as particularly suitable for multivariate time series analyses of the land surface, as they naturally cover diverse spheres of the Earth. Many remote sensing missions with different characteristics are available to monitor and characterize the land surface. Yet, only a few spaceborne remote sensing missions enable the generation of spatio-temporally consistent time series with equidistant observations over large areas, such as the Moderate Resolution Imaging Spectroradiometer (MODIS) instrument.

In order to summarize available remote sensing-based analyses of land surface dynamics in large river basins, a detailed literature review of 287 studies was performed and several research gaps were identified. In this regard, it was found that studies rarely analyzed an entire river basin, but rather focused on study areas at subbasin or regional scale. In addition, it was found that transboundary river basins remained understudied and that studies largely focused on selected riparian countries. Moreover, the analysis of environmental change was generally conducted using a single EO-based land surface variable, whereas a joint exploration of multivariate land surface variables across spheres was found to be rarely performed.

To address these research gaps, a methodological framework enabling (1) the preprocessing and harmonization of multi-source time series as well as (2) the statistical analysis of a multivariate feature space was required. For development and testing of a methodological framework that is transferable in space and time, the transboundary river basins Indus, Ganges, Brahmaputra, and Meghna (IGBM) in South Asia were selected as study area, having a size equivalent to around eight times the size of Germany. These basins largely depend on water resources from monsoon rainfall and High Mountain Asia which holds the largest ice mass outside the polar regions. In total, over 1.1 billion people live in this region and in parts largely depend on these water resources which are indispensable for the world's largest connected irrigated croplands and further domestic needs as well. With highly heterogeneous geographical settings, these river basins allow for a detailed analysis of the interplays between multiple spheres, including the anthroposphere, biosphere, cryosphere, hydrosphere, lithosphere, and atmosphere.

In this thesis, land surface dynamics over the last two decades (December 2002 – November 2020) were analyzed using EO time series on vegetation condition, surface water area, and snow cover area being based on MODIS imagery, the DLR Global WaterPack and JRC Global Surface Water Layer, as well as the DLR Global SnowPack, respectively. These data were evaluated in combination with further climatic, hydrological, and anthropogenic variables to estimate their influence on the three EO land surface variables. The preprocessing and harmonization of the time series was conducted using the implemented framework. The resulting harmonized feature space was used to quantify and analyze land surface dynamics by means of several statistical time series analysis techniques which were integrated into the framework. In detail, these methods involved (1) the calculation of trends using the Mann-Kendall test in association with the Theil-Sen slope estimator, (2) the estimation of changes in phenological metrics using the Timesat tool, (3) the evaluation of driving variables using the causal discovery approach Peter and Clark Momentary Conditional Independence (PCMCI), and (4) additional correlation tests to analyze the human influence on vegetation condition and surface water area.

These analyses were performed at annual and seasonal temporal scale and for diverse spatial units, including grids, river basins and subbasins, land cover and land use classes, as well as elevation-dependent zones. The trend analyses of vegetation condition mostly revealed significant positive trends. Irrigated and rainfed croplands were found to contribute most to these trends. The trend magnitudes were particularly high in arid and semi-arid regions. Considering surface water area, significant positive trends were obtained at annual scale. At grid scale, regional and seasonal clusters with significant negative trends were found as well. Trends for snow cover area mostly remained stable at annual scale, but significant negative trends were observed in parts of the river basins during distinct seasons. Negative trends were also found for the elevation-dependent zones, particularly at high altitudes. Also, retreats in the seasonal duration of snow cover area were found in parts of the river basins. Furthermore, for the first time, the application of the causal discovery algorithm on a multivariate feature space at seasonal temporal scale revealed direct and indirect links between EO land surface variables and respective drivers. In general, vegetation was constrained by water availability, surface water area was largely influenced by river discharge and indirectly by precipitation, and snow cover area was largely controlled by precipitation and temperature with spatial and temporal variations. Additional analyses pointed towards positive human influences on increasing trends in vegetation greenness. The investigation of trends and interplays across spheres provided new and valuable insights into the past state and the evolution of the land surface as well as on relevant climatic and hydrological driving variables. Besides the investigated river basins in South Asia, these findings are of great value also for other river basins and geographical regions.

Deutsche Kurzfassung

Die Untersuchung von Erdsystemkomponenten und deren Wechselwirkungen ist von großer Relevanz, um das Prozessverständnis sowie die Auswirkungen des globalen Klimawandels auf die Landoberfläche zu verbessern. In diesem Zusammenhang liefert die Erdbeobachtung (EO) wertvolle Langzeitaufnahmen zu einer Vielzahl an Landoberflächenvariablen. Diese können als Indikator für die Erdsystemkomponenten genutzt werden und sind essenziell für großflächige Analysen. Flusseinzugsgebiete sind besonders geeignet um Landoberflächendynamiken mit multivariaten Zeitreihen zu analysieren, da diese verschiedene Sphären des Erdsystems umfassen. Zur Charakterisierung der Landoberfläche stehen zahlreiche EO-Missionen mit unterschiedlichen Eigenschaften zur Verfügung. Nur einige wenige Missionen gewährleisten jedoch die Erstellung von räumlich und zeitlich konsistenten Zeitreihen mit äquidistanten Beobachtungen über großräumige Untersuchungsgebiete, wie z.B. die MODIS Sensoren.

Um bisherige EO-Analysen zu Landoberflächendynamiken in großen Flusseinzugsgebieten zu untersuchen, wurde eine Literaturrecherche durchgeführt, wobei mehrere Forschungslücken identifiziert wurden. Studien untersuchten nur selten ein ganzes Einzugsgebiet, sondern konzentrierten sich lediglich auf Teilgebietsgebiete oder regionale Untersuchungsgebiete. Darüber hinaus wurden transnationale Einzugsgebiete nur unzureichend analysiert, wobei sich die Studien größtenteils auf ausgewählte Anrainerstaaten beschränkten. Auch wurde die Analyse von Umweltveränderungen meistens anhand einer einzigen EO-Landoberflächenvariable durchgeführt, während eine synergetische Untersuchung von sphärenübergreifenden Landoberflächenvariablen kaum unternommen wurde.

Um diese Forschungslücken zu adressieren, ist ein methodischer Ansatz notwendig, der (1) die Vorverarbeitung und Harmonisierung von Zeitreihen aus mehreren Quellen und (2) die statistische Analyse eines multivariaten Merkmalsraums ermöglicht. Für die Entwicklung und Anwendung eines methodischen Frameworks, das raum-zeitlich übertragbar ist, wurden die transnationalen Einzugsgebiete Indus, Ganges, Brahmaputra und Meghna (IGBM) in Südasien, deren Größe etwa der achtfachen Fläche von Deutschland entspricht, ausgewählt. Diese Einzugsgebiete hängen weitgehend von den Wasserressourcen des Monsunregens und des Hochgebirges Asiens ab. Insgesamt leben über 1,1 Milliarden Menschen in dieser Region und sind zum Teil in hohem Maße von diesen Wasserressourcen abhängig, die auch für die größten zusammenhängenden bewässerten Anbauflächen der Welt und auch für weitere inländische Bedarfe unerlässlich sind. Aufgrund ihrer sehr heterogenen geographischen Gegebenheiten ermöglichen diese Einzugsgebiete eine detaillierte sphärenübergreifende Analyse der Wechselwirkungen, einschließlich der Anthroposphäre, Biosphäre, Kryosphäre, Hydrosphäre, Lithosphäre und Atmosphäre.

In dieser Dissertation wurden Landoberflächendynamiken der letzten zwei Jahrzehnte anhand von EO-Zeitreihen zum Vegetationszustand, zu Oberflächengewässern und zur Schneebedeckung analysiert. Diese basieren auf MODIS-Aufnahmen, dem DLR Global WaterPack und dem JRC Global Surface Water Layer sowie dem DLR Global Snow-Pack. Diese Zeitreihen wurden in Kombination mit weiteren klimatischen, hydrologischen und anthropogenen Variablen ausgewertet. Die Harmonisierung des multivariaten Merkmalsraumes ermöglichte die Analyse von Landoberflächendynamiken unter Nutzung von statistischen Methoden. Diese Methoden umfassen (1) die Berechnung von Trends mittels des Mann-Kendall und des Theil-Sen Tests, (2) die Berechnung von phänologischen Metriken anhand des Timesat-Tools, (3) die Bewertung von treibenden Variablen unter Nutzung des PCMCi Algorithmus und (4) zusätzliche Korrelationstests zur Analyse des menschlichen Einflusses auf den Vegetationszustand und die Wasseroberfläche.

Diese Analysen wurden auf jährlichen und saisonalen Zeitskalen und für verschiedene räumliche Einheiten durchgeführt. Für den Vegetationszustand wurden weitgehend signifikant positive Trends ermittelt. Analysen haben gezeigt, dass landwirtschaftliche Nutzflächen am meisten zu diesen Trends beitragen haben. Besonders hoch waren die Trends in ariden Regionen. Bei Oberflächengewässern wurden auf jährlicher Ebene signifikant positive Trends festgestellt. Auf Pixelebene wurden jedoch sowohl regional als auch saisonal Cluster mit signifikant negativen Trends identifiziert. Die Trends für die Schneebedeckung blieben auf jährlicher Ebene weitgehend stabil, jedoch wurden in Teilen der Einzugsgebiete zu bestimmten Jahreszeiten signifikant negative Trends beobachtet. Die negativen Trends wurden auch für höhenabhängige Zonen festgestellt, insbesondere in hohen Lagen. Außerdem wurden in Teilen der Einzugsgebiete Rückgänge bei der saisonalen Dauer der Schneebedeckung ermittelt. Darüber hinaus ergab die Untersuchung des multivariaten Merkmalsraums auf kausale Zusammenhänge auf saisonaler Ebene erstmals Aufschluss über direkte und indirekte Relationen zwischen EO-Landoberflächenvariablen und den entsprechenden Einflussfaktoren. Zusammengefasst wurde die Vegetation durch die Wasserverfügbarkeit, die Oberflächengewässer durch den Abfluss und indirekt durch den Niederschlag sowie die Schneebedeckung durch Niederschlag und Temperatur mit räumlichen und saisonalen Unterschieden kontrolliert. Zusätzliche Analysen wiesen auf einen positiven Zusammenhang zwischen dem menschlichen Einfluss und den zunehmenden Trends in der Vegetationsfläche hin. Diese sphärenübergreifenden Untersuchungen zu Trends und Wechselwirkungen liefern neue und wertvolle Einblicke in den vergangenen Zustand von Landoberflächendynamiken sowie in die relevanten klimatischen und hydrologischen Einflussfaktoren. Neben den untersuchten Einzugsgebieten in Südasien sind diese Erkenntnisse auch für weitere Einzugsgebiete und geographische Regionen von großer Bedeutung.

Table of Contents

Acknowledgement	vii
English Abstract	ix
Deutsche Kurzfassung	xi
Table of Contents	xiii
List of Figures	xvii
List of Tables	xxiii
Abbreviations and Acronyms	xxv
1 Introduction	1
1.1 Scientific Relevance	1
1.1.1 Relevance of Geoscientific Time Series	3
1.1.2 Relevance of River Basins	6
1.2 Research Motivation	9
1.3 Research Objectives	9
1.4 Thesis Outline	11
2 Theoretical Background on Time Series	13
2.1 Time Series Terminology	13
2.2 Geoscientific Time Series Data	14
2.3 Time Series Analysis	17
2.4 Summary	20
3 A Review on Remote Sensing-Based Analyses of Large River Basins	21
3.1 Results of the Literature Review	22
3.1.1 Distribution of Identified Study Topics	24
3.1.2 Geospatial Distribution of Studies	24
3.1.3 Spatial Extent of Studies	28
3.1.4 Applied Remote Sensing Sensor Types	29
3.1.5 Temporal Resolution of Studies	30
3.1.6 Studies with River Basin Wide Applications	33

3.2	Discussion of Potentials and Future Requirements	38
3.2.1	Potentials and Challenges of Remote Sensing for Large River Basin Monitoring	38
3.2.2	Requirement of a Higher Spatial and Temporal Coverage for Anal- yses in Large River Basins	39
3.2.3	Requirement of Comparability between Large River Basins and Transferability of Methods	40
3.3	Summary	41
4	Study Area: Indo-Gangetic River Basins	43
4.1	Overall River Basin Characteristics	44
4.2	Physical Geography of the Indus, Ganges, Brahmaputra, and Meghna River Basins	46
4.2.1	Climatology	46
4.2.2	Hydrology	50
4.2.3	Land Cover	50
4.3	Human Footprint	55
5	A Framework for the Analysis of Multi-Source Geoscientific Time Series	59
5.1	Input Data	61
5.1.1	Remote Sensing-Based Land Surface Variables	61
5.1.1.1	MODIS Normalized Difference Vegetation Index	63
5.1.1.2	DLR Global WaterPack	63
5.1.1.3	DLR Global SnowPack	64
5.1.2	Climatic and Hydrological Variables	64
5.1.3	Auxiliary Data	66
5.2	Methodological Framework	66
5.2.1	Time Series Preparation	67
5.2.2	Feature Space Harmonization	69
5.2.3	Time Series Analysis Techniques	70
5.2.3.1	Trend Test	70
5.2.3.2	Derivation of Phenological Metrics	74
5.2.3.3	Application of a Causal Discovery Algorithm	75
5.3	Results	79
5.3.1	Trend Analyses	80
5.3.2	Change in Phenological Metrics	84
5.3.3	Relationships between Land Surface Dynamics and Environmental Controls	89
5.4	Transferability of Implemented Framework in Space and Time	95
5.5	Discussion	96
5.5.1	Trends and Seasonality	96
5.5.2	Influence of Drivers on Land Surface Dynamics	99

5.5.3	Limitations and Future Requirements	101
5.6	Summary	102
6	Evaluation of Seasonal Trends and Drivers of Land Surface Variables for the Indo-Gangetic River Basins	107
6.1	Input Data	108
6.1.1	Remote Sensing-Based Land Surface Variables	108
6.1.2	Climatic and Hydrological Variables	109
6.1.3	Anthropogenic Variables	110
6.2	Methods	111
6.2.1	Time Series Preprocessing and Harmonization	111
6.2.2	Application of Statistical Time Series Analysis Techniques	112
6.2.2.1	Seasonal Trend Estimation	112
6.2.2.2	Causal Networks at Seasonal Scale	113
6.2.2.3	Evaluation of Human Influence	114
6.3	Results	115
6.3.1	Seasonal Trends	115
6.3.1.1	Trends at Basin Scale	115
6.3.1.2	Trends at Grid Scale	119
6.3.1.3	Elevation-Dependent Trends	122
6.3.2	Analysis of Driving Variables	124
6.3.2.1	Direct Controls on Land Surface Variables at Grid Scale	125
6.3.2.2	Interdependencies Among Time Series Variables at Basin Scale	126
6.3.2.3	Analysis of Anthropogenic Influences	129
6.4	Discussion	130
6.4.1	Seasonal Trends and Drivers of Land Surface Dynamics	131
6.4.1.1	Vegetation Condition	131
6.4.1.2	Surface Water Area	133
6.4.1.3	Snow Cover Area	134
6.4.2	Potential Future Implications for the Indo-Gangetic River Basins	135
6.5	Summary	136
7	Synthesis and Outlook	139
7.1	Summary and Conclusive Findings	139
7.2	Future Challenges and Opportunities	148
	Bibliography	151
	Eidesstattliche Erklärung	179

List of Figures

Figure 1.1	A conceptual diagram of the Earth System including the main components geosphere and biosphere together with the anthroposphere as a fully integrated component. This figure is published by Steffen et al. 2020. Copyright 2022 by Springer Nature. Reprinted with permission .	2
Figure 1.2	Changes of the land surface temperature and global surface temperature between 1860 and 2020	3
Figure 1.3	Simplified illustration of land surface variables and processes in combination with selected land-atmosphere interactions	6
Figure 1.4	Schematic overview of a river basin including selected land surface variables and related processes	8
Figure 2.1	Exemplary time series of the normalized difference vegetation index decomposed into the time series components remainder, seasonal, and trend	14
Figure 2.2	General steps performed during time series analysis.	17
Figure 3.1	Features of the worldwide 28 largest river basins. Vector data outlining the river basins and rivers as well as area and mean annual discharge are obtained from the Global Runoff Data Centre. Population counts are extracted from the WorldPop data. The spatial characteristics on land use classes are calculated based on HILDA+	23
Figure 3.2	Frequency of identified study topics per research category	25
Figure 3.3	Categorization of reviewed studies by investigated river basin and research category	25
Figure 3.4	Maps demonstrating the spatial distribution of the number of reviewed research articles per large river basin and the number of reviewed research articles per investigated country	26
Figure 3.5	Counts of identified first author affiliations by nation and continent. The numbers in brackets denote the sum of the reviewed studies	27
Figure 3.6	Count of reviewed research articles with respect to the selected large river basins and the spatial scale of the study area	28
Figure 3.7	The utilized sensor types and their combinational use in the reviewed research articles	29

Figure 3.8	Share of utilized remote sensing sensor types categorized by the research categories biosphere, hydrosphere, and cryosphere as well as respective study topics	30
Figure 3.9	Count of published research articles per year and the temporal resolution of the used input data with respect to change detection analyses and employed satellite imagery	31
Figure 3.10	The length of the investigated temporal periods of all reviewed research articles per publication year	32
Figure 4.1	Overview of countries intersecting with the transboundary river basins, topography of the Indus, Ganges, Brahmaputra, and Meghna river basins, location of study area in South Asia, and differentiation of river basins by 117 subbasins	45
Figure 4.2	Overview of the Köppen-Geiger climate classes for the study area . . .	47
Figure 4.3	Schematic overview of the main wind systems for the study area . . .	48
Figure 4.4	Maps showing the mean annual temperature, mean accumulated precipitation, mean accumulated precipitation over the winter season, and mean accumulated precipitation over the monsoon season between 1991–2020 based on ERA5-Land reanalysis. The climate charts for the selected cities in the Indus-Ganges-Brahmaputra-Meghna river basins are based on the WorldClim data for the reference period 1981-2010	49
Figure 4.5	Annual mean of daily gridded river discharge for the investigated river basins based on the GloFAS-ERA5 river discharge version 3.1 between 1991–2020 and the river discharge of the Indus, Ganges, Brahmaputra, and Meghna rivers close to the outlet	51
Figure 4.6	Overview of land cover and land use distributions for the study area by means of the ESA CCI land cover 2019 dataset and illustration of percentages of the land cover and land use classed per investigated spatial unit. For visualization purposes, labels of percentages lower than 5 are excluded	52
Figure 4.7	Overview of vegetation greenness by means of a long-term mean of the normalized difference vegetation index derived from MODIS imagery between 2003 and 2020 and the phenology of vegetation greenness for the respective river basins based monthly means for the same period . .	53
Figure 4.8	Average of snow cover area for the period 2003–2020 based on the daily DLR Global SnowPack data and visualization of the snow cover phenology for the respective basins based on monthly means	54

Figure 4.9	Average of surface water area for the period 2003–2020 based on the DLR Global WaterPack and JRC Global Surface Water Layer data as well as visualization of the surface water phenology for the respective basins based on monthly means	56
Figure 4.10	Development of the settlement area in the respective river basins between 1985 and 2015. These statistics are extracted from the DLR World Settlement Footprint Evolution data	57
Figure 4.11	Overview of the gridded population counts for the year 2020 and the gridded total GDP (purchasing power parity) in constant 2011 international US dollars for the year 2015. The four labeled cities in the study area are megacities exceeding a population of 10 million people	58
Figure 5.1	Overview of used geoscientific monthly time series to analyze land surface dynamics	62
Figure 5.2	Simplified overview of workflow for the developed and implemented framework including data preparation, feature space harmonization, and statistical time series analyses	67
Figure 5.3	Workflow for the database generation step, where the prepared multi-source time series are spatially aggregated to a selected uniform grid. This spatial grid might be replaced by any geographical entity	70
Figure 5.4	Exemplary diagram of the MODIS normalized difference vegetation index at monthly scale showing the original and the seasonally anomalized as well as the detrended anomalized time series values	72
Figure 5.5	Workflow for the application of the trend test including the Mann-Kendall test and the Theil-Sen slope estimator. The time series are prewhitened if the lag-1 autocorrelation is statistically significant	73
Figure 5.6	Overview of selected phenological metrics	75
Figure 5.7	Overview of scenarios leading to a spurious correlation	76
Figure 5.8	Application of a temporal mask	78
Figure 5.9	Influence of detrending and anomaly calculation on the correlation coefficient. Correlation between original precipitation and NDVI time series as well as temperature and normalized difference vegetation index. Map derived with PCMCI, showing the strength of the MCI value	79
Figure 5.10	Magnitude of significant trends in consideration of the applied prewhitening method prior to the trend test	80
Figure 5.11	Magnitude of significant trends by means of the seasonal Mann-Kendall test for the normalized difference vegetation index	81
Figure 5.12	Magnitude of significant trends by means of the seasonal Mann-Kendall test for surface water area using the DLR Global WaterPack	82

Figure 5.13	Magnitude of significant trends by means of the seasonal Mann-Kendall test for snow cover area using the DLR Global SnowPack	83
Figure 5.14	Average timing of the seasonal peak value retrieved with Timesat	85
Figure 5.15	Average duration of the season retrieved with Timesat	86
Figure 5.16	Difference of the average seasonal amplitude and average seasonal peak value between the first and second decade	87
Figure 5.17	The spatial distribution of the dominant driving variables for the normalized difference vegetation index and their respective temporal lags at monthly scale	89
Figure 5.18	Influence of respective drivers on the normalized difference vegetation index after conditioning out all other driving variables	90
Figure 5.19	The spatial distribution of the dominant driving variables for surface water area and their respective temporal lags at monthly scale	91
Figure 5.20	Influence of respective drivers on surface water area after conditioning out all other driving variables	92
Figure 5.21	The spatial distribution of the dominant driving variables for snow cover area and their respective temporal lags at monthly scale	93
Figure 5.22	Influence of respective drivers on snow cover area after conditioning out all other driving variables	94
Figure 5.23	Simplified overview of the processing pipeline for multi-source time series preparation and multivariate analyses on the HPC infrastructure of the DFD at the DLR with minimal user intervention	95
Figure 6.1	Simplified overview of the workflow as part of the developed and implemented framework	113
Figure 6.2	Time series variables for the river basins at annual temporal scale for the years between 2003 and 2020. The dashed line represents the respective average value of the time series	116
Figure 6.3	Magnitude of significant trends derived with the seasonal Mann-Kendall test in association with the Theil-Sen slope estimator for the normalized difference vegetation index at seasonal and annual temporal scale	120
Figure 6.4	Same as Figure 6.3, but for surface water area	121
Figure 6.5	Same as Figure 6.3, but for snow cover area	122
Figure 6.6	Seasonal and annual trends of the normalized difference vegetation index, surface water area, and snow cover area in dependence of elevation zones	123
Figure 6.7	The spatial distribution of the dominant driving variables for the normalized difference vegetation index, surface water area, and snow cover area at seasonal scale	124

Figure 6.8	The temporal lags of the identified causal links between the target and the respective dominant driving variable at seasonal scale in Figure 6.7	125
Figure 6.9	Causal graphs visualizing the interactions between the geoscientific time series, including the normalized difference vegetation index, surface water area, and snow cover area	127
Figure 6.10	Relation between the trends of the land surface variables normalized difference vegetation index and surface water area with trends derived from annual anthropogenic time series	130

List of Tables

Table 2.1	Summary of selected open gridded geospatial time series characterizing land surface parameters across spheres. The temporal resolution of the time series is denoted as yearly, monthly, biweekly, daily, hourly, multi-temporal, and composites.	16
Table 3.1	List of defined categories and identified study topics.	22
Table 4.1	Characteristics of the investigated river basins including the riparian countries, the drainage area, and the population count extracted from the gridded WorldPop 2020 dataset	44
Table 4.2	Further information with respect to the selected locations in Figure 4.4	48
Table 5.1	Overview of utilized parameter settings for PCMCI	77
Table 5.2	Comparison of the amount of significant trends and their direction based on the application of different prewhitening algorithms prior to the seasonal Mann-Kendall test. Results are listed as percentages for the normalized difference vegetation index, surface water area, as well as snow cover area and include each season and trends at annual scale	84
Table 6.1	Seasonal and annual trends at river basin scale for the period covering December 2002 and November 2020	117
Table 6.2	Long-term average of the normalized difference vegetation index, surface water area, and snow cover area for the period between December 2002 and November 2020 at seasonal and annual temporal scale	118
Table 6.3	Seasonal and annual trends at river basin scale for the period covering December 2002 and November 2020 denoted at decadal scale. The covered period is split into two periods	119
Table 6.4	Annual and seasonal trends of the normalized difference vegetation index stratified by vegetation classes for the period between December 2002 and November 2020	129

Abbreviations and Acronyms

ALOS-PALSAR	Advanced Land Observing Satellite-Phased Array L-Band Synthetic Aperture Radar
AMSR-E	Advanced Microwave Scanning Radiometer for EOS
AOI	Area of Interest
API	Application Programming Interface
ARD	Analysis Ready Data
ASAR	Advanced Synthetic Aperture Radar
AVHRR	Advanced Very High Resolution Radiometer
BEAST	Bayesian Estimator of Abrupt change, Seasonal change, and Trend
BFAST	Breaks for Additive Season and Trend
CCI	Climate Change Initiative
CDS	Climate Data Store
CHIRPS	Climate Hazards Group Infrared Precipitation with Station data
CRU	Climatic Research Unit
CRUTEM5	Climatic Research Unit temperature version 5
DEM	Digital Elevation Model
DFD	German Remote Sensing Data Center
DJF	December-January-February
DLR	German Aerospace Center
DMSP-OLS	Defense Meteorological Satellite Program-Operational Linescan System
ECMWF	European Centre for Medium-Range Weather Forecasts
Envisat	Environmental Satellite
EO	Earth Observation
EOC	Earth Observation Center
ERA5	ECMWF Reanalysis 5th Generation
ERS	European Environmental Satellites
ESA	European Space Agency
EVI	Enhanced Vegetation Index
FAO	Food and Agriculture Organization
GEE	Google Earth Engine
GBM	Ganges-Brahmaputra-Meghna
GDAL	Geospatial Data Abstraction Library
GDP	Gross Domestic Production
GHG	Greenhouse Gas
GLAS	Geoscience Laser Altimeter System
GLEAM	Global Land Evaporation Amsterdam Model

GloFAS	Global Flood Awareness System
GRACE	Gravity Recovery And Climate Experiment
GRDC	Global Runoff Data Centre
GSWL	Global Surface Water Layer
HadCRUT5	Met Office Hadley Centre/Climatic Research Unit global surface temperature version 5
HDF	Hierarchical Data Format
HPC	High-Performance Computing
HydroSHEDS	Hydrological data and maps based on shuttle elevation derivatives at multiple scales
ICESat	Ice, Cloud, and land Elevation Satellite
IDE	Integrated Development Environment
IGBM	Indus-Ganges-Brahmaputra-Meghna
IMD	Indian Meteorological Department
IMF	International Monetary Fund
IPCC	Intergovernmental Panel on Climate Change
ITSG	Institute of Geodesy at Graz University of Technology
JERS-1	Japanese Earth Resources Satellite 1
JJAS	June-July-August-September
JRC	Joint Research Center
ON	October-November
LAI	Leaf Area Index
LandTrendr	Landsat-based Detection of Trends in Disturbance and Recovery
MAM	March-April-May
MCI	Momentary Conditional Independence
MERRA-2	Modern-Era Retrospective analysis for Research and Applications, version 2
MERIS	Medium Resolution Imaging Spectrometer
MODIS	Moderate Resolution Imaging Spectroradiometer
MK	Mann-Kendall
NASA	National Aeronautics and Space Administration
NetCDF	Network Common Data Form
NDSI	Normalized Difference Snow Index
NDVI	Normalized Difference Vegetation Index
NOAA	National Oceanic and Atmospheric Administration
NOPW	No Prewhitening
PC	Peter and Clark
PCMCI	Peter and Clark Momentary Conditional Independence
PPP	Purchasing Power Parity
PROBA	Project for On-Board Autonomy
QGIS	Quantum Geographic Information System
RA	Radar Altimeter
SAR	Synthetic Aperture Radar
SEVIRI	Spinning Enhanced Visible and Infrared Imager
SCA	Snow Cover Area
SCI	Science Citation Index
SMOS	Soil Moisture and Ocean Salinity
SPOT	Satellite Pour l'Observation de la Terre

SRTM	Shuttle Radar Topography Mission
SWA	Surface Water Area
TanDEM-X	TerraSAR-X-Add-on for Digital Elevation Measurements
TFPW-Y	Trend-Free Prewhitening after Yue et al.
TFPW-WS	Trend-Free Prewhitening after Wang and Swail
TRMM	Tropical Rainfall Measuring Mission
TS	Theil-Sen
TWAP	Transboundary Waters Assessment Programme
TWSA	Terrestrial Water Storage Anomaly
UNEP	United Nations Environment Programme
USGS	United States Geological Survey
VCPW	Variance Corrected Prewhitening
VIIRS	Visible Infrared Imaging Radiometer Suite
WGS84	World Geodetic System
WRI	World Resources Institute
WSF	World Settlement Footprint

Chapter 1

Introduction

1.1 Scientific Relevance

In times of amplified global climate change, Earth System Science received an ever-emerging attention. The Earth system is composed of the biosphere and the geosphere, whereas the latter includes the hydrosphere, cryosphere, atmosphere, and lithosphere. Additionally, as illustrated in Figure 1.1, recent research stresses the importance and challenge of fully integrating the anthroposphere as a component of the Earth system (Steffen et al., 2020). The functioning of the entire system can only be understood in consideration of the forcing and feedback mechanisms among the spheres. In this regard, human influences and the Earth's land surface play a pivotal role in the climate system (Arneth et al., 2019).

In general, the Earth's land surface provides the foundation “for human livelihoods and well-being through primary productivity, the supply of food, freshwater, and multiple other ecosystem services” (Shukla et al., 2019). The Intergovernmental Panel on Climate Change (IPCC) reports that more than 70 % of the global ice-free land surface is directly influenced by human land use (IPCC, 2019a). Given the global population growth, increasing consumption of resources, and intensification in human land use, e.g. over agricultural areas, these developments have greatly contributed to increasing greenhouse gas (GHG) emissions and the loss of natural ecosystems (IPCC, 2019a). In this connection, global warming is particularly accelerated over land areas compared to the average global temperature over land and ocean during the last decades (Figure 1.2). Moreover, the Climatic Research Unit temperature version 5 (CRUTEM5) data (Osborn et al., 2021) revealed that twenty of the warmest observed years occurred between 2000 and 2021. These unprecedented increases in surface and ocean temperatures had severe implications on processes at the land surface and respective spheres (Jia et al., 2019). To start with, warming temperatures led to an increase in the frequency, intensity, and duration of heatwaves over most

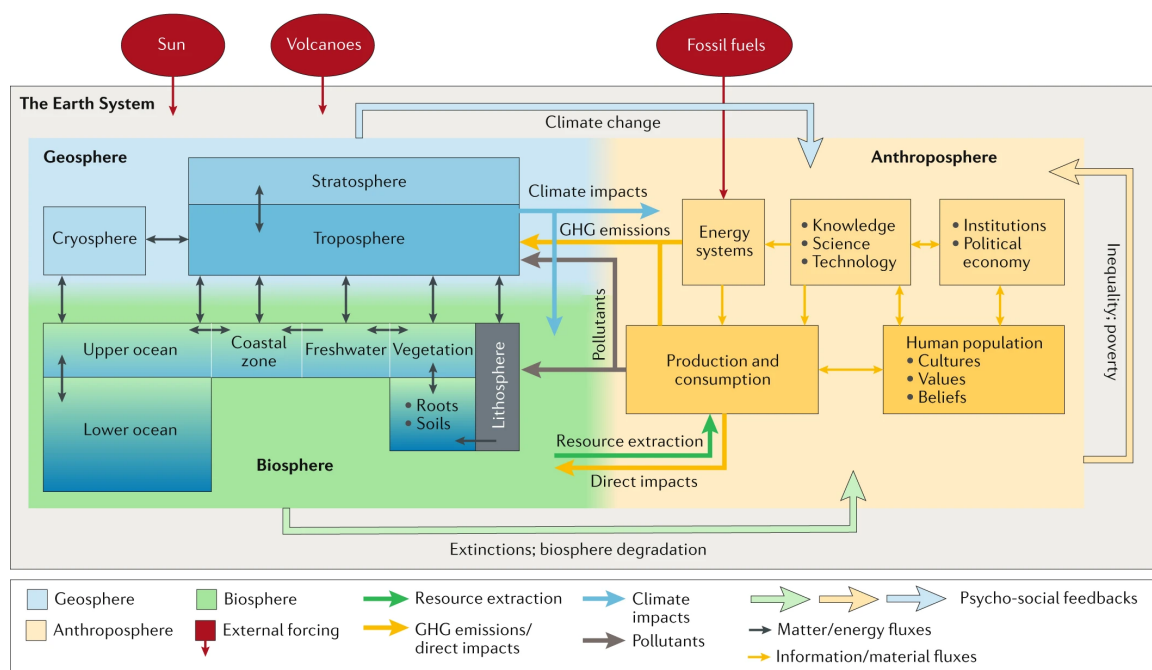


Figure 1.1: A conceptual diagram of the Earth System including the main components geosphere and biosphere together with the anthroposphere as a fully integrated component. This figure is published by Steffen et al. 2020. Copyright 2022 by Springer Nature. Reprinted with permission.

land areas. Likewise, the frequency and intensity of droughts amplified (IPCC, 2019a). On the contrary, long-term observational data indicates changing patterns of precipitation and a higher frequency and intensity of extreme precipitation events (IPCC, 2021). In general, changes in the hydrological cycle appear to intensify through an increase in the exchange of water between the surface and the atmosphere (Chen et al., 2021a). Changes of the cryosphere are particularly rapid and dramatic (IPCC, 2019b). At lower elevations of high mountain areas, snow cover duration was found to decrease by 5 days on average (IPCC, 2019c). In addition, glacier mass changed by $-490 \pm 100 \text{ kg m}^{-2} \text{ yr}^{-1}$ in all mountain regions between 2006 and 2015 (IPCC, 2019c). Furthermore, dramatic decreases have been observed for the Arctic sea ice extent being particularly pronounced in September with a reduction of $-12.8 \pm 2.3 \%$ per decade between 1979–2018 (IPCC, 2019c). Warming of the land surface is also accompanied by primal changes of the terrestrial biosphere (IPCC, 2021). These include an increase in both the duration of the growing season in large areas of the Northern Hemisphere extratropics and, since the 1960s, the amplitude of the seasonal cycle of atmospheric CO_2 beyond 45°N (Arias et al., 2021). Additionally, a consistent increase in vegetation greenness was observed at global scale since the 1980s (Arias et al., 2021; Piao et al., 2020).

In the light of warming temperatures, climate zones are shifting in various regions of the globe (Chan and Wu, 2015; Chen and Chen, 2013; Spinoni et al., 2015). In future

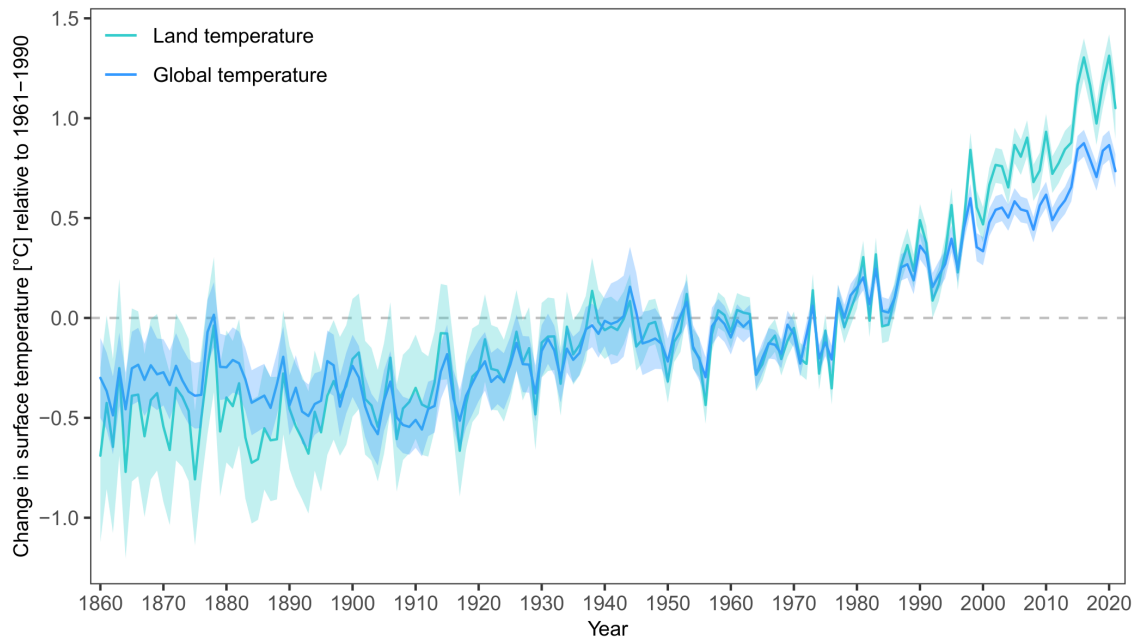


Figure 1.2: Changes of the land surface temperature and global mean surface temperature between 1860 and 2020. The turquoise color indicates the annual mean land surface temperature by means of the CRUTEM5 dataset (Osborn et al., 2021). The annual mean global surface temperature is illustrated by the blue line and is based on the Met Office Hadley Centre/Climatic Research Unit global surface temperature version 5 (HadCRUT5) data (Morice et al., 2021).

projections, climate zones are suggested to further shift poleward, particularly in middle to high latitudes (IPCC, 2019a). This will be particularly pronounced since an ongoing increase in global temperatures is expected until at least mid-century, while the threshold of 1.5 and 2 °C will be surpassed within the 21st century if CO₂ and other greenhouse gas (GHG) emissions are not reduced (IPCC, 2021). With every rate of increase in air temperatures, extreme events, including precipitation (Formayer and Fritz, 2017; Guerreiro et al., 2018; Zhang et al., 2019) and drought events (Berg and Sheffield, 2018; Cook et al., 2020; Gu et al., 2020; Vicente-Serrano et al., 2020), will cumulate. Considering changes in permafrost during the 21st century, it is very likely that thawing will increase significantly (Hock et al., 2019; Lu et al., 2017; Zhao et al., 2019b). Likewise, with additional warming, the loss of seasonal snow cover, land ice and Arctic sea ice will intensify (IPCC, 2021; Mudryk et al., 2020).

1.1.1 Relevance of Geoscientific Time Series

Despite the observed and projected changes, it remains challenging to account for the complex interactions among the Earth system components (Mahecha et al., 2020; Reichstein et al., 2019). In this context, spaceborne remote sensing is a valuable tool for the monitoring of long-term changes at the Earth's land surface and its interactions across spheres.

A continuous monitoring of these transformation processes using Earth observation (EO) is of great importance to quantify and understand their characteristics, drivers, and impacts (Piao et al., 2020). While EO-based investigations of land surface change by means of a single land surface variable are commonplace, a joint exploitation of multivariate features covering several spheres is still rarely performed. In light of this, long-term observations from various platforms including airborne and spaceborne remote sensing, surface-based instrumental stations, or in-situ measurements from airplanes and balloons are fundamental to enable progress in our understanding of global climate and environmental change (Arias et al., 2021). More specifically, geospatial time series and respective analysis methods are essential to identify spatio-temporal patterns of Earth system processes and examine changes over time.

Since decades, EO provides ever-increasing amounts of data streams over the entire globe (Kuenzer et al., 2015a; Reichstein et al., 2019). The open data policies of the corresponding agencies offer free of charge access to various data archives of multiple satellite missions, such as the European Copernicus Sentinel, the United States Geological Survey (USGS) Landsat, and Moderate Resolution Imaging Spectroradiometer (MODIS) missions. These missions include optical, synthetic aperture radar (SAR), or altimetry instruments. In consideration on the investigated research questions and respective requirements, remote sensing time series allow the analysis of land surface dynamics to be performed at high to coarse spatial resolution (e.g. 10 to 1000 m) and at local to global scale. Apart from characteristics with respect to the spatial resolution, the temporal resolution of remote sensing data might limit the desired application, as it defines the intervals within time series observations. For example, the optical Landsat mission enables long-term analyses on land surface change since 1972 at a spatial resolution of 30 m. Based on these optical data, it is possible to derive information on i.e. land cover, vegetation greenness, and water color at a temporal resolution of 16 days (Nyland et al., 2018; Broich et al., 2018; Lobo et al., 2015). In regard of time series analysis with high observation frequencies, optical satellite missions with low revisit times such as the Landsat mission might be hampered by cloud obscuration and sunlight availability. These factors can drastically reduce the temporal resolution and, thus, the number of available observations over the Earth's surface. With the launch of the optical Sentinel-2 mission in 2015, it is possible to increase the frequency of time series observations using optical imagery through harmonizing Landsat and Sentinel-2 imagery. The Sentinel-2 mission acquires imagery at 10 to 20 m spatial resolution and revisits the Earth's surface roughly every 5 days. Besides these mission, additional optical remote sensing instruments with a high temporal resolution up to twice a day are available, however, at the cost of the corresponding spatial resolution. In particular, these include the MODIS (launched in 2000) and National Oceanic and Atmospheric

Administration (NOAA) Advanced Very High Resolution Radiometer (AVHRR) (launched in 1978) missions. Both missions provide multispectral imagery at a comparatively coarse spatial resolution (250 to 1 km). Yet, these missions paved the way for EO-based time series analyses at very high temporal resolution over multiple decades. Exemplary large-scale applications include, e.g. the monitoring of vegetation or inundation dynamics (Chen et al., 2019; Huang et al., 2014; Sakamoto et al., 2006; Wu et al., 2015). Furthermore, the usage of spaceborne SAR missions provides the opportunity to monitor the Earth's surface independent of daylight and weather conditions. Nowadays, the Sentinel-1 instrument is a widely used SAR mission having a spatial resolution of 10 m and, depending on the geographical location, a temporal resolution up to 3 days (Baumhoer et al., 2019; Cao et al., 2018a; Dirscherl et al., 2021).

Apart from raw EO data, many subsequently generated analysis ready data (ARD) that characterize the state of the global land surface exist. These include geophysical variables such as land surface temperature, net primary productivity, gross primary productivity, and albedo (e.g. Duan et al. 2019; Zhao et al. 2005; Wang et al. 2015a), index variables such as the normalized difference vegetation index (NDVI) and the leaf area index (LAI) (e.g. Didan and Munoz 2019; Claverie et al. 2016), and thematic variables representing, e.g. forest cover change, surface water area as well as snow cover area dynamics, and settlement growth (e.g. Hansen et al. 2013; Pekel et al. 2016; Klein et al. 2017; Dietz et al. 2015; Naegeli et al. 2021a; Marconcini et al. 2020; Pesaresi et al. 2013). Besides EO time series characterizing the land surface, further geoscientific time series on the state of the atmosphere and fluxes between the Earth's surface and the atmosphere are crucial for studying climate change (IPCC, 2021). In this connection, reanalyses are of particular importance. These data combine observations and models by means of data assimilation methods to provide spatial and temporal consistent estimates of various variables describing the climate system (Arias et al., 2021). A prominent example is generated at the European Centre for Medium-Range Weather Forecasts (ECMWF) and is named ECMWF Reanalysis 5th Generation (ERA5) (Hersbach et al., 2020). ERA5 represents atmospheric, ocean-wave, and land surface variables at hourly temporal resolution and at approximately 31 km spatial resolution from 1950 to present (Hersbach et al., 2020). Figure 1.3 illustrates exemplary variables that can be characterized by geoscientific time series.

The large availability of EO and further geoscientific time series enables the joint exploration of interactions among the spheres of the Earth system at global scale and has the potential to considerably enhance our understanding of environmental change (Mahecha et al., 2020; Salcedo-Sanz et al., 2020; Steffen et al., 2020). However, the investigation of EO-based multivariate time series on land surface characteristics in combination with cli-

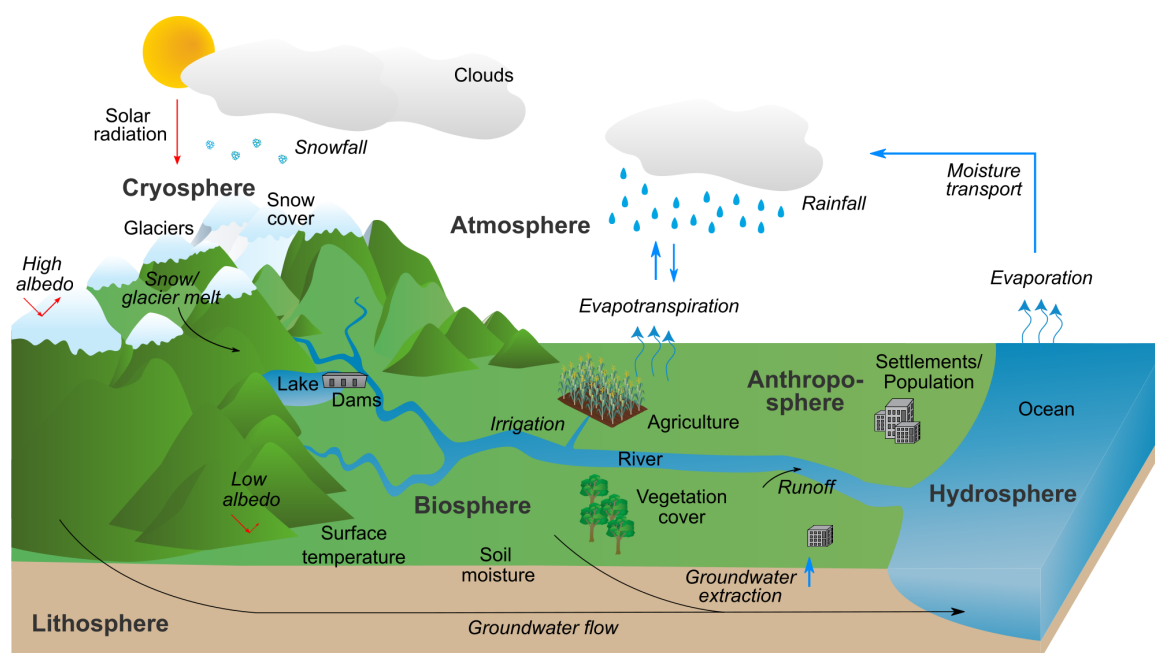


Figure 1.3: Simplified illustration of land surface variables and processes in combination with selected land-atmosphere interactions (several symbols are adopted or modified according to courtesy of the Integration and Application Network, University of Maryland Center for the Environmental Science).

matic, hydrological, and anthropogenic variables remains underexploited and is hampered by varying data characteristics in terms of spatial and temporal resolution standards as well as processing and storage capacities.

1.1.2 Relevance of River Basins

Rivers have been hotspots for the origin and evolution of human civilization since ancient times (Best, 2018; Grill et al., 2019; Macklin and Lewin, 2015). Irrespective of administrative boundaries, river basins are a natural functional unit of the Earth’s land surface and supply an abundance of resources for ecosystems and humans (Abell et al., 2016). Considering freshwater resources, food production, hydropower generation, and transportation opportunities, river systems are of great importance to human societies (Best, 2018; Grill et al., 2019; Viviroli et al., 2020). For example, Mesopotamia is referred to as the cradle of civilization and is formed by the Tigris and Euphrates river systems. These rivers provided rich soils and direct access to freshwater for livelihoods and agricultural productivity. However, in times of climate change, the Tigris-Euphrates river basin faced extreme drought events over the last decades that greatly contributed to repeated crop failures (Chao et al., 2018; Rateb et al., 2021). On the other hand, the Mekong river is regarded as the lifeline of Southeast Asia and has passed through large human-induced changes. Specifically, the natural river system has been deeply modified by the construction of hydropower dams which

tremendously influenced the ecosystems and sediment fluxes (Hecht et al., 2019). In this context, large-area coastal erosion in the Mekong river delta was linked to less sediment transportation caused by dam constructions (Anthony et al., 2015). Furthermore, the Indus valley civilization is considered as one of the earliest Bronze Age civilizations and was located in the northwest of the Indo-Gangetic Plain (Kathayat et al., 2017). Here, the Indus and Ganges rivers, originating at Asia's water towers, have been fundamental elements for society, culture, and economy since early times (Nie et al., 2021; Pritchard, 2019).

Apart from climate change impacts on river basins and freshwater resources, a growing human population and land use intensification highly pressure the river systems worldwide (Grill et al., 2019; Vörösmarty et al., 2010; Haddeland et al., 2014). Since freshwater resources are not equally distributed, many regions on the globe have to handle water scarcity (Vanham et al., 2018). In this context, Mekonnen and Hoekstra (2016) assessed that 4 billion people already experience major water stress over a period of at least one month per year and 1.8 billion people over a period of at least six months per year. With accelerating climate change, the number of humans facing climatic and hydrological extreme events might increase rapidly.

With water being one of the most fundamental natural resources, the monitoring of river systems and their drainage area is of vital importance (Sheffield et al., 2018; Vörösmarty et al., 2010). For example, human interventions into river systems, such as land use change, urbanization, and construction of irrigation systems might have irreversible implications for water resources as well as ecosystems, especially with respect to upstream-downstream processes. Additionally, as elaborated in the previous sections, climate change will likely cause reductions of elements of the cryosphere (glaciers, snow cover) which are a fundamental component of the upstream regions of many large river basins. In regards of these examples, changes of upstream river basins might have important implications on downstream ecosystems. Thus, regarding land and water resources management, the monitoring of river basins is of highest relevance, specifically for researchers, stake holders and decision makers. Also, governance of large river basins is an important requirement to prevent political conflicts and sustain environmental health and economic progress, in particular with respect to transboundary river basins (de Stefano et al., 2017). Figure 1.4 briefly visualizes features and processes within the spatial entity of a river basin.

In this connection, various inventories and data portals providing information on large river basins are available. For example, the hydrological data and maps based on shuttle elevation derivatives at multiple scales (HydroSHEDS) project encompasses a suite of geospatial data with respect to hydrographic information on river basins worldwide (Lehner et al., 2008; Linke et al., 2019). Further, the Global Runoff Data Centre (GRDC) supplies data on

hydrographic information as well, including tabular inventories on drainage area and mean annual discharge. Moreover, the Transboundary Waters Assessment Programme (TWAP) river basin component is a platform assessing essential information for 286 transboundary river basins worldwide. This service, coordinated by the United Nations Environment Programme (UNEP), includes a variety of indicators such as water scarcity as well as pollution, governance aspects, and socio-economic variables. A similar service is accessible on the Aqeduct platform by the World Resources Institute (WRI). On the other hand, Aquastat, being maintained by the Food and Agriculture Organization (FAO), gathers statistics on water resources at national scale. Given the availability of large amounts of geoscientific time series on diverse land surface variables, a consistent monitoring of spatio-temporal land surface dynamics within large river basins across spheres is required yet lacking (e.g. Broich et al. 2018; Wohlfart et al. 2016). In order to provide more detailed insights into land surface dynamics within large river basins as well as to investigate related direct and

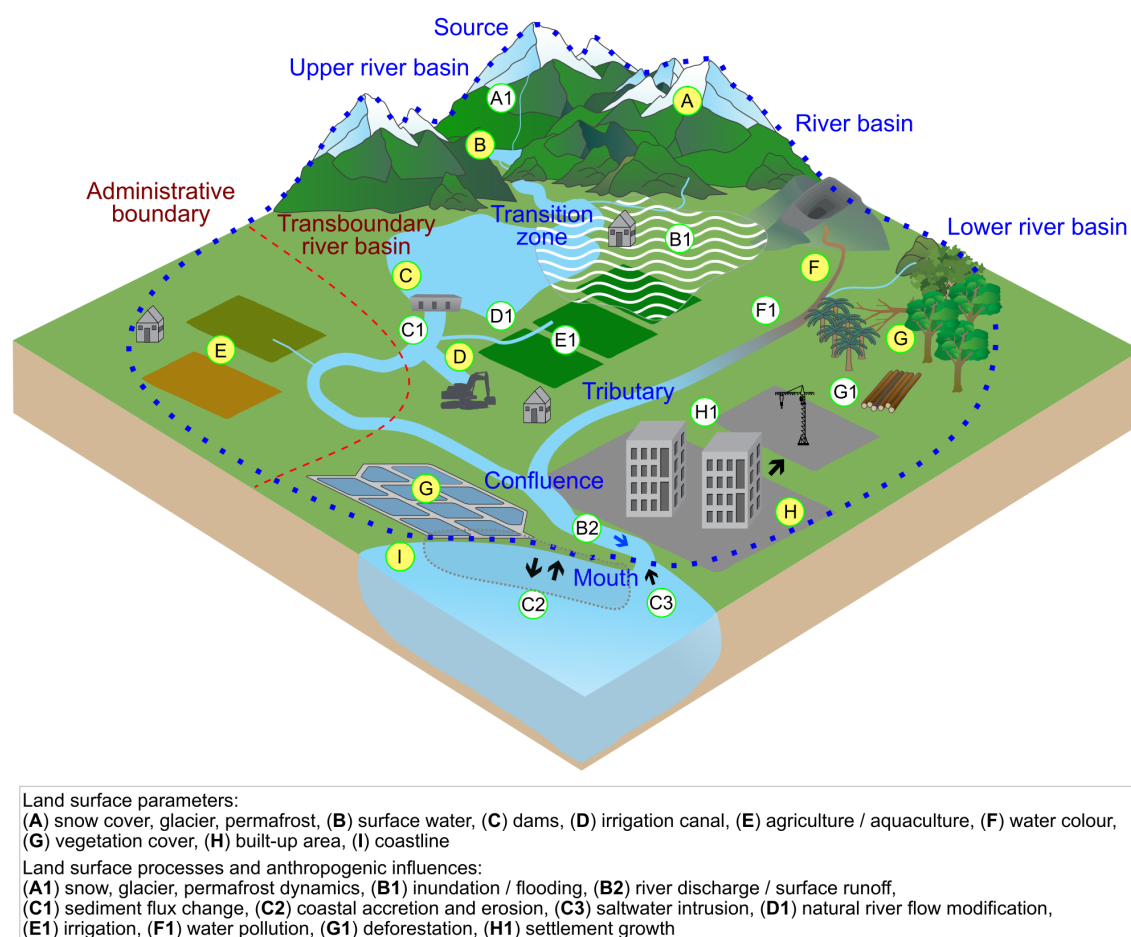


Figure 1.4: Schematic overview of a river basin including selected land surface variables and related processes (several symbols are adopted or modified according to courtesy of the Integration and Application Network, University of Maryland Center for the Environmental Science).

indirect drivers, interactions among spheres, and impacts of environmental change, the development of methodological strategies using multivariate geoscientific time series is necessary. As stated in the previous section, the analysis of multivariate time series covering multiple spheres remains underexploited. In this context, the geographical entity of large river basins enables the quantification and evaluation of environmental change and drivers within a natural functional unit covering various components of the Earth system.

1.2 Research Motivation

Based on the presented scientific background information in the previous sections, the main motivation of the present thesis is to exploit the potential of multivariate geoscientific time series for an improved scientific understanding and knowledge of land surface dynamics in large river basins deducing (1) key characteristics of land surface dynamics and their temporal and spatial patterns, (2) direct and indirect control mechanisms on environmental change using a high dimensional feature space, and (3) the vulnerability of the natural environment under a warming climate.

1.3 Research Objectives

In order to address the lack of multivariate time series analyses for the quantification and investigation of land surface dynamics across spheres as well as to comply with the research motivation presented in Section 1.2, the overarching objective of this thesis is to develop a novel and automated methodological framework enabling the analysis of multi-source geospatial time series that is transferable in space and time and applicable to any spatial entity. In this thesis, the analyses are performed for the geographical entities of large river basins. Accordingly, this thesis investigates multisource EO time series characterizing, i.e. vegetation condition, surface water area, snow cover area, and settlement area in combination with further geospatial time series on climatic, hydrological, and anthropogenic variables. With more detail, the specific objectives of this thesis can be formulated as follows:

- **Objective 1:** The first research objective includes a comprehensive literature review on available EO-based analyses with respect to land surface dynamics in large river basins. Here, the focus lies on the quantitative assessment of investigations focusing on the 28 largest river basins worldwide, their spatio-temporal coverage, analyzed land surface variables, and used remote sensing sensor types. Furthermore, available and relevant EO as well as further geospatial time series with respect to the analysis of land surface dynamics need to be identified.

- **Objective 2:** The second and primary research objective of this thesis covers the development and implementation of a novel and automated framework for the (1) pre-processing of univariate time series data, (2) generation of a harmonized multivariate feature space, and (3) statistical analysis of the time series to assess and evaluate land surface dynamics and to investigate corresponding driving variables. The Indus, Ganges, Brahmaputra, and Meghna river basins in South Asia are used as study area to develop and test the methodological framework.
- **Objective 3:** Following the implementation of the methodological framework, the last research objective is associated with detailed analyses of seasonal trends as well as controls on land surface variables for the study area. The analysis of control mechanisms includes the assessment of direct and indirect drivers on vegetation, surface water area, and snow cover area dynamics. Also, the interdependencies within the entire multivariate feature space are analyzed.

In order to meet the defined objectives of this thesis, several research questions have to be formulated and investigated. In consideration of the objectives, the first group of research questions address the literature review. In particular, the following questions shall be answered:

Research Questions 1

- What is the potential of Earth observation time series for the analysis of land surface dynamics?
- Which Earth observation and further geoscientific time series are available?
- What is the geographical relevance of large river basins for multivariate time series analyses?
- How many studies investigated large river basins and what was their spatio-temporal coverage and resolution?
- Which spheres were most frequently analyzed in the context of large river basins and which spaceborne remote sensing instruments were most frequently utilized?
- Which research gaps exist with respect to remote sensing-based river basin analyses and how can they be addressed?

Furthermore, the second group of research questions addresses the implementation of a methodological framework for time series preparation, harmonization, and analysis with respect to the quantification of land surface dynamics and drivers. In this regard, potentials and challenges of remote sensing time series and relevant methods for time series preparation and analysis are evaluated.

Research Questions 2

- What are the challenges in using multisource time series for joint analyses to characterize land surface dynamics and how can they be addressed?
- Which novel methods can be integrated in the methodological framework to analyze land surface dynamics and interdependencies across spheres?
- What needs to be considered to ensure the transferability of the developed methodological framework to any spatial entity or time series data?
- Are the results of the quantitative analyses of land surface dynamics consistent with existing literature?

Ultimately, the third group of research questions deals with a more detailed application of the developed framework to derive seasonal characteristics of land surface dynamics and respective driving variables in the Indus, Ganges, Brahmaputra, and Meghna river basins. Considering the driving variables, the analysis shall include the assessment of direct and indirect influences within the high dimensional feature space consisting of EO-based land surface variables and further climatic, hydrological, and anthropogenic time series.

Research Questions 3

- What are the seasonal patterns of trends with respect to vegetation condition, surface water area, and snow cover area between December 2002 and November 2020? Are there any changes in phenological characteristics?
- What are the dominant controls on vegetation condition, surface water area, and snow cover area dynamics? Are there differences in the prevalent environmental controls with respect to the investigated river basins?
- What are the interdependencies among the respective feature spaces?
- What are future implications of climate change for the investigated Indo-Gangetic river basins in South Asia?

1.4 Thesis Outline

In Chapter 1.1, an introduction into the scientific relevance of land surface change under a warming climate was given. Exemplary impacts of climate variability on the land surface covering multiple spheres were emphasized. In this context, the relevance and need for multivariate time series analyses as well as corresponding research gaps were briefly introduced. Next, the relevance as well as importance of large river basins as a geographical entity were explained and corresponding research gaps were stated. Subsequently, Chapters 1.2 and 1.3 outlined the main research motivation and research objectives of this thesis. Following this introductory chapter, the next chapters can be summarized as follows:

Chapter 2 provides fundamental information on time series terminology and respective analysis methods.

Chapter 3 reviews analyses of land surface dynamics in large river basins based on the application of spaceborne remote sensing. This literature review summarizes the status and spatial distribution of EO-based investigations in the 28 largest river basins across the globe.

Chapter 4 addresses the geographical characteristics of the selected river basins in South Asia, including the Indus, Ganges, Brahmaputra, and Meghna rivers, with particular focus on their general properties, physical geography, and socio-economic characteristics. This study area is used for both the method development and geoscientific analyses.

Chapter 5 introduces the novel methodological framework for the preparation of geospatial and multisource time series, their harmonization to a common spatio-temporal coverage and resolution, and the application of statistical time series analysis techniques to characterize land surface dynamics across spheres. To this end, the utilized time series data are presented. Here, the focus lies on the EO-based variables vegetation greenness, surface water area, and snow cover area. Next, relevant statistical analysis methods for quantification of trends and changes in seasonality as well as for estimation of controlling variables through the application of a causal discovery algorithm are introduced. Subsequently, the results derived for the selected river basins are presented and evaluated with respect to existing literature.

Chapter 6 investigates seasonal characteristics of land surface dynamics and relevant driving variables for the Indus, Ganges, Brahmaputra, and Meghna river basins. These analyses are performed at different spatial scales, including grids, river basins, elevation zones, and land use classes and include detailed analyses on direct and indirect influences on the land surface variables vegetation greenness, surface water area, and snow cover area.

Chapter 7 summarizes and concludes the entire thesis and investigates the fulfillment of the defined research questions and objectives (Chapter 1.2 and 1.3). Furthermore, challenges and opportunities for future developments are briefly discussed.

Chapter 2

*Theoretical Background on Time Series**

This chapter introduces fundamental information on time series terminology (Chapter 2.1), suitable remote sensing as well as further geospatial data for time series analysis (Chapter 2.2), and methods for time series analysis (Chapter 2.3).

2.1 Time Series Terminology

A time series is a collection of observations recorded sequentially in time. Time series are frequently used in a variety of disciplines, including economic and financial time series (e.g. wheat price, company profits), physical time series (e.g. meteorology), and demographic time series (e.g. population counts) (Chatfield and Xing, 2019). Furthermore, time series observations can be distinguished in continuous or discrete measurements. The term 'continuous' is used when measurements are conducted continuously through time. In comparison, the term 'discrete' denotes time series with observations recorded only at specific times, usually equally spaced points in time (Chatfield and Xing, 2019). In this thesis, discrete time series are utilized. When only using one variable, the time series is considered to be univariate. On the other hand, time series are categorized as multivariate when including observations of multiple variables. Moreover, time series usually consist of three components, including the trend, seasonal, and random or remainder component (Kuenzer et al., 2015a; Verbesselt et al., 2010). Using a traditional additive decomposition model, the respective components can be retrieved as demonstrated in Figure 2.1. With more detail, the seasonal component might characterize the impacts of meteorological seasons on vegetation greenness, whereas the trend component might capture the long-term effect of increasing agricultural land use intensity (greening) or vegetation degradation (browning). The remainder component might reflect short term influences of e.g. drought events.

*Parts of this chapter have been published in Uereyen and Kuenzer (2019); Uereyen et al. (2022a)

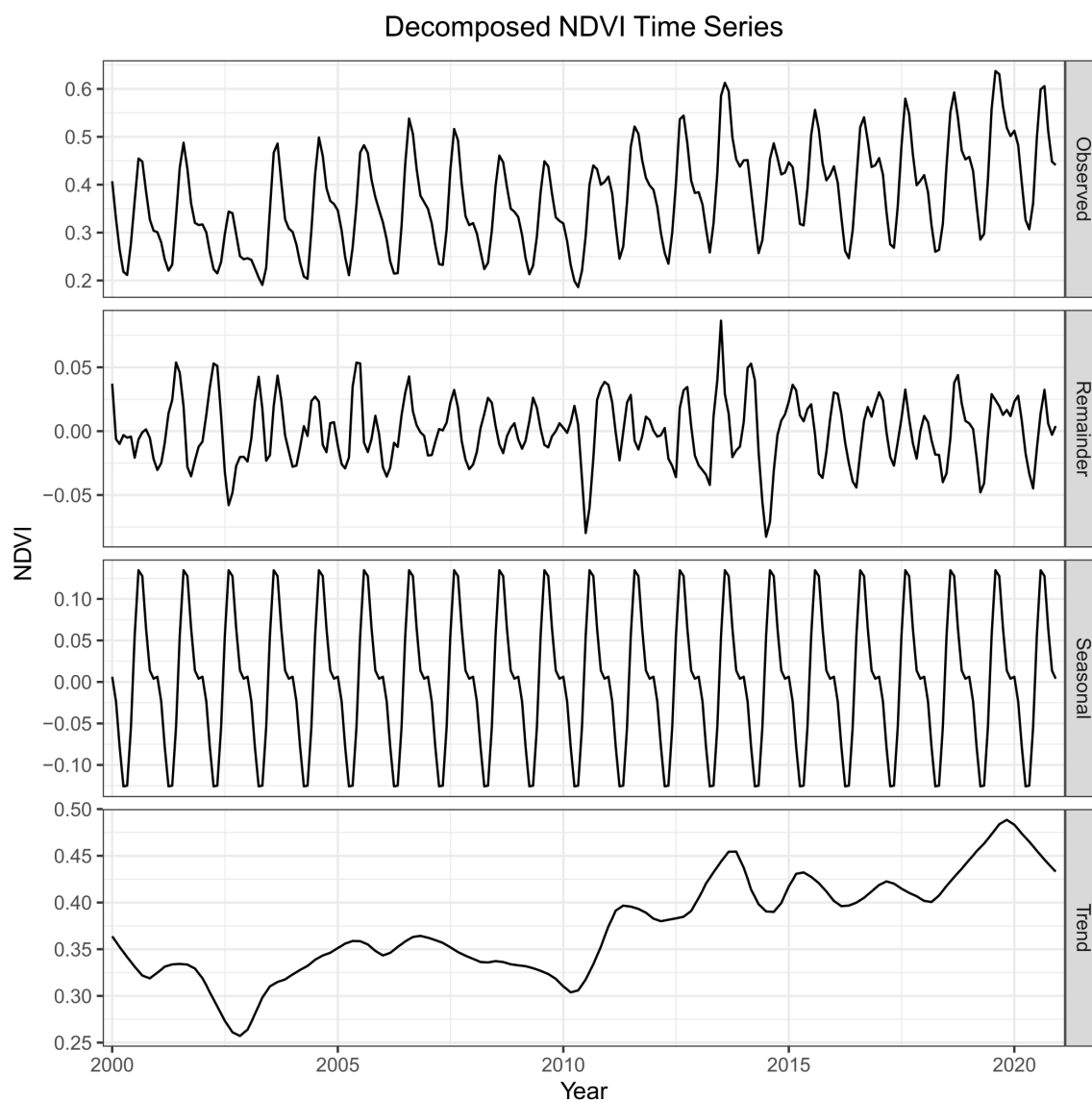


Figure 2.1: Exemplary time series of the normalized difference vegetation index (NDVI) decomposed into the time series components remainder, seasonal, and trend.

2.2 Geoscientific Time Series Data

In this thesis, the term “geoscientific time series” covers the range of all geospatial time series data, including remote sensing-based, modeled, and reanalyses data. Some years ago, mapping land surface change with a few remote sensing images covering a certain time period, such as a decade, was already considered as a detailed time series analysis (Southworth and Muir, 2021; Woodcock et al., 2020). Nowadays, spatially and temporally detailed EO-based time series analyses of the Earth system are enabled in the course of open data policies and ever-increasing amount of remote sensing imagery at global scale (Sudmanns et al., 2019; Wulder et al., 2012). Not only the emerging availability of remote sensing time series, but also the increasing programming skills of researchers and the ever-enhancing data storage and processing capacities facilitated this progress (Kuenzer et al., 2015a). With

numerous satellite missions observing the Earth's surface, only a limited number of EO instruments can be utilized for multidecadal time series analysis. Considering optical remote sensing missions, these include the AVHRR and the Landsat missions. These two missions allow time series analysis covering several decades. Specifically, the AVHRR and Landsat missions were launched in 1978 and 1972, respectively. As previously mentioned, the AVHRR mission provides images at coarse spatial (1 km) and daily temporal resolution, whereas the Landsat mission records images at medium spatial resolution (30 m), but has a minimum revisit time of 16 days. Recently, the archive of the MODIS instrument on board the Terra platform crossed a period of 20 years. Terra MODIS was launched in 1999 and in comparison to AVHRR, MODIS provides a spatial resolution of 250 and 500 m and a daily temporal resolution as well. With an additional MODIS sensor on board the Aqua platform (launched in 2002), it is possible to generate temporally dense time series for analysis of land surface dynamics. Furthermore, with the launch of the European Copernicus Sentinel-2 instrument in 2015, harmonized datasets of optical EO sensors (e.g. Landsat, Sentinel-2) will provide a long-term archive for analyses at higher spatial resolution than the AVHRR and MODIS sensors. A joint use of optical Landsat and Sentinel-2 data enables the generation of time series at higher temporal resolution. Here, it has to be noted that the revisit time of optical sensors might be considerably reduced due to cloud coverage. In this connection, SAR missions have the capability to monitor the Earth's surface independently of daylight and weather conditions. The European Environmental Satellites (ERS)-1 and ERS-2 missions with several instruments on board, including SAR were launched in 1991 and 1995. Together, both SAR missions provide time series over a long period. Today, these missions are continued by successor missions such as the Sentinel-1 platform being launched in 2014. In addition, observations from spaceborne SAR missions such as the Shuttle Radar Topography Mission (SRTM) or the TerraSAR-X mission are used to derive Digital Elevation Models (DEMs) at global scale. A DEM is fundamental to applications with respect to the topography.

Moreover, as introduced in Chapter 1.1.1, many subsequently generated products based on the aforementioned satellite missions exist. As already stressed, studies investigating land surface dynamics by means of remote sensing data usually focus on single EO-based land surface variables, whereas a joint analysis of multivariate time series involving several spheres is still rarely performed. For example, the Terra and Aqua MODIS instruments provide a comprehensive product suite encompassing various geophysical and thematic variables, such as vegetation indices or binary as well as multiclass land cover classifications. A variety of gridded time series data covering various spheres is listed in Table 2.1. These gridded geospatial products can be used to generate long-term time series and to analyze Earth surface dynamics. Additional time series on climatic, hydrological, and an-

thropogenic variables are available through various sources and foster the generation of a multivariate feature space. Multivariate time series encompassing divers components of the Earth system enable the quantification and evaluation of interdependencies across spheres.

Besides gridded time series data, further geospatial data describing i.e. the topography or climate zones might be integrated into the multivariate analysis of land surface dynamics. In this regard, the SRTM DEM is widely used to characterize the topography and retrieve

Table 2.1: Summary of selected open gridded geospatial time series characterizing land surface parameters across spheres. The temporal resolution of the time series is denoted as yearly (Y), monthly (M), biweekly (B), daily (D), hourly (H), multi-temporal (MT), and composites (C).

Time Series	Spatial Res. [km]	Temporal Res.	Reference
Biosphere			
MODIS Surface Reflectance ¹	0.5	2000–pr. (D)	Vermote and Wolfe (2015)
MODIS NDVI	0.25, 0.5, 1, 5.6	2000–pr. (C, M)	Didan and Munoz (2019)
Global Forest Change	0.03	2000–2020 (Y)	Hansen et al. (2013)
AVHRR LAI	5	1981–pr. (D)	Claverie et al. (2016)
AVHRR NDVI	8	1981–2015 (B)	Pinzon and Tucker (2014)
DLR Bethy NPP/GPP	1	1998–2015 (M)	Wißkirchen et al. (2013)
MODIS GPP	1	2000–pr. (C)	Running et al. (2015a)
MODIS NPP	1	2000–pr. (Y)	Running et al. (2015b)
Copernicus Global Land Service LAI	0.3	2014–pr. (D)	Fuster et al. (2020)
Hydrosphere			
JRC Global Surface Water Layer	0.03	1984–2019 (M)	Pekel et al. (2016)
DLR Global WaterPack	0.25	2003–pr. (D)	Klein et al. (2017)
GloFAS-ERA5 River Discharge	10	1979–pr. (D)	Harrigan et al. (2020)
ITSG-Grace	100	2003–2016 (D)	Kvas et al. (2019)
Copernicus Global Land Service Water Level ²	virtual stations	2002–pr. (D)	Calmant et al. (2013); Crétaux et al. (2011)
Cryosphere			
DLR Global SnowPack	0.5	2000–pr. (D)	Dietz et al. (2015)
ESA CCI Snow Cover (MODIS)	1	2000–2019 (D)	Nagler et al. (2021)
ESA CCI Snow Cover (AVHRR)	5	1982–2019 (D)	Näegeli et al. (2021b)
ESA CCI Snow Water Equivalent	25	1979–2018 (D)	Luoju et al. (2020)
Lithosphere			
GLEAM Soil Moisture	25	1980–2020 (D)	Martens et al. (2017)
ESA CCI Soil Moisture	25	1978–2020 (D)	Dorigo et al. (2017)
Anthroposphere			
ESA CCI Land Cover	0.3	1992–2019 (Y)	European Space Agency (2017)
MODIS Land Cover	0.5	2001–2019 (Y)	Friedl et al. (2002)
HILDA+ Land Cover/Land Use	1	1960–2019 (Y)	Winkler et al. (2021)
DLR World Settlement Footprint Evolution	0.03	1985–2015 (Y)	Marconcini et al. (2021)
JRC Global Human Settlement Layer	0.03	1975, 1990, 2000, 2014 (MT)	Pesaresi et al. (2013)
DMSP-OLS/VIIRS Nighttime Lights	1	1992–pr. (Y)	Li and Zhou (2017)
Gridded Population Counts	1	2000–2020 (Y)	WorldPop and CIESIN (2018)
Land-Atmosphere Interactions, Meteorological Variables			
ERA5/ERA5-Land ³	25/10	1950–pr. (M, H)	Hersbach et al. (2020); Muñoz-Sabater et al. (2021)
TerraClimate ³	4	1958–2020 (M)	Abatzoglou et al. (2018)
Climate Research Unit ³	50	1901–2020 (M)	Harris et al. (2020)
CHIRPS Precipitation ⁴	5	1981–pr. (D, M)	Funk et al. (2015)
PERSIANN-CDR Precipitation ⁵	25	1983–pr. (D)	Nguyen et al. (2019)
MODIS Land Surface Temperature	1, 5.6	2000–pr. (D, C, M)	Wan et al. (2015)
MODIS Fractional Cloud Cover	100	2000–pr. (D, M)	Platnick et al. (2017)

¹ Surface reflectance might be used to calculate index variables covering any sphere.

² River water level estimations at intersection of river and satellite ground track.

³ Product suite includes multiple variables.

⁴ Only covering 50°S–50°N.

⁵ Only covering 60°S–60°N.

further topographical features, such as the slope and aspect (Farr et al., 2007). Recently, the Copernicus DEM was published at a spatial resolution of 30 and 90 m for license free use (European Space Agency and Sinergise, 2021). The Copernicus DEM is an updated version of the TerraSAR-X-Add-on for Digital Elevation Measurements (TanDEM-X) DEM (Wessel et al., 2018) and the WorldDEMTM (Collins et al., 2015), with the latter being produced by Airbus for commercial use. In addition, the HydroSHEDS data provide hydrographic information for regional to global scale applications, including river systems and river basin boundaries (Lehner et al., 2008). Furthermore, Beck et al. (2018) published global maps of Köppen-Geiger climate classification at a spatial resolution of 1 km. This data is useful i.e. to geographically stratify the land surface into climate zones of interest.

2.3 Time Series Analysis

In general, time series analysis is performed to extract meaningful insights from series of observations through exploration of the series' characteristics and identification of patterns in the past (Krispin, 2019; Shumway and Stoffer, 2017). In this context, Figure 2.2 illustrates the overall steps that are conducted during time series analysis. In the following,

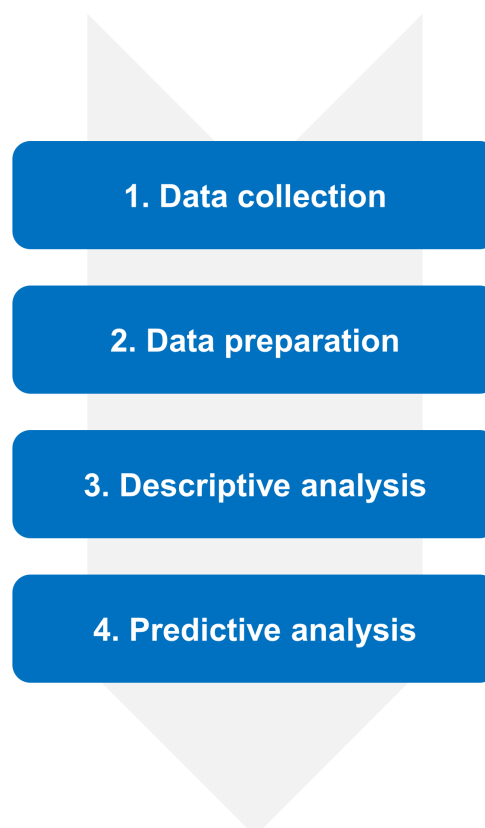


Figure 2.2: General steps performed during time series analysis.

these steps are described with respect to analysis of geoscientific time series. First, openly available time series data are collocated from various sources, such as data portals of space agencies or other initiatives. The second step covers data preparation, where the investigated time series mostly require the application of tailored preprocessing steps. Specifically, the raw data are usually present in unstructured data format, which is why data cleaning and gap-filling might be necessary. For example, this includes the exclusion of pixels with cloud contamination or other artifacts and then the interpolation of respective missing values (e.g. Eckert et al. 2015; Cao et al. 2018b). Also, an important prerequisite for joint analysis of multivariate time series is the harmonization of the multisource feature space to common characteristics with respect to their spatial and temporal features. This step might require the transformation of spatial characteristics, such spatial resolution and projection as well as aggregation of temporal intervals, e.g., from daily to weekly or monthly observations. Afterwards, the prepared feature space can be used to perform descriptive analysis to gain insights from the time series (Uereyen et al., 2022a). Considering descriptive time series analysis with remote sensing data, methods include the calculation of summary statistics at temporal or spatial scales, the extraction of patterns through data visualization or statistical methods, the calculation of phenological shifts, and the attribution of changes in a time series through the statistical analysis of relationships between multiple variables (de Beurs et al., 2015; Kuenzer et al., 2015a; Woodcock et al., 2020).

Over the last decades, numerous studies dealt with time series analyses investigating, i.e., the change of vegetation condition as well as its relation to driving variables. Respective time series analysis techniques can be categorized into univariate and multivariate approaches. The univariate domain measures one variable over time and includes monotonic trend estimation (e.g. Chen et al. 2019; Fensholt and Proud 2012; Hu et al. 2020; Lamchin et al. 2018; Xu et al. 2020), changepoint detection (e.g. Detsch et al. 2016a; Forkel et al. 2013; Kennedy et al. 2010; Li et al. 2021; Verbesselt et al. 2010; Zhao et al. 2019a), and calculation of phenological metrics (e.g. Chen et al. 2015; Jönsson and Eklundh 2004; Park et al. 2020; Tomaszewska et al. 2020). The existence of a monotonic trend and its magnitude can be calculated by means of statistical methods such as the Mann-Kendall test in association with the Theil-Sen slope estimator or regression coefficient tests (Wang et al., 2020). Regarding the derivation of changes within time series and breakpoints in the trend and seasonal component, the methods Breaks for Additive Season and Trend (BFAST) (Verbesselt et al., 2010) and Landsat-based Detection of Trends in Disturbance and Recovery (LandTrendr) (Kennedy et al., 2010) are widely employed. Recently, a further algorithm called Bayesian Estimator of Abrupt change, Seasonal change, and Trend (BEAST) to estimate breakpoints was proposed (Zhao et al., 2019a). For calculation of phenological metrics, several approaches exist. A widely applied tool allowing for analysis of seasonal

properties of time series is named Timesat (Jönsson and Eklundh, 2002, 2004). A simpler approach to derive basic phenological metrics such as beginning as well as end of season and length of season is applied by Chen et al. (2015). Another study investigates changes in seasonal properties by computing the difference in the amplitude and phase of the seasonal component of a time series for two periods (Detsch et al., 2016a).

Furthermore, multivariate time series analyses have mostly the objective to assess the relation between two or even more variables as well as to explore interplays in a high dimensional feature space. In this regard, methods include traditional correlative approaches between two variables (e.g. Gessner et al. 2013; Notarnicola 2020; Sarmah et al. 2018) or partial correlation using additional controlling variables, including temporal lags (cross-correlation) (e.g. John et al. 2018; Tan et al. 2015; You et al. 2021; Wang et al. 2018c). For example, studies evaluate the relation between vegetation condition and climatic variables within meteorological seasons or perform correlation analysis with temporal lags to identify effects of past influences on a variable (Gessner et al., 2013; Sarmah et al., 2018). However, correlation analysis might result in spurious links, which is why interpretations need to be conducted carefully. To avoid spurious links due to time series variables having a co-varying trend, studies usually remove the trend component from the time series, also called detrending, prior to the calculation of the correlation coefficient (e.g. Peng et al. 2013). Likewise, studies apply methods, which have their origin in econometric literature, such as the Granger-causality concept (Granger, 1969), to quantify the evidence for a true causal link between investigated time series variables (IPCC, 2013). Over the last years, further investigations on causal inference from empirical data provided important insights and directions on the usage of causal discovery algorithms (Krich et al., 2020; Papagiannopoulou et al., 2017; Reygadas et al., 2020; Runge et al., 2019a,b). In this context, new methods enabling the derivation of causal networks became available. A causal network describes and quantifies the relationship between variables at different time steps in the past. Besides the Granger-causality concept, which was initially developed for bivariate time series (e.g. Xie et al. 2019), but was lately also applied to a feature space consisting of multiple time series variables (Papagiannopoulou et al., 2017), Runge (2018) proposed a new approach called Peter and Clark Momentary Conditional Independence (PCMCI) to construct time series graphs and evaluate causal networks. More specifically, PCMCI utilizes causal graphs to evaluate the relation between multiple variables at past temporal lags while being capable of handling a high dimensional feature space, highly autocorrelated variables, and direct and indirect links (Runge, 2018).

Ultimately, as depicted in Figure 2.2, the fourth step of time series analysis might involve the application of statistical methods to forecast future values of a given time series

(Koehler and Kuenzer, 2020). The general purpose of time series analysis is to understand the mechanisms that impact the observed series and past patterns and characteristics. Based on the obtained knowledge through time series analysis, a prediction or forecast of future values is enabled (Montgomery et al., 2015). Since time series prediction is not within the scope of this thesis, this topic will not be covered in more depth.

2.4 Summary

First, this chapter provided background information on time series terminology in general. Afterwards, remote sensing time series and their spatial and temporal characteristics were presented. It was noted that remote sensing time series with comparatively high spatial resolution come at the cost of a reduced temporal resolution and vice versa. In this regard, it was emphasized that only a reduced number of remote sensing missions enable the generation of spatially and temporally consistent time series over multiple decades. A detailed overview of available time series products was provided and the term “geoscientific time series” including the full range of geospatial time series data was introduced. Apart from remote sensing time series further variables, e.g., based on climate reanalyses, enable not only the investigation of land surface change, but also the influence of respective drivers. In this context, time series analysis techniques with respect to remote sensing applications were presented, including the collection and preprocessing of time series as well as descriptive analysis methods.

Chapter 3

*A Review on Remote Sensing-Based Analyses of Large River Basins**

This chapter provides a detailed review on EO-based analyses for large river basins worldwide. To this aim, a systematic review based on 287 research articles is presented (Chapter 3.1). The results of the review comprise the spatial and temporal availability of studies investigating EO-based analyses of the worldwide 28 largest river basins by their drainage area. Furthermore, potentials and challenges of remote sensing and further geospatial time series with respect to monitoring of large river basins are discussed (Chapter 3.2). Finally, requirements of EO-based analyses for large river basins is elucidated.

As previously introduced in Chapter 1.1.2, river basins are a functional unit of the Earth's surface. In hydrology, a river basin is the most common geographical entity of consideration (Davie and Quinn, 2019). In this context, the terms “catchment”, “watershed”, and “drainage area” are used synonymously. A river basin can be defined as “the area of land from which water flows towards a river and then in that river to the sea” (Davie and Quinn, 2019) or outlet unless it is i.e. evaporated or stored in a reservoir. Based on topographical data and the assumption that all water on the Earth's surface flows downhill, it is possible to delineate the boundaries of a river basin. A sketch of a river basin is illustrated in Figure 1.4. In the headwater or upper river basin, the river streams are generally smaller and steeper. In comparison, rivers are broader and gently sloping in downstream or lower river basins close to the mouth of the river (Strahler, 2013). Furthermore, a large river basin, e.g. at continental scale, can be hierarchically divided into smaller subbasins. Regarding all land area above the outlet point, environmental change, human-induced or not, might have considerable impacts not only on the water budget of a river basin, but also on all sector that depend on water resources. Since climate and human-induced changes are already widespread on

*Parts of this chapter have been published in Uereyen and Kuenzer (2019)

the Earth's surface, monitoring of river basins by means of spaceborne remote sensing enables the assessment and analysis of trends in land surface variables as well as drivers of land surface dynamics across spheres within a natural system.

3.1 Results of the Literature Review

This review summarizes all existing research articles investigating EO-based characterization of large river basins between 2000 and the first quarter of 2019. Where appropriate recent studies are included in this review as well. In addition, this review quantifies how EO can contribute to monitoring of land surface and surface water parameters in regards of large river basins. River basins are usually characterized by their mean annual discharge, total length of the river, or the total size of the drainage area. Here, the selection of relevant river basins was conducted based on the size of their drainage area. In order to include at least one large river basin per continent, all river basins having a greater drainage area than 500,000 km² were selected. This criterion results in the 28 largest river basins worldwide being visualized in Figure 3.1 along with selected key characteristics. For a systematic review of the literature, all existing Science Citation Index (SCI) listed research articles investigating EO-based analyses on land surface dynamics in large river basins, particularly focusing on land surface parameters directly measurable at the Earth's surface by means of spaceborne remote sensing instruments, were identified. It has to be emphasized, that this review only considers studies dealing with the spatial entity of river basins. Respective literature search was performed on the databases of Web of Science as well as Scopus and resulted in 287 research articles. In order to gather relevant information for this review, the identified literature was evaluated with the aim of extracting details on defined parameters such as research topic, utilized remote sensing sensor type, spatial scale of the study area, and temporal resolution of the used remote sensing data. During literature review, the spheres biosphere, hydrosphere, and cryosphere were identified as superordinate categories. Further subcategories were defined based on the respective study topics of the reviewed research articles and assigned to one of the spheres. In the following, the study topic "urban", as part of the anthroposphere was assigned to the category biosphere. The categories and corresponding study topics are listed in Table 3.1.

Table 3.1: List of defined categories and identified study topics.

Category	Study topic
Biosphere	Agriculture, coastline, land cover and land use, urban, vegetation
Hydrosphere	River discharge, river water level, surface water, water quality
Cryosphere	Permafrost, river and lake ice, snow and ice cover

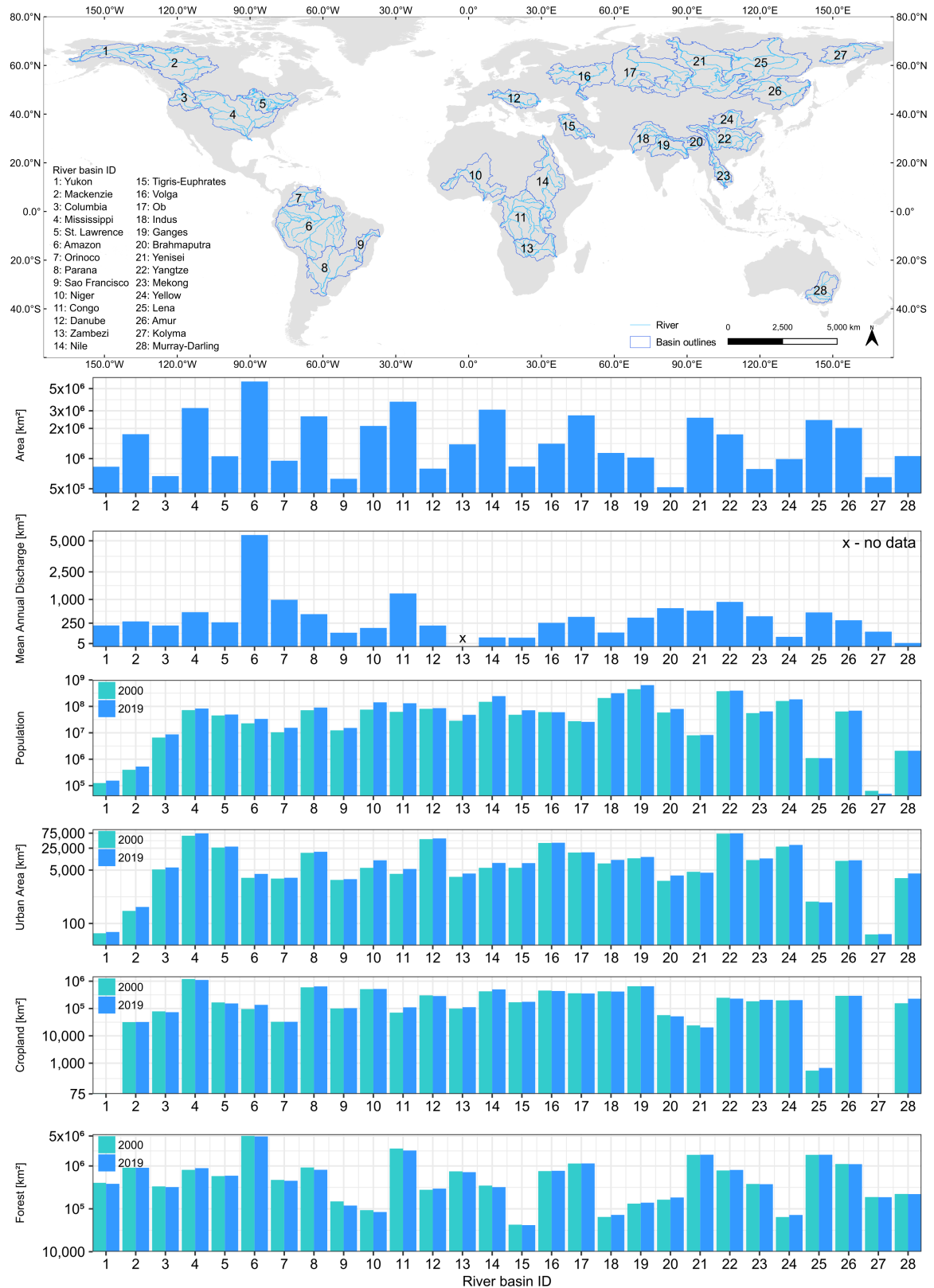


Figure 3.1: Features of the worldwide 28 largest river basins. Vector data outlining the river basins and rivers as well as area and mean annual discharge are obtained from the GRDC (GRDC, 2020; Lehner et al., 2008). Population counts are extracted from the WorldPop data (Lloyd et al., 2019). The spatial characteristics on land use classes are calculated based on HILDA+ (Winkler et al., 2021). Modified after Ureyen and Kuenzer (2019).

3.1.1 Distribution of Identified Study Topics

As previously stated, all reviewed studies were categorized into one of the research categories biosphere, hydrosphere, and cryosphere. To perform a further classification, more detailed study topics were defined (see Table 3.1). As illustrated in Figure 3.2, more than half of the 287 reviewed research articles were found to belong to the category biosphere (~53 %). With more detail, the most investigated study topic dealt with monitoring of vegetation parameters (~39 %). Next, ~32 % of the reviewed research articles performed multi-class land cover and land use classifications. The identified study topics urban and agriculture had a percentage of ~12 %, respectively (see Figure 3.2). Moreover, mapping of coastlines was conducted in approximately 5 % of all reviewed studies. In comparison, ~39 % of all reviewed research articles were associated with the research category hydrosphere. More specifically, this research category involved study topics focusing on the monitoring of surface water area and further detailed river properties with spaceborne remote sensing. The study topic surface water area was investigated most with a share of ~45 %. Furthermore, reviewed studies investigating the river properties water quality, river water level, and river discharge had a percentage of ~27 %, ~16 %, and ~12 %, respectively. On the other hand, ~8 % of all reviewed studies were found to belong to the research category cryosphere. The identified study topics snow and ice cover, permafrost, and river and lake ice had a share of ~62 %, ~19 %, and ~19 %, respectively.

In addition, Figure 3.3 depicts the number of reviewed studies per large river basin in consideration of the investigated research category. For example, for the Amazon, Congo, Mekong, Yangtze, and Yellow river basin, the research category biosphere was studied in more than half of the total number of studies in each of the respective river basin. On the other hand, in case of the Brahmaputra, Columbia, Orinoco, Sao Francisco, St. Lawrence and Volga river basin, the study topic of all reviewed research articles was associated with the research category hydrosphere. Regarding large river basins being located in the Arctic region or those having their source region in a highly mountainous environment, such as the Lena, Indus, or Tigris-Euphrates rivers, the research category cryosphere was found to have a higher share.

3.1.2 Geospatial Distribution of Studies

Considering the geospatial distribution of the reviewed studies, the results of this literature review are displayed in Figure 3.4. More specifically, this figure differentiates between investigated river basin (see Figure 3.4a) and country (see Figure 3.4b). In this context, the Amazon river basin was identified as the most studied large river basin. In particular, ~21 %

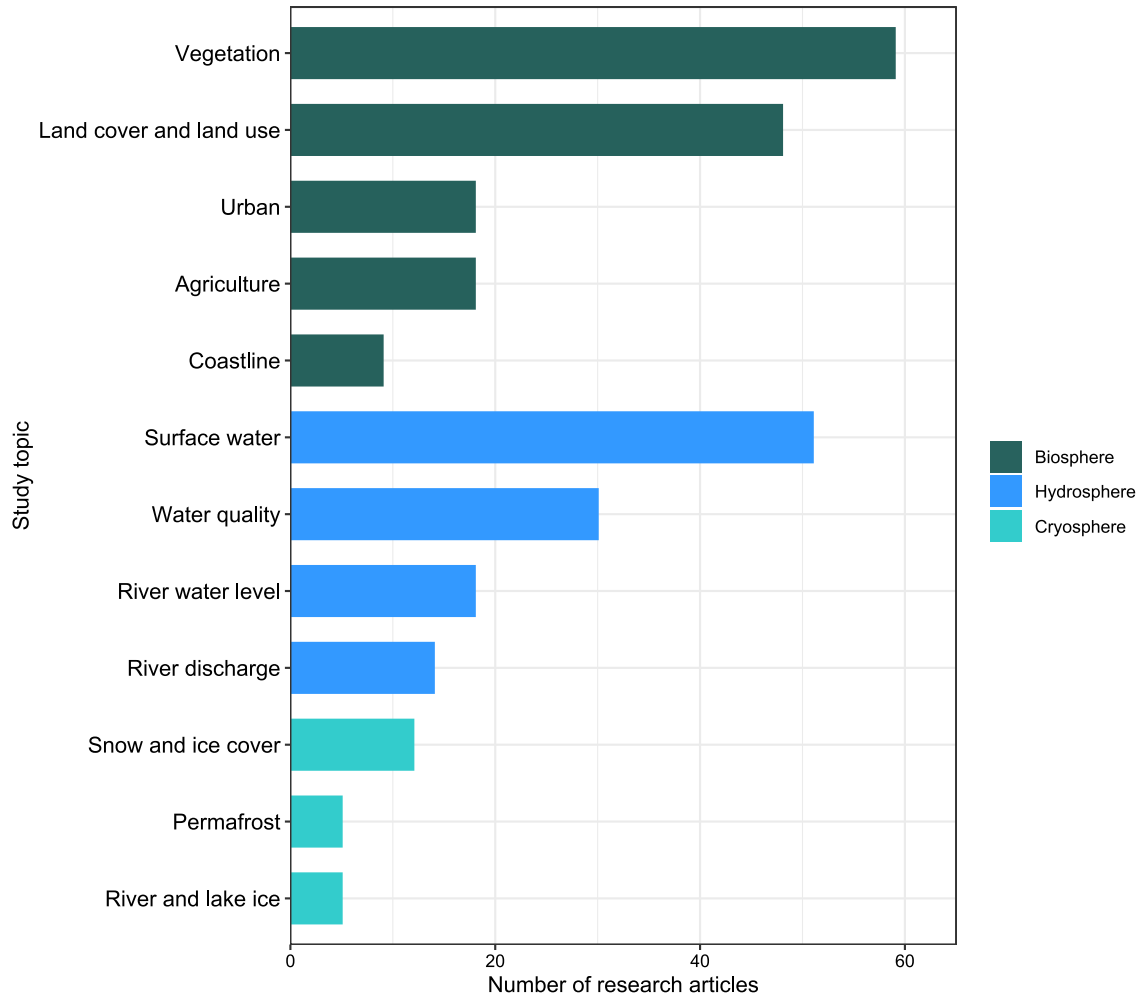


Figure 3.2: Frequency of identified study topics per research category. Modified after Uereyen and Kuenzer (2019).

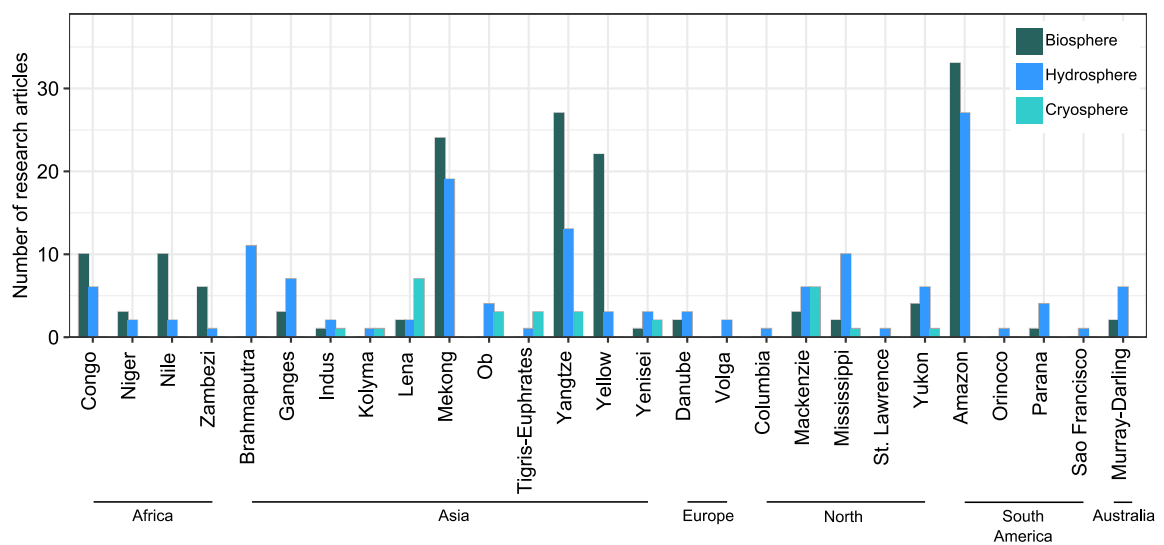


Figure 3.3: Categorization of reviewed studies by investigated river basin and research category. Modified after Uereyen and Kuenzer (2019).

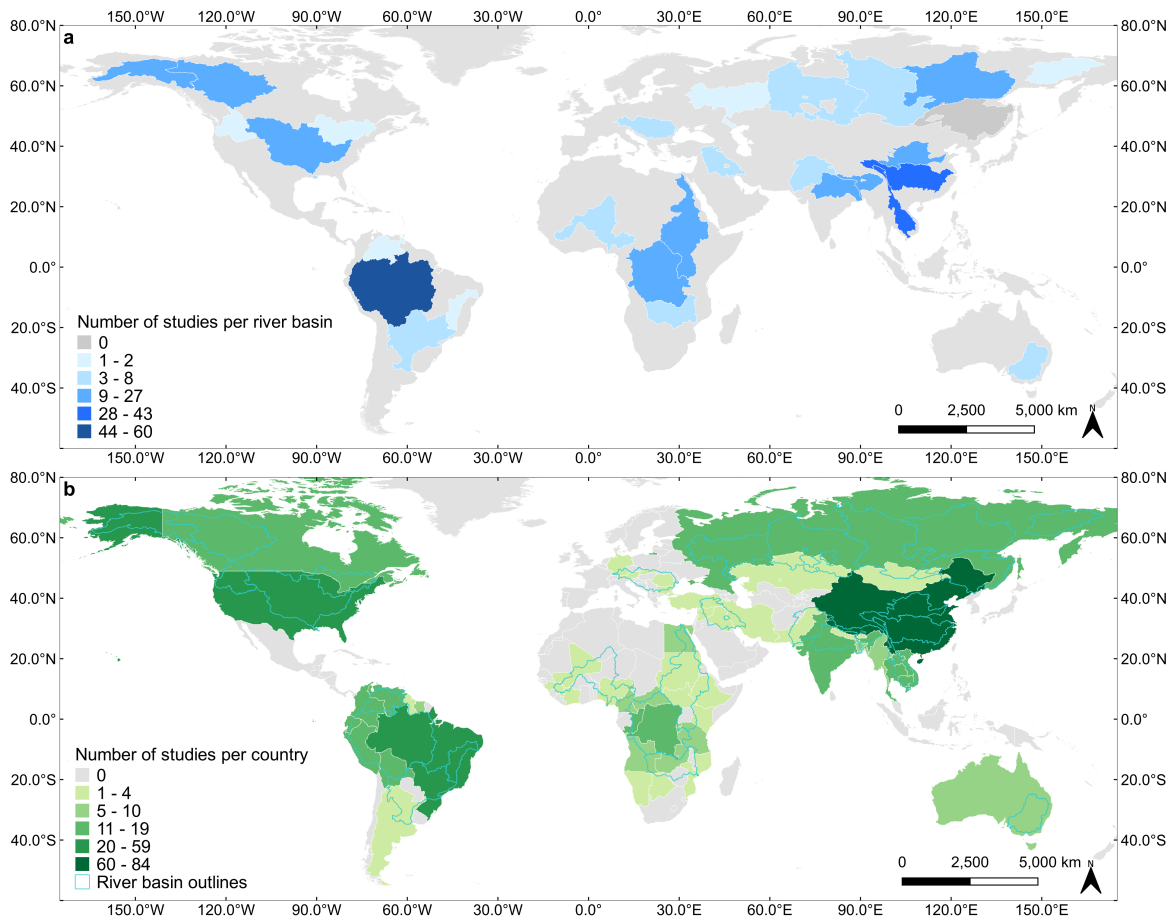


Figure 3.4: Maps demonstrating (a) the spatial distribution of the number of reviewed research articles per large river basin and (b) the number of reviewed research articles per investigated country. Modified after Uereyen and Kuenzer (2019).

of all reviewed studies dealt with the Amazon (e.g. Hilker et al. 2015; de Moura et al. 2015). River basins being located in Southeast Asia, particularly the Yangtze, Mekong, and Yellow river basin were found to feature a comparatively high number of research articles (e.g. Leinenkugel et al. 2013; Rao et al. 2018; Wang et al. 2018b). Here, the share of studies with regards to the total number of reviewed studies amounts to $\sim 15\%$, $\sim 15\%$, and $\sim 9\%$, respectively. Moreover, the Congo river basin follows the Amazon river basin having the second largest drainage area. Yet, only $\sim 6\%$ of the reviewed research articles investigated the Congo river basin (e.g. Duveiller et al. 2008; Yan et al. 2017). The Mackenzie and Mississippi river basins are both located in North America and were each investigated in $\sim 5\%$ of all reviewed studies (e.g. Du et al. 2016; Lam et al. 2018). Additionally, Figure 3.4a reveals that river basins being located in the Arctic regions were comparatively studied less. In particular, two research articles were identified for the Kolyma (Nitze et al., 2017; Griffin et al., 2018) and Volga river basins (Zhu et al., 2013; Troitskaya et al., 2014), respectively.

The number of reviewed studies with respect to the investigated country is shown in Figure 3.4b. Besides the quantification of the frequency in studied river basins, a differentiation

by administrative boundaries enables a further detailed assessment of regions within the river basins being of particular interest. In this connection, Figure 3.4b unravels countries of particular interest, despite river basins being a functional unit independent of administrative boundaries. For example, among all studies investigating the Amazon river basin, parts of this river basin being within the administrative units of Brazil were explored most (e.g. Arvor et al. 2018; Costa et al. 2002; Pereira et al. 2002; Furtado et al. 2016). Except Brazil ($\sim 21\%$), the countries China, Vietnam, and the United States of America were found to be of special interest as well. These countries were studied in $\sim 29\%$, $\sim 11\%$, and $\sim 8\%$ of all reviewed articles, respectively. Also, it becomes evident that for a number of transboundary river basins, such as the Danube, Niger, Nile, and Zambezi some riparian countries were not included in the investigations.

In regards of the investigated administrative units, Figure 3.5 summarizes the first author's institutional affiliations. At this, a coherence between the institutional affiliations and the number of reviewed research articles per country is discernible (see Figure 3.4b). For example, research conducted by first authors associated with an institution in China also investigated a river basin located in China in $\sim 89\%$ of the cases. Likewise, considering first authors with an institutional affiliation in Brazil, the share amounts to $\sim 75\%$. First authors affiliated with the United States of America investigated river basins located on the entire American continent in $\sim 60\%$ of all respective studies. On the other hand, first authors

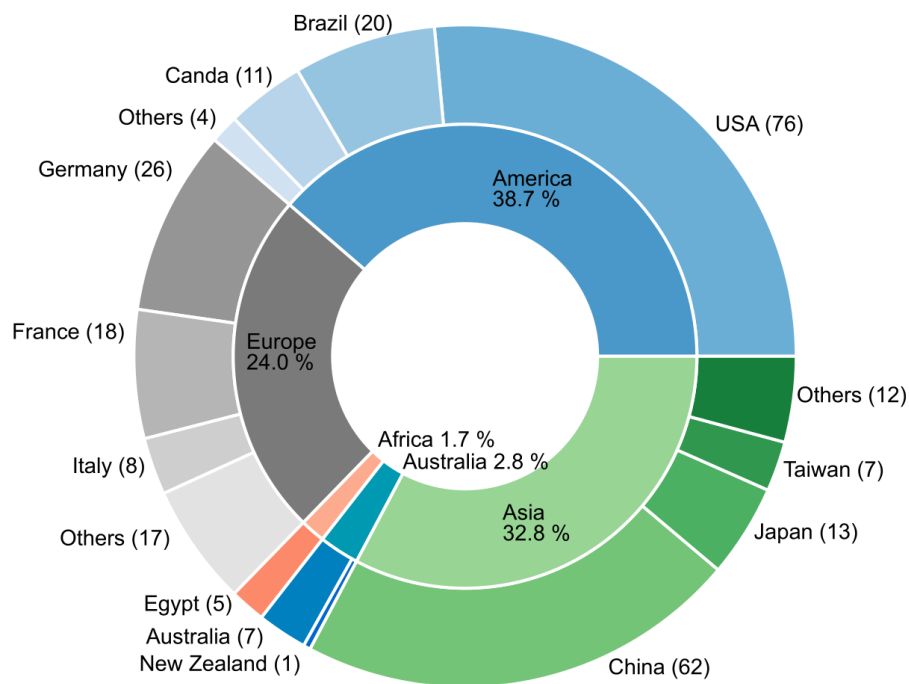


Figure 3.5: Counts of identified first author affiliations by nation and continent. The numbers in brackets denote the sum of the reviewed studies. Modified after Uereyen and Kuenzer (2019).

having their institutional affiliation in Germany are studying river basins located in Asia in $\sim 85\%$ of the cases. It is also noteworthy, that $\sim 42\%$ of all reviewed research articles were conducted by co-authors with cross-border collaborations.

3.1.3 Spatial Extent of Studies

Furthermore, the reviewed studies were classified in consideration of the spatial extent of investigated river basin. In detail, the research articles were assigned to one of the category “basin”, “subbasin”, and “regional”. In case a study investigated one of the large river basins at the spatial scale of the entire basin, it was associated with the category basin. In comparison, the category subbasin was used, if a study dealt with a functional subset of one of the large river basins, including e.g. the source or delta region. Ultimately, a study was assigned to the category regional, if it has a research focus in regards of one of the selected large river basins, but is spatially not related to the functional unit of a river basin.

Accordingly, Figure 3.6 summarizes the spatial extent of the reviewed studies for each of the large river basin and reveals that the number of studies at the entire spatial scale of a river basin were found to be comparatively low. Only $\sim 14\%$ of all studies conducted analyses at the scale of an entire basin. On the other hand, $\sim 37\%$ of the investigations were at subbasin and $\sim 49\%$ at regional scale. More specifically, basin wide studies were mostly performed for the Amazon river basin ($\sim 4\%$) (e.g. Chapman et al. 2015; Frohling et al. 2011). Next, as demonstrated in Figure 3.6, the second most basin wide applications were conducted for the Murray-Darling river basin in Australia ($\sim 2\%$) (e.g. Heimhuber et al. 2017; Tulbure et al. 2016). Considering the category subbasin, most studies were

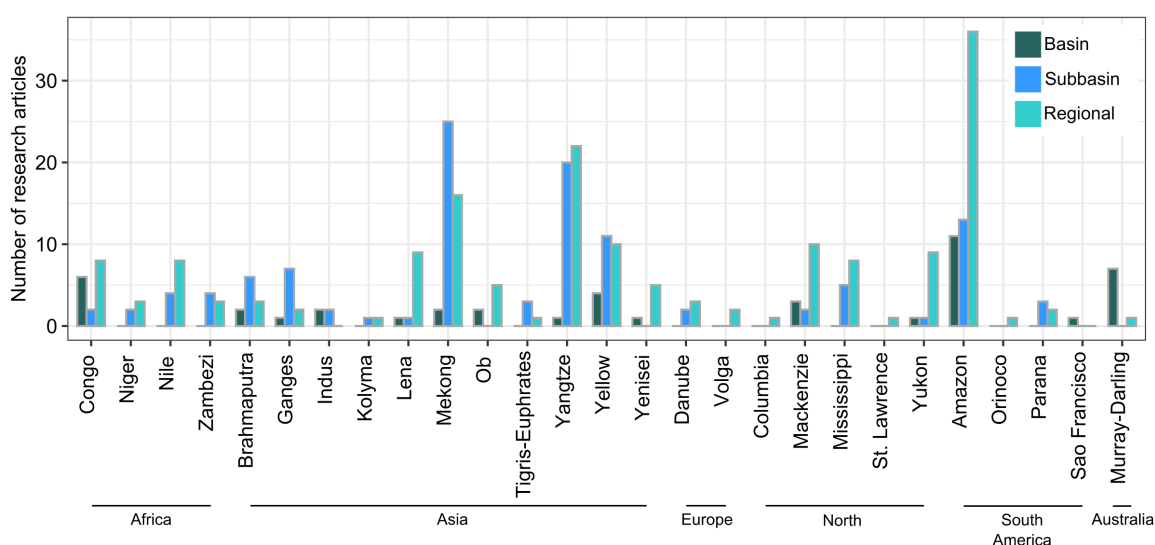


Figure 3.6: Count of reviewed research articles with respect to the selected large river basins and the spatial scale of the study area. Modified after Uereyen and Kuenzer (2019).

conducted for the Mekong, Yangtze, and Yellow river basins. Here, most of these studies are spatially associated with the delta regions (e.g. Buono et al. 2017; Kontgis et al. 2015). At regional scale, most studies were performed for the Amazon (~13 %), Yangtze (~8 %), and Mekong (~6 %) river basins. Moreover, this literature review indicates that ~94 % of all studies investigated one river basin (e.g., Wang et al. 2018b; Ge et al. 2018; Broich et al. 2018). Only, the remaining ~6 % of all studies dealt with more than one river basin at the same time (e.g., Du et al. 2016; Kuenzer et al. 2015b; Thenkabail et al. 2005). Moreover, this review revealed that ~69 % of all research articles investigated a transboundary river basin. Yet, ~67 % of these transboundary studies only focused on the river basin area within one riparian country only.

3.1.4 Applied Remote Sensing Sensor Types

Figure 3.7 visualizes the utilized spaceborne remote sensing sensor types. The review indicates that optical remote sensing imagery were most frequently applied in the context of river basin analyses. In particular, ~61 % of all studies only used optical imagery. SAR imagery was used in ~13 % of the reviewed studies. In comparison, ~6 % solely relied

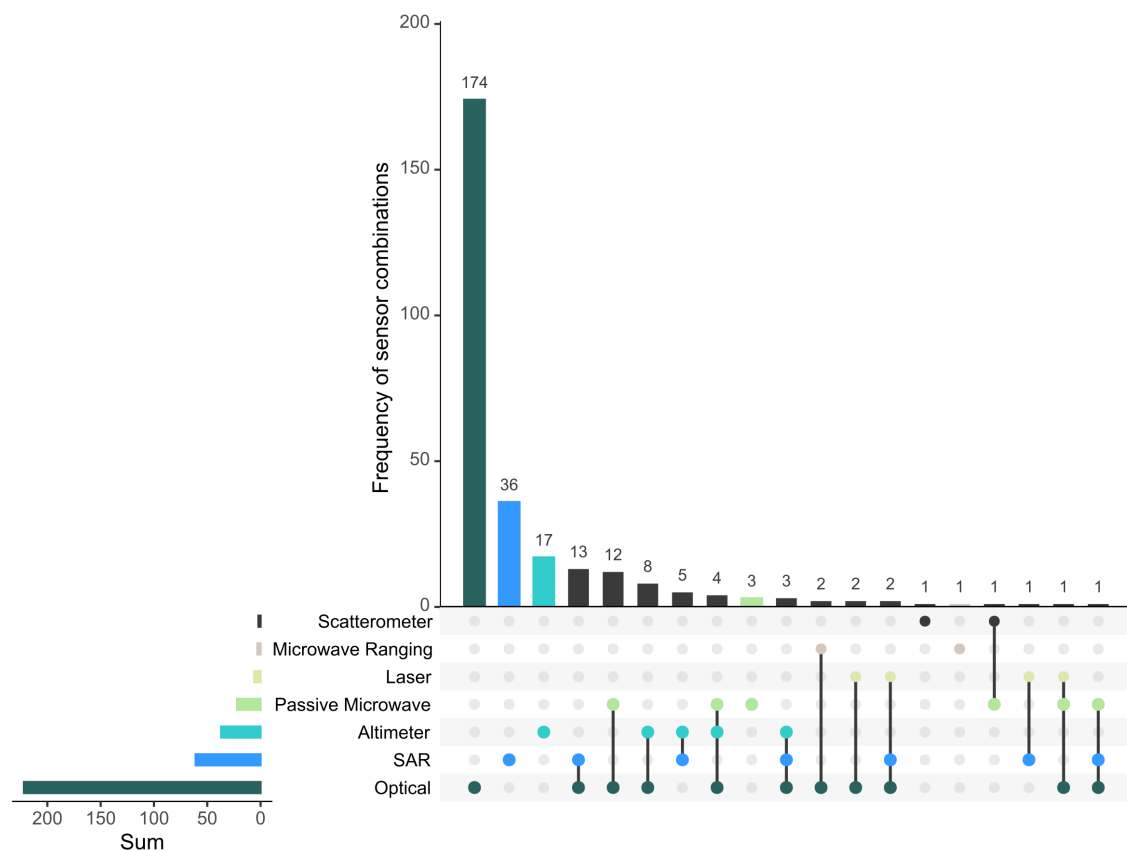


Figure 3.7: The utilized sensor types and their combinational use in the reviewed research articles. Modified after Uereyen and Kuenzer (2019).

on altimetry data. Furthermore, Figure 3.7 provides information on the synergistic use of remote sensing sensors. In this connection, optical and SAR imagery were most frequently used together ($\sim 5\%$). Optical and passive microwave imagery were utilized in $\sim 4\%$ of all reviewed studies.

Accordingly, a further differentiation of the used sensor types by research category and study topic in Figure 3.8 shows that optical imagery was also the most used sensor type across all research categories. Optical imagery was most frequently applied in the context of the study topics vegetation ($\sim 14\%$), land cover and land use ($\sim 13\%$), and surface water area ($\sim 9\%$). With respect to the topics vegetation and surface water area, SAR imagery was also widely used with a share of $\sim 6\%$ and $\sim 5\%$, respectively. Furthermore, investigations estimating water level ($\sim 5\%$) and river discharge ($\sim 3\%$) commonly used measurements from altimetry mission.

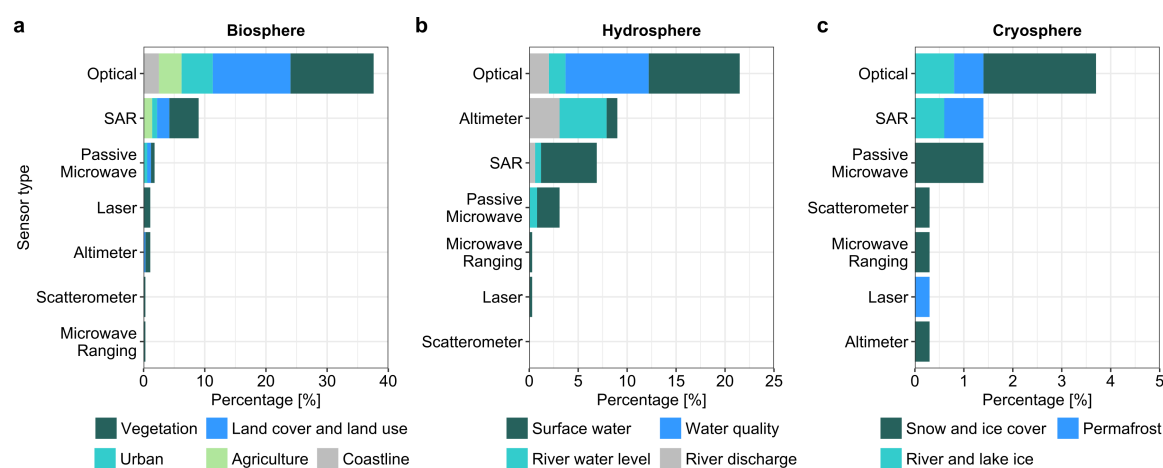


Figure 3.8: Share of utilized remote sensing sensor types categorized by the research categories (a) biosphere, (b) hydrosphere, and (c) cryosphere as well as respective study topics. Modified after Uereyen and Kuenzer (2019).

3.1.5 Temporal Resolution of Studies

In this section, the temporal resolution and the investigated study periods of the reviewed research articles are summarized in Figure 3.9 and Figure 3.10. To this end, the categories single, intra-annual, and inter-annual were defined with respect to the performed change detection analyses. The category single covers all investigations that did not conduct any change analysis. In case the remote sensing-based change analysis was performed at a temporal interval or resolution with less than 12 months the corresponding studies were associated with the category intra-annual. The category inter-annual includes all studies investigating observations with a temporal interval greater than a year. The results of this literature review indicate that $\sim 12\%$ of all studies are associated with the category sin-

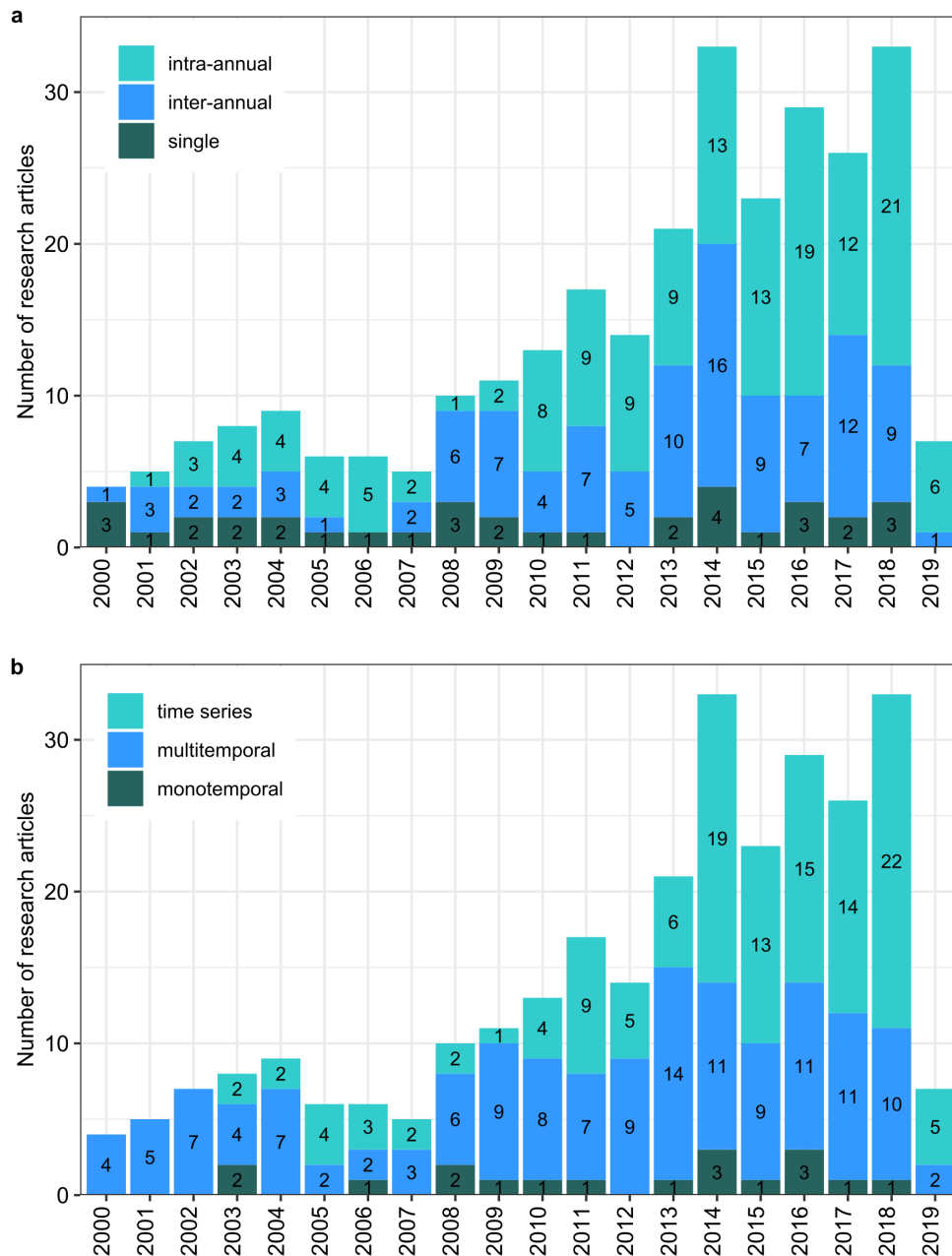


Figure 3.9: Count of published research articles per year and the temporal resolution of the used input data with respect to (a) change detection analyses and (b) employed satellite imagery. Modified after Uereyen and Kuenzer (2019).

gle and, hence, performed no change analysis (e.g. de Grandi et al. 2000; Saatchi et al. 2000; Thenkabail et al. 2005). On the other hand, $\sim 51\%$ of all reviewed research articles performed analyses at an intra-annual temporal scale (e.g. Broich et al. 2018; Du et al. 2016; da Silva et al. 2010), while $\sim 37\%$ of all studies were found to investigate inter-annual changes of a respective study topic (e.g. Domeneghetti et al. 2014; Wohlfart et al. 2016; Yan et al. 2017). Moreover, the results suggested that studies performing analyses at inter-annual temporal scale cover a greater study period than intra-annual studies. In detail,

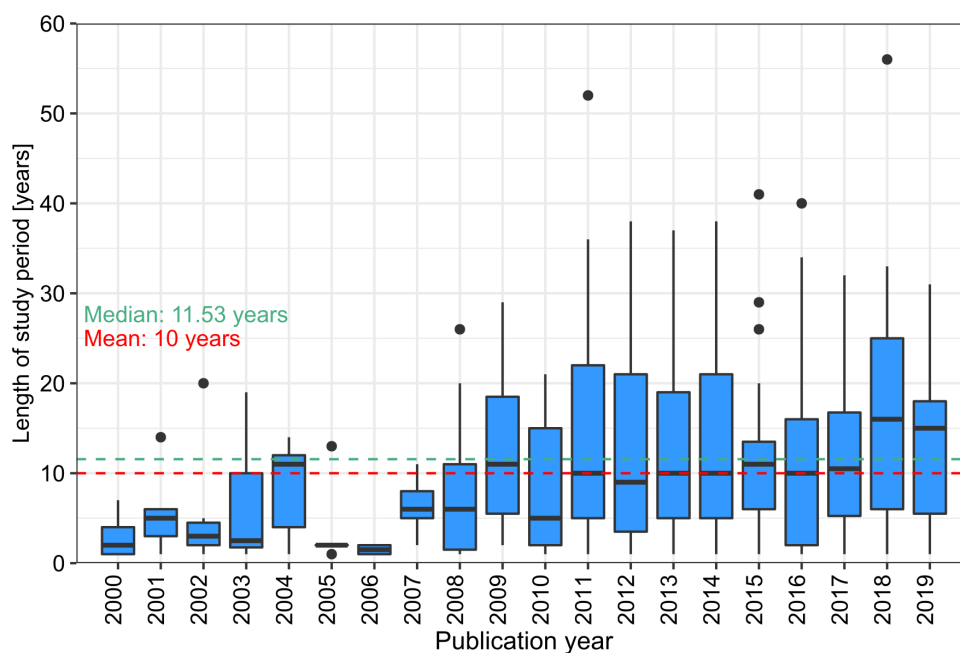


Figure 3.10: The length of the investigated temporal periods of all reviewed research articles per publication year. Modified after Ureyen and Kuenzer (2019).

intra-annual studies have a maximum study period of 29 years, whereas for inter-annual studies the maximum study period amounts to 56 years. Figure 3.9a also shows that over the investigated two decades in this review, the number of research articles conducting no change analysis stayed at a similar level. On the contrary, a considerable increase was found in the frequency of published research articles performing analyses at intra-annual scale starting in 2010 (see Figure 3.9a). Likewise, an increase was also determined for studies at inter-annual scale starting in 2008.

A further categorization of the reviewed studies was carried out to differentiate between studies utilizing mono-temporal, multi-temporal, and time series remote sensing data. In this regard, the category mono-temporal involved studies that only used remote sensing imagery for a single date. On the other hand, the category multi-temporal comprised investigations using more than one remote sensing image at multiple time steps. Studies using a series of remote sensing images at a constant temporal interval were assembled in the category time series. Figure 3.9b demonstrates the results obtained through the classification of the studies with respect to their temporal resolution. In summary, only $\sim 6\%$ of all studies used mono-temporal remote sensing imagery as input (e.g. Niculescu et al. 2016; Liu et al. 2016). $\sim 49\%$ of the reviewed research articles were found to utilize multi-temporal remote sensing images (e.g. Huang et al. 2013; Tsarouchi et al. 2014) and in $\sim 45\%$ of the investigations remote sensing time series were used (e.g. Pham et al. 2018; Villadsen et al. 2015). Moreover, an increase in the number of studies using remote sensing time series was noticeable since 2011 (see Figure 3.9b). This growth in time series applications was in alignment

with the previously mentioned increase in intra-annual studies (see Figure 3.9a). Accordingly, a slight increase in studies that investigated multi-temporal remote sensing imagery since 2008 can be reported as well. Studies employing mono-temporal remote sensing data remained at a low level.

Furthermore, Figure 3.10 visualizes the length of the studied periods of all reviewed investigations. The results show that $\sim 54\%$ of all studies had study periods below or equal to 10 years, while $\sim 18\%$ of the studies had an investigation period longer than 20 years. Figure 3.10 indicates a general increase in the length of the study periods since 2009.

3.1.6 Studies with River Basin Wide Applications

In this section, studies investigating entire river basins for any of the identified study topics is presented. As introduced in Chapter 1.1 the assessment and monitoring of the state of the Earth's surface is crucial to enhance the understanding of global environmental change. With respect to river basins, e.g., data on land cover and land use properties tailored to regional settings of a river basin represent a fundamental information basis for researchers as well as decision makers and promote river basin and water management activities. Overall, $\sim 17\%$ of all studies investigated multi-class land cover and land use mapping. However, only $\sim 10\%$ of these studies mapped and evaluated land cover and land use for an entire large river basin (Leinenkugel et al., 2013; Matsuoka et al., 2007; Saatchi et al., 2000; Wang et al., 2009; Wohlfart et al., 2016). Here, most of the land cover and land use classifications were performed for the Yellow river basin. Wohlfart et al. (2016) mapped land cover change between the years 2003 and 2013 using MODIS time series at a spatial resolution of 250 m. In comparison, Wang et al. (2009) quantified land cover change for the Yellow river basin using Landsat imagery at a spatial resolution of 30 m including the years 1990, 1995, and 2000. A further study, studied the land cover for East China, covering the Yellow river basin (Matsuoka et al., 2007). The authors utilized MODIS and nighttime light imagery for the year 2000 and applied a decision tree classifier to derive land cover classes. In a recent study, Ji et al. (2021) propose a classification approach to derive land cover maps for the Yellow river basin based on Landsat imagery. In particular, they used the Google Earth Engine (GEE) to compute land cover and land use dynamics for the period 1986–2018 at 90 m spatial resolution. Leinenkugel et al. (2013) generated a land cover map for the Mekong river basin for the year 2010 by means of MODIS-based vegetation index and surface reflectance time series covering 11 years. The authors used phenological metrics and temporal composites to derive land cover classes. Recently, Tang et al. (2021) presented an approach to retrieve annual land cover data for the Mekong river basin between 2001–2019 using MODIS time series. The authors used additional MODIS vegetation cover fraction

products to enhance the accuracy of the land cover maps and performed detailed analyses on land cover change. A basin wide land cover map was also computed for the Amazon river basin based on a mosaic of Japanese Earth Resources Satellite 1 (JERS-1) SAR imagery of 1995 (Saatchi et al., 2000). This land cover map focused mainly on vegetation types.

Vegetation modulates water, carbon fluxes, land-atmosphere interactions and supplies food and further valuable resources and ecosystem services (Piao et al., 2020). Considering analyses of river basins, ~21 % of the reviewed studies focused on vegetation parameters. Among these studies, ~19 % analyzed vegetation parameters at the spatial scale of an entire large river basin. As previously elaborated in Chapter 3.1.3, the Amazon river basin was investigated most (e.g. Frohking et al. 2011; Hilker et al. 2015; de Moura et al. 2015). In this context, de Moura et al. (2015) evaluated vegetation response to drought events by means of Terra and Aqua MODIS surface reflectance time series in combination with data on LAI and remote sensing-based precipitation measurements covering the period between 2000–2012. Furthermore, MODIS vegetation products were analyzed by means of the Amazon river basin to determine changes in vegetation leaf area between 2000–2012 (Hilker et al., 2015). Additional basin wide applications associated with vegetation characteristics were performed for the Congo river basin (e.g. Duveiller et al. 2008; Yan et al. 2016, 2017). Yan et al. (2016) assessed the quality of several vegetation products including those based on Spinning Enhanced Visible and Infrared Imager (SEVIRI) and MODIS to analyze land surface phenology parameters, particularly the canopy greenness cycle. The authors performed analyses for the period 2006 to 2013 and concluded that the SEVIRI instrument was more suitable for analyzing land surface phenology parameters in tropical rainforests due to frequent diurnal observations (Yan et al., 2016). In a following study, Yan et al. (2017) investigated land surface phenology in the Congo river basin using SEVIRI data in combination with remote sensing-based rainfall and land cover data. Based on the joint analysis, the authors analyzed implications of land cover on the relationship between the timing of vegetation greenness and timing of the rainy season. Accordingly, Yan et al. (2017) found that vegetation greenness in regions with low tree cover, including grasslands and shrublands is particularly impacted by the onset of the rainy season. Furthermore, applications at basin scale were available for the Murray-Darling and Yellow river basin in Australia and China, respectively (Broich et al., 2018; Wang et al., 2018b). In this connection, vegetation response to drought and flooding events using Landsat imagery between 1986–2011 was investigated for the Murray-Darling river basin (Broich et al., 2018). The authors identified varying vegetation responses with respect to timing, magnitude, and duration depending on rainfall and flooding events. In comparison, Wang et al. (2018b) analyzed drought events in the Yellow river basin during 2000–2015 by means of several

remote sensing-based drought indices. Also, Zhou et al. (2021) analyzed vegetation condition in combination with geospatial data on climatic, hydrological, and anthropogenic variables for the Amur river basin covering the period 1982–2013. The synergetic analysis indicated that natural and anthropogenic controls jointly impacted vegetation condition with significant spatial-temporal heterogeneity in the Amur river basin.

Monitoring of surface water is required for quantifying the availability of freshwater resources being elementary for human and natural ecosystems (Huang et al., 2018a). Surface water area mapping is enabled by means of spaceborne remote sensing e.g. through optical (e.g. Arvor et al. 2018) or SAR imagery (e.g. Arnesen et al. 2013). The results of this review indicated that ~18 % of the studies investigated mapping of surface water area. Thereof, ~22 % of the studies were conducted at basin scale, including the Amazon (Chapman et al., 2015), Congo (Rosenqvist and Birkett, 2002), Indus (Khan et al., 2014; Kwak et al., 2014), Murray–Darling (Huang et al., 2014; Donchyts et al., 2016; Heimhuber et al., 2016; Tulbure et al., 2016; Heimhuber et al., 2017), Yangtze (Rao et al., 2018), and multiple Arctic river basins (Du et al., 2016). With more detail, Advanced Land Observing Satellite-Phased Array L-Band Synthetic Aperture Radar (ALOS-PALSAR) ScanSAR data was used to classify surface water and inundated vegetation area for the Amazon river basin between 2006–2010 (Chapman et al., 2015). However, the authors stated that L-band imagery was not sensitive enough to map inundated herbaceous vegetation in the Amazon river basin. Moreover, Khan et al. (2014) classified surface water area for the Indus river basin using MODIS and Environmental Satellite (Envisat)-Advanced Synthetic Aperture Radar (ASAR) imagery jointly. The temporal period of this study covered the Indus flood event in 2010. In addition to the optical and SAR imagery, the authors also quantified spatial and temporal patterns of precipitation and streamflow using Tropical Rainfall Measuring Mission (TRMM) and Advanced Microwave Scanning Radiometer for EOS (AMSR-E) brightness temperature data (Khan et al., 2014). Likewise, flooded areas during Indus flood event in 2010 were also mapped by (Kwak et al., 2014). Here, the authors applied a rule-based classification scheme using a MODIS-based land surface water index together with SRTM elevation data. Monitoring of fractional surface water was also carried out for Arctic river basins, including the Mackenzie, Yukon, Lena, Yenisei, and Ob river basins by means of multiple remote sensing data (Du et al., 2016). The data basis comprised AMSR-E brightness temperature as well as MODIS land cover products in combination with further auxiliary datasets in order to derive fractional surface water maps at a spatial resolution of 5 km and a temporal resolution of 10 days. Furthermore, multiple studies investigated the Murray-Darling river basin in Australia. Huang et al. (2014) used MODIS surface reflectance imagery in combination with gauge measurements to characterize flood inundation dynamics between 2001–2010. More specifically, they assessed river flow peaks using

the gauge data and then identified and classified corresponding MODIS imagery by means of the open water likelihood algorithm (Guerschman et al., 2011) to generate maps at a spatial resolution of 500 m. These were validated using Landsat imagery at higher spatial resolution and afterwards temporally aggregated to annual composites. Also, inundation dynamics were analyzed for the Murray-Darling river basin using the Landsat archive at 30 m spatial resolution for a period of 26 years (1986–2011) (Tulbure et al., 2016). In a subsequent study, a joint analysis of multi-source time series data was conducted to analyze drivers of inundation dynamics based on precipitation, evapotranspiration, soil moisture, and gauge measurements (Heimhuber et al., 2017). For example, the authors identified prevailing local climate conditions being of high relevance for spatially heterogeneous inundation dynamics. Recently, Tulbure and Broich (2019) evaluated surface water area dynamics for the Murray-Darling river basin as well. In this study, the authors additionally considered land use data and performed a detailed analysis with respect to further spatial and temporal units. Considering the Yangtze river basin, a study generated time series of surface water area maps using MODIS surface reflectance 8-day composites at 250 and 500 m spatial resolution (Rao et al., 2018). For this purpose, the authors used the Random Forest classifier. In a recent study, Deng et al. (2019) derived surface water area maps for the Yangtze river basin using the Landsat archive between 1984–2018. For classification, the authors used the GEE platform and they differentiated permanent and seasonal surface water based on observed inundation frequencies. A currently published article investigated surface water area monitoring in the Congo river basin between 2010–2017 and applied Soil Moisture and Ocean Salinity (SMOS) data with a dual-polarized passive L-band instrument (Fatras et al., 2021). Mapping of surface water area in the Congo river basin is particularly challenging due to cloud coverage and dense vegetation cover (Fatras et al., 2021).

Regarding river water level measurement, the network of gauging stations tends to decline globally and is particularly sparse in developing and emerging economies (Grimaldi et al., 2016; Schneider et al., 2017). To overcome these issues, there is a great potential for spaceborne remote sensing-based water level measurements to monitor floods and to obtain measurements on water level even from data sparse regions (Grimaldi et al., 2016; Huang et al., 2018a). In this regard, the measurements are usually conducted at so-called virtual stations denoting the intersection of a remote sensing sensors ground track with a water body (da Silva et al., 2012). To this end, most of the reviewed studies were available for the Amazon (e.g. Frappart et al. 2006; da Silva et al. 2010, 2012), Brahmaputra (e.g. Schneider et al. 2017; Huang et al. 2018b), Congo (e.g. Becker et al. 2014; Kim et al. 2017), Ganges (e.g. Siddique-E-Akbor et al. 2011; Pandey et al. 2014), and Mekong river basin (e.g. Boergens et al. 2016; Pham et al. 2018). Out of all studies associated with river water level estimation, ~33 % retrieved the water level for virtual stations distributed over

the entire river basin, while the rest of the studies only at regional and subbasin scale. For example, da Silva et al. (2010) estimated river water level for the Amazon river basin at 45 virtual stations using altimetry measurements from the ERS-Radar Altimeter (RA) and Envisat-RA2 instrument. These estimations were validated using crossovers of altimetry tracks and gauge measurements resulting in partially high variations with 12 cm in the best cases and several meters in the worst cases.

Components of the cryosphere, including snow cover, glaciers, permafrost, and river as well as lake ice, are fundamental for river basins, as these e.g. modulate the runoff and, hence, the availability of freshwater resources in lower reaches of river basins (Azam et al., 2021). Therefore, observing the cryosphere and dynamics of the components is of high relevance to assess and evaluate potential implications for downstream areas (e.g. Viviroli et al. 2020). Although studies analyzing the research category of the cryosphere are spatially limited to the upper river basins, a brief overview of these studies is provided as well. Among all studies associated with the cryosphere, ~54 % investigated snow and ice cover (e.g. Akyurek et al. 2011; Chao et al. 2017; Tekeli et al. 2005; Wang et al. 2017a, 2015b). For example, altimetry data from the Ice, Cloud, and land Elevation Satellite (ICESat)-Geoscience Laser Altimeter System (GLAS) instrument was utilized to estimate glacier elevation change in the source region of the Yangtze river basin (Chao et al., 2017). In fact, the authors identified declining glaciers between the period 2000–2009. A further study, analyzed glacier change in the Yangtze river basin as well (Wang et al., 2017a). Here, the authors used two Landsat images from 1992 and 2009 in combination with in-situ measurements of runoff data between 1957–2009. The results of this study indicated an accelerated decrease in glacier area amounting to a total of around 45 km². Next, Wang et al. (2015b) analyzed snow cover dynamics between 2000–2012 for the upper Yangtze river basin. Based on this study, snow cover area increased during the investigated period. Recent studies investigating snow cover area are available for the Ganges (Thapa et al., 2021), Indus (Ali et al., 2020), and Yukon river basin (Pan et al., 2021). For example, Thapa et al. (2021) applied MODIS snow cover products between 2002–2014 to analyze changes in snow cover in the upper Ganges river basin. The authors identified slight decreases of snow cover area for most of the subbasins, but only a few of these indicated significant declines during winter months. Moreover, Ali et al. (2020) investigated changes in snow cover area for the period 2008–2018 based on MODIS normalized difference snow index (NDSI) data. The authors used linear least squares regression analysis for trend analysis and the results pointed towards declining snow cover area in the upper Indus river basin for the investigated period. Besides snow and ice, further studies dealing with lake and river ice characterization were identified for the Arctic region, including the Mackenzie, Lena, Yenisei, and Ob river basins (Pavelsky and Smith, 2004; Mermoz et al., 2014; Sakai et al., 2015; Antonova

et al., 2016a; Cooley and Pavelsky, 2016). As an example, the breakup dates for river ice were determined for the aforementioned Arctic river basins based on NOAA-AVHRR and MODIS imagery (Pavelsky and Smith, 2004). In a following study, Landsat imagery was employed for a study area in the Lena river basin to map river ice breakup and subsequently induced floods (Sakai et al., 2015). Additionally, permafrost was investigated for the Lena, Yukon, and Kolyma river basins (Antonova et al., 2016b; Nitze et al., 2017; Stettner et al., 2018; Strozzi et al., 2018; Whitley et al., 2018). For instance, Stettner et al. (2018) analyzed changes in cliff-top lines in association with soil erosion in permafrost riverbanks during summer months between 2013–2015 by means of TerraSAR-X time series.

3.2 Discussion of Potentials and Future Requirements

3.2.1 Potentials and Challenges of Remote Sensing for Large River Basin Monitoring

Spaceborne remote sensing facilitates the mapping of land surface parameters enabling detailed and continuous monitoring of land surface dynamics in large river basins around the globe. Particularly, the ever-increasing amount of data streams, open data policies of the space agencies, and the improving data storage and processing capacities foster remote sensing applications for large river basins at continental scales. Here, it is noteworthy that the mapping of land surface parameters using open remote sensing image time series at medium to high spatial resolution (30 m) is only possible since the opening of the Landsat archive in 2008. Additional multispectral imagery at 10 m spatial resolution is available from the European Copernicus Sentinel-2 missions since 2015. In consideration of these developments, a remarkable increase in intra-annual and inter-annual investigations using remote sensing time series was detected (see Figure 3.9). Accordingly, an increase in the length of the investigated study periods was identified as well (see Figure 3.10). Yet, as already mentioned in Chapter 1.1.1, the Landsat and Sentinel-2 missions are characterized by comparatively low temporal revisit times. This circumstance makes dense time series analysis impossible, particularly over cloud prone areas. To overcome low temporal resolution, remote sensing sensors with moderate to coarse spatial resolution such as MODIS, Sentinel-3, or NOAA-AVHRR can be used. However, this literature review highlighted that the remote sensing archives and subsequently generated geoscientific products are not used adequately considering applications at large river basin scale. Indeed, this might be caused by insufficient data storage and processing capabilities of institutions constituting a challenge for the handling of large amounts of remote sensing data. Nowadays, this can be alleviated by using cloud computing services such as the GEE (Gorelick et al., 2017). This

type of platform is quite beneficial with respect to the availability of geoscientific datasets and processing capacities. But, depending on the research motivation as well as methods and algorithms to be used, cloud computing services might not be flexible enough to implement the entire processing chain.

3.2.2 Requirement of a Higher Spatial and Temporal Coverage for Analyses in Large River Basins

As summarized in Chapter 3.1.3 and 3.1.6, the majority of studies applying spaceborne remote sensing data for analysis of large river basins were characterized by limited spatial coverage. In fact, EO-based basin wide analyses are needed over large river basins with e.g. sparse in-situ measurement networks, shared drainage areas with more than one country to enable consistent observations, or scarce as well as incomplete inventories on land surface parameters. However, studies investigating one of the reviewed large river basins usually focused on study areas at regional or subbasin scale (see Figure 3.6). In this context, this review revealed that the spatial coverage of the study areas was largely limited by administrative boundaries and not by the functional boundaries of a river basin (see Figure 3.4). Even though spaceborne remote sensing enables the monitoring and analysis of large-scale study areas irrespective of administrative units. This finding is quite important with respect to the analysis of transboundary river basins, where data exchange and cross border collaborations between riparian countries might be problematic (Best, 2018; de Stefano et al., 2017; Farinosi et al., 2018). In fact, there are more than 260 transboundary river basins at global scale covering around 45 % of the entire Earth's land surface (Linke et al., 2019; Wolf et al., 1999). In total 145 countries have their territory within a transboundary river basin. Yet, transboundary cooperation agreements are only reported by 24 countries in 2020 (UN-Water, 2021). In this respect, monitoring of transboundary river basins irrespective of national boundaries is needed. Furthermore, it appears that the limitation in the spatial coverage of an entire large river basin might be favored by aspects such as research funding or motivation. The summary of the institutional affiliation of the first authors (see Figure 3.5) and the investigated extent of the river basins (see Figure 3.4b) are supporting this finding. Additionally, due to the fact that most studies were conducted at regional or subbasin scale, it remains a challenge to compare findings with respect to land surface changes within or across large river basins. Figure 3.6 also unravels that studies performed at basin scale were not available for 12 of the reviewed large river basins and it was identified that basin wide applications were lacking for some of the identified study topics at all. In this regard, studies rarely performed EO-based analyses for multiple large river basins at once. In this review,

just a few studies investigating more than one large river basin were identified (e.g. Du et al. 2016; Kuhn et al. 2019).

Besides basin wide applications, multivariate time series on the evolution of the land surface at intra-annual and inter-annual temporal resolution are required for an enhanced analysis and understanding of land surface dynamics across spheres in river basins. As summarized in Chapter 3.1.5, the number of studies using remote sensing time series data increased considerably. In general, remote sensing time series applications over large spatial scales are fostered by open data policies of space agencies as well as cloud computing services with free access to academia such as the GEE or the recently activated Microsoft Planetary Computer platform (Gorelick et al., 2017; Sudmanns et al., 2019). In this regard, a few studies also focused on the remote sensing-based application of multivariate time series to analyze land surface dynamics (e.g. Ouyang et al. 2020; Wang et al. 2018a; Zhou et al. 2021). Notwithstanding, most studies focus on a single EO-based land surface variable such as vegetation or surface water in consideration of relevant driving variables. Overall, a joint evaluation of multiple EO-based land surface features in combination with driving variables covering several spheres is still rarely conducted. This applies to both river basin analyses as well as multivariate time series analyses in general (Estupinan-Suarez et al., 2021; Mahecha et al., 2020). Also, it has to be noted, that utilizing spaceborne remote sensing data at a high temporal resolution (e.g. up to twice a day) comes along with a comparatively lower spatial resolution (e.g. greater than 250 m). Overall, a trade-off between temporal and spatial resolution needs to be considered when applying spaceborne remote sensing data (Huang et al., 2018a).

3.2.3 Requirement of Comparability between Large River Basins and Transferability of Methods

As summarized in Table 2.1, a wealth of geoscientific time series became available during the last decades, including land surface variables based on remote sensing and reanalyses. These time series usually cover the entire land surface or depending on the variable the oceans as well and are crucial for a variety of applications including monitoring and modeling of e.g. the climate system, hydrological cycle, or environmental change. In consideration of river basins, several data portals summarizing and presenting e.g. geospatial data and indicators associated with environmental vulnerability or water scarcity are available. An overview of these databases and international initiatives is provided in Chapter 1.1.2. Even though these databases provide a valuable source for river basins and issues related to governance and water security (Best, 2018), they are mostly not up to date and focus on selected indicators at basin scale only. Accordingly, databases that gather geospatial data

and geoscientific time series on land surface variables for large river basins worldwide are needed. This would allow for spatially and temporally consistent studies. Additional standardized definitions on the spatial and temporal resolution of used geoscientific datasets could be defined to enable consistent analyses on land surface dynamics and comparisons between large river basins.

Furthermore, Chapter 2.3 provided an overview of time series analysis techniques commonly applied to spaceborne remote sensing data. In this regard, the development of a methodological framework that allows for the exploitation and analysis of multi-source geoscientific time series supporting the monitoring and quantification of land surface dynamics across spheres in large river basins is needed. Through the usage of globally available datasets on land surface parameters, the development of statistical time series analysis techniques with a global parameter set, and the implementation of the workflow on a high-performance computing environment, the transferability of applications to any large river basin could be ensured. Obtained insights and results on land surface dynamics and the influence of driving variables in large river basins would greatly support decision makers, stakeholders, and researchers as well as international or transboundary river basin commissions.

3.3 Summary

This chapter summarized previous studies utilizing spaceborne remote sensing for the analysis of land surface dynamics in the worldwide 28 largest river basins and discussed the potentials and challenges of remote sensing, including geoscientific time series as well as geospatial data for land surface monitoring in large river basins. The key findings of this review emphasized that only $\sim 14\%$ of the reviewed research articles performed basin wide applications and that transboundary river basins remained understudied. Many studies analyzing a transboundary river basin, such as the Amazon, Indus, Ganges, or Brahmaputra river basin, focused on one of the riparian countries and did not consider the natural boundaries of the respective drainage area. In this respect, a close relation between the investigated river basin and the institutional affiliation of the first authors was identified. Also, the number of investigations that studied multiple large river basins at once was found to be low. Moreover, most of the identified studies explored vegetation parameters, surface water area and inundation dynamics, as well as land cover and land use. To this end, optical and SAR imagery were most frequently used. In the advent of open data policies (NOAA-AVHRR, MODIS, Landsat, European Copernicus Programme) and emerging cloud computing services, including the Google Earth Engine and the Microsoft Planetary Computer, studies employing multi-temporal and time series analyses were found to be in-

creasing. In the context of global climate change, it was stressed that the exploitation of multi-source geoscientific time series fostering the quantification of land surface dynamics across spheres in large river basins is of great relevance to promote consistent monitoring of environmental change and assess the influence of natural and anthropogenic drivers. These analyses and corresponding findings could greatly support existing databases and initiatives of international organizations, river basin commissions, governments, and researchers.

Chapter 4

Study Area: Indo-Gangetic River Basins

This chapter presents the characteristics of the study area covering the Indus, Ganges, Brahmaputra, and Meghna river basins in South Asia. The Indus-Ganges-Brahmaputra-Meghna (IGBM) rivers have been of significant importance since ancient times. The fertile Indo-Gangetic Plain, being shaped by these river systems and alluvial deposits from the Himalaya mountains has been home to some of the world's oldest civilizations, including the Indus Valley civilization (Kathayat et al., 2017; MacDonald et al., 2016). Today, these river basins are among the most densely populated areas and feature the largest connected irrigated cropland area worldwide (Biemans et al., 2019). The Ganges, Brahmaputra, and Meghna rivers have their confluence north of the Bay of Bengal and are characterized by the third largest global riverine discharge to the Earth's oceans, being surpassed by the Amazon and Congo rivers only (Chowdhury and Ward, 2004). This delta region also exhibits the world's largest mangrove forest ecosystem, the Sundarbans (Iftekhar and Saenger, 2007).

In this regard, the focus of this thesis is on four neighboring and connected transboundary river basins representing environments with heterogeneous climates, topography, and land cover as well as land use properties. Furthermore, these river basins cover a considerable area of approximately 2.8 million km² (being around 8 times the size of Germany) and include the countries Afghanistan, Pakistan, India, China, Nepal, Bhutan, and Bangladesh. Considering the objectives of this thesis, the selected river basins are greatly suitable for multivariate time series analysis to quantify and evaluate land surface dynamics across spheres, with e.g. the cryosphere being prevalent in high mountainous areas of the upper Indus, Ganges, and Brahmaputra river basins; on the other hand, the downstream areas covering the Indo-Gangetic Plains are largely influenced by humans and enable a detailed analysis of the interconnection between multiple spheres, including the anthroposphere, biosphere, hydrosphere, lithosphere, and atmosphere. Also, in agreement with the results

of the literature review, this thesis aims to analyze transboundary river basins irrespective of administrative boundaries, which were found to remain largely understudied.

4.1 Overall River Basin Characteristics

The Indus river (Chinese: Shendu) begins at the confluence of the rivers Sengge and Gar on the Tibetan Plateau and has a total length of about 3,200 km. The Indus river basin stretches from the Himalayan-Karakoram mountains in the north to the dry plains in Pakistan in the south (see Figure 4.1). Ultimately, the river has its outlet to the Arabian Sea. The Indus river has a total drainage area of around 1.1 million km², where Pakistan has the largest share of the drainage area, followed by India. This river basin inhabits approximately 300 million people (see Table 4.1).

The Ganges river (also known as Ganga in India and as Padma in Bangladesh) is formed by the two main headwater rivers Bhagirathi and Alaknanda having their origin at the Gangotri glacier and Satopanth as well as Bhagirath Kharak glaciers in the Uttarakhand Himalayas in India. The total length of the river amounts to 2,500 km. First, the Ganges flows southwest in northern India and then turns southeast as it is joined by many tributaries (see Figure 4.1). In Bangladesh the Ganges river joins with the Brahmaputra and Meghna rivers. The river basin has an area of approximately 900,000 km² and inhabits more than 580 million people (see Table 4.1). Furthermore, the Ganges river is not only an important freshwater source for many sectors, but it has a great social and religious relevance as well (Shukla et al., 2018).

The Brahmaputra river (also known as Yarlung Tsangpo in China and as Jamuna in Bangladesh) originates at the Angsi glacier in the Himalayan Mountains in China at an elevation of 5,300 meters above sea level (Patel et al., 2020). The river flows east through southern China, enters India in the northeast and turns southwest, and finally flows into Bangladesh (see Figure 4.1). In total, the Brahmaputra river has length of around 3,900 km.

Table 4.1: Characteristics of the investigated river basins including the riparian countries, the drainage area, and the population count extracted from gridded population data for the year 2020 (WorldPop and CIESIN, 2018). The countries are listed in alphabetical order.

Basin	Countries	Area [km ²]	Population count
Indus	Afghanistan, China, India, Pakistan	1,131,090	300,364,670
Ganges	Bangladesh, China, India, Nepal	954,206	586,119,928
Brahmaputra	Bangladesh, Bhutan, China, India	540,783	83,723,373
Meghna	Bangladesh, India	95,711	91,212,172
GBM-Delta	Bangladesh, India	83,568	94,637,377
All basins	-	2,805,358	1,156,057,520

The river drains a total area of more than 540,000 km² (see Table 4.1) and is the third largest sediment-laden river after the Amazon and Yellow river (Rahman et al., 2018; Viers et al., 2009). Moreover, the Brahmaputra is considered among the largest braided rivers worldwide being characterized by considerable migration of the river banks (Baki and Gan, 2012).

The Meghna river is formed in Bangladesh through the rivers Surma and Kushiyara, which have their origin in northeast India. The Meghna river basin has a size of about 95,000 km² and has a population of 90 million (see Table 4.1). Compared to the other investigated rivers, the origin of the Meghna river is not in the Himalayan Mountains. To-

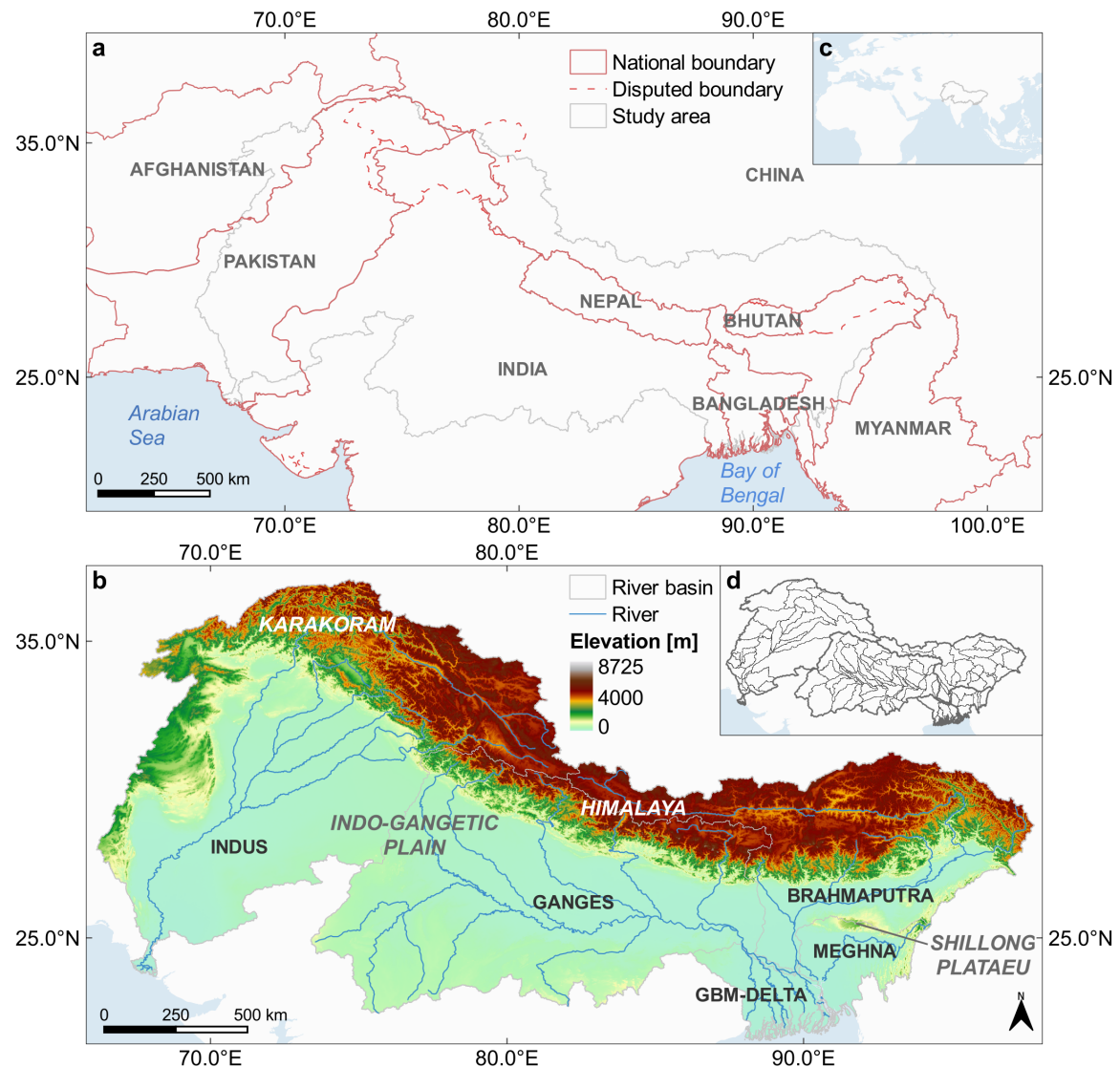


Figure 4.1: (a) Overview of countries intersecting with the transboundary river basins, (b) topography of the Indus, Ganges, Brahmaputra, and Meghna river basins, (c) location of study area in South Asia, (d) and differentiation of river basins by 117 subbasins. National and disputed boundaries are based on NaturalEarth data. Outlines of the river basins are extracted from HydroSHEDS (Lehner et al., 2008) and the elevation is represented by the Copernicus DEM (European Space Agency and Sinergise, 2021).

gether, the Ganges-Brahmaputra-Meghna (GBM) rivers shape the largest delta region in the world (Becker et al., 2020). After their confluence in the GBM-Delta, these rivers drain into the Bay of Bengal. As already mentioned before, this river system releases the third largest amount of discharge volume into the ocean's (Chowdhury and Ward, 2004). Furthermore, the population density in the delta region in Bangladesh is among the highest in the world with more than 1,000 people per square kilometer (Becker et al., 2020). The total population of the IGBM river basins amounts to more than 1.1 billion people covering almost 14 % of the global population (see Table 4.1).

4.2 Physical Geography of the Indus, Ganges, Brahmaputra, and Meghna River Basins

In the following the physical characteristics of the IGBM river basins are explained. Here, the focus lies on the climate system, the hydrological properties, as well as land cover and land use characteristics of the respective river basins.

4.2.1 Climatology

The IGBM river basins can be divided into three typical physiographic zones based on their topographical and climatic characteristics. These physiographic zones include the Tibetan Plateau in the north with altitudes more than 4,000 m above sea level, the Himalayan belt as a transition zone, and the downstream floodplains at low altitudes in the south (see Figure 4.1 and Figure 4.2). In the following, the climate zones of the investigated trans-boundary river basins are described by means of the Köppen-Geiger climate classification system. Accordingly, an overview of the prevalent climate zones is illustrated in Figure 4.2. Here, the geospatial dataset on the Köppen-Geiger climate classification is available from Beck et al. (2018) and is representative for the period 1980–2016 at a spatial resolution of 1 km. As visualized, the climate in the Indus river basin is mainly arid in the south and central plains. Towards the Himalayan mountain range (see Figure 4.1), the climate in the Indus, Ganges, and Brahmaputra river basins is temperate with mostly dry winters and hot summers. At high altitudes of the Indus, Ganges, and Brahmaputra cold and polar climate is dominant with cold steppe and desert climate in the valleys (see Figure 4.2). The climate in the western Himalayan belt is cold with dry and warm summers and in the eastern belt cold with dry winters and warm summers. The floodplains of the Ganges river basin are mostly characterized by temperate and in western areas by semi-arid climate. Likewise, the downstream areas of the Brahmaputra river basin have temperate climate. In the south, to-

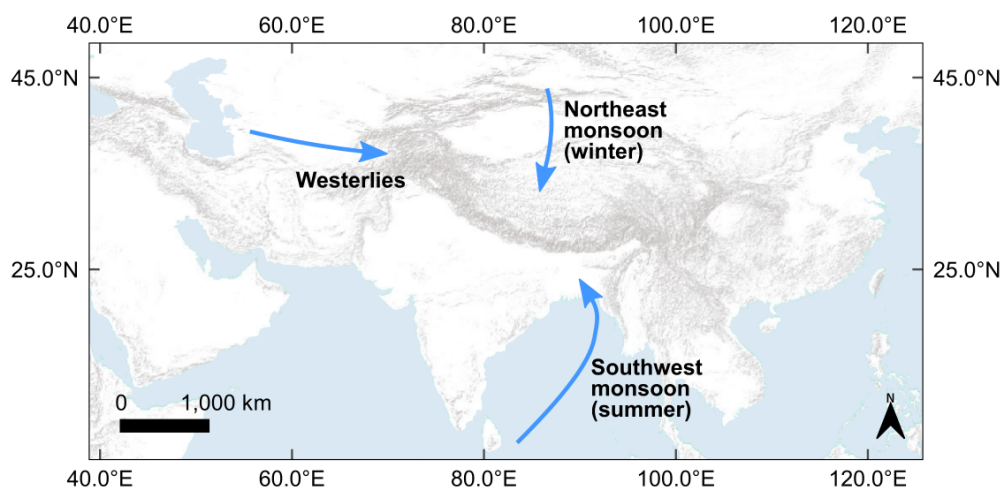


Figure 4.3: Schematic overview of the main wind systems for the study area (Source of background terrain image: ESRI, USGS, NOAA).

ure 4.3) (Dimri et al., 2015). During the northeast monsoon the precipitation weakens from west to east (Azam et al., 2021). In this context, the total amount of received precipitation in the Karakoram and the Western Himalayas during the winter monsoon, is higher than that during the southwest monsoon. Moreover, investigations identified a significant weakening of the southwest monsoon over South Asia since 1950 (Mishra et al., 2012; Patel et al., 2020). This decline in total precipitation is accompanied by higher occurrences of dry spells (Singh et al., 2014), declines in soil moisture, and occurrences of more intense drought events over the Indo-Gangetic Plains (Ganeshi et al., 2020; IPCC, 2021; Mujumdar et al., 2020; Ramarao et al., 2018). At the same time, the frequency of extreme rainfall events over shorter timescales in South Asia increased since 1950, leading to severe flood events over the IGBM river basins (Mujumdar et al., 2020).

Next, the heterogeneity in climate in the IGBM river basins is demonstrated by means of the climate charts in Figure 4.4e–j and statistics in Table 4.2. The selected locations are distributed over diverse climate and elevation zones. The climate charts are calculated by means of WorldClim version 2.1 climate data for the period 1970-2000 (Fick and Hijmans,

Table 4.2: Further information with respect to the selected locations in Figure 4.4. Details on the abbreviations of the climate classes can be found in Figure 4.2.

Parameter	Hyderabad	Skardu	Gwalior	Thimphu	Sylhet	Lhasa
Coordinates [Lat.; Long.]	68.4; 25.4	75.6; 35.3	78.2; 26.2	89.6; 27.5	91.9; 24.9	91.1 29.7
Climate class	BWh	BWk	Cwa	Cwb	Am	BSk
Height [m]	30	2228	218	2352	22	3654
Annual Precipitation [mm]	159	307	920	1001	3918	418
Annual Mean Temperature [°C]	27.4	11.0	25.8	13.6	24.7	7.4

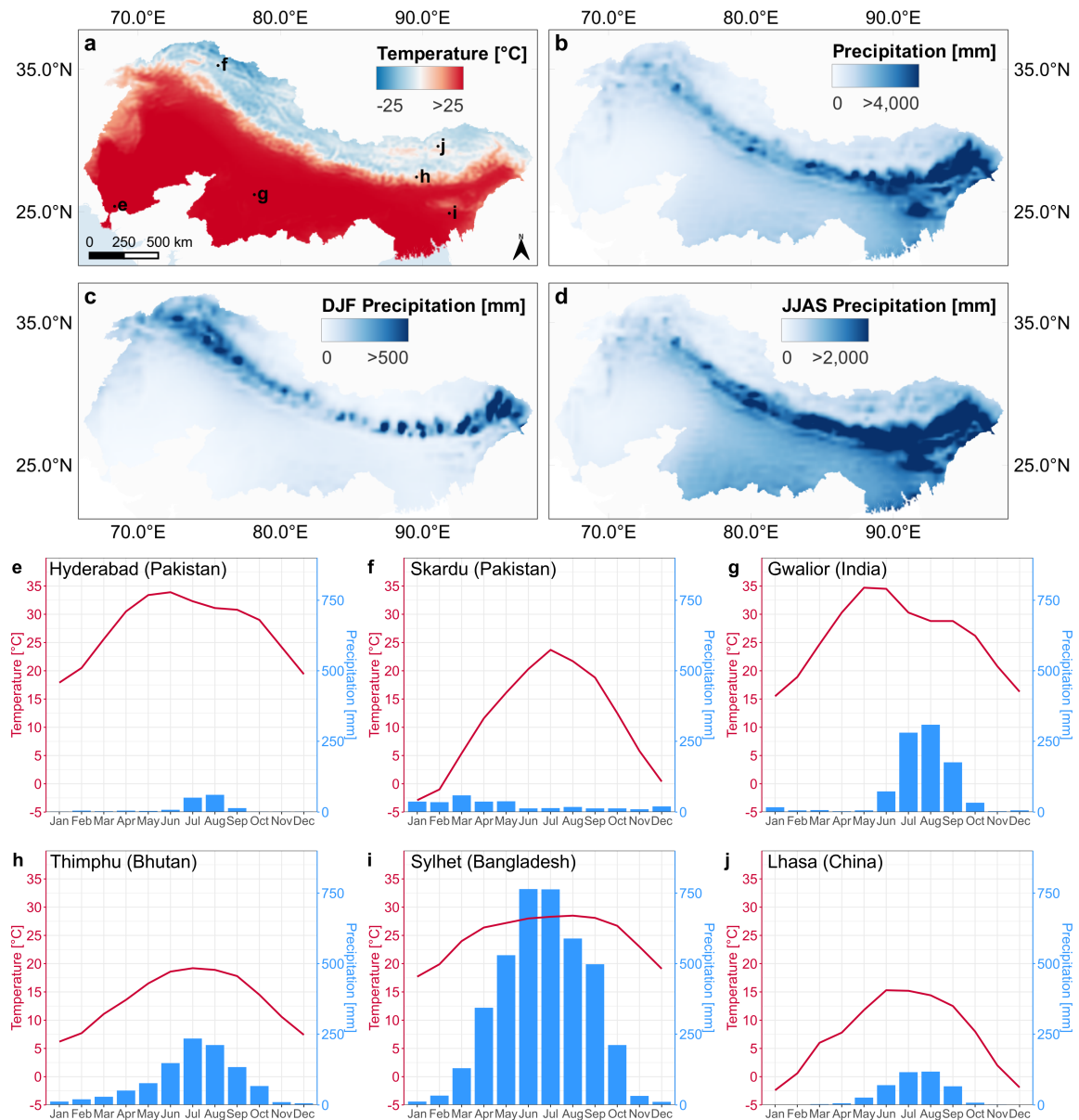


Figure 4.4: Maps showing (a) the mean annual temperature, (b) mean accumulated precipitation, (c) mean accumulated precipitation over the winter season (DJF; December, January, February), and (d) mean accumulated precipitation over the monsoon season (JJAS; June, July, August, September) between 1991–2020 based on ERA5-Land reanalysis (Muñoz-Sabater et al., 2021). (e–j) The climate charts for the selected cities in the Indus-Ganges-Brahmaputra-Meghna river basins are based on the WorldClim data for the reference period 1970–2000 (Fick and Hijmans, 2017). The location of the cities in (e–j) are depicted in subfigure (a).

2017). This dataset has a spatial resolution of 1 km. For example, Figure 4.4e features the city Hyderabad in the Lower Indus river basin having a hot desert climate (BWh). According to the WorldClim data, the mean annual precipitation amounts to 159 mm in Hyderabad. In contrast, the city Sylhet in the Meghna river basin at an elevation of 22 m above sea level is characterized by tropical monsoon climate (Am) and receives an annual precipitation of 3918 mm. Ultimately, the annual climate of South Asia can be dis-

tinguished by four seasons: the pre-monsoon (March-April-May (MAM)), monsoon (June-July-August-September (JJAS)), post-monsoon (October-November (ON)), and winter season (December-January-February (DJF)) (Islam and Cartwright, 2020; Janes et al., 2019).

4.2.2 Hydrology

The hydrology of the Indo-Gangetic river basins is modulated on the one hand, by the monsoon precipitation and, on the other hand, by glacial melt and snowmelt. In this context, the Himalaya and Karakoram mountains (see Figure 4.1) extend over 650,000 and 90,000 km², respectively, and cover almost half of the glacial ice volume in High Mountain Asia (Nie et al., 2021). Also, High Mountain Asia contains the largest ice volume outside the polar regions (Farinotti et al., 2019) emphasizing its importance with respect to freshwater availability in downstream areas of the river basins. Considering the annual river discharge, the inter-annual variability of precipitation and glacial as well as snowmelt is greatly impacting the discharge volume in the respective seasons. The peaks in river discharge are reached during the monsoon season, between July and September (see Figure 4.5). More specifically, river discharge is highest for the Indus river in August, for the Ganges river in September, and for the Brahmaputra as well as Meghna in July (see Figure 4.5b–e). These graphs also demonstrate that the difference in river discharge between the monsoon and dry seasons is very large. Moreover, as shown in the previous chapter, the southwest monsoon (Indian Summer Monsoon) loses its intensity from east to west. Accordingly, the contribution of glacial and snowmelt to the river discharge in the Indus river is larger than those in the Ganges, Brahmaputra, and Meghna rivers (Biemans et al., 2019). In years with less rainfall during the monsoon season, the river flow is modulated by groundwater and glacier as well as snowmelt (Azam et al., 2021). Furthermore, among the IGBM rivers, the annual mean river discharge of the Brahmaputra river is largest and amounts to 33,600 m³ s⁻¹ being followed by the Ganges river with 15,000 m³ s⁻¹. Regarding river discharge, the Brahmaputra river is only exceeded by the Amazon, Congo, and Yangtze rivers (Wohl, 2007). For the Indus river the annual mean discharge is 7,500 m³ s⁻¹ (Wohl, 2007) and for the Meghna river 4,600 m³ s⁻¹ (Sarker et al., 2003).

4.2.3 Land Cover

The distribution of land cover classes in the IGBM river basins is represented by the European Space Agency (ESA) Climate Change Initiative (CCI) Land Cover classification for the year 2019 in Figure 4.6a (European Space Agency, 2017; Plummer et al., 2017). The available 37 land cover classes are reclassified into 11 classes in consideration of the scheme by Mousivand and Arsanjani (2019) and the IPCC land cover categories (Arneth

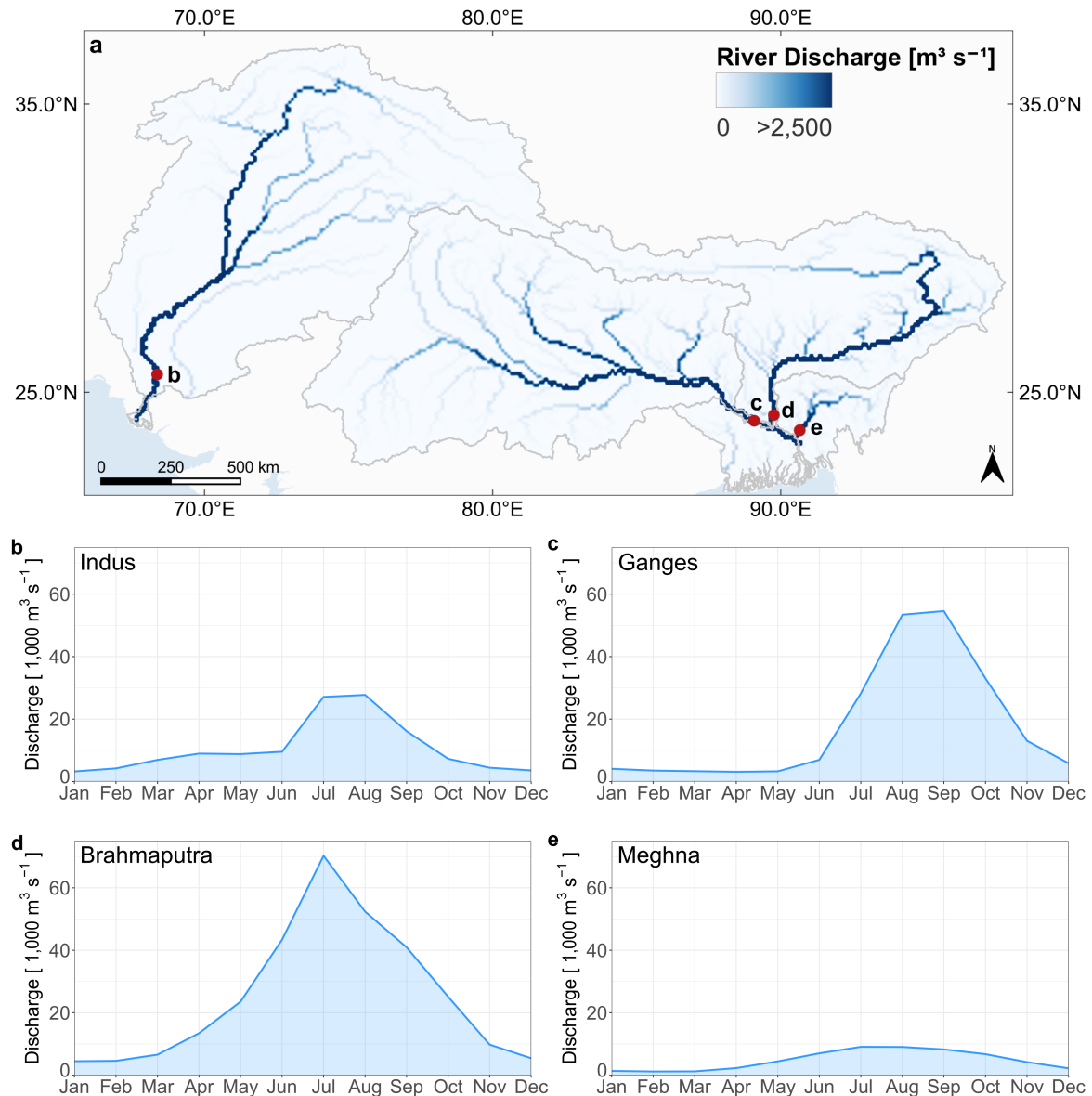


Figure 4.5: (a) Annual mean of daily gridded river discharge for the investigated river basins based on the Global Flood Awareness System (GloFAS)-ERA5 river discharge version 3.1 between 1991–2020 (Harrigan et al., 2020), whereas (b–e) illustrate the river discharge of the Indus, Ganges, Brahmaputra, and Meghna rivers close to the outlet.

et al., 2019). Regarding the spatial resolution of 300 m, it is important to note that this data cannot map all land surface features accurately. However, in terms of the annual temporal and spatial resolution, the ESA CCI land cover data has to be considered as an improvement with respect to other available land cover classifications at global scale such as the Global Land Cover 2000 or MODIS products (Bartholomé and Belward, 2005; Friedl et al., 2002).

According to the ESA CCI land cover data, irrigated and rainfed croplands in combination have the highest share in the Indus, Ganges, Meghna, and GBM-Delta (see Figure 4.6b–f). On the other hand, the Brahmaputra river basin, particularly in high altitudes,

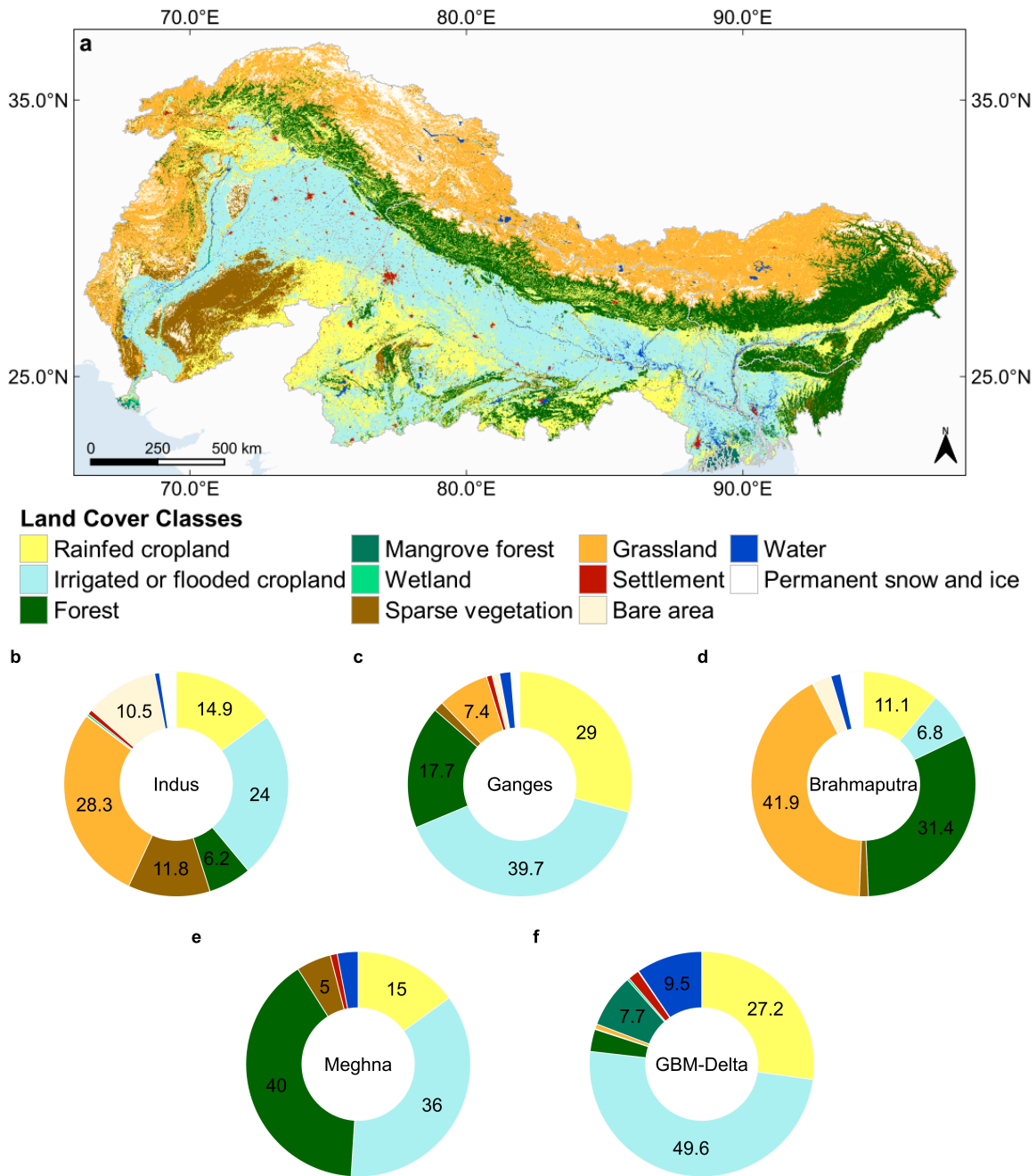


Figure 4.6: (a) Overview of land cover and land use distributions for the study area by means of the ESA CCI land cover 2019 dataset (European Space Agency, 2017) and (b–f) illustration of percentages of the land cover and land use classed per investigated spatial unit. For visualization purposes, labels of percentages lower than 5 are not shown in (b–f).

is dominated by grasslands. Forests are primarily occurring at the Himalayan belt and north of the Meghna river basin, at the Shillong plateau (see Figure 4.6a). In downstream areas, particularly in the Indo-Gangetic Plain, the land surface is largely used for agricultural activities. Furthermore, dry regions in the southeast of the Indus river basin are covered by sparse vegetation or bare area. In the Indus and GBM-Delta, close to the river mouth of both rivers, the land cover classes wetlands and mangrove forests are dominant.

To provide further details on the vegetation cover, snow cover area, and surface water area, Figure 4.7–4.9 visualize the long-term mean of those variables for the period 2003 to 2020 as well as the variables phenology for the respective river basins. According to the land cover distribution, Figure 4.7a demonstrates that the long-term mean in the NDVI is particularly high over forested areas in the Himalayan belt and the Shillong plateau and

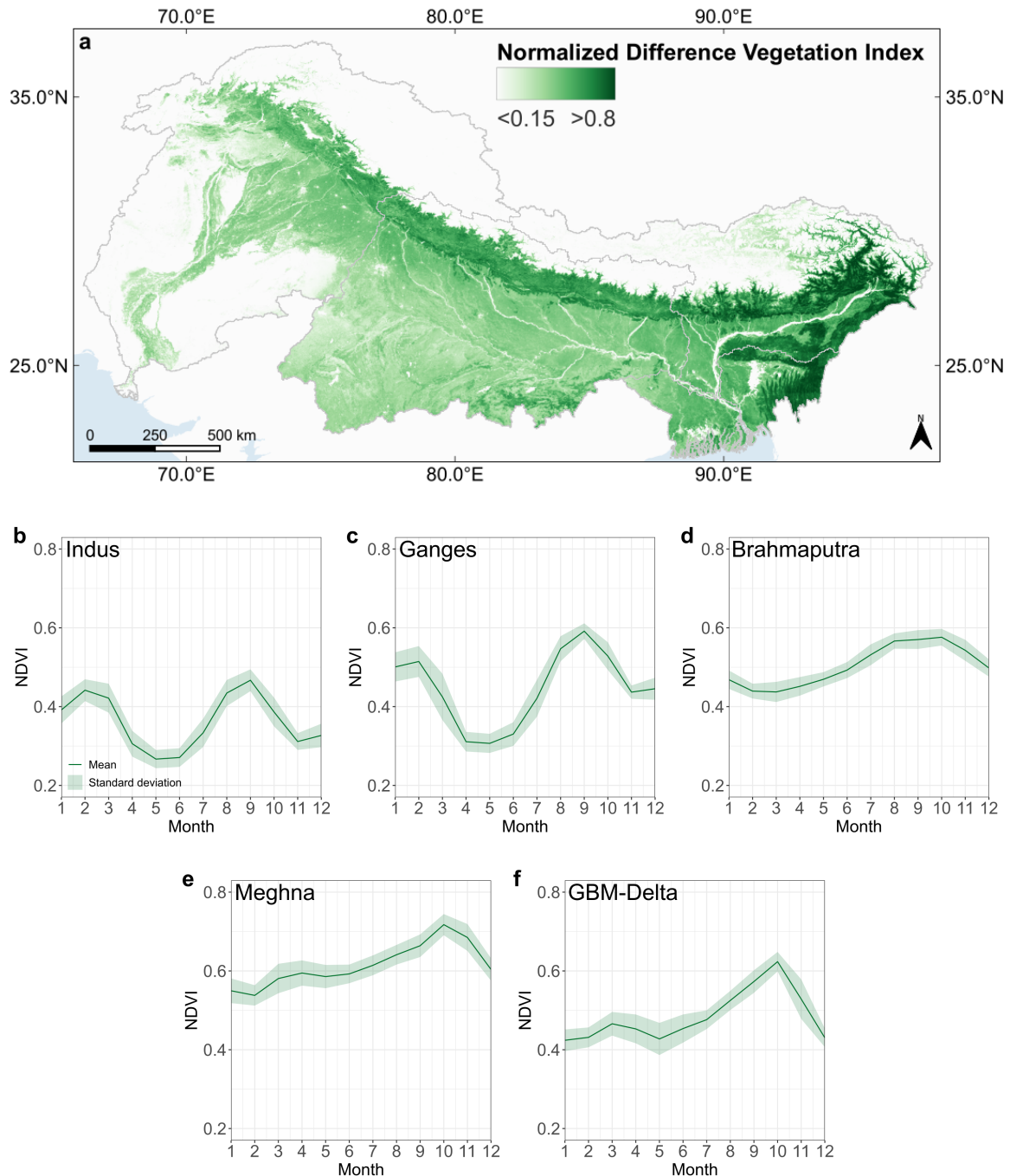


Figure 4.7: (a) Overview of vegetation greenness by means of a long-term mean of the normalized difference vegetation index (NDVI) derived from MODIS imagery between 2003 and 2020 (Vermote and Wolfe, 2015), whereas (b–f) illustrate the phenology of vegetation greenness for the respective river basins based monthly means for the same period. The NDVI value range is between -1 and 1.

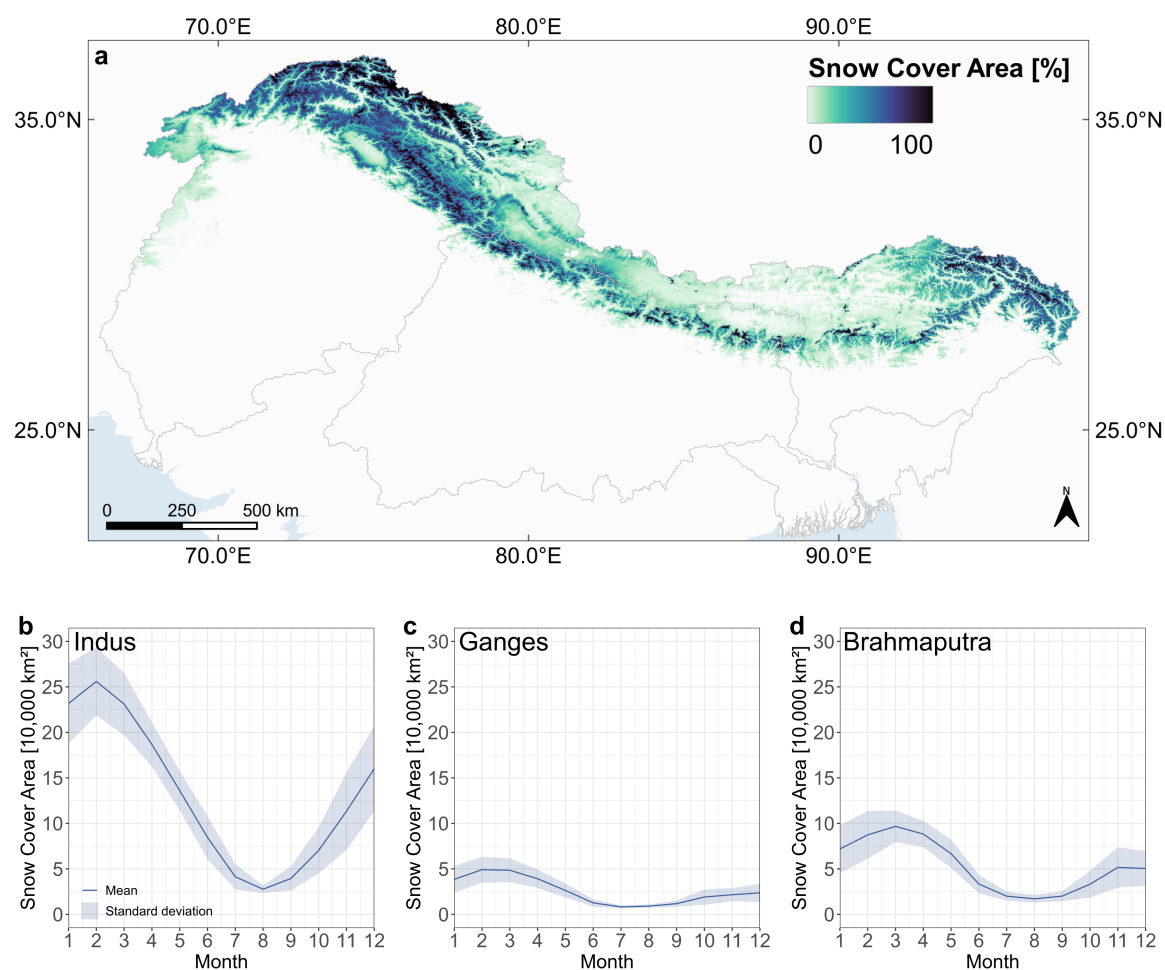


Figure 4.8: (a) Average of snow cover area for the period 2003–2020 based on the daily DLR Global SnowPack data (Dietz et al., 2015) and (b–f) visualization of the snow cover phenology for the respective basins based on monthly means for the same period.

weakens from east to west. In this context, the NDVI is commonly calculated for remote sensing measurements to characterize the amount of green vegetation cover on the land surface. Moreover, Figure 4.7b–f outlines the intra-annual course of the NDVI averaged for the entire river basins, respectively. Here, the NDVI indicates two growing seasons for vegetation in the Indus and Ganges river basins, with a peak in February and September. On the contrary, the monthly NDVI values reveal an increase in vegetation greenness between May and October for the Brahmaputra, Meghna, and GBM-Delta, with a peak in October.

Considering the average snow cover area for the period 2003–2020 in Figure 4.8a, it can be seen that the occurrence of snow cover area is comparatively higher in the northwest for the upper Indus river basin than for the Ganges and Brahmaputra. This is also reflected in Figure 4.8b–d, where the course of snow cover area is displayed by means of the monthly averages between 2003–2020. In particular, snow cover area in the Indus river basin peaks in February and covered an area around 250,000 km² on average for the investigated period. During the monsoon season, in August, snow cover area reaches the lowest point with a

coverage less than 30,000 km². Likewise, in the Ganges river basin the maximum snow cover extent is reached in February in amounts to approximately 50,000 km², whereas in July it reduces to less than 9,000 km². In the Brahmaputra river basin, the peak in snow cover area is achieved one month later in March with around 100,000 km². The ablation period ends around August with snow cover area being lowest (approximately 17,000 km²). Afterwards, snow cover area starts to increase again in the Brahmaputra river basin.

Surface water area dynamics are largely related to precipitation as well as glacial and snowmelt. In this regard, Figure 4.9a displays the occurrence of surface water area in the IGBM river basins during 2003–2020, where the main river streams in the downstream areas are particularly striking. In agreement with the previously explained patterns of precipitation (see Chapter 4.2.1), river discharge (see Chapter 4.2.2), and snow cover area, surface water area reaches its maximum coverage approximately in September for the Indus, Ganges, and Brahmaputra river basins (see Figure 4.9b–f). In the Meghna river basin, the coverage of surface water area declines down to 1,000 km² at the end of the dry period in March. In comparison, in the monsoon season the surface water area expands up to approximately 9,000 km².

4.3 Human Footprint

As introduced in Chapter 1.1, human actions influence the environment in various ways. Therefore, the quantification as well as the integration of anthropogenic influences into the analysis of environmental change is of great importance. In this regard, numerous geospatial data characterizing the human footprint are available (e.g. Table 2.1). Besides the previously presented percentages of land cover classes, Figure 4.10 presents the evolution of the total settlement area for the period 1985–2015 within each river basin. Here, the settlement area is extracted at a spatial resolution of 30 m from the global World Settlement Footprint (WSF) Evolution data, which is based on the Landsat archive (Marconcini et al., 2020, 2021). Due to the higher spatial resolution compared to the ESA CCI land cover, this dataset enables a more accurate characterization of settlement area. For example, the settlement area in the Ganges river basin is largest and increased by around 70 % between 1985–2015, from approximately 13,600 km² to 23,200 km² (see Figure 4.10). Considering the relative share of settlement area within each river basin, it is highest for the GBM-Delta with approximately 6.35 % in 2015.

Also, as already pointed out in Table 4.1, the IGBM river basins are home to approximately 14 % of the world population. In addition to these population numbers, Figure 4.11a demonstrates the spatial distribution of population counts for the study area using the grid-

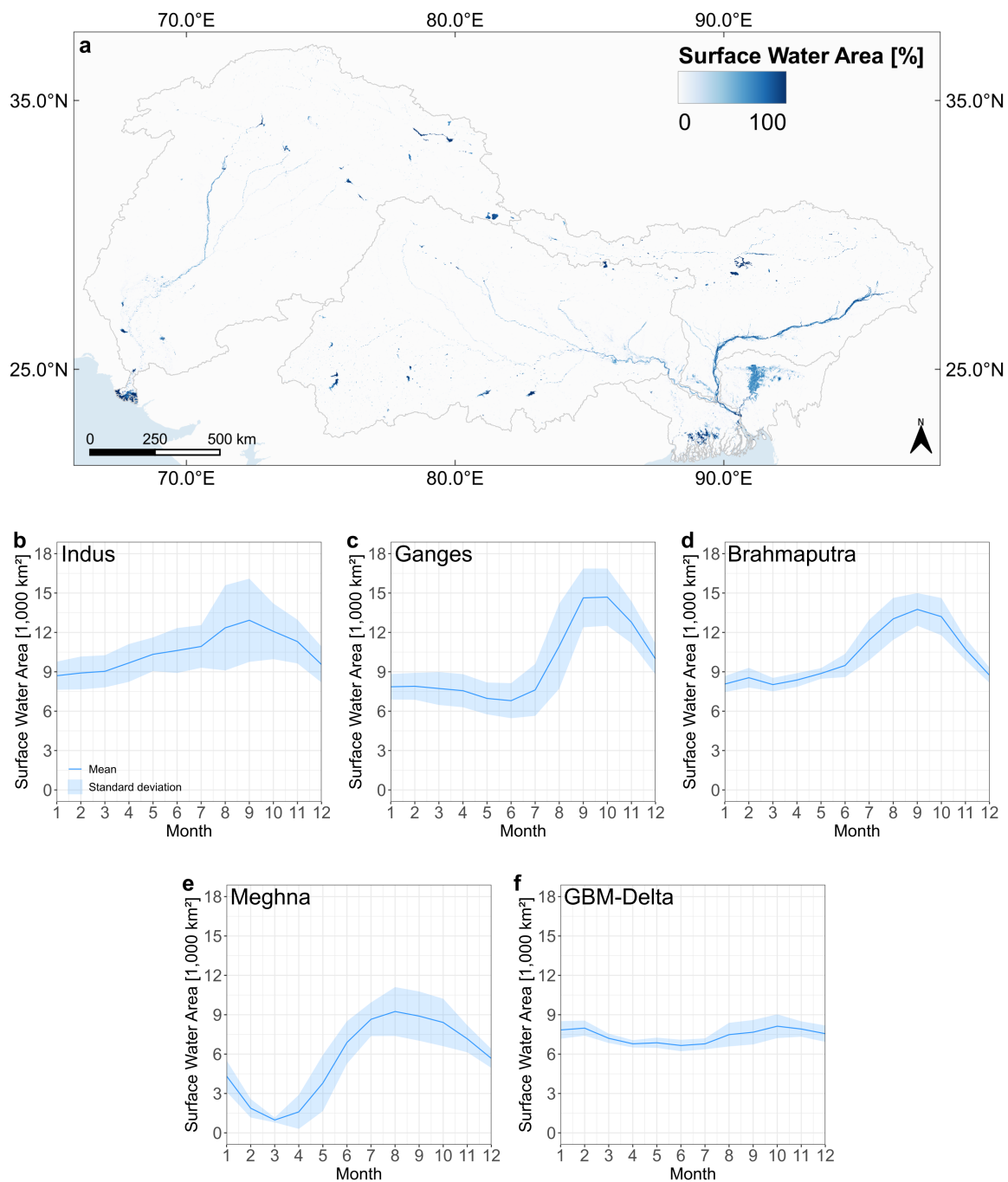


Figure 4.9: (a) Average of surface water area for the period 2003–2020 based on the DLR Global WaterPack (Klein et al., 2017) and JRC Global Surface Water Layer (Pekel et al., 2016) data as well as (b–f) visualization of the surface water phenology for the respective basins based on monthly means for the same period.

ded WorldPop dataset (Lloyd et al., 2019; WorldPop and CIESIN, 2018). Here, it is visible that the population is concentrated in the low altitude areas of the river basins and to large urban agglomerations, such as the denoted megacities Lahore (Pakistan), Delhi (India), Kolkata (India), and Dhaka (Bangladesh). In case of the Lower Indus river basin, it is also striking that the population is focused in close vicinity to the river streams.

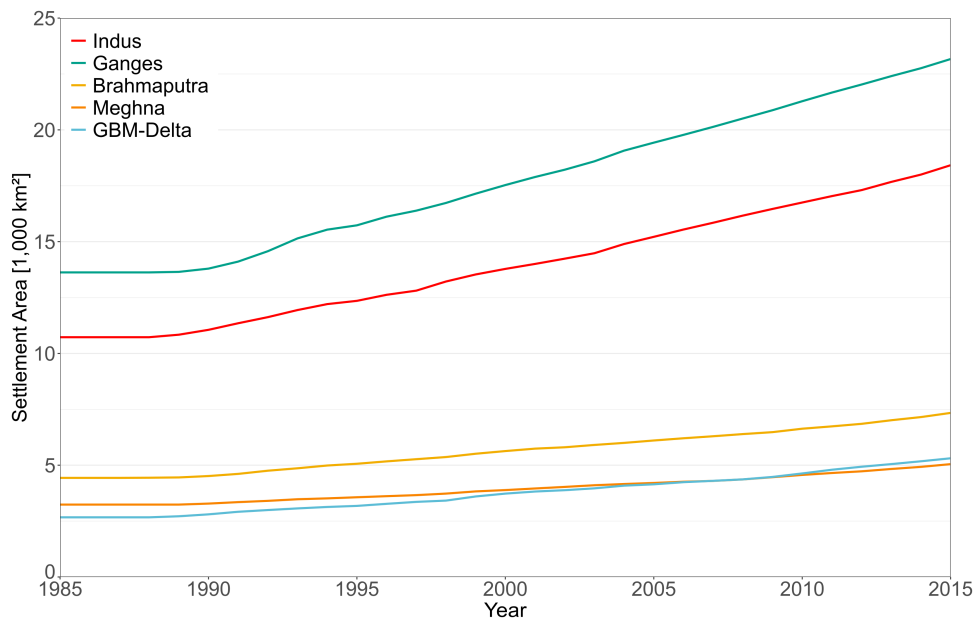


Figure 4.10: Development of the settlement area in the respective river basins between 1985 and 2015. These statistics are extracted from the DLR World Settlement Footprint (WSF) Evolution data (Marconcini et al., 2020, 2021).

Furthermore, Figure 4.11b visualizes the total Gross Domestic Production (GDP) based on purchasing power parity (PPP) for the year 2015. To obtain the total GDP (PPP) per pixel, Kummu et al. (2018) multiplied sub-national GDP per capita statistics with gridded population data. Statistics on GDP are usually available at national scale and are considered as a key indicator among human and economic development measures (Kummu et al., 2018). According to statistics of the International Monetary Fund (IMF) with respect to GDP per capita (PPP), India, for example, is ranked 128th among 195 considered countries (IMF, 2021). However, in the list of total GDP (PPP), India is ranked third behind China and the United States (IMF, 2021). This is also reflected in Figure 4.11b, where gridded total GDP (PPP) is comparatively high for the investigated river basins.

Apart from these statistics, human influence in the IGBM river basins, particularly in the Indo-Gangetic plains, is also expressed by the intensive agricultural land use, boosted by the green revolution in India (Evenson and Gollin, 2003). The green revolution started around the 1960s and caused considerable land use conversions to agricultural land use at the cost of forests and shrublands (Mathur and AchutaRao, 2019). Today, most of the agricultural areas are equipped with irrigation systems and together with further sectors including the industry and domestic needs, they greatly depend on the availability of freshwater (Biemans et al., 2019). Also, considering the river flows, large parts of the river segments of the IGBM rivers are impacted by human-induced changes, such as dams for hydropower generation or river water diversion (Grill et al., 2019; Gain and Giupponi, 2014; Grumbine and Pandit, 2013).

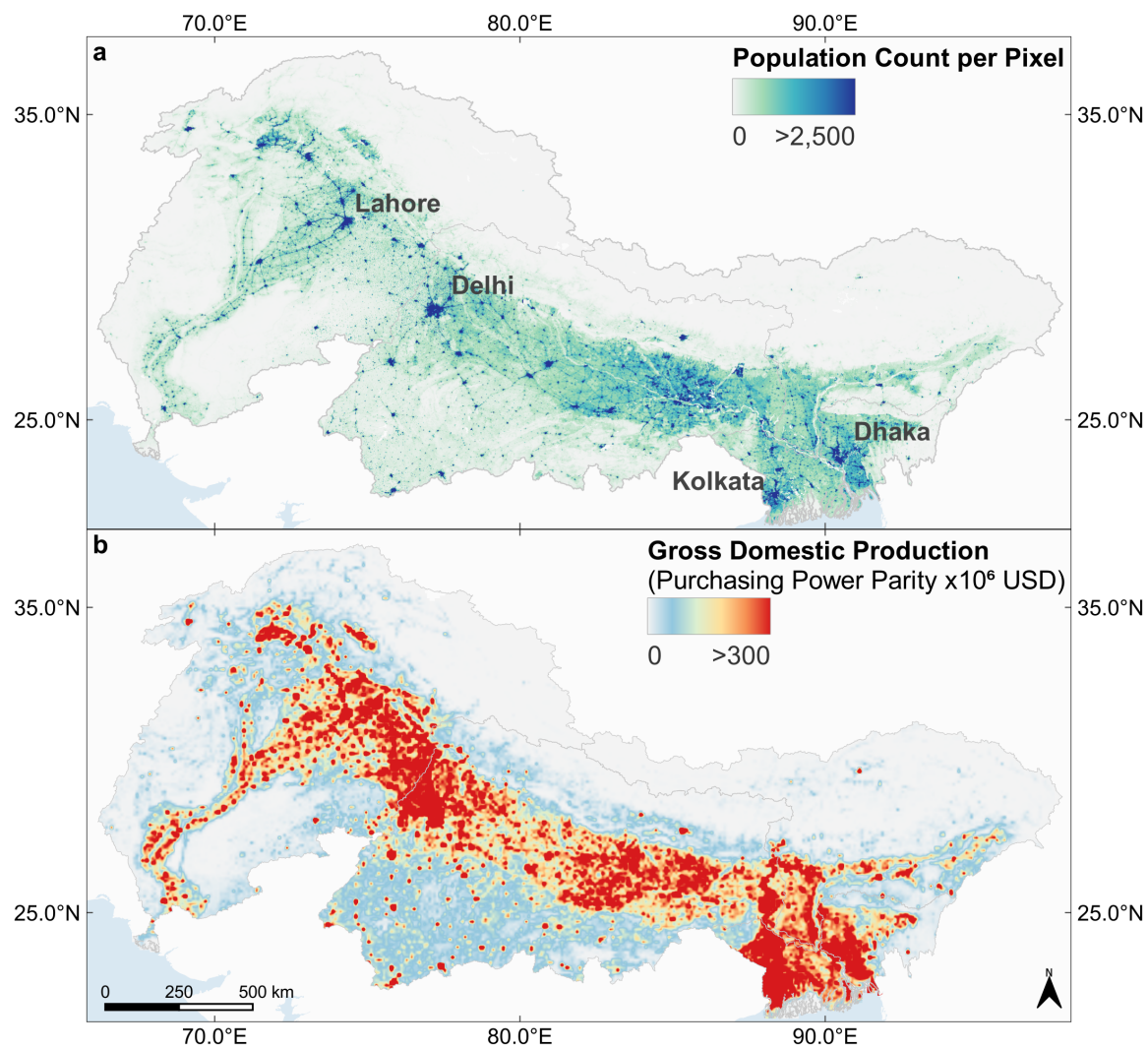


Figure 4.11: (a) Overview of the gridded population counts for the year 2020 (Lloyd et al., 2019; WorldPop and CIESIN, 2018) and (b) the gridded total Gross Domestic Production (GDP) (purchasing power parity) in constant 2011 international US dollars for the year 2015 (Kummu et al., 2018). The four labeled cities in the study area are megacities exceeding a population of 10 million people.

Chapter 5

*A Framework for the Analysis of Multi-Source Geoscientific Time Series**

This chapter describes the methods and techniques that are applied to prepare a multi-source feature space consisting of multivariate geoscientific time series. This feature space is then used to quantify and analyze land surface dynamics in transboundary river basins. As summarized in Chapter 2 and 3, the investigation of multivariate geoscientific time series characterizing the land surface across spheres is of great importance to enhance the understanding of environmental change and assess the influence of natural and anthropogenic drivers. Also, the literature review indicated that the analysis of land surface dynamics in large river basins with spaceborne remote sensing is largely limited to studies at regional and subbasin scale. In case of transboundary river basins, the study areas were largely restricted by administrative boundaries. In consideration of the ever-increasing amount of remote sensing data streams that cover the entire Earth's surface for already several decades, the generation and exploitation of high dimensional feature spaces with respect to the analysis of land surface dynamics still remains understudied. Factors exacerbating multivariate time series analysis are often associated with different data properties in terms of data format, spatial as well as temporal resolution, and data storage and processing capabilities.

To address these issues and be able to make use of the full potential of multivariate geoscientific time series, frameworks comprising both the preprocessing of multi-source geospatial time series and the utilization of statistical time series analysis techniques are needed. In this regard, an overview of available frameworks and online cloud services enabling the access to and the evaluation of massive amounts of remote sensing data, specifically ARD, is given by Sudmanns et al. (2019). Considering online cloud services, the GEE platform is amongst the most widely used utility, encompassing freely available data

*Parts of this chapter have been published in Uereyen et al. (2022a)

of many remote sensing missions and subsequently generated products (Gorelick et al., 2017). Besides the various geospatial datasets, the user has access to the web-based GEE integrated development environment (IDE) and the JavaScript application programming interface (API) including tools e.g. with respect to image processing and analysis without the requirement of downloading the remote sensing data to the local machine. Although, depending on the use case and research objectives, the GEE API might be considered as a restricted programming framework and the free version only comes with processing and storage limitations. Furthermore, the data cube concept provides a further solution to save, maintain, and analyze multi-source remote sensing as well as further geospatial data (Sudmanns et al., 2019; Baumann et al., 2018; Simoes et al., 2021). In this context, various EO data cubes have been implemented at regional scale using the Open Data Cube framework and are in operational use (e.g. Asmaryan et al. 2019; Chatenoux et al. 2021; Ferreira et al. 2020; Giuliani et al. 2017; Killough 2019; Lewis et al. 2017). Recent advances in data cubes with respect to remote sensing applications and methods for the analysis of high dimensional feature spaces emphasize the importance of multivariate time series analyses rather than considering single variables (Mahecha et al., 2020; Estupinan-Suarez et al., 2021).

In agreement with these developments, a novel framework integrating both, the preparation and statistical analysis of multi-source geoscientific time series is developed and implemented as part of this thesis on a high-performance computing (HPC) environment of the German Remote Sensing Data Center (DFD) at the German Aerospace Center (DLR). The developed framework should be easy-to-implement, time efficient, and flexible with respect to the entire processing pipelines, including the harmonization of the multi-source input data. Also, the framework is developed with the objective of being transferable to any geographical entity or temporal resolution as well as any geoscientific time series data. The integrated statistical time series analysis techniques will be used to reveal land surface dynamics with particular focus on vegetation condition, surface water area, and snow cover area over last two decades.

The following chapters first introduce the used data basis, including remote sensing-based land surface parameters as well as climatic and hydrological variables (Chapter 5.1). Next, the developed and implemented methodological framework for time series preparation, generation of the harmonized database, and the application of statistical time series analysis is presented (Chapter 5.2). Here, the time series analysis includes the calculation of trends, changes in phenological parameters, and computation of driving variables. In the subsequent chapters, the results of the statistical analyses are illustrated (Chapter 5.3) and discussed with respect to relevant literature and remaining limitations (Chapter 5.5). Ultimately, Chapter 5.6 provides a summary of the entire Chapter 5

5.1 Input Data

The following chapters describe the used input data to characterize land surface dynamics in the IGBM river basins (see Figure 5.1). These include geoscientific time series on vegetation condition, surface water area, and snow cover area derived from MODIS acquisitions (Chapter 5.1.1). In Chapter 5.1.2, the used climatic and hydrological variables are presented. These variables are included to estimate their influence on the remote sensing-based land surface variables. Further employed auxiliary data are introduced in Chapter 5.1.3.

5.1.1 Remote Sensing-Based Land Surface Variables

The collocated remote sensing-based features characterizing the land surface area are based on optical imagery from the MODIS instruments aboard the Terra and Aqua satellites operated by the National Aeronautics and Space Administration (NASA). The Terra satellite was launched on 18th December 1999 into a sun-synchronous orbit at an altitude of 705 km. The sister satellite, Aqua, was launched approximately 2 years later on 4th May 2002 (Justice et al., 2002). Besides the MODIS sensor, which is recording multispectral imagery, both satellites carry further instruments acquiring daily imagery of the entire Earth's surface. MODIS imagery from both sensors are consistent and can be used jointly. This increases the chances of generating cloud-free temporal composites over cloud prone areas and enables intra-annual as well as inter-annual analyses. The MODIS instruments record images covering 36 spectral frequencies of sunlight reflected from the Earth's surface in a 2,300 km wide swath mode. In this regard, the relevant spectral bands of MODIS imagery have a spatial resolution of 250 m for the red and infrared bands as well as 500 m for 5 further spectral bands (Justice et al., 2002). The MODIS product suite provides many datasets on land surface properties, including surface reflectance and vegetation characteristics. Depending on the product, the temporal resolution might be daily or composites of images acquired within a 4-day, 8-day, 16-day, monthly, or yearly interval. Furthermore, MODIS products are supplied in a non-overlapping tile grid and are mapped in the equal-area sinusoidal grid projection. At this, one MODIS granule covers an area of 1,200*1,200 km, corresponding to an area of 1,440,000 km² (Justice et al., 2002). The IGBM river basins are covered by 8 granules, including h23v05, h23v06, h24v05, h24v06, h25v05, h25v06, h26v05, and h26v06. All products used in this thesis are based on Collection 6.

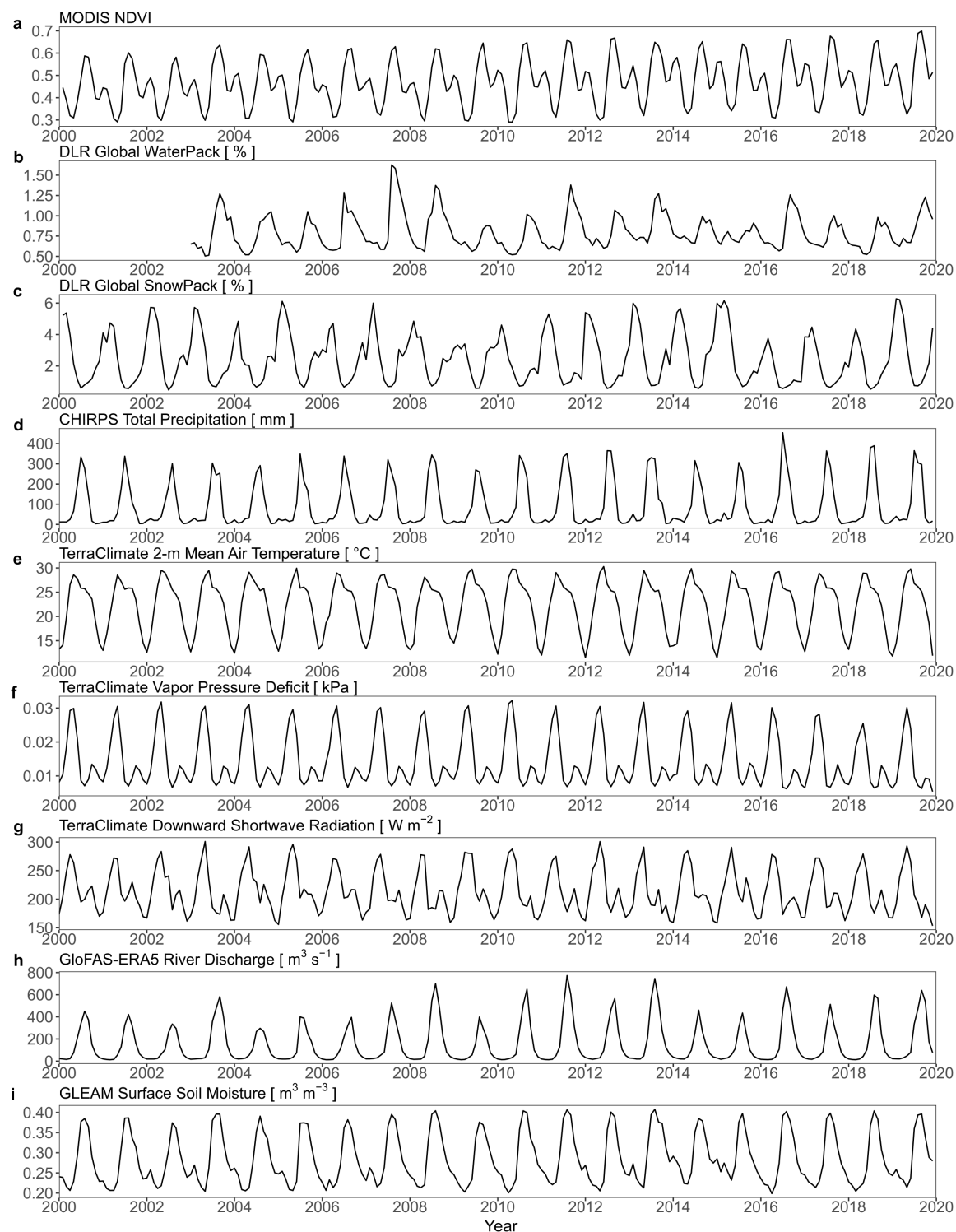


Figure 5.1: Overview of used geoscientific monthly time series to analyze land surface dynamics, including (a) MODIS NDVI (Didan and Munoz, 2019), (b) DLR Global WaterPack (Klein et al., 2017), (c) DLR Global SnowPack (Dietz et al., 2015), (d) CHIRPS total precipitation (Funk et al., 2015), (e) TerraClimate 2-m mean air temperature, (f) TerraClimate vapor pressure deficit, (g) TerraClimate downward shortwave radiation (Abatzoglou et al., 2018), (h) GloFAS-ERA5 river discharge (Harrigan et al., 2020), and (i) GLEAM surface soil moisture (Martens et al., 2017; Miralles et al., 2011). The illustrated time series are averages for the entire Ganges river basin.

5.1.1.1 MODIS Normalized Difference Vegetation Index

MODIS vegetation products provide consistent spatial and temporal time series on vegetation condition at global scale and are available at either 16-day or monthly temporal resolution. The vegetation products are produced at a spatial resolution of 250 m, 500 m, 1 km, or 5.6 km (Didan and Munoz, 2019). Here, the MOD13C2.006 product is employed, which is available at 5.6 km spatial resolution and monthly temporal resolution. This dataset consists of 13 bands, including the NDVI, enhanced vegetation index (EVI), spectral bands, pixel reliability, and quality assurance layers. In this thesis, the NDVI is selected and used to characterize vegetation condition. The NDVI is widely used and is considered to be the “continuity index” of the existing AVHRR NDVI time series data (Didan and Munoz, 2019). The NDVI is the normalized ratio of red and near infrared wavelength and is calculated as follows:

$$NDVI = \frac{(Near\ Infrared - Red)}{(Near\ Infrared + Red)} \quad (1)$$

It has to be noted, that in search of remote sensing sensors suitable for time series analysis, the Landsat mission at 30 m spatial resolution was considered as well. In this context, the IGBM river basins are covered by 164 Landsat tiles. A query on available Landsat images for these tiles between 1985–2020 at a cloud coverage of less than 60 % resulted in 99,420 images in total. A further detailed evaluation indicated that the median of available images per tile and year amounts to 12 images for most of the tiles. Therefore, it was concluded that the generation of time series with equidistant observations is not possible with Landsat images for the IGBM river basins.

5.1.1.2 DLR Global WaterPack

The Global WaterPack is processed at the DFD of the DLR and characterizes inland surface water area using remote sensing imagery from both MODIS sensors aboard Terra (MOD09GQ.006) and Aqua (MYD09GQ.006) at a spatial resolution of 250 m and a daily temporal resolution (Klein et al., 2017). The processing of the Global WaterPack requires images from both sensors, resulting in images up to twice a day. Therefore, the surface water area time series are available since 2003, where both MODIS sensors recorded remote sensing imagery. Surface water area is classified based on dynamic thresholding, which jointly incorporates the distribution of near infrared values as well as near infrared and red values. In addition, the processing involves further auxiliary data, including multispectral imagery, settlement areas, topographical data, and thermal information. Furthermore, the MOD10A1.006 and MYD10A1.006 are used to mask clouds as well as snow and ice cov-

ered areas. The classification procedure results in a binary water mask, which is finalized through a temporal interpolation of gaps. This interpolation results in a consistent and gap-free time series of surface water area. The reported accuracy measures by Klein et al. (2017) indicate very high overall accuracies for pixels covered fully with surface water, whereas the accuracy declines for pixels covered only partially with surface water.

5.1.1.3 DLR Global SnowPack

The Global SnowPack processor (Dietz et al., 2015) at the DFD of the DLR is used to generate time series on snow cover area by means of products from both MODIS sensors aboard Terra (MOD10A1.006) and Aqua (MYD10A1.006) (Hall et al., 2002). These MODIS data provide the NDSI, which is used to derive snow cover area and is based on following formula:

$$NDSI = \frac{(Green - Shortwave\ Near\ Infrared)}{(Green + Shortwave\ Near\ Infrared)} \quad (2)$$

Using the NDSI, the Global SnowPack processor generates cloud free binary masks on snow cover area at a spatial resolution of 500 m and a daily temporal resolution (Dietz et al., 2015; Rößler et al., 2021). In a first step, an adaptive thresholding is applied to the NDSI layer to differentiate between “snow” and “non-snow”. Next, images from both sensors are combined to a daily composite to reduce cloudy pixels. Remaining pixels with cloud coverage are temporally interpolated considering the snow coverage in the preceding and following day. Furthermore, a topographical interpolation is carried out, if the degree of cloud coverage is lower than a defined threshold. Further details on the DLR Global SnowPack processor are available in Dietz et al. (2015) and Rößler et al. (2021). A detailed validation of MODIS snow products was conducted by Hall and Riggs (2007). The results indicated high overall accuracies, but highly depending on land cover classes and snow condition. Further investigations outline improvements in MODIS Collection 6 products in comparison to prior versions (Masson et al., 2018; Notarnicola, 2020). Besides providing a binary product on snow cover area, the Global SnowPack also includes information on snow cover duration and start as well as end of season.

5.1.2 Climatic and Hydrological Variables

In this chapter, all climatic and hydrological time series employed for the quantification of environmental controls on the vegetation condition, surface water area, and snow cover area are introduced. These time series and the datasets in particular, were selected based on the relevance as a driving variable, the spatial and temporal resolution, and the availability

over the last two decades. In this regard, gridded time series for the variables precipitation, soil moisture, river discharge, temperature, downward shortwave radiation, and vapor pressure deficit were assembled. Precipitation was characterized by the Climate Hazards Group Infrared Precipitation with Station data (CHIRPS) version 2.0, which is a blend of station measurements, satellite acquisitions, and long-term climatology (Funk et al., 2015). This product comes at a spatial resolution of 0.05° (approx. 5 km) and a monthly temporal resolution. It has to be noted, that this data is limited to areas between 50°N – 50°S . CHIRPS data is available since 1981 and its suitability in capturing precipitation patterns over India and South Asia was investigated in many studies showing good performance (e.g. Banerjee et al. 2020; Gupta et al. 2019; Prakash 2019). To assess the quality of gridded precipitation data over India, gridded precipitation time series from the Indian Meteorological Department (IMD) at a spatial resolution of 0.25° (approx. 25 km) are often used as reference. This data is created by means of gauge measurements of over 6,000 stations (Gupta et al., 2019). Yet, considering transboundary analyses, the usage of IMD precipitation is not suited for this thesis, as it is limited by the national boundaries of India. For example, Prakash (2019) reported a root mean square error of 0.40 mm day^{-1} for CHIRPS compared to the IMD precipitation, which was the lowest error considering further datasets.

Furthermore, monthly mean 2-m air temperature was derived using the minimum and maximum 2-m air temperature from the TerraClimate data (Abatzoglou et al., 2018). This dataset has a spatial resolution of $1/24^\circ$ (approx. 4 km) and is computed based on climatologically aided interpolation. To this end, high spatial resolution monthly climatology from the WorldClim data was combined with coarse spatial resolution monthly anomalies from the Climatic Research Unit (CRU) Ts4.0 and the Japanese 55-year Reanalysis data (Abatzoglou et al., 2018). In addition to 2-m air temperature, downward shortwave radiation and vapor pressure deficit was also incorporated from the TerraClimate product suite. Due to its comparatively high spatial resolution and good validation metrics, climatic variables from TerraClimate have been widely employed (e.g. Kath et al. 2020; Zhang et al. 2020a). Abatzoglou et al. (2018) presented the results of the conducted accuracy assessment, which was performed using numerous in-situ station measurements of diverse networks, including the Global Historical Climatology Network and FLUXNET stations. For example, for mean 2-m air temperature, the mean absolute error amounts to 0.32°C .

Global Flood Awareness System (GloFAS)-ERA5 gridded river discharge version 3.1 is used to analyze surface water area dynamics (Harrigan et al., 2020). This data is available at a spatial resolution of 0.1° (approx. 10 km). A validation of the estimated river discharge is undertaken using more than 1,800 station measurements. Harrigan et al. (2020) reported

a mean absolute error of 0.41 mm day^{-1} at global scale and amongst others parts of India and South Asia were highlighted as areas with comparatively low errors.

Next, surface soil moisture based on the Global Land Evaporation Amsterdam Model (GLEAM) version 3.5a is utilized to evaluate its influence on vegetation condition (Martens et al., 2017; Miralles et al., 2011). This dataset features a spatial resolution of 0.25° (approx. 25 km) and a monthly temporal resolution. The provided accuracy measures of this dataset in Martens et al. (2017) point towards good correlations with in-situ measurements.

5.1.3 Auxiliary Data

In this chapter, auxiliary data used for preprocessing of the time series variables are presented. These include the ESA CCI land cover data version 2.0.7 (1992–2015) and 2.1.1 (2016–2019), which was already introduced in Chapter 4.2.3. This land cover data provides global annual land cover classifications since 1992 at 300 m spatial resolution (European Space Agency, 2017; Plummer et al., 2017). The classifications starting from 2013 use remote sensing imagery from the Ocean and Land Colour Instrument aboard the Sentinel-3 satellite and the Project for On-Board Autonomy (PROBA)-Vegetation mission. The previous years were classified based on Envisat Medium Resolution Imaging Spectrometer (MERIS), NOAA AVHRR, and Satellite Pour l'Observation de la Terre (SPOT)-Vegetation instruments (European Space Agency, 2017). Compared to other available global land cover classifications, the ESA CCI land cover is of high relevance, as it is featuring a finer spatial and temporal resolution (Mousivand and Arsanjani, 2019). Furthermore, topographic data was utilized during preprocessing and analysis as well. For this purpose, the recently published Copernicus DEM at a spatial resolution of 90 m was used (European Space Agency and Sinergise, 2021). As stated in Chapter 2.2, the Copernicus DEM is an edited version of the WorldDEMTM (Collins et al., 2015), which is based on the TanDEM-X DEM (Wessel et al., 2018). Additionally, gridded Köppen-Geiger climate classification was used for the preprocessing of selected time series variables. This data is available at a spatial resolution of 1 km and was derived by combining various climatic datasets (Beck et al., 2018). Finally, the outlines of the river basins were delineated from a vector dataset being available at the Aquastat platform of the FAO (FAO, 2009) and which is based on the HydroSHEDS dataset (Lehner et al., 2008).

5.2 Methodological Framework

This chapter presents the entire methodological framework for analysis of land surface dynamics using multivariate geoscientific time series. Figure 5.2 illustrates briefly the de-

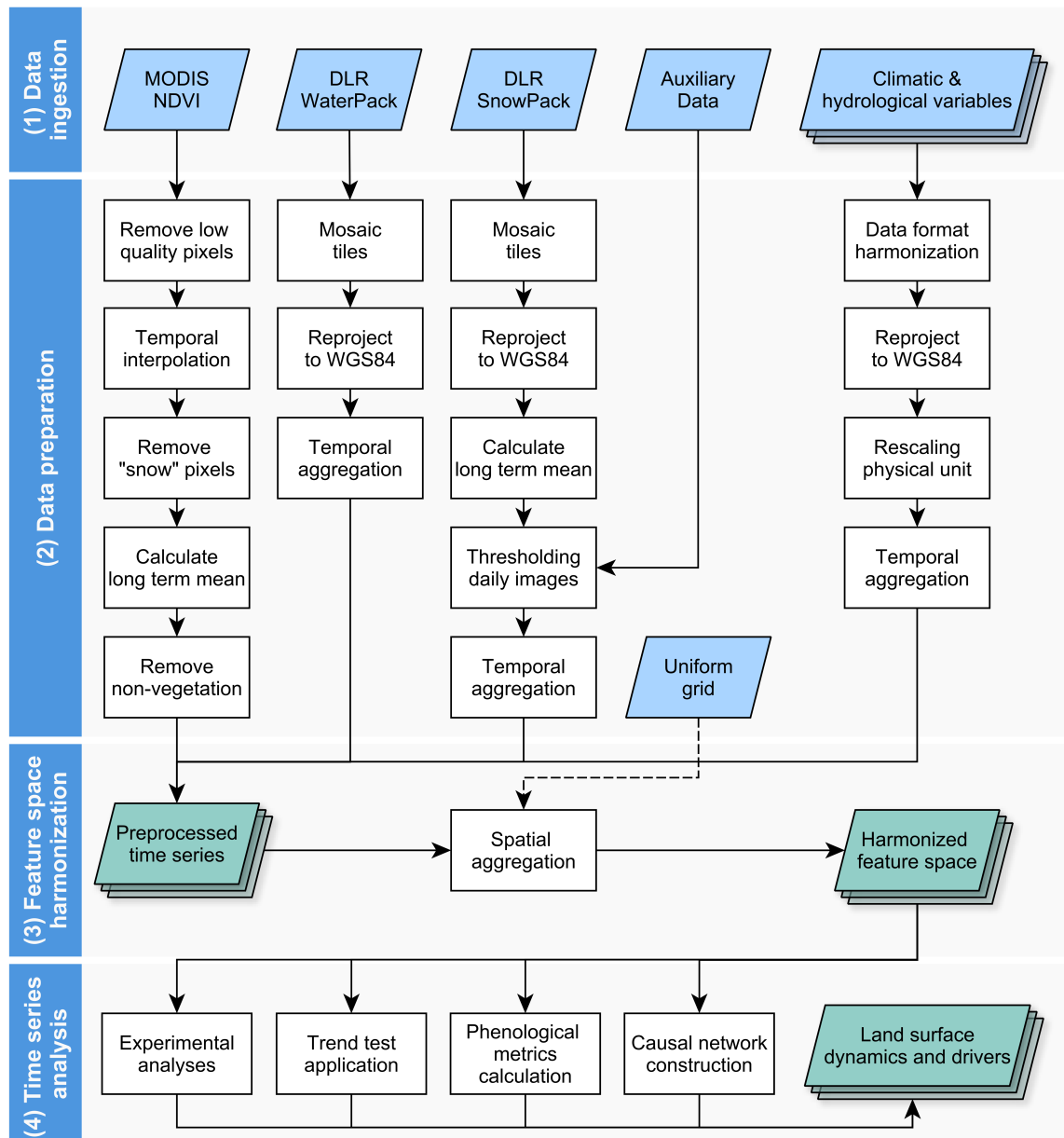


Figure 5.2: Simplified overview of workflow for the developed and implemented framework including data preparation, feature space harmonization, and statistical time series analyses.

veloped and implemented framework. First, the required preprocessing steps of the time series are described (Chapter 5.2.1). Chapter 5.2.2 outlines the approach to harmonize the multi-source time series to a common grid space and geographical entity. Afterwards, the employed statistical time series analysis techniques are explained (Chapter 5.2.3).

5.2.1 Time Series Preparation

This chapter describes the conducted preprocessing steps of all time series variables. In brevity, each variable requires specific preprocessing tasks as illustrated in Figure 5.2. Prior to the preprocessing, the geoscientific time series and auxiliary data are gathered

from various sources, including internal services at DLR such as the Earth Observation Center (EOC) Geoservice (<https://geoservice.dlr.de/>; last accessed on: 2021-12-01), NASA EarthData platform (<https://earthdata.nasa.gov/>; last accessed on: 2021-12-01), Copernicus Climate Data Store (CDS) (<https://cds.climate.copernicus.eu/>; last accessed on: 2021-12-01), and further sources with respect to other climatic variables. All downloaded time series variables and auxiliary data were ingested on the internal HPC environment at DLR-DFD.

To begin with, the preprocessing of the global MODIS NDVI (MOD13C2.006) time series covering the period 2000 to 2019 (Didan and Munoz, 2019), included the exclusion of low quality pixels and interpolation of resulting gaps. Low quality pixels were determined through the usage of the supplied reliability and quality assurance layers, which are included in each Hierarchical Data Format (HDF) file and store the information in 8 and 16-bits. Several classes in these layers are associated with low quality, such as pixels flagged as “mixed cloud”, “adjacent cloud”, and “possible shadow”. These pixels were classified by means of configured scripts to extract the relevant classes from the stored bits. After excluding these pixels from the NDVI time series, the resulting gaps were filled through linear interpolation as suggested by Fensholt and Proud (2012). Subsequently to the temporal interpolation, pixels covered by snow were extracted from the reliability layer for each time step and excluded from the geospatial time series, since these pixels should not be interpolated. Finally, a long-term mean by means of all images within the investigated period was calculated. This long-term mean was used to mask pixels with an NDVI value greater than 0.15, since values above this threshold are considered as pixels covered by vegetation (Wittich and Hansing, 1995).

Snow cover products being processed by the DLR Global SnowPack processor based on daily MODIS data (M*D10A1.006) are subject to further preprocessing steps. First, the daily images covering the MODIS tiles are mosaicked and reprojected from the sinusoidal projection to the World Geodetic System (WGS84) coordinate system. Next, rulesets were defined and applied to decrease the amount falsely classified snow pixels and ephemeral snow. In this regard, ephemeral snow was excluded based on the filtering of patches with less than 10 pixels as suggested by Notarnicola (2020) and water bodies were excluded using the ESA CCI land cover product (European Space Agency, 2017). Moreover, the number of false positives is comparatively high during the monsoon season in low altitudes, where clouds are partially labeled as snow. To remove these false positives, a long-term mean was calculated for both the entire period as well as the monsoon (JJAS) and post-monsoon (ON) season. In a next step, a ruleset incorporating the aforementioned long-term averages, climate zones (Beck et al., 2018), and elevation data (European Space Agency and Sinergise, 2021) was defined. More specifically, pixels at an elevation lower than 1500 m,

being located in temperate or tropical climate, and with a long-term mean lower than 0.2 were excluded. In a last step, the preprocessed and reprojected daily binary snow cover products were aggregated to monthly composites covering the period between 2000–2019. The monthly composites characterized fractional snow cover area.

On the contrary, the DLR Global WaterPack, which is based on daily MODIS surface reflectance imagery (M*DGQ09.006), required only a few preprocessing steps (Klein et al., 2017, 2021). These include mosaicking, reprojection to WGS84 coordinate system, and temporal aggregation to monthly composites. The monthly composites represented fractional surface water area. Compared to the NDVI, and Global SnowPack, the Global WaterPack is available for the period 2003–2019, as it relies on the joint usage of both MODIS sensors aboard Terra and Aqua (see Chapter 5.1.1.2 and Figure 5.1).

The climatic and hydrological variables being listed in Chapter 5.1.2 were ingested on the HPC environment and preprocessed, to prepare these time series for the feature space harmonization as well. Most of these variables were available as NetCDF files and, thus, were converted to single GeoTiff files per time step in accordance to the remote sensing-based variables. Moreover, time series at daily temporal resolution were temporally aggregated to monthly composites.

5.2.2 Feature Space Harmonization

This chapter introduces the implemented approach to automatically harmonize multi-source time series that come with different characteristics. In this regard, the preparation of a harmonized feature space in terms of spatial and temporal resolution of the used geoscientific time series is required, to enable joint analyses with the multivariate feature space. The corresponding workflow is illustrated in Figure 5.3. In consideration of the spatial resolution of all input data, a common grid space covering the IGBM river basins at a spatial resolution of 0.1° (approx. 9 km) was defined and generated using the open source Quantum Geographic Information System (QGIS) version 3.20.3 software (<https://www.qgis.org/de/site/>; last accessed on 2021-11-10). This common grid space is then utilized to harmonize the multivariate feature space in terms of their spatial resolution. The harmonization is performed automatically for all of the time series by means of a spatial aggregation procedure, which is averaging all pixels that intersect a given grid cell. Here, weighted averaging is applied, where the weight of a value is determined by the fraction of the pixel that is covered by a given grid cell. The developed approach and spatial aggregation is applicable to any other geographical entity and temporal intervals, respectively, e.g. to river basins or biomes and daily or biweekly time steps. This harmonization procedure was written using the R and Python programming language and further open source tools, such as the Geospatial

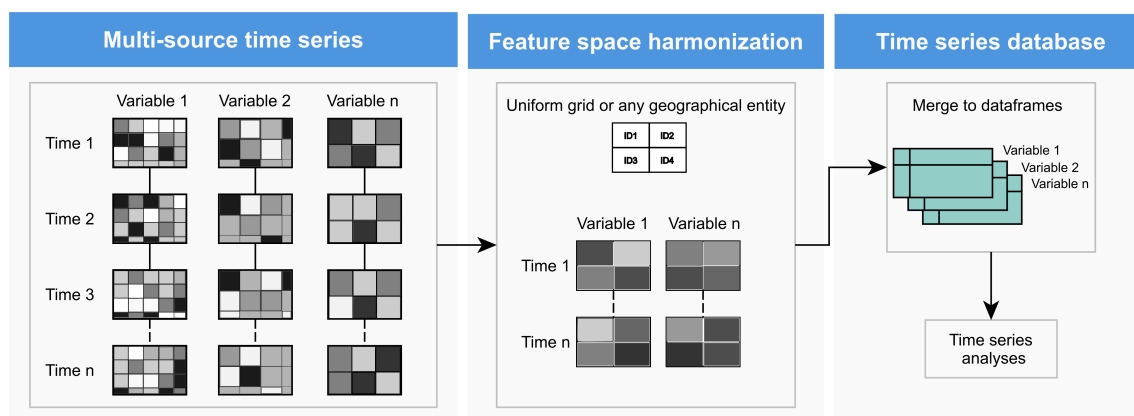


Figure 5.3: Workflow for the database generation step, where the prepared multi-source time series are spatially aggregated to a selected uniform grid. This spatial grid might be replaced by any geographical entity. The abbreviations ID and T denote unique feature identifier and time step, respectively. Modified after Uereyen et al. (2022a).

Data Abstraction Library (GDAL). In this context, the weighted averaging is conducted using the exact extract library (<https://github.com/isciences/exactextract/>; last accessed on 2021-11-10). As stated before, the preprocessing and harmonization of the geoscientific time series was implemented on an HPC environment using docker containers with minimal user interaction. Furthermore, the harmonized features are stored in data frames, which include the respective time series variable for each grid cell and time step. As visualized in Figure 5.3, these data frames are then used as input for the subsequent time series analyses to analyze land surface dynamics.

5.2.3 Time Series Analysis Techniques

This chapter describes the implemented time series analysis methods and used global parameter settings to quantify and evaluate land surface dynamics for the transboundary river basins. These methods include the application of the Mann-Kendall trend test in association with the Theil-Sen slope estimator, the Timesat tool to derive phenological metrics, as well as the PCMCi approach to compute causal networks and then derive the influence of the driving variables on vegetation condition, surface water area, and snow cover area.

5.2.3.1 Trend Test

In this thesis, monotonic trends of the land surface variables vegetation condition (MODIS NDVI), surface water area (DLR Global WaterPack), and snow cover area (DLR Global SnowPack) were derived to measure change over time in the investigated large river basins. In this regard, the significance of trends and the magnitude of change per unit time were computed. As can be seen in Figure 5.1, the investigated land surface vari-

ables have clear seasonal cycles. Therefore, the seasonal Mann-Kendall (MK) test (Mann, 1945; Kendall, 1975), a rank-based non-parametric approach, in conjunction with the Theil-Sen (TS) slope estimator (Theil, 1950; Sen, 1968) was employed. Non-parametric tests have no requirement with respect to the distribution of the data sample and are less sensitive to extreme values compared to parametric tests such as the linear regression test (Hamed and Ramachandra Rao, 1998; Onoz and Bayazit, 2003; Wang et al., 2020). For the application of the seasonal MK test, the time series were split into the meteorological seasons keeping the monthly resolution. The seasons, which were introduced in Chapter 4.2.1, include the winter (DJF), pre-monsoon (MAM), monsoon (JJAS), and post-monsoon season (ON).

More specifically, the MK test measures if there is a monotonic increasing or decreasing trend. To this end, the test determines the frequency of the sign of the difference between all pair-wise combinations of observations ($x_j - x_i$, where $j > i$). Each observation is compared to all previous data points leading to $n(n-1)/2$ pair-wise combinations, where n is the total number of observations. Accordingly, the test statistic S may result in a large positive or negative number indicating a positive or negative trend. In case of the seasonal MK test, the statistics are first calculated for each season separately. Then, to assess the test statistic for the entire time series at annual scale, the S statistic and its variance from all seasons are considered to retrieve the global Z statistic (Gocic and Trajkovic, 2013; Wang et al., 2020). The null hypothesis (H_0) of the trend test assumes no monotonic trend, whereas the alternative hypothesis (H_a) an increasing or decreasing monotonic trend. Throughout this thesis, trends were considered statistically significant at a confidence level of 95 % (p -value < 0.05). Trends with a p -value above this defined threshold were considered as no change.

Next, the TS slope is calculated by means of the slope of each adjacent observation and denotes the median of all slopes as global slope value. In particular, the TS slope is calculated as follows:

$$\beta = \frac{x_j - x_i}{j - i}, (1 \leq i < j \leq n) \quad (3)$$

where x_j and x_i are the observations at time i and j for all adjacent data points (n). A positive or negative slope value indicates the direction and magnitude of the trend (Zhang et al., 2020b). In accordance to the calculation of the seasonal MK test, the TS slope is calculated for each season separately. Next, the slope value at annual scale is derived using the median of all seasonal slope values and is only considered if these are homogenous at a confidence level of 90 % (Collaud Coen et al., 2020). To retrieve the slope magnitude at decadal temporal scale, the resulting annual slope value was multiplied with the number of years per decade.

Moreover, when using the MK test and the TS slope estimator one has to consider that the data should be independent, because these tests are not robust against serial correlation (Wang et al., 2020). Methods to counteract serial correlation include temporal aggregation of the time series to e.g. annual resolution or the usage of prewhitening algorithms before the application of the trend test. In this regard, the temporal aggregation of the time series reduces the available number of data samples and, thus, would most likely result in smaller statistical significance (Collaud Coen et al., 2020). To this end, to minimize the seasonal influence and serial correlation, seasonal anomalies were calculated for the time series using following equation:

$$x_{anom} = x_i - \bar{x}_{season} \quad (4)$$

where x_{anom} is the departure of the actual monthly observation (x_i) from the long-term mean of the respective season (\bar{x}_{season}) (see Figure 5.4). In the following step, the statistical significance of the lag-1 autocorrelation (r_1) is determined using:

$$r_1 = \frac{\sum_{i=1}^{N-1} (x_i - \bar{x})(x_{i+1} - \bar{x})}{\sum_{i=1}^N (x_i - \bar{x})^2}. \quad (5)$$

The workflow regarding the trend test is visualized in Figure 5.5. In case of a non-significant lag-1 autocorrelation, the MK test and TS slope estimator were employed on the anomalized time series (see Figure 5.5). On the contrary, if lag-1 autocorrelation was statistically significant at the confidence level, the anomalized time series was additionally prewhitened. The application of prewhitening removes serial correlation from the series. In this context, the MK test is characterized by two types of errors. The first one being the

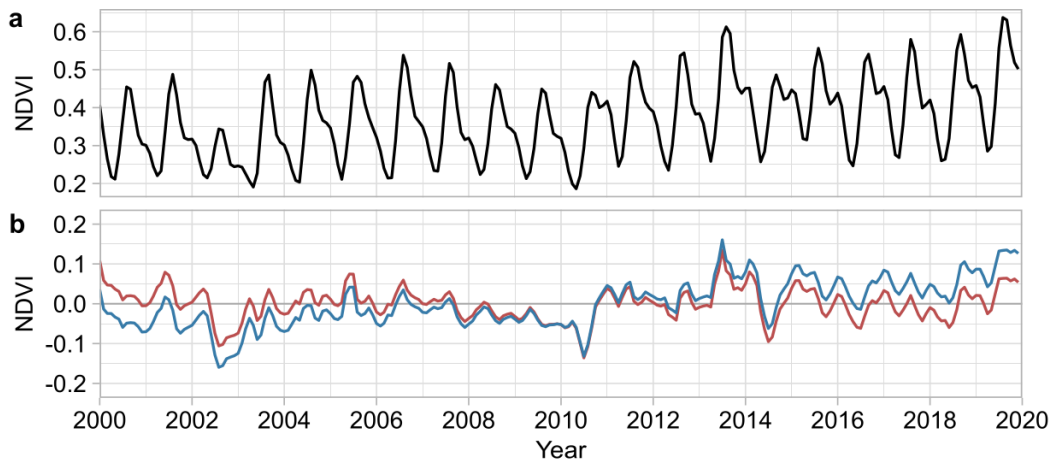


Figure 5.4: Exemplary diagram of the MODIS NDVI at monthly scale showing (a) the original and (b) the seasonally anomalized (blue line) as well as the detrended anomalized (red line) time series values.

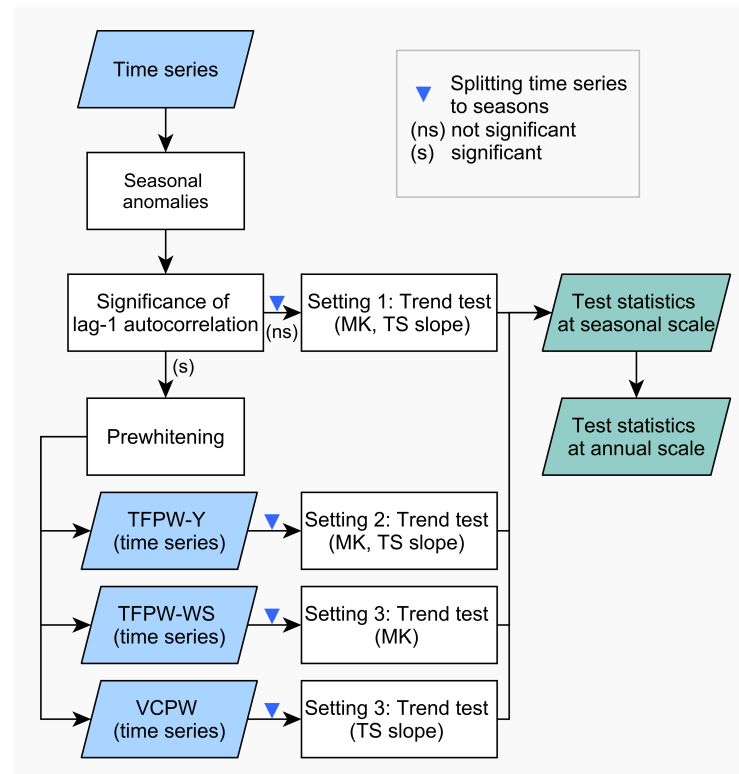


Figure 5.5: Workflow for the application of the trend test including the Mann-Kendall (MK) test and the Theil-Sen (TS) slope estimator. The time series are prewhitened (trend-free prewhitening after Yue et al. (TFPW-Y), trend-free prewhitening after Wang and Swail (TFPW-WS), variance corrected prewhitening (VCPW)) if the lag-1 autocorrelation is statistically significant. Modified after Ureyen et al. (2022a).

type I error (false positives) and the second, the type II error (false negatives). Serial correlation usually leads to an inflation of the type I error (Bayazit and Onoz, 2007). Depending on the used prewhitening method, the results might be affected by high or low type I error as well as a biased slope estimation. When the type I error is reduced through prewhitening, the risk of a type II error might increase (Wang et al., 2020). In fact, the magnitude of serial correlation is affected by the presence of a trend, which is why the test power of the MK test will worsen after prewhitening (Yue et al., 2002). For this reason, Yue et al. (2002) proposed an approach called TFPW-Y, where the time series are detrended prior to the prewhitening. This approach has a high test power and is among the most used prewhitening methods (Collaud Coen et al., 2020). Yet, past studies demonstrated that the utilization of TFPW-Y can lead to a high type I error and an inflated slope value (Collaud Coen et al., 2020; Wang et al., 2015c). Further detailed insights on advantages and disadvantages of respective prewhitening methods is provided by Collaud Coen et al. (2020). In this context, the TFPW-WS features a low type I and a high test power as well (Wang and Swail, 2001). TFPW-WS eliminates lag-1 autocorrelation in an iterative process while retaining the trend. Moreover, the aforementioned prewhitening algorithms lead to a biased slope estimation,

which is why Collaud Coen et al. (2020) suggest to use a VCPW procedure proposed by Wang et al. (2015c). In this connection, studies recommend to use multiple prewhitening algorithms instead of relying on only one (Collaud Coen et al., 2020; Wang et al., 2015c).

Ultimately, Figure 5.5 demonstrates the design of the implemented trend test. In agreement with suggestions in literature, multiple prewhitening algorithms were used to account for serial correlation. One setting involves the widely used TFPW-Y approach for the MK test and TS slope estimation. Next, a further setting applies TFPW-WS and VCPW in combination to quantify the significance of the trend and retrieve an unbiased slope estimate, respectively. For comparison purposes, the seasonal MK test and TS slope estimator were also applied without prewhitening.

5.2.3.2 Derivation of Phenological Metrics

Besides monotonic trends, this framework also includes the analysis of changes in seasonal characteristics of the time series. In this context, the open source Timesat tool (version 3.3) (Jönsson and Eklundh, 2002, 2004) was used to retrieve phenological metrics that are illustrated in Figure 5.6. Specifically, these include the metrics seasonal amplitude, timing of seasonal peaks, value of seasonal peak, and duration of season. Timesat is widely used for remote sensing applications, including phenological analysis of vegetation (e.g. Li et al. 2018; Wang et al. 2018c) and surface water area parameters (Klein et al., 2021) or time series preprocessing (e.g. Fassoni-Andrade and de Paiva 2019; Fensholt and Proud 2012). In this thesis, Timesat was applied on the land surface variables vegetation condition, surface water area, and snow cover area. With more detail, the tool calculates phenological metrics for $n - 1$ center most seasons, with n being the total number of years. Therefore, to incorporate the full extent of the studied period, the observations of the first year were duplicated and attached to the beginning of the time series, as suggested by Eklundh and Jönsson (2017). Moreover, the time series were not smoothed before the calculation of phenological metrics, as noise in the time series was already reduced through temporal and spatial aggregation. Regarding the seasonal amplitude setting, a 50 % fraction of the amplitude was defined to retrieve the beginning and ending of the season. Also, one annual season was assumed for the time series variables, except for NDVI, where two annual growing seasons were allowed to be detected. In consideration of the phenological analysis of the time series on surface water area and snow cover area, the hydrological calendar starting in June and ending in May was used (Mishra, 2020). Finally, the phenological metrics, seasonal amplitude, timing of seasonal peaks, value of seasonal peak, and duration of season were utilized to compute the difference between the two investigated decades (2000–2009, 2010–2019). For this purpose, the time series were split into the two decades and, next, the derived phe-

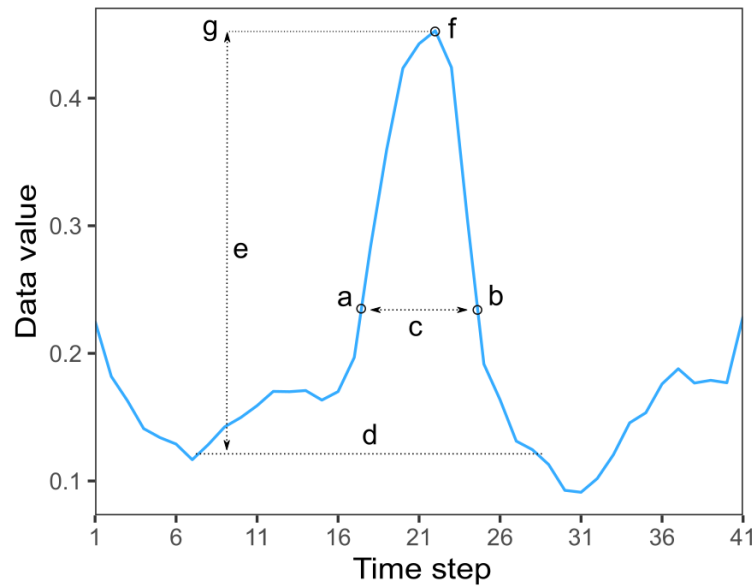


Figure 5.6: Overview of selected phenological metrics, including (a) start of season, (b) end of season, (c) duration of season, (d) base value, (e) seasonal amplitude, (g) seasonal peak value, and (f) timing of seasonal peak. Sketched after Eklundh and Jönsson (2017).

nological metrics were averaged per decade. Finally, the change was calculated by means of the difference between the two decades.

5.2.3.3 Application of a Causal Discovery Algorithm

As emphasized in Chapter 3.3, the analysis of multivariate time series is important to reveal land surface dynamics across spheres. To this end, a harmonized feature space based on multi-source geoscientific time series was generated. The collocated feature space allows for a detailed analysis of drivers for the land surface variables vegetation condition, surface water area, and snow cover area. These three variables are in the following denoted as targets. The used driving variables involve the climatic and hydrological variables presented in Chapter 5.1.2. As introduced in Chapter 2.3, past studies widely applied traditional correlative approaches or partial correlation using additional controlling variables. However, the detected correlation might be spurious and lead to false interpretations, due to common drivers or indirect paths (see Figure 5.7). In addition, a correlation analysis is not providing any insights on the direction of the relationship (Kretschmer et al., 2016). To overcome these issues, the causal discovery algorithm PCMCI was integrated into the framework (Runge, 2018; Runge et al., 2019b).

Overall, PCMCI is a causal discovery algorithm fostering the analysis of a multivariate feature space and it overcomes issues arising through autocorrelation, indirect paths, or common drivers (Runge et al., 2019b). To quantify the direction of influence and causal links, PCMCI incorporates the analysis of relations within a defined number of temporal

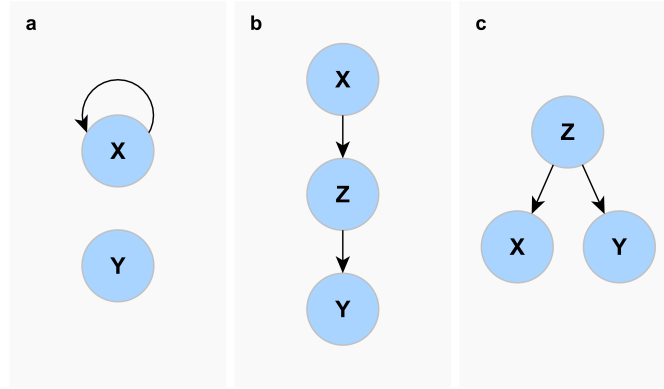


Figure 5.7: Overview of scenarios leading to a spurious correlation without a direct causation between variable X and Y, due to (a) autocorrelation, (b) an indirect path via variable Z, and (c) a common driver Z. Sketched after Kretschmer et al. (2016).

lags (τ) (Runge, 2018). In this connection, a number of assumptions have to be considered when performing causal analysis (Runge, 2018). For example, in this thesis, the captured causal links are considered to be relative in regards of the used geoscientific time series variables. This means that the detected causal links could vary, if the used feature space is modified. In addition, the partial correlation measure was selected as independence test, which is why stationarity in time series is required (Runge, 2018; Runge et al., 2019b). Stationarity in time series means that the mean and variance are constant over time and that the time series is not characterized by seasonality (Montgomery et al., 2015). To meet this requirement the time series were detrended and the seasonal cycle was removed by anomaly calculation (see Figure 5.4) as suggested by (Runge et al., 2019b). Subsequently, PCMCI utilizes all detrended anomaly time series with a two-step procedure, which involves a modified version of the Peter and Clark (PC) and the momentary conditional independence (MCI) algorithm (Runge, 2018).

More specifically, the PC step is the condition selection stage. For example, when snow cover area (SCA) is the target variable X_t^j , further variables (X_t^i) are considered as potential drivers or parents, with i being the variable and t the time index, i.e. $i \in \{T, P, DSR\}$ and $t \in \{1, \dots, \tau_{max}\}$, respectively. In case one of these three drivers is found to be significantly influencing the target variable SCA, the driver is included in the set of parents $\tilde{P}(X_t^j)$. Depending on the significance level α_{pc} , which is determined by the user, a potential driver might be regarded as irrelevant and excluded during the PC step. During the second part, the MCI algorithm considers all identified lagged drivers in combination with contemporaneous pairs, those at a temporal lag of 0, accounting for autocorrelation, indirect paths, and common drivers (Runge et al., 2019b). As stated before, partial correlation is used for the independence test in the MCI step, whereas the statistical significance is determined by means of two-sided t -test. Further details on the theory behind PCMCI is

available in Krich et al. (2020), Runge (2018), and Runge et al. (2019b). So far, PCMCI has been applied in several studies, including the analysis of biosphere-atmosphere interactions (Krich et al., 2020) or in the context of teleconnections (Di Capua et al., 2020a,b; Kretschmer et al., 2016). PCMCI is provided with the python package tigramite (version 4.2; <https://github.com/jakobrunge/tigramite>; last accessed on: 2021-11-24).

Table 5.1 provides an overview of the defined parameter settings for PCMCI. With more detail, a maximum temporal lag of 3 was considered during causal network generation. In general, vegetation responses to climatic factors are usually expected to be shorter than three months (Wu et al., 2015). Since the time series have a monthly temporal resolution, this lag corresponds to three months, being in agreement with other studies considering temporal lags (e.g. Krich et al. 2020; Papagiannopoulou et al. 2017; Wu et al. 2015). In theory, causal links are identified based on temporally lagged dependencies, because a variable is influenced by processes lying in the past and the time order provides an orientation of

Table 5.1: Overview of utilized parameter settings for PCMCI. Default values were used for parameters not included in table. Further details on PCMCI are available in Runge (2018) and Runge et al. (2019b). Source: Uereyen et al. (2022a).

Parameter	Description	Used value
Data frame	Includes time series variables and temporal information. If data mask is used, it is appended to the data frame.	Targets and drivers
Data mask	Mask defining time steps to include and exclude (0: False, 1: True).	Seasons
Mask type	Definition of which variables and time steps to mask. E.g. type “y” masks target variable as defined in mask, but allows drivers depending on temporal lags to be outside of mask.	“y”
Lags	Temporal lags to test (minimum, maximum).	min:0, max:3
Independence test	Conditional independence test including linear (e.g. partial correlation) and nonlinear dependencies.	“ParCorr”
α_{pc}	Significance threshold in condition selection step (PC), comparable to hyperparameter optimization in model selection process. If “None” is used, optimal value is selected via Akaike information criterion score.	“None”
α	Threshold to extract significant links detected for each target variable in MCI test.	0.05
Selected links	Definition of potential causal links to be tested. A detailed specification of i.e. a target variable, potential parents, and maximum lags is possible. We only consider parents for the three target variables.	$X_{t-\tau}^i \rightarrow X_t^j$
False discovery rate	Parameter to account for inflated p -value due to multiple testing in MCI step.	“fdr_bh”

the influence (Runge, 2020). Therefore, detected contemporaneous links with PCMCI, usually cannot be associated with a direction. Here, only drivers for the target variables NDVI, SCA, and surface water area (SWA) were computed, which is why the direction of influence could also be assessed for contemporaneous links. Moreover, PCMCI enables the usage of a temporal mask option, which can be implemented for the target variables to build the causal networks for a limited temporal scale, i.e. meteorological seasons (see Figure 5.8). In this context, the target variable NDVI was limited to the growing season by removing all time steps with both an NDVI value less than 0.2 and temperature less than 0°C as suggested by Wu et al. (2015). Likewise, for SCA and SWA, all time steps with a value less than 0.5 % fractional cover were removed. This mask option only restricts the target variables NDVI, SCA, and SWA. The potential drivers also include values for the masked time steps in the past of the targets to account for the temporal lags (see Figure 5.8). Finally, PCMCI incorporates the correction of retrieved p -values from the MCI step, to account for false positive discoveries arising through multiple testing (Runge, 2018).

Figure 5.9 shows correlation as well as causal maps to demonstrate the difference between a correlation analysis and the PCMCI approach. Also, this figure emphasizes the influence of the time series preprocessing, specifically the impact of the removal of the linear trend and seasonal cycle on the correlation coefficient. In regards of the strong seasonal characteristics of the investigated time series variables (see Figure 5.1), the correlation coefficient is inflated when using the original time series, as illustrated in Figure 5.9a,b. The reduction of the influence of the trend and seasonality weakens the correlation coefficient values as well as the number of significant correlation coefficients (see Figure 5.9c,d). In comparison, Figure 5.9e,f shows the results of the causal discovery algorithm PCMCI, applied with a temporal lag of 1 month for the driving variables (precipitation in Figure 5.9e; temperature in Figure 5.9f). In addition, temperature and precipitation were used as conditions for the links $P_{\tau=-1} \rightarrow NDVI_{\tau=0}$ and $T_{\tau=-1} \rightarrow NDVI_{\tau=0}$, respectively. For example, for the causal link $P_{\tau=-1} \rightarrow NDVI_{\tau=0}$, the detected link strength remains distinct for the arid and semi-arid zones of the study area. Yet, with the inclusion of temperature as a condition, many grids with a significant correlation in the Ganges river basin disappear (see Fig-

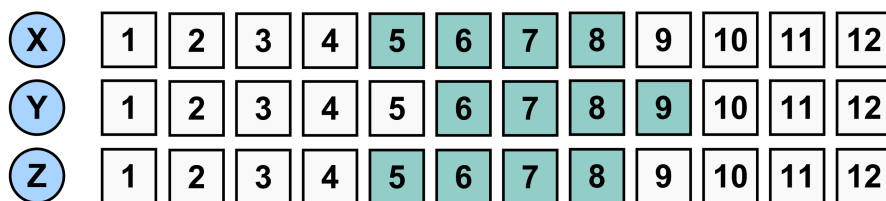


Figure 5.8: Application of a temporal mask with the setting to limit the target variable ('Y') to the monsoon season (JJAS). The driving variable ('X') and conditions ('Z') with a temporal lag of 1 month, are allowed to be outside the temporal mask.

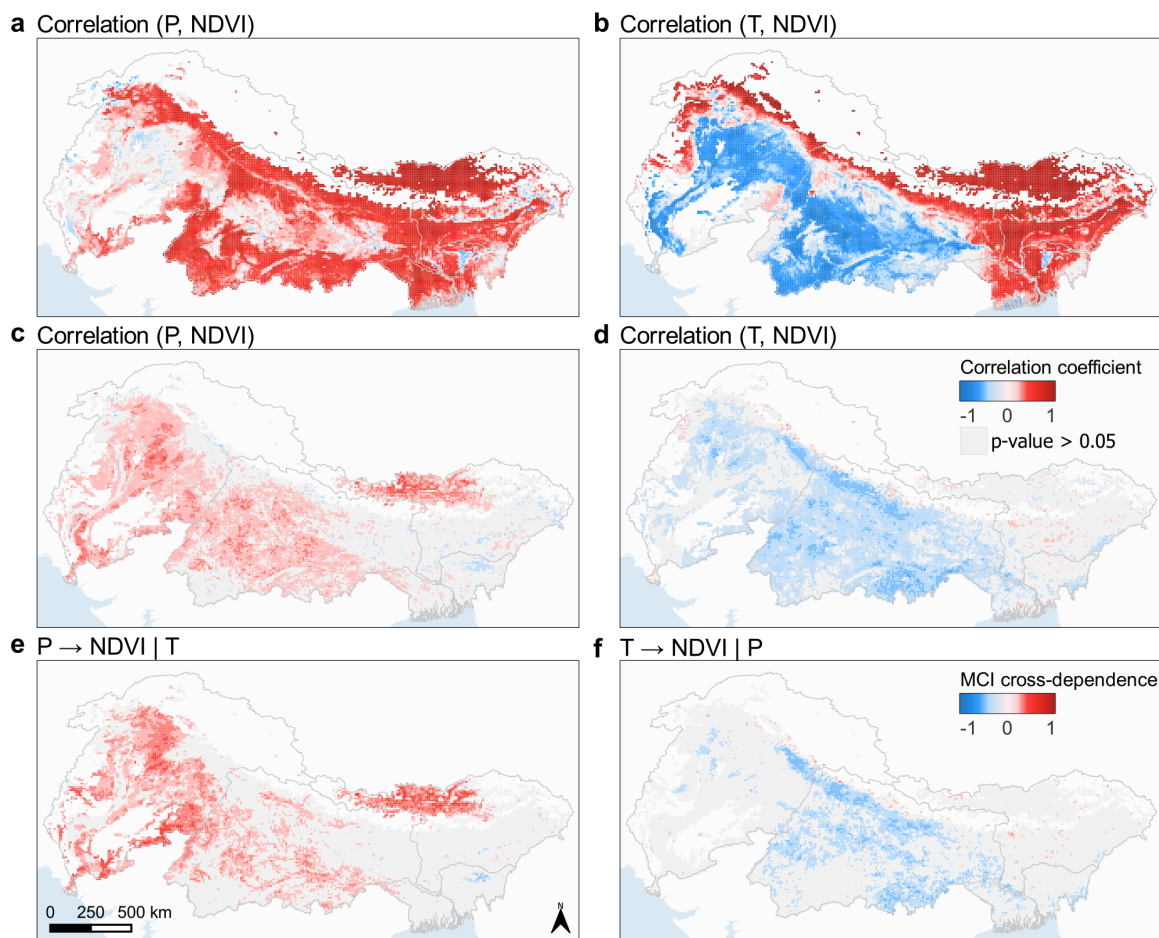


Figure 5.9: Influence of detrending and anomaly calculation on the correlation coefficient. (a) Correlation between original precipitation (P) and NDVI time series as well as (b) temperature (T) and NDVI. (c, d) Same as (a, b) but detrended anomaly time series were correlated. (e) Map derived with PCMCI, showing the strength of the MCI value for the temporally lagged precipitation and NDVI ($P_{\tau=-1} \rightarrow NDVI_{\tau=0}$), where 'l' denotes the conditioned out variable temperature. (f) MCI value for $T_{\tau=-1} \rightarrow NDVI_{\tau=0}$, with precipitation being conditioned out.

ure 5.9e). Likewise, for the causal link $T_{\tau=-1} \rightarrow NDVI_{\tau=0}$, the negative coupling between temperature and the NDVI remains pronounced in the Ganges river basin, but detected significant correlations in the Indus river basin (see Figure 5.9d) were largely mediated through the consideration of precipitation as condition (see Figure 5.9f).

5.3 Results

The following chapters present the results of the implemented time series analysis techniques of the presented methodological framework. First, the results of the trend analysis for the three land surface variables NDVI, surface water area (SWA), and snow cover area (SCA) are presented for the Indus-Ganges-Brahmaputra-Meghna (IGBM) river basins. Subsequently, the seasonal characteristics and changes of phenological metrics at decadal

scale are shown. Finally, the results obtained with the causal discovery algorithm PCMCI, outlining the influencing factors on the three land surface variables, are presented.

5.3.1 Trend Analyses

Figure 5.10 shows that the magnitude of statistically significant trends vary depending on the respective prewhitening algorithm. To reduce the influence of serial correlation, the time series were prewhitened with the TFPW-Y as well as the TFPW-WS in combination with the VCPW approach. In fact, the investigation of the lag-1 autocorrelation showed that 100.0%, 99.8%, and 99.8% of all grids were significantly serially correlated for the NDVI, surface water area, and snow cover area, respectively. The application of the VCPW approach resulted in the lowest absolute slope values (see Figure 5.10). More specifically, the average absolute slope value for the NDVI, surface water area, and snow cover area amounts to 0.034, 0.034, and 0.014; 1.885, 1.690, and 0.873; as well as 2.815, 2.615, and 1.658 computed using no prewhitening, TFPW-Y, and VCPW, respectively.

Figure 5.11, Figure 5.12, and Figure 5.13 visualize the spatial distribution of the derived significant trends, their direction, and magnitude. It is visible that the design of the

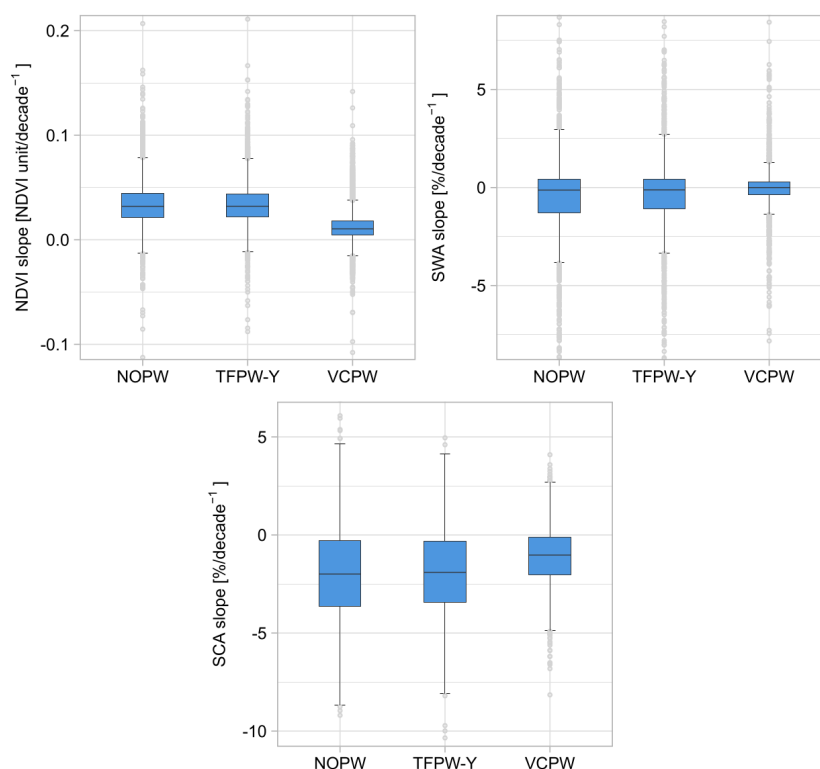


Figure 5.10: Magnitude of significant trends in consideration of the applied prewhitening method prior to the trend test, specifically no prewhitening (NOPW), trend-free prewhitening after Yue et al. (TFPW-Y), and variance corrected prewhitening (VCPW). Modified after Uereyen et al. (2022a).

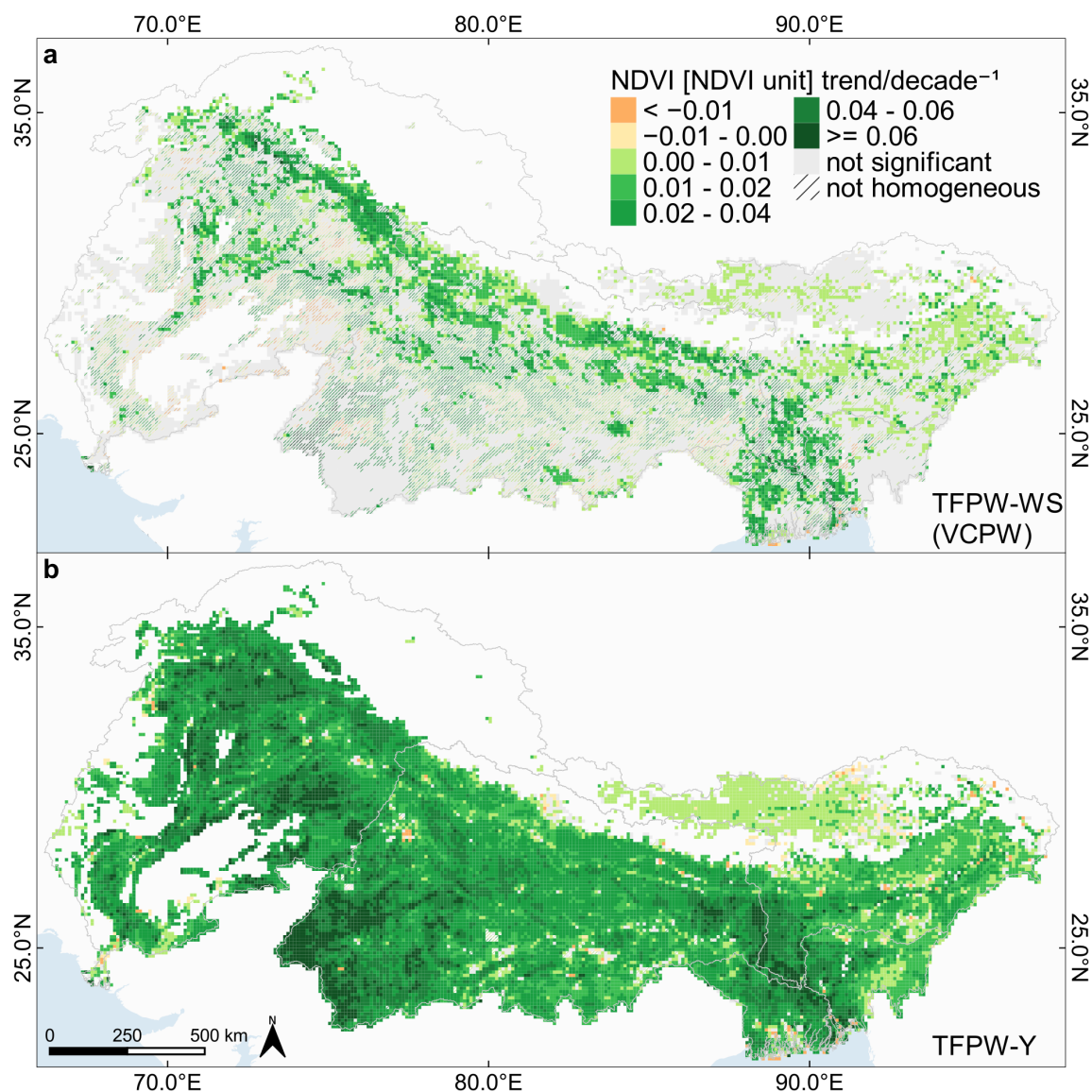


Figure 5.11: Magnitude of significant trends (p -value < 0.05) by means of the seasonal Mann-Kendall test for the normalized difference vegetation index (NDVI) at annual temporal scale, whereas the magnitude is denoted at decadal scale. (a) Map showing trends computed with trend-free prewhitening after Wang and Swail (TFPW-WS) in combination with variance corrected prewhitening (VCPW) for the magnitude and (b) with trend-free prewhitening after Yue et al. (TFPW-Y). Only trends being significant and homogeneous over the seasons are colored. Not homogeneous trends at annual scale are represented by diagonal lines with the same color scale. Modified after Ureyen et al. (2022a).

trend test's, in particular the previously applied prewhitening algorithms (see Figure 5.5), influence the resulting amount of statistically significant trends. In general, statistically significant NDVI trends at annual temporal scale are illustrated in Figure 5.11, showing mostly increasing trends in vegetation greenness for the entire IGBM river basins. The increasing trends were most distinct in the southwest of the Ganges river basin. In comparison, in high altitudes and the Himalayan belt in the east, the positive trends found to be comparatively

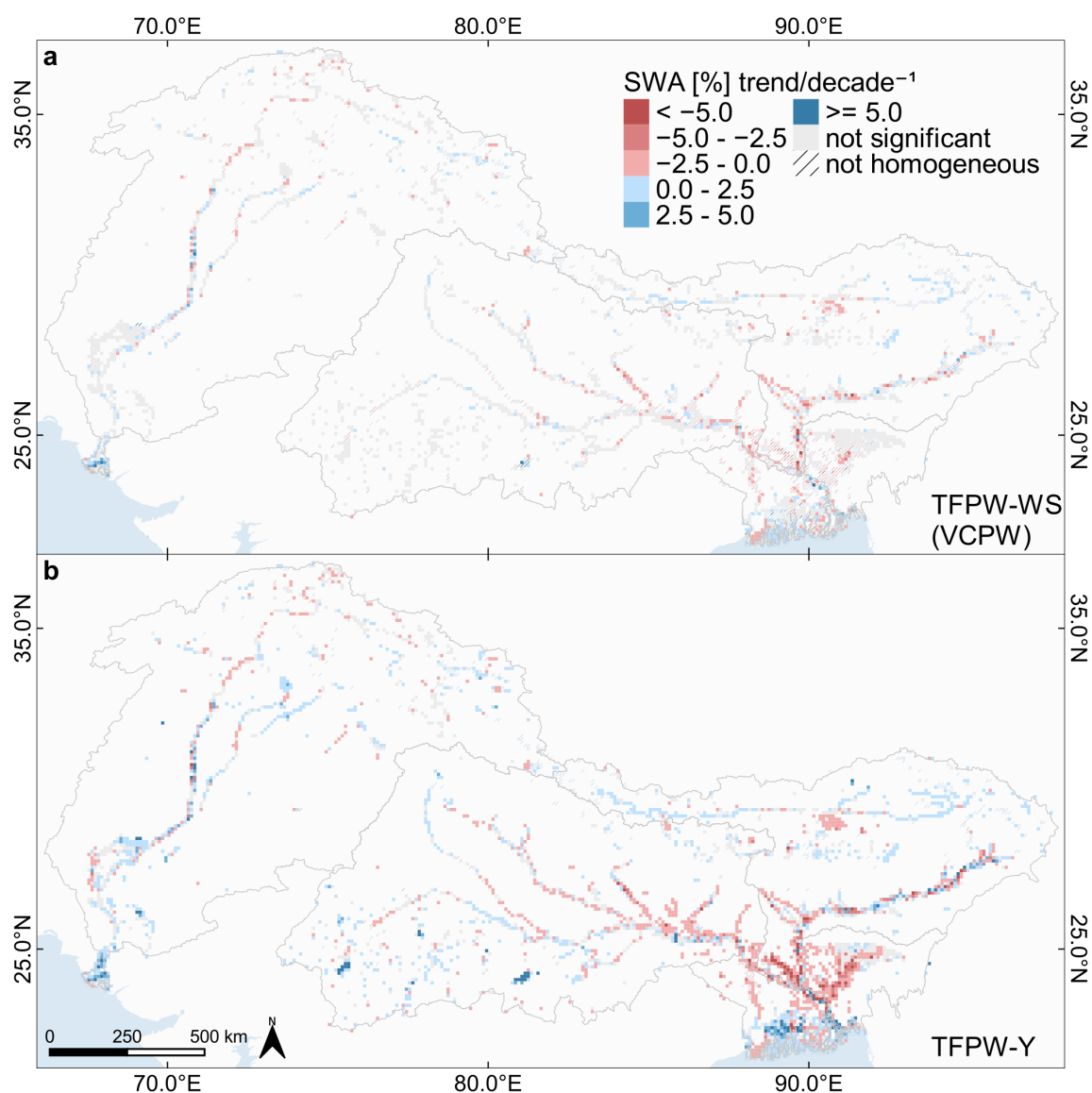


Figure 5.12: Magnitude of significant trends (p -value < 0.05) by means of the seasonal Mann-Kendall test for surface water area (SWA) using DLR Global WaterPack at annual temporal scale, whereas the magnitude is denoted at decadal scale. (a) Map showing trends computed with TFPW-WS in combination with VCPW for the magnitude and (b) with TFPW-Y. Only trends being significant and homogeneous over the seasons are colored. Not homogeneous trends at annual scale are represented by diagonal lines with the same color scale. Modified after Ureyen et al. (2022a).

weaker. However, a large percentage of trends derived based on the TFPW-WS approach were not homogeneous at annual temporal scale (see Figure 5.11a). Considering trends in surface water area in Figure 5.12b, the results indicated rather heterogeneous spatial patterns of significant increasing and decreasing trends. Here, negative trends were dominant at the confluences of the Ganges, Brahmaputra, and Meghna north of the Bay of Bengal. Also, mixed spatial patterns of increasing and decreasing trends were detected along the Brahmaputra river in the downstream area. In the south of the Ganges river basin and north of the Sundarbans mangrove forest at the Bay of Bengal, significant positive trends were

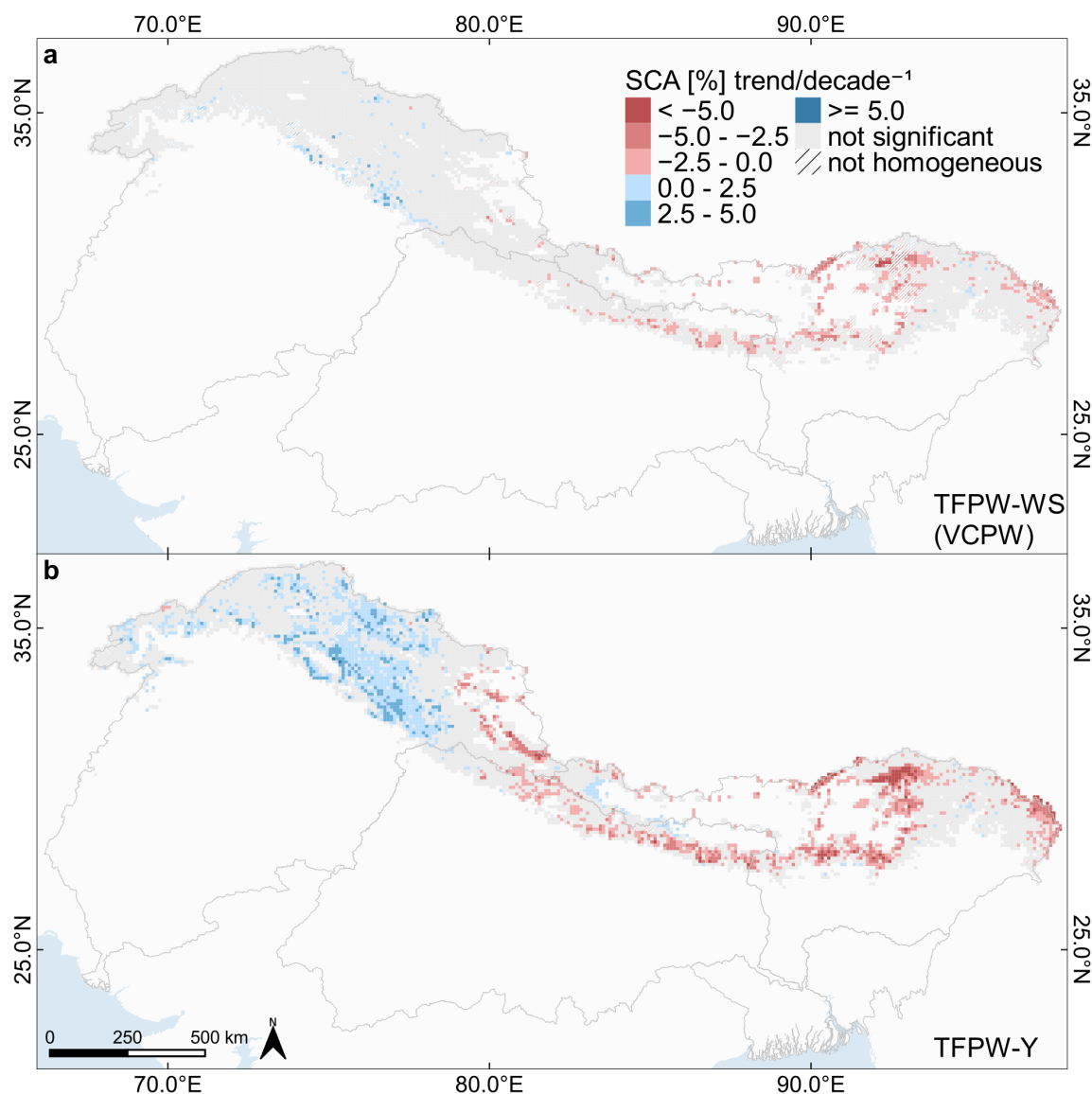


Figure 5.13: Magnitude of significant trends (p -value < 0.05) by means of the seasonal Mann-Kendall test for snow cover area (SCA) using DLR Global SnowPack at annual temporal scale, whereas the magnitude is denoted at decadal scale. (a) Map showing trends computed with TFPW-WS in combination with VCPW for the magnitude and (b) with TFPW-Y. Only trends being significant and homogeneous over the seasons are colored. Not homogeneous trends at annual scale are represented by diagonal lines with the same color scale. Modified after Uereyen et al. (2022a).

present (see Figure 5.12b). Furthermore, trends computed for snow cover area based on DLR Global SnowPack data, revealed a two-fold spatial pattern at annual temporal scale (see Figure 5.13). While identified significant trends for the upper Indus river basin were mostly positive, significant trends in the upper Ganges and Brahmaputra river basins were found to be largely negative.

Table 5.2 summarizes the percentages of significant positive and negative trends at seasonal and aggregated annual scale for the three land surface variables. As can be seen in

Table 5.2: Comparison of the amount of significant trends and their direction (+, positive; –, negative) based on the application of different prewhitening algorithms prior to the seasonal Mann-Kendall test. Results are listed as percentages for the normalized difference vegetation index (NDVI), surface water area (SWA), as well as snow cover area (SCA) and include each season and trends at annual scale (NH: not homogeneous, NS: not significant). Modified after Uereyen et al. (2022a).

Variable (Σ grids)	Setting	DJF		MAM		JJAS		ON		Annual			
		+	–	+	–	+	–	+	–	+	–	NH	NS
NDVI (19,333)	NOPW	81.1	1.1	73.5	0.9	79.8	1.4	81.7	0.8	91.0	0.9	1.1	7.0
	TFPW-Y	92.2	1.5	86.9	1.4	90.8	1.1	84.7	1.1	94.3	1.5	0.7	3.5
	TFPW-WS	52.6	3.9	26.1	23.6	47.3	2.0	20.0	19.5	23.3	0.1	48.8	27.8
SWA (3,395)	NOPW	28.5	19.4	29.1	15.9	22.0	27.1	26.5	23.3	32.6	27.0	11.2	29.2
	TFPW-Y	29.7	21.8	32.7	25.3	28.0	29.0	31.3	22.1	38.6	32.7	9.5	19.2
	TFPW-WS	17.1	15.6	17.8	11.5	12.5	21.9	20.9	17.0	12.0	9.6	28.7	49.7
SCA (6,394)	NOPW	0.6	5.5	14.2	4.5	11.3	6.2	1.5	7.0	15.8	13.1	0.6	70.5
	TFPW-Y	0.6	3.0	18.6	4.3	5.6	11.0	3.0	8.8	18.3	16.7	0.7	64.3
	TFPW-WS	0.5	4.8	10.6	4.5	3.7	5.9	1.5	6.2	1.9	7.1	7.1	83.9

Figures 5.11–5.13, trends derived from time series prewhitened with the VCPW approach were found to yield more frequently heterogeneous trends at annual scale. On the other hand, time series prewhitened with the TFPW-Y method resulted in more significant and homogeneous trends at annual scale compared to TFPW-WS and VCPW, respectively. In comparison, time series, where no prewhitening (NOPW) was applied the results showed similar shares of significant increasing and decreasing trends as TFPW-Y, with TFPW-Y yielding slightly higher shares.

5.3.2 Change in Phenological Metrics

Considering the quantification of phenological measures in the implemented framework, a global parameter setting was used for all land surface variables. For NDVI, an additional setting was included to enable the assessment of two annual growing seasons as well. In this regard, the analysis showed that 52.3 % and 47.7 % of the vegetation areas in the IGBM river basins were characterized by one and two annual growing seasons, respectively. Here, areas having two annual growing seasons largely occurred in the Indo-Gangetic Plains (see Figure 5.14c). The quantified timing and changes of the seasonal peak values for the NDVI are visualized in Figure 5.14a–d. During the first decade, between 2000–2009, vegetation covered areas with one annual growing season had reached their seasonal peak largely between September and October. On the contrary, for areas with two annual growing seasons, the first seasonal peak was mostly reached in February and March (see Figure 5.14c) and the second peak in September and October (see Figure 5.14a). Vegetation in high altitudes had their seasonal peak mostly in August. Figure 5.14b illustrates the difference for areas during the first season. Backward shifts in the timing of the seasonal peak are prevalent in the Lower Indus river basin. In total, 12.0 % and 12.7 % of the grids indicated a forward and

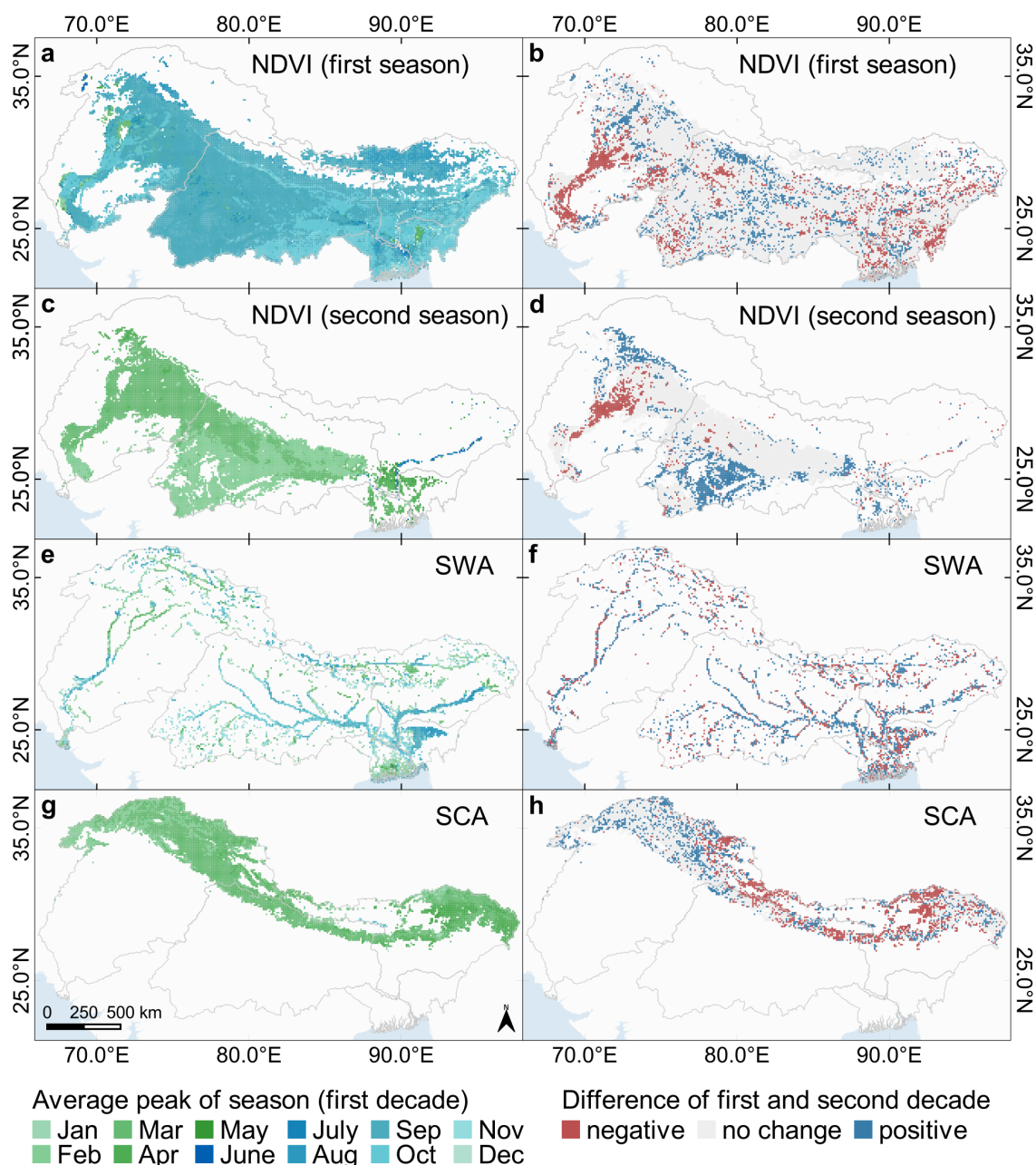


Figure 5.14: Average timing of the seasonal peak value retrieved with Timesat. (a, c, e, g) Average seasonal peak value between 2000 (DLR Global WaterPack: 2003) and 2009. (b, d, f, h) Difference between the average peak value of the first (2000–2009) and second (2010–2019) decade. The NDVI is partially characterized by two annual growing seasons (a, b: values of the first growing season together with areas characterized by one annual growing season; c, d: values of the second growing season). Considering the right panel, “no change” indicates a difference in the average seasonal peak values of the two decades ranging between -0.25 and 0.25 . A “positive” change indicates a forward shift in time of the seasonal peak in the second study period compared to the first and vice versa. Modified after Ureyen et al. (2022a).

backward shift during the first growing season, respectively. In comparison, Figure 5.14d shows that a forward and backward shift in the timing of the seasonal peak values during the second season largely occurred in the southern Ganges river basin and the Lower Indus

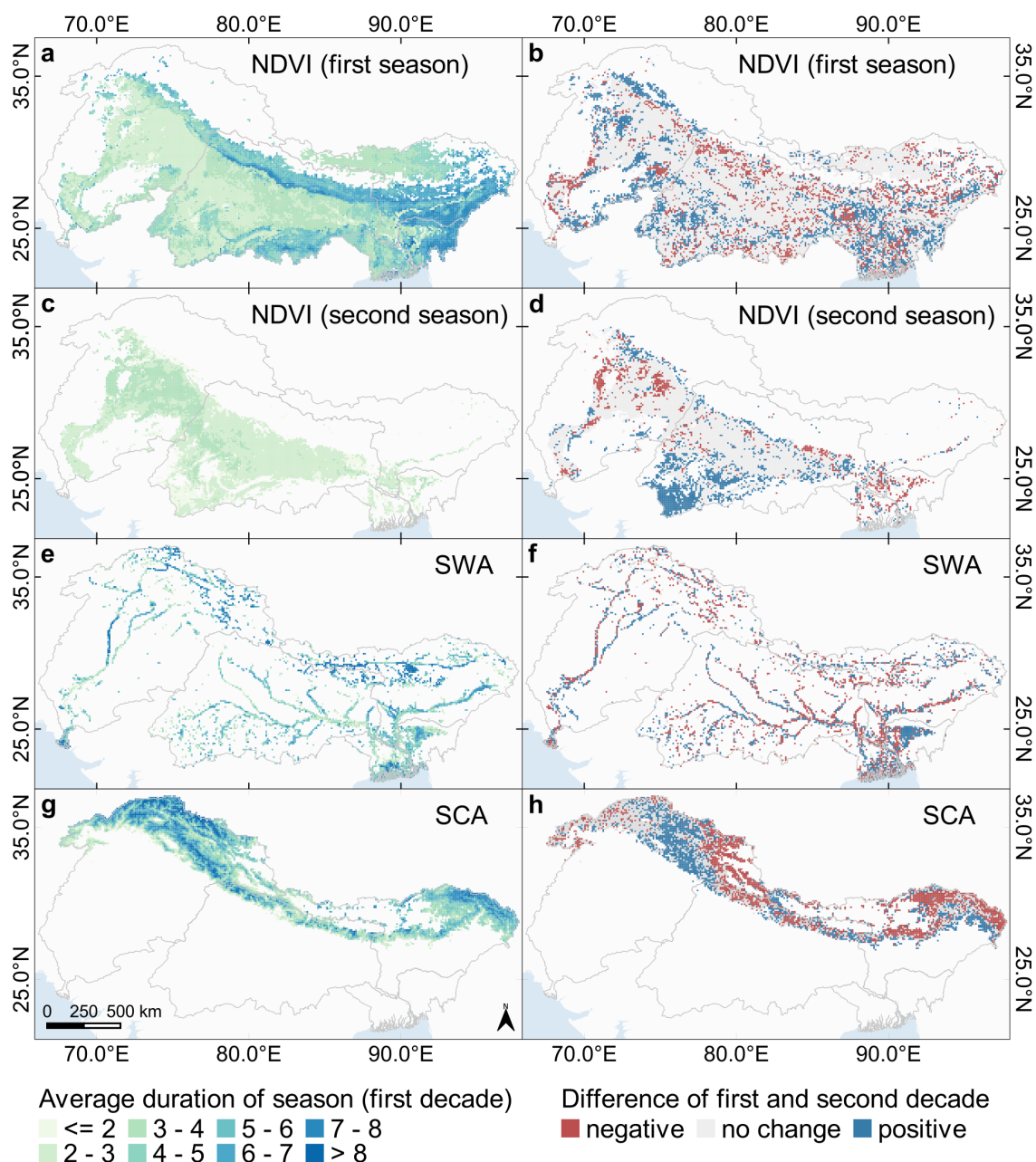


Figure 5.15: Average duration of the season retrieved with Timesat. (a, c, e, g) Average duration of the season between 2000 (DLR Global WaterPack: 2003) and 2009. (b, d, f, h) Difference between the average duration of the first (2000–2009) and second (2010–2019) decade. The NDVI is partially characterized by two annual growing seasons (Details in caption of Figure 5.14). Considering the right panel, “no change” indicates a difference in average seasonal duration of the two decades ranging between -0.25 and 0.25 . A “positive” difference indicates an increase in the seasonal duration in the second study period compared to the first and vice versa. Modified after Uereyen et al. (2022a).

river basin, respectively. In detail, during the second annual growing season, a forward and backward shift in the timing of the seasonal peak value could be identified for 19.8 % and 7.9 % of the grids, respectively. Considering the seasonal duration during the first decade, it

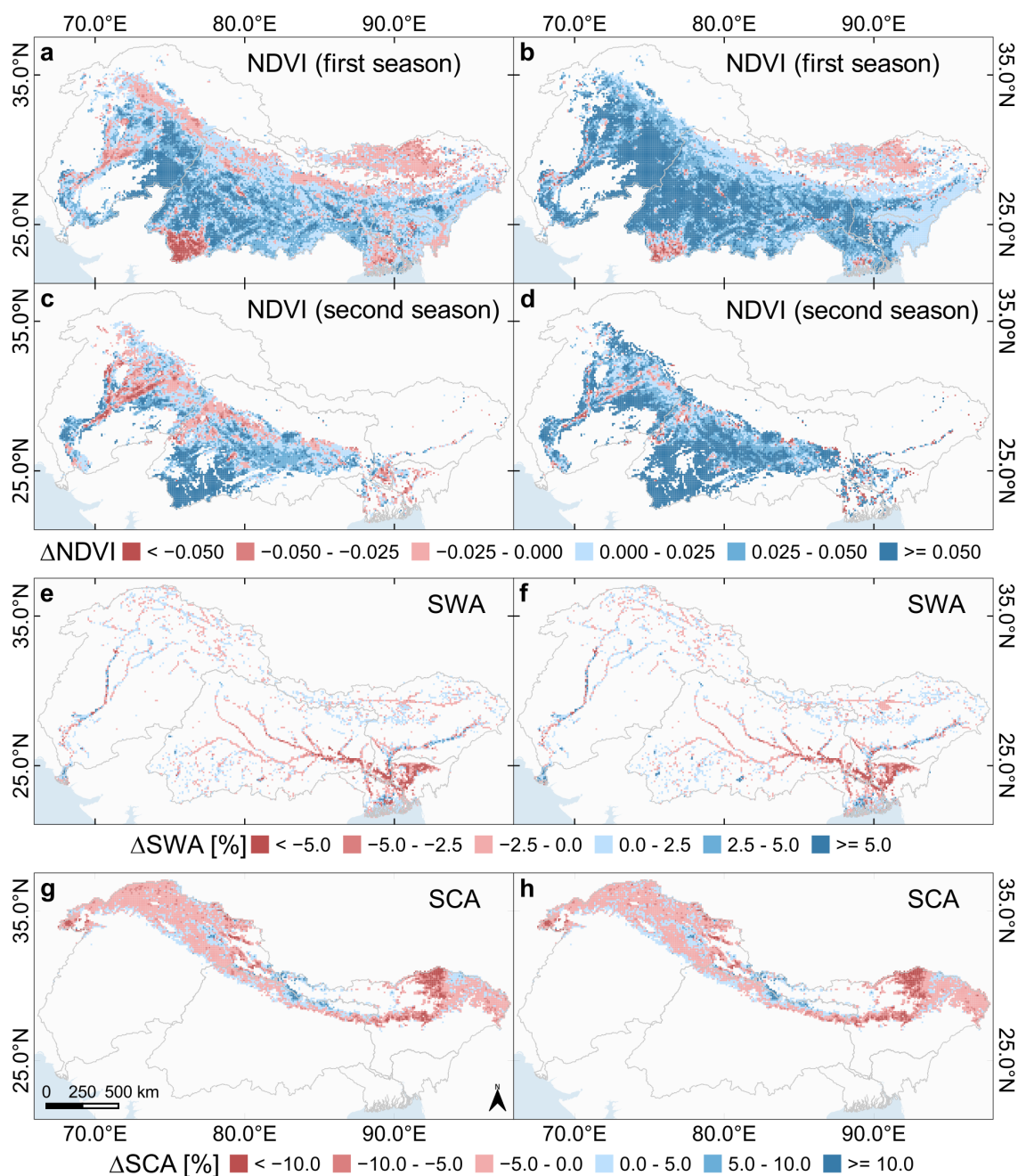


Figure 5.16: Difference of average seasonal amplitude (a, c, e, g) and average seasonal peak value (b, d, f, h) between the first (2000–2009) and second (2010–2019) decade. The NDVI is partially characterized by two annual growing seasons (Details in caption of Figure 5.14). A “positive” difference indicates an increase in the phenological metric in the second study period compared to the first and vice versa. Modified after Ureyen et al. (2022a).

generally ranges between five to eight months and to four months for areas at high altitudes and areas having two annual growing seasons, respectively (see Figure 5.15a,c). The obtained results for the first season showed a mixed pattern of positive and negative changes (see Figure 5.15b). On the other side, the results for the second growing season indicated a positive change in the seasonal duration for the southwest of the Ganges river basin (see

Figure 5.15d). Moreover, negative changes in the seasonal amplitude were striking in the southwest of the Ganges river basin, in the downstream area of the Indus river basin, and at higher elevation during the first season (see Figure 5.16a,c). Yet, these negative change were mostly not present in changes of the seasonal peak value (see Figure 5.16b,d).

In regards of surface water area, the results indicated that the timing of the seasonal peak mostly occurred between February and April in the northern and parts of the Central Indus river basin (see Figure 5.14e). In comparison, in the Ganges, Brahmaputra, and Meghna river basins the seasonal peak was largely reached between the months August and October (see Figure 5.14e). In terms of changes between the two decades, the spatial patterns of positive and negative changes appeared to be heterogeneous (see Figure 5.14f), with positive shifts (43.2 %) outweighing the negatives (26.0 %). Furthermore, the seasonal duration was longest at high elevation areas as well as along the Indus river in downstream areas and amounts to more than seven months (see Figure 5.15e). However, the seasonal duration was found to be between three and seven months for most of the grids. The differences in the seasonal duration between the two investigated decades appeared to be quite heterogeneous in terms of their spatial distribution. For example, positive changes in the seasonal duration were found in the wetlands south of the Shillong plateau in the Meghna river basin and negative changes were striking in proximity of the confluences of the Ganges and Brahmaputra rivers (see Figure 5.15f). The results for the changes in the phenological metrics amplitude and seasonal peak value showed consistent spatial patterns (see Figure 5.16e,f). For example, at study area scale, the share of grids with positive changes for the parameter amplitude was 46.9 % and for the seasonal peak value 50.4 %.

Furthermore, the results indicated that 83.3 % of the grids had their maximum snow cover extent in February and March and 14.5 % in April (see Figure 5.14g). Grids having their seasonal peak in April were mostly located in the upper Brahmaputra river basin. In comparison, grids with a maximum snow cover extent in February were mostly located in the upper Indus river basin. Considering changes in the timing of the seasonal peak, Figure 5.14h demonstrates that negative changes were dominant in the eastern regions and positives in the western regions of the upper Indus, Ganges, and Brahmaputra river basins. Likewise, the results for the changes in the seasonal duration indicated similar spatial patterns. With more detail, negative changes in the seasonal duration were prevalent in the upper Ganges and Brahmaputra river basins and positive changes in the upper Indus river basin (see Figure 5.15h). Overall, the negative changes (33 %) in the seasonal duration outweighed the positives (29.4 %). Figure 5.16g,h illustrates that differences in the seasonal amplitude and peak value of snow cover area showed comparable spatial patterns for the upstream areas of the river basins.

5.3.3 Relationships between Land Surface Dynamics and Environmental Controls

Apart from the quantification of trends and changes in seasonal characteristics, the implemented framework involves the estimation of driving variables for the NDVI, surface water area, and snow cover area using the causal discovery algorithm PCMCI. It has to be

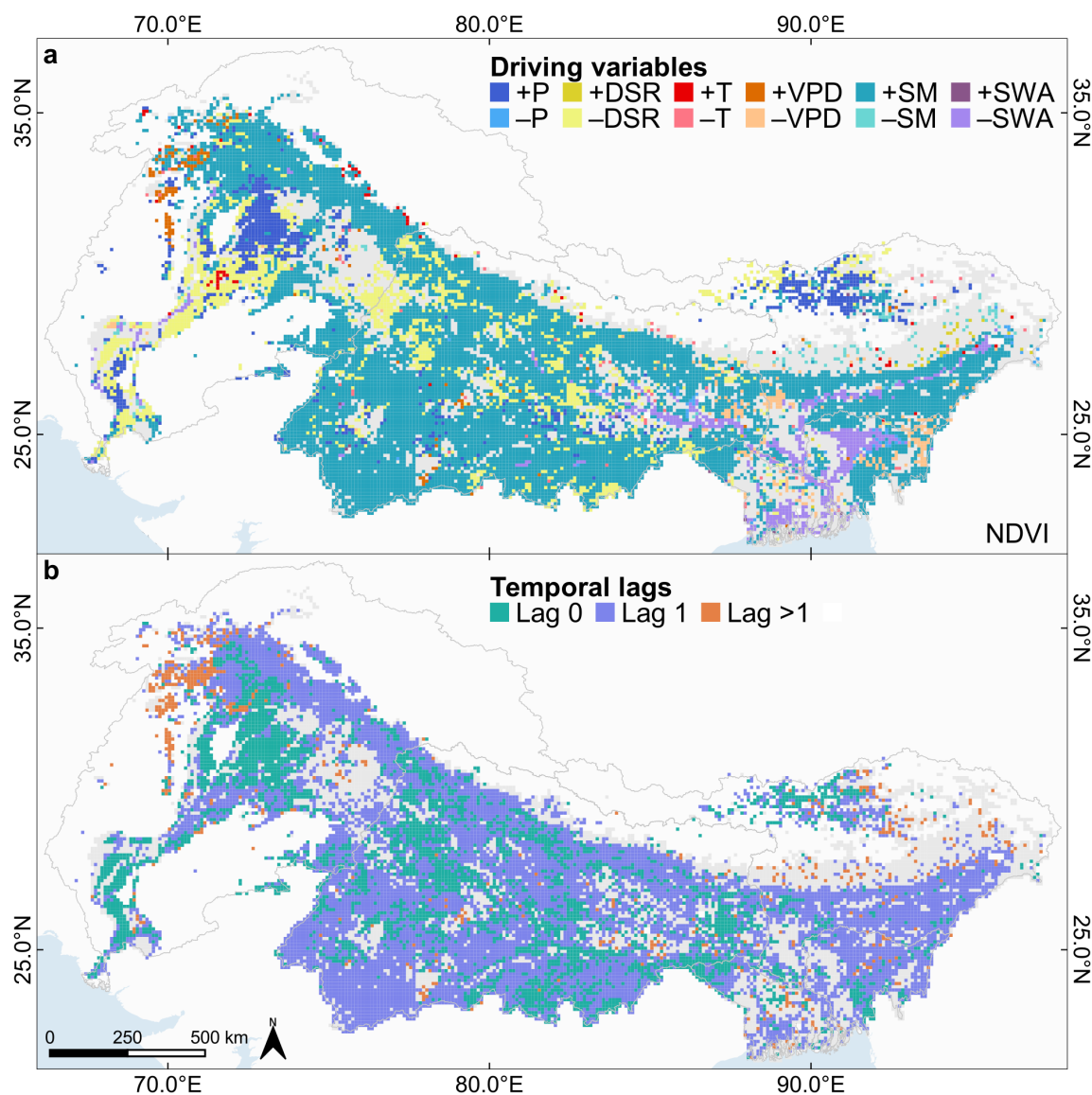


Figure 5.17: (a) The spatial distribution of the dominant driving variables for the normalized difference vegetation index (NDVI) and (b) their respective temporal lags at monthly scale. The driving variables include precipitation (P), soil moisture (SM), temperature (T), downward shortwave radiation (DSR), vapor pressure deficit (VPD), and surface water area (SWA). The prefixes ‘+’ and ‘-’ of the driving variables denote a positive and negative MCI cross-dependence, respectively. In this thesis, the MCI measure is based on the partial correlation coefficient. Gray colored grids indicate that no causal link exists between the NDVI and the driving variables. Modified after Ureyen et al. (2022a).

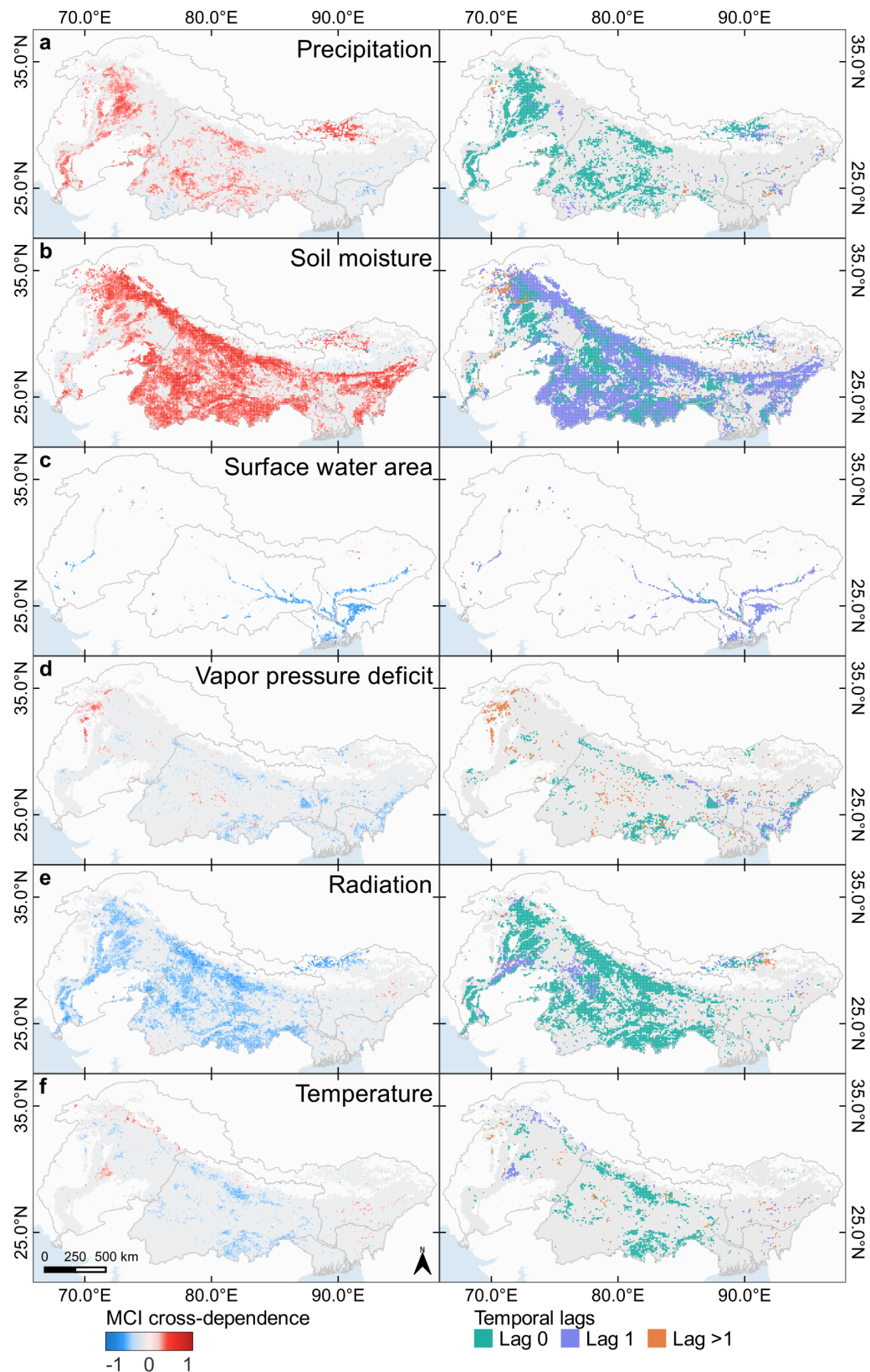


Figure 5.18: Influence of respective drivers on normalized difference vegetation index (NDVI) after conditioning out all other driving variables. The maximum MCI value is extracted considering all temporal lags, which are visualized on the right panel. Temporal lags are denoted at monthly scale. Modified after Uereyen et al. (2022a).

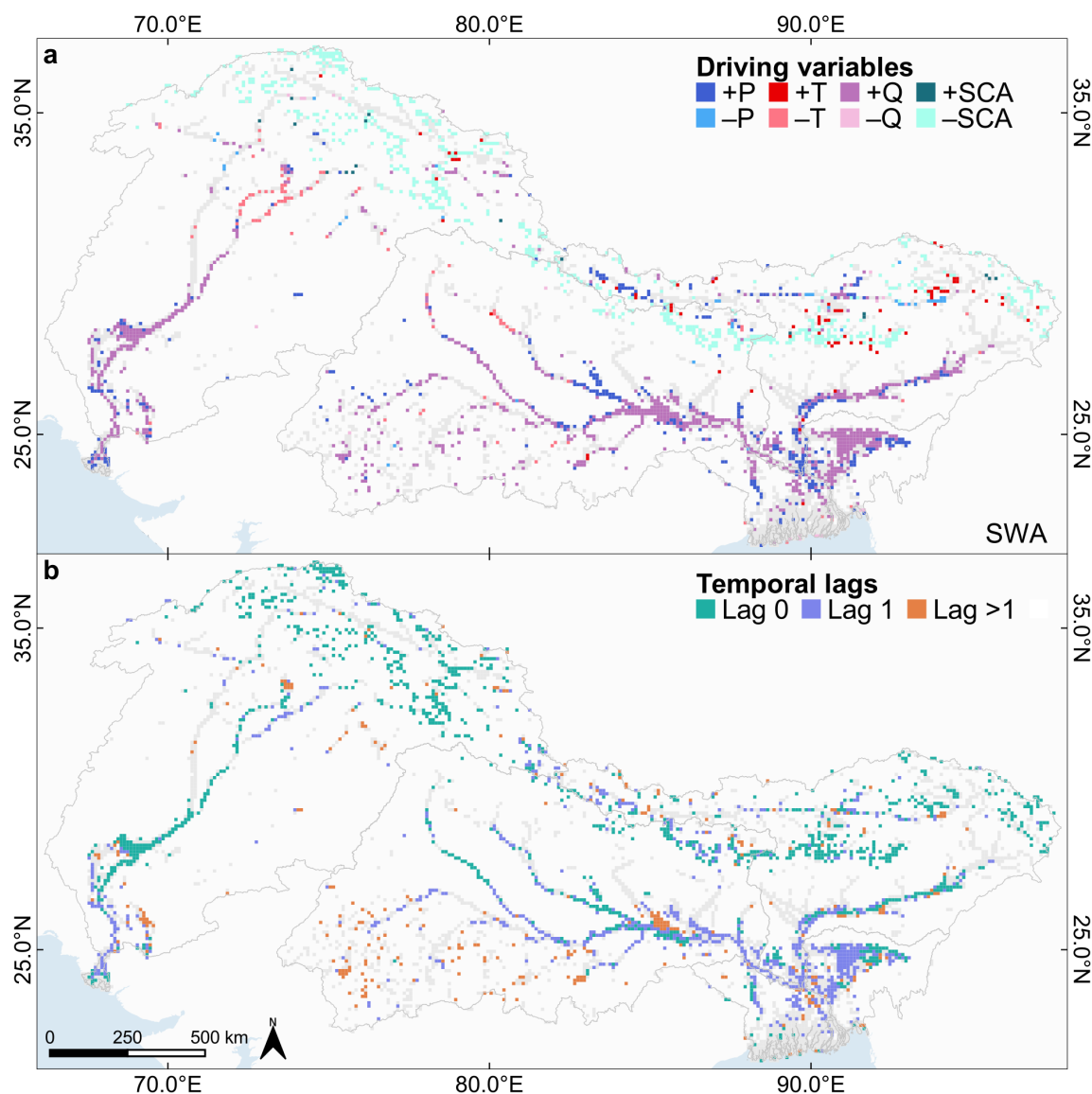


Figure 5.19: (a) The spatial distribution of the dominant driving variables for surface water area (SWA) and (b) their respective temporal lags at monthly scale. The driving variables for SWA include precipitation (P), temperature (T), discharge (Q), and snow cover area (SCA). The prefixes ‘+’ and ‘-’ of the driving variables denote a positive and negative MCI cross-dependence, respectively. In this thesis, the MCI measure is based on the partial correlation coefficient. Gray colored grids indicate that no causal link exists between SWA and the driving variables. Modified after Uereyen et al. (2022a).

noted that the investigated three target variables might be impacted by human influences as well. However, at this point these were not considered. The following figures visualize the obtained results by means of the maximum MCI cross-dependence value per grid, which is reached by one of the respective driving variable at a temporal lag between 0 and 3 months.

Figure 5.17 shows the spatial distribution of the relationships between NDVI and the respective driving variables. According to the defined feature space and parameter settings, NDVI was most frequently positively coupled with soil moisture (49.6 %) (Figure 5.17a).

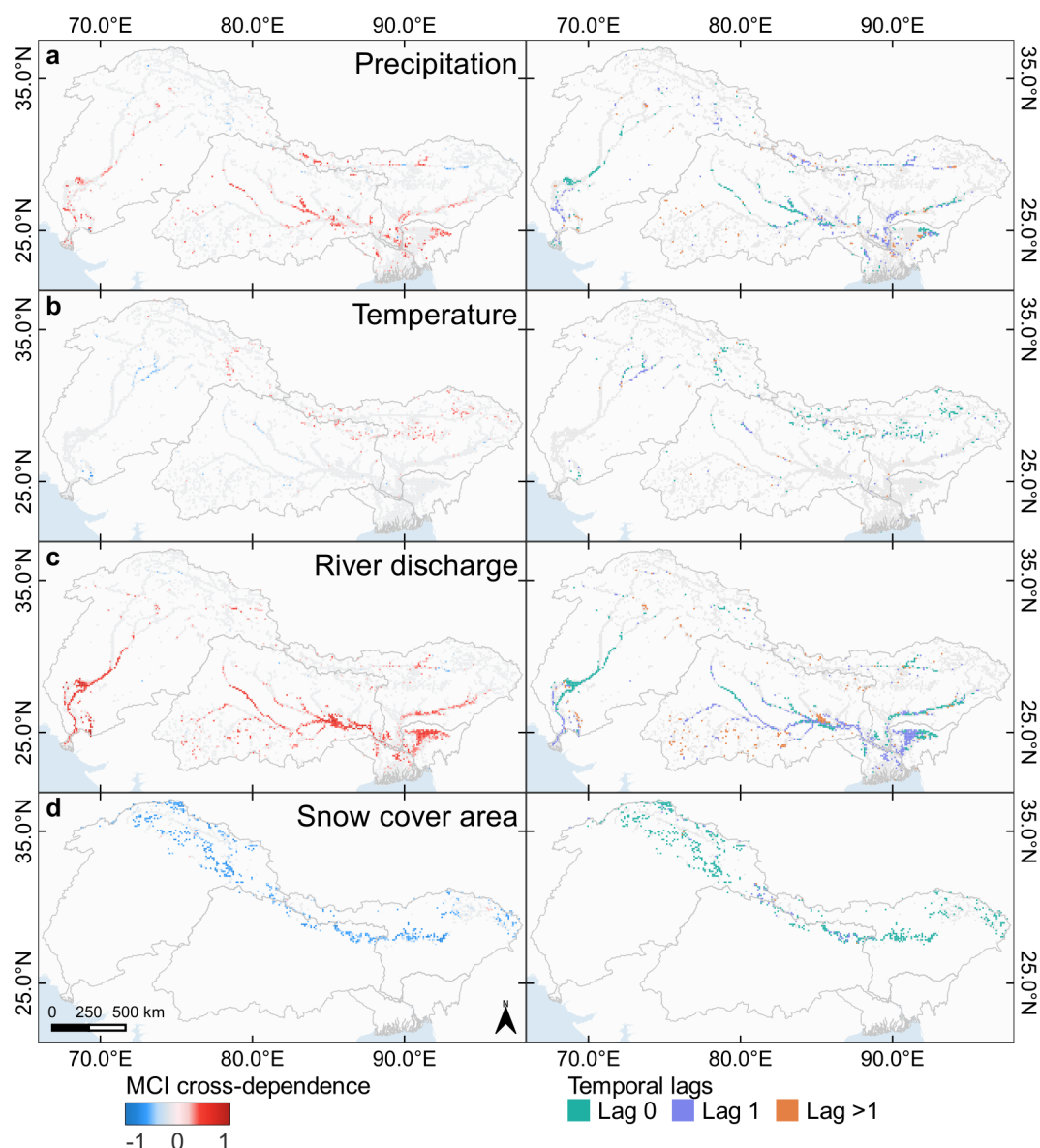


Figure 5.20: Influence of respective drivers on surface water area (SWA) after conditioning out all other driving variables. The maximum MCI value is extracted considering all temporal lags, which are visualized on the right panel. Temporal lags are denoted at monthly scale. Modified after Ureyen et al. (2022a).

The coupling between NDVI and soil moisture was largely associated with a temporal lag of 1 month (see Figure 5.17b and 5.18b). Moreover, it is striking that in arid and semi-arid regions in the west of the IGBM river basins, the NDVI was largely positively coupled with precipitation at a temporal lag of 0 and 1 month (see Figure 5.17a and 5.18a). In total, precipitation had the highest effect size on NDVI for 6.0 % of the grids. Downward shortwave radiation had the highest effect size on NDVI regionally, e.g., mostly in the Ganges river basin, where the percentage amounts to 10.8 % of the grids and this link was mostly contemporaneous (see Figure 5.17a and 5.18e). Moreover, when NDVI was positively coupled to precipitation, it showed a negative response to radiation (see Figure 5.18a,e). Also, for

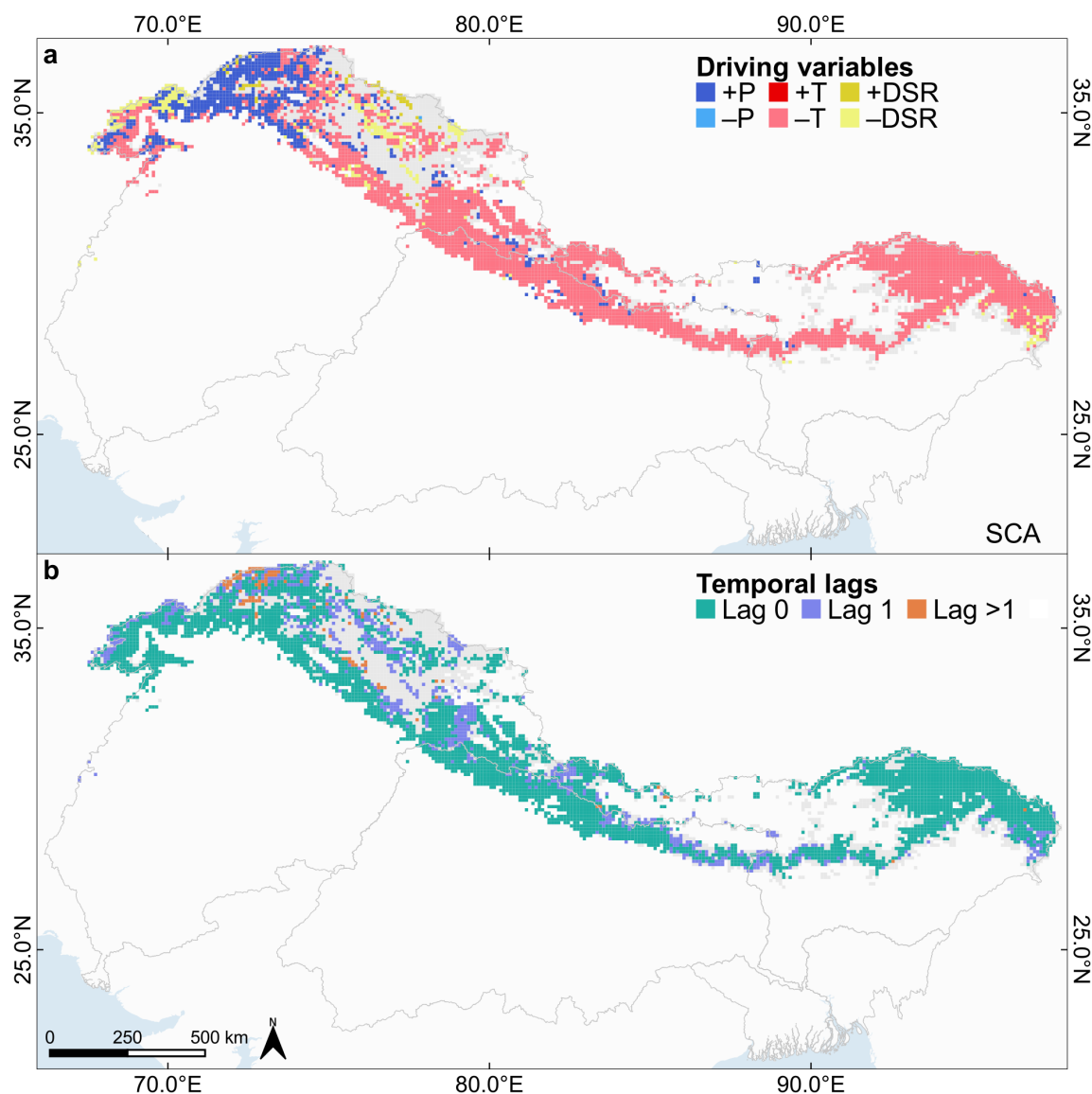


Figure 5.21: (a) The spatial distribution of the dominant driving variables for snow cover area (SCA) and (b) their respective temporal lags at monthly scale. The driving variables for SCA include precipitation (P), temperature (T), and downward shortwave radiation (DSR). The prefixes ‘+’ and ‘-’ of the driving variables denote a positive and negative MCI cross-dependence, respectively. In this thesis, the MCI measure is based on the partial correlation coefficient. Gray colored grids indicate that no causal link exists between SCA and the driving variables. Modified after Uereyen et al. (2022a).

a very small fraction of areas where NDVI is negatively driven by precipitation, a positive coupling was found with radiation. Vapor pressure deficit appeared to have a small effect on NDVI and was mostly negatively coupled to it at lag 0 (see Figure 5.18d). In proximity to the large river streams of the Ganges, Brahmaputra, and Meghna as well as their confluences north of the Bay of Bengal, PCMCI identified vegetation strongly responding negatively to surface water area at a temporal lag of 1 month (see Figure 5.17a and 5.18c). Vegetation cover in the upper Brahmaputra river basin, located on the Tibetan Plateau, showed a positive response to precipitation as well as soil moisture at lag 0 and 1 (see Figure 5.17a,b).

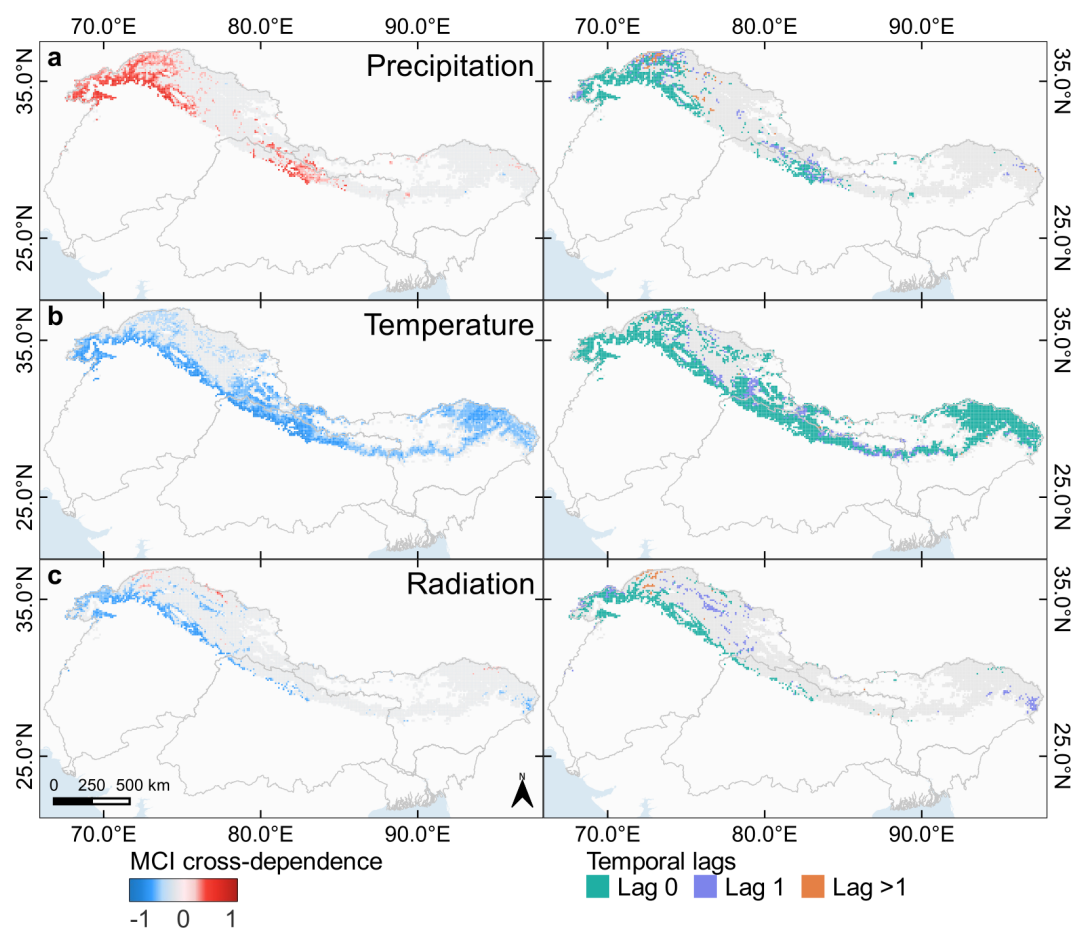


Figure 5.22: Influence of respective drivers on snow cover area (SCA) after conditioning out all other driving variables. The maximum MCI value is extracted considering all temporal lags, which are visualized on the right panel. Temporal lags are denoted at monthly scale. Modified after Uereyen et al. (2022a).

In total, the results indicated that 26.0 % of the grids had no significant link between the NDVI and the respective driving variables.

Considering surface water area, which is based on the DLR Global WaterPack, the evaluation of causal links showed that it responds negatively to snow cover area at lag 0 in high elevation areas (see Figure 5.19 and Figure 5.20d). At the same time, a positive contemporaneous coupling with temperature was identified at high altitudes (see Figure 5.19 and Figure 5.20b). On the other hand, in downstream areas with lower elevation, the coupling with temperature was negative. Yet, this only accounts for a small number of grids (2.2 %). Expectedly, surface water area was strongly positively linked with river discharge and precipitation, where river discharge appeared to have a larger influence (see Figure 5.19 and Figure 5.20a,c). With more detail, river discharge was found to positively influence surface water area for 20.0 % of the grids, and precipitation for 7.4 % of the grids. However, for 53.5 % of the total amount of grids no significant link was detected with any of the investigated driving variable.

Figure 5.21 visualizes the identified links between snow cover area and the respective climatic driving variables. A particular strong negative influence of temperature on snow cover area could be identified for large areas of the upper Indus, Ganges, and Brahmaputra river basins (see Figure 5.21 and Figure 5.22b). This link was mostly contemporaneous (46.1 %) and for 5.6 % of the grids at a lag of 1 month. Snow cover area was found to respond positively to precipitation, particularly in the western areas of the upper Indus river basin and central regions of the upper Ganges river basin (see Figure 5.21 and Figure 5.22a). This link was also dominant at lag 0. Likewise, for areas where precipitation had a positive influence, downward shortwave radiation was found to affect snow cover area negatively at lag 0 (see Figure 5.21 and Figure 5.22c). In case of snow cover area, significant links were not available for 27.1 % of the grids.

5.4 Transferability of Implemented Framework in Space and Time

This chapter briefly presents the automated implementation of the developed methodological framework for preparation and analysis of multivariate geoscientific time series on the high-performance computing (HPC) environment “calvalus” of the DFD at the DLR. Figure 5.23 provides a simplified overview of the implemented framework. In fact, the final version of the implemented framework includes all presented processing and time series analysis steps. If necessary, further statistical analysis techniques can be easily incorporated

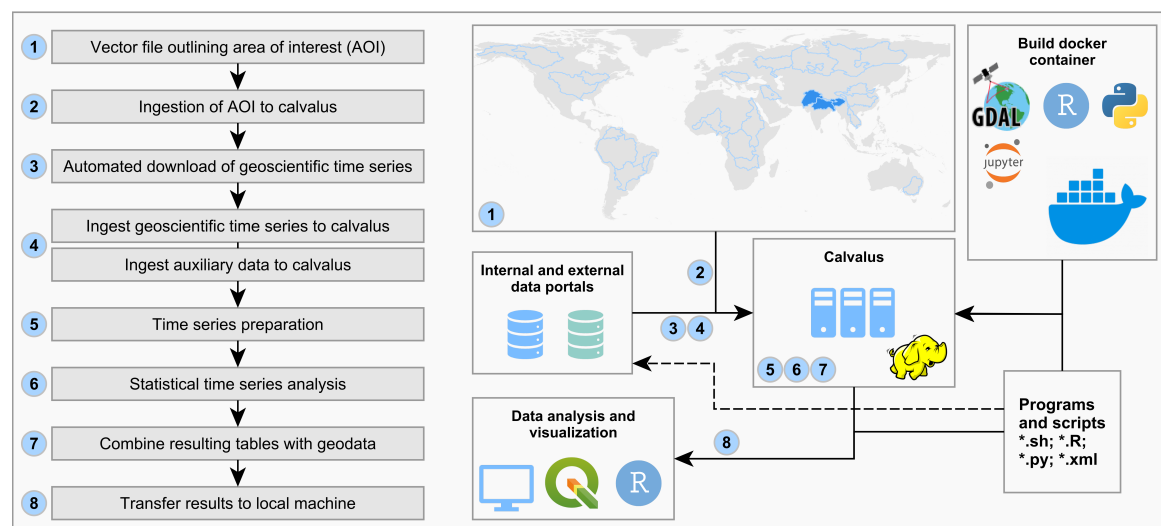


Figure 5.23: Simplified overview of the processing pipeline for multi-source time series preparation and multivariate analyses on the high-performance computing (HPC) environment of the German Remote Sensing Data Center (DFD) at the German Aerospace Center (DLR) with minimal user intervention. The copyright of the logos belongs to the respective institutions.

to the processing pipeline. Also, this framework can be easily transferred to any other river basin, geographical entity, or spatial entity as well as geoscientific time series of any temporal coverage. To this end, the user has to define an area of interest (AOI) and provide the framework with a respective vector file. After downloading, preprocessing, and ingestion of the relevant geoscientific time series from various providers via shell and python scripts, the supplied vector file is used to perform the feature space harmonization. Note that the geoscientific time series can be ingested at global coverage. During the feature space harmonization, only the intersection of the vector file and geoscientific time series are considered. To enable the statistical time series analyses on the HPC infrastructure, docker images were built. These images include necessary libraries, such as Python and R programming language and respective libraries for time series analyses and those to handle geospatial data as well as specific data formats such as Network Common Data Form (NetCDF). The docker images were deployed on the HPC environment and the corresponding docker containers are used to perform the processing steps by means of shell wrapper scripts, which then call a Python or R program to start a respective task. The results from the time series analysis techniques are stored in tables and joined with vector files for further handling. For visualization and evaluation purposes the resulting datasets can be downloaded to a local machine.

5.5 Discussion

This chapter discusses the implemented time series analysis techniques as well as the obtained results in the context of available literature. Also, future requirements are addressed based on remaining limitations of the framework and used geoscientific time series.

5.5.1 Trends and Seasonality

The previous chapter presented a methodological framework that incorporates both, the preparation and analysis of multivariate geoscientific time series to quantify and evaluate land surface dynamics for a study area covering the Indo-Gangetic river basins. Therefore, monotonic trends and changes in seasonality of vegetation greenness, surface water area, and snow cover area were first assessed. In this regard, the obtained results indicated that the design of the MK trend test and the TS slope estimator strongly affect the number of identified statistically significant trends as well as the magnitude of slope values (see Chapter 5.3.1). Also, if the investigated time series are characterized by seasonality, serial correlation has to be considered. Accordingly, the seasonal MK test was employed and if the lag-1 autocorrelation was statistically significant, prewhitening algorithms were applied on the time series. To account for serial correlation, studies frequently prewhitened

the time series prior to trend estimation (e.g. Detsch et al. 2016b; Erasmi et al. 2014; Gao et al. 2012; Praveen et al. 2020; You et al. 2021). Furthermore, one may reduce seasonality and serial correlation by aggregating monthly time series to a larger temporal scale such as annual intervals (Chen et al., 2019; Erasmi et al., 2014). However, aggregation to coarser temporal scale does not ensure the elimination of serial correlation. Additionally, temporal aggregation reduces the number of available data points, which in turn weakens the power of the trend test and increases uncertainties in relation to the estimated slope value (Collaud Coen et al., 2020). Moreover, the choice of a respective prewhitening algorithm may strongly influence the results of the trend test. Thus, it is important to consider advantages and disadvantages of the respective approaches. A comprehensive overview of diverse prewhitening methods is provided by Collaud Coen et al. (2020). In this context, studies quantified the power of the trend tests, frequency of type I errors, and biases in the magnitude of the slope values in dependence of a respective prewhitening algorithm, summarizing that a single approach is not capable of meeting all mentioned aspects satisfactory (Collaud Coen et al., 2020; Wang et al., 2015c). For example, using the TFPW-Y results in much more statistically significant trends than the application of the TFPW-WS (see Figure 5.11, Figure 5.12, Figure 5.13, and Table 5.2). This also applies to the delineated mean absolute slope values, which are generally higher for the TFPW-Y than those derived with the VCPW (see Figure 5.10). As previously outlined in Chapter 5.2.3.1, the magnitude of the slope can be inflated due to high serial correlation, which is also found to increase the probability of type I errors (Militino et al., 2020). In order to alleviate disadvantages of the respective prewhitening algorithms, multiple approaches can be used in combination and trends should be considered as significant when there is a high agreement between different methods (Wang et al., 2015c). For example, Patakamuri et al. (2020) applied five prewhitening algorithms on time series and classified the result as a trend, if at least three approaches resulted in significant trends.

Compared to available literature, the obtained results with respect to the significance of trends, their direction, and spatial distribution are found to be consistent. But, it has to be noted that a comparison of estimated trends between studies is challenging due to several facts. These include potential variations in the data source, the performed preprocessing steps, the investigated study period, the design of the trend test, the applied prewhitening algorithms, and the used confidence level. Accordingly, results should be compared carefully as the defined confidence level might vary among studies and studies might also consider non-significant trends, which by definition should not be considered as trends (Collaud Coen et al., 2020). For example, vegetation condition was analyzed using the leaf area index (LAI) and largely greening trends were identified for the period between 1992–2009 for the Indo-Gangetic river basins (Zhu et al., 2016). In detail, the authors used LAI data

at a spatial resolution of 0.5° (approx. 50 km) and they considered the annually aggregated growing season composites only. LAI was also used by Chen et al. (2019). The authors detected strongly increasing trends between 2000–2017 for the investigated river basins within this thesis. In the mentioned study, LAI was temporally aggregated to annual composites and the TFPW-Y was applied prior to the trend test. Trends were considered as significant at a p -value less than 0.1. On the other hand, Liu et al. (2015) evaluated trends in annual NDVI composites between 1982–2012 and also found positive trends for the IGBM river basins. Furthermore, trends in surface water area showed regionally heterogeneous patterns of increasing and decreasing slope values, particularly along the Brahmaputra river in the downstream areas (see Figure 5.12). These mixed patterns in the trends are most likely influenced by the highly braided river system, which was already mentioned in Chapter 4.1. Striking patches with positive trends in the south of the Ganges river basin are most likely associated with the construction of dams and respective increases in surface water area (see Figure 5.12b). Considering snow cover area, investigations generally apply MODIS data to perform trend analysis (e.g. Ackroyd et al. 2021; Notarnicola 2020; Wang et al. 2017b). Notarnicola (2020) assessed the significance of trends using the MK test on annual and seasonal composites of snow cover area data. A comparison of the results shows matching patterns in the direction of obtained trends in the northwest and northeast of the IGBM river basins.

The evaluation of the derived phenological metrics for the three land surface variables, partially and regionally revealed matching patterns of increasing and decreasing trends with forward and backward shifts of the seasonal characteristics (e.g. see Figure 5.11 and Figure 5.16b,d). Considering phenological analyses, investigations noted challenges with respect to the assessment of both one and two growing seasons with a globally applicable approach (de Jong et al., 2011; Klein et al., 2021). In this thesis, this issue was dealt with by implementing two versions of the phenology model, where one model classifies grids with one and another with two growing seasons in case of the NDVI. The spatial distribution of the grids with one and two growing seasons in vegetation cover (e.g. see Figure 5.14a,c) showed high agreement with a land use classification including single and double cropping systems in the Indo-Gangetic Plain (Gumma et al., 2019). A comparison with studies performing phenological analyses for the IGBM region showed similar findings. For example, Cheng et al. (2017) determined the duration of the growing season by means of the NDVI for the Tibetan Plateau. The findings indicated a length of three to five months for the upper Brahmaputra river basin being comparable to the seasonal duration derived in this thesis (see Figure 5.15a). Resulting phenological metrics for surface water area, particularly with respect to the timing of the maximum extent between July and August were found to be consistent for the river mouths of the Indus, Ganges, and Brahmaputra rivers (Biemans

et al., 2019). Disagreement was detected for the central Indus river in the obtained values for the timing of the seasonal peak. More specifically, the timing of the maximum surface water area extent was found to be reached around April (Figure 5.14e), which is not consistent with the timing of the maximum in river discharge in literature (Biemans et al., 2019; Lutz et al., 2014). On the other hand, computed phenological metrics of snow cover area were congruent with findings in available studies. For example, significant negative trends were found for snow cover duration between 2000 and 2018 in the east and non-significant positive values in the west of the upper IGBM river basins (see Figure 5.15h) (Notarnicola, 2020). Comparable trends for snow cover area were also reported by Wang et al. (2017b).

5.5.2 Influence of Drivers on Land Surface Dynamics

Using a multivariate feature space consisting of geoscientific time series provides the opportunity to improve the credibility of causal interpretation with respect to land surface dynamics. Including more time series variables could potentially reveal further spurious links, however, besides increasing the dimensionality, the inclusion of more variables could also yield a lower power of the tests and could weaken the chances of detecting causal links (Runge et al., 2019b). The Peter and Clark Momentary Conditional Independence (PCMCI) approach alleviates this issue by excluding irrelevant variables and through the conditioning on the few relevant variables only (Runge et al., 2019b). When using PCMCI, the causal interpretations are resting on several assumptions that need to be considered, such as causal sufficiency, causal stationarity, and if employing partial correlation as conditional independence test also stationarity in time series (Runge, 2018) (stationarity was defined in Chapter 5.2.3.3). In this context, the time series were detrended and anomalized to establish stationarity in time series. Yet, detrending and the removal of the seasonal cycle is not always making the time series strictly stationary, which might potentially result in a violation of this assumption. A further possibility towards the establishment of stationarity in time series is the consideration of causal stationarity, which is a less strict form of stationarity (Runge, 2018). This implies the consideration of time steps in the causal analysis, which belong to a defined set of time steps (Runge, 2018), i.e. a meteorological season. For example, the influence of temperature on the snow cover could be neglected during summer, when snow cover has already melted. Moreover, it is important to include all relevant driving variables, which is described by the causal sufficiency assumption (Runge et al., 2019b). In this context, the generation of a multivariate feature space is of great importance for the quantification and analysis of causal links. As outlined before, the causal analysis is used to quantify the influences of climatic and hydrological variables on vegetation condition, surface water area, and snow cover area. Nevertheless, the causal sufficiency assumption might be violated in most of the applications, since not all drivers can be measured and,

thus, included. This circumstance also applies to the fact that the time series were temporally aggregated to monthly composites, which might induce disappearing causal links (Runge, 2018).

The presented results on the causal network analysis demonstrated the driving variables with the largest MCI effect size per grid (see Figure 5.17, Figure 5.19, and Figure 5.21). Currently, there is only one more study available using PCMCI to analyze the relationship between the NDVI and considered the climatic variables precipitation, temperature, and radiation (Krich et al., 2020). With more detail, the analysis was conducted at a spatial resolution of 0.5° (approx. 50 km) at global scale and three driving variables. Therefore, a direct comparison is hampered. Yet, the spatial distribution of prevalent driving variables and the interaction between the target and the drivers appear to be comparable (see Figure 5.18). As an example, the contrasting behavior of downward shortwave radiation and precipitation is also reflected in the results of this chapter. In addition, Krich et al. (2020) also identified water availability as a dominant driver in the upper Brahmaputra river basin at a temporal lag of 0 and 1 month. Apart from investigations using PCMCI, further studies used the Granger causality or regression approaches to quantify temporally lagged dependencies of NDVI (e.g. Papagiannopoulou et al. 2017; Wu et al. 2015; Yuan et al. 2019). Here, Papagiannopoulou et al. (2017) used a feature space composed of radiation, temperature, and several indicators for water availability, including precipitation, soil moisture, and snow water equivalent to assess their impact on the NDVI. For the IGBM river basins, the authors identified water availability as the most important climatic driver and in western regions partially radiation, whereas the temporal lag for water was dominant at 0 and 1 month. Next, Yuan et al. (2019) analyzed the influence of atmospheric vapor pressure deficit on vegetation condition, which is impacting plant photosynthesis when increasing. In agreement with this study, the obtained results in this thesis mostly indicated a negative coupling of NDVI with vapor pressure deficit. However, compared to the other investigated drivers, vapor pressure deficit showed a weaker influence (see Figure 5.17 and Figure 5.18d). Wu et al. (2015) applied multiple linear regression between the NDVI and precipitation, temperature, and radiation. A comparison of the obtained results showed that the temporal lags for each driving variable were higher than those derived with PCMCI. For example, for precipitation the temporal lag was mostly between 1 and 3 months. In this regard, Krich et al. (2020) noted that the resulting temporal lags might be lower with PCMCI due to the reduced serial correlation.

Considering the land surface variable surface water area, river discharge was found to be the dominant driver (see Figure 5.19). It has to be noted, that this detected linear dependency might not be always valid, since river discharge is potentially also positively coupled

to precipitation and snow cover area. More specifically, precipitation as well as melting ice and snow greatly contribute to river discharge in the IGBM river basins (see Chapter 4.2.2), and, thus, the identified causal link $Q \overset{\pm}{\rightarrow} SWA$ could be potentially a result of the indirect path $P \overset{\pm}{\rightarrow} Q \overset{\pm}{\rightarrow} SWA$ or $SCA \overset{\pm}{\rightarrow} Q \overset{\pm}{\rightarrow} SWA$, where Q stands for river discharge. These links could not be resolved, as indirect interactions among the investigated time series variables were not considered in this chapter. Moreover, as the results demonstrated, temperature was found to be the prevalent driving factor and was negatively influencing snow cover area in the Himalayan and Karakoram mountains (see Figure 5.21). Likewise, Huang et al. (2017) identified a negative coupling between temperature and snow cover area for the entire Tibetan Plateau. In addition, Notarnicola (2020) investigated the impact of temperature and precipitation on snow cover area over meteorological seasons. Due to the temporal and spatial aggregation of the target and driving variables at large spatial zones as well as methodological differences, a direct comparison of the spatial distribution of influencing factors is complicated. However, Notarnicola (2020) identified a significant negative correlation between temperature and snow cover area being prominent during all seasons and most regions overlapping with the IGBM river basins.

5.5.3 Limitations and Future Requirements

Overall, the implemented and presented methodological framework for time series analysis shows good functionality for the investigated large river basins in South Asia which feature heterogeneous characteristics with respect to the climate, elevation, and land cover. This emphasizes the potential of the framework and the applied methods for transferability to any other river basin or geographical entity as well as time series data. The performed analyses on land surface dynamics included time series on NDVI, surface water area (SWA), and snow cover area (SCA), which were all based on MODIS imagery. Additional climatic and hydrological variables were utilized to evaluate their influence on the remote sensing-based land surface variables. In this regard, the temporal and spatial properties of the remote sensing-based time series were mainly limited by the characteristics of the MODIS sensors. Here, it has to be noted that the analysis of surface water area by means of the DLR Global WaterPack might be complicated due to the spatial resolution of the data. More specifically, river streams and inland water bodies which are smaller than the 250 m pixel resolution might not be represented by the DLR Global WaterPack due to mixed pixel issues. Yet, it is of great importance to note that spatially and temporally consistent remote sensing-based time series providing data over several decades and high temporal revisit times are currently only available at the cost of their spatial resolution (see Chapter 2.2). In this regard, inconsistencies of the DLR Global WaterPack were discussed, concerning the timing of the maximum surface water area extent of the Indus river basin,

which is not matching with the timing of the seasonal peak in river discharge. This could be most likely explained by potential underestimations of the surface water area classification during the months July to September, where the water color is changing due to high sediment load. This might be caused by high contributions of ice and snowmelt in the Indus river basin. Despite these underestimations, Huang et al. (2018a) emphasized that the monitoring of surface water area with multispectral remote sensing imagery at large spatial scales still remains a challenge. This makes the DLR Global WaterPack an indispensable time series to perform intra-annual analyses on changes in surface water area. The detected underestimations might be alleviated by fusing this dataset with time series having higher spatial, but lower temporal resolution. These findings might apply on the MODIS-based NDVI and DLR Global SnowPack as well.

Moreover, for testing purposes of the implemented framework and due to the availability of most climatic data at monthly temporal scale as well as the required data harmonization, all time series were temporally aggregated to monthly composites. However, MODIS data would also enable the analysis of land surface dynamics at much higher temporal resolution, such as weekly or biweekly intervals. The finer temporal granularity of the time series could improve intra-annual and seasonal analysis as well as potentially the identification of causal links that might vanish due to the temporal compositing to monthly intervals.

Furthermore, the design of the trend test's was stressed regarding the generation of reliable and comparable trend estimations. However, it has to be noted that for the analysis of land surface dynamics over multiple decades, the computation of monotonic trends might not be sufficient, e.g., due to potentially existing changepoints in the time series. In this regard, the application of further methods such as BFAST (Verbesselt et al., 2010) and BEAST (Zhao et al., 2019a) could enhance the analysis and provide more insight into the dynamics. In addition, the impact of anthropogenic forcing has to be considered as well, when analyzing land surface dynamics. Anthropogenic pressure might be measured through the integration of time series on settlement areas as well as population data (Lloyd et al., 2019; Marconcini et al., 2020; Palacios-Lopez et al., 2019), and land use change (Winkler et al., 2021).

5.6 Summary

This chapter presented a novel approach for the analysis of multivariate Earth observation time series enabling the quantification and evaluation of land surface dynamics across spheres (see Chapter 5.2). The used Earth observation time series characterized vegetation condition, surface water area, and snow cover area, by means of the MODIS Normalized

Difference Vegetation Index (NVDI), the DLR Global WaterPack, and the DLR Global SnowPack data. With the implemented methodological framework, Earth observation time series were jointly analyzed with time series on climatic and hydrological variables to estimate their influence on the used remote sensing-based land surface variables for the period 2000–2019 (see Chapter 5.1). These multivariate time series covering multiple decades were collocated for a large-scale study area, including the transboundary Indus, Ganges, Brahmaputra, and Meghna river basins in South Asia. This study area was particularly suitable for both, the development of a transferable methodological framework and the exploration of a multivariate feature space with statistical time series analysis techniques due to their heterogeneous characteristics in terms of climate zones, elevation zones, as well as land cover and land use classes (see Chapter 4.1).

After harmonizing the multi-source time series to a common grid space (see Chapter 5.2.2), statistical time series analysis techniques were applied at a monthly temporal resolution. These included the calculation of trends (see Chapter 5.2.3.1) and changes in phenological metrics (see Chapter 5.2.3.2), as well as the application of the causal discovery algorithm Peter and Clark Momentary Conditional Independence (PCMCI) (see Chapter 5.2.3.3). It was shown that the use of the Mann-Kendall trend test in association with the Theil-Sen slope estimator requires the consideration of seasonality and serial correlation. In this regard, the seasonal Mann-Kendall test was applied on the prewhitened monthly time series, where prewhitening aims to reduce the lag-1 autocorrelation in time series. It was also stressed that advantages and disadvantages of respective prewhitening methods have to be taken into account. In order to investigate changes in phenological metrics between the two investigated decades, the Timesat tool was employed. Besides the global parameter setting, an additional set was defined for the NDVI to enable the consideration of areas being characterized by two annual growing seasons. In general, the derived changes in the phenological metrics were found to be consistent with the delineated statistically significant positive and negative trends, respectively. Furthermore, for the first time, a high dimensional feature space involving several spheres was utilized to evaluate the influence of driving variables on the vegetation condition, surface water area, and snow cover area using PCMCI. The identified couplings and dependencies between the time series variables were found to be consistent with reported findings in literature, confirming the functionality of the implemented approach.

Furthermore, the time series analyses revealed the following land surface dynamics and influences for the investigated transboundary river basins in South Asia (see Chapter 5.3):

- The MODIS NDVI was used as an indicator for vegetation condition and the trend analysis indicated mostly significant positive trends at annual scale for the Indo-

Gangetic river basins. The phenology of the NDVI showed decreases in the seasonal amplitude, when comparing the decades 2000–2009 and 2010–2019. These decreases were associated with constant or increasing seasonal peak values. Complementary to the results of the trend analysis, the changes in the computed phenological metrics indicated an ongoing increase in vegetation greenness. On the other hand, the analysis of the driving variables showed that water availability was the dominant factor influencing the NDVI during the investigated period.

- The DLR Global WaterPack represented surface water area. The trend analysis at annual temporal scale revealed significant negative trends being prevalent at the confluences of the Ganges and Brahmaputra as well as in the wetlands of the Meghna river basin. In comparison, striking significant positive trends were identified north of the Sundarbans mangrove forest and in the south of the Ganges river basin. The quantification of influencing factors on surface water area showed a negative and positive coupling with snow cover area and temperature in high elevation areas, respectively. In downstream areas of the Indo-Gangetic river basins, river discharge and precipitation were positively influencing surface water area during the studied period.
- The DLR Global SnowPack was used as indicator for snow cover area. Based on the trend analysis, weak significant positive trends could be identified for the upper Indus river basin, whereas significant negative trends were dominant for the upper Ganges and Brahmaputra river basins at annual scale. In addition, the computed changes in the phenological metrics revealed matching spatial patterns of forward and backward shifts with significant positive and negative trends, respectively. For example, complementary to significant negative trends, decreases in the duration of snow cover area were identified in the upper Ganges and Brahmaputra river basin. It was also found, that snow cover area was mostly negatively coupled to temperature in the river basins, whereas a positive coupling could be revealed for the western parts of the upper Indus river basin.

Moreover, the methodological framework was implemented on a high-performance computing (HPC) infrastructure at the German Aerospace Center (DLR) and its transferability in space and time was emphasized (see Chapter 5.4). For example, the framework can easily be complemented with further geoscientific time series, applied to further river basins or any other geographical and spatial entity, or easily amended by additional time series analysis techniques. Considering the discussed potentials and future requirements in Chapter 3.2, the implemented framework and included time series analyses greatly contribute to their fulfillment. In particular, these include the analysis of large-scale transboundary river basins as well as land surface dynamics across spheres. Additionally, limitations

and future requirements regarding the developed framework were discussed (see Chapter 5.5.3). In brevity, these included the increase of the temporal resolution of the time series to enhance intra-annual and seasonal analyses, the fusion of geoscientific time series (e.g. surface water area), and the inclusion of anthropogenic influences into the analysis of land surface dynamics. These aspects will be addressed in the following chapter.

Chapter 6

*Evaluation of Seasonal Trends and Drivers of Land Surface Variables for the Indo-Gangetic River Basins**

High mountain Asia holds the largest ice mass on Earth apart from the polar regions. Monsoon rainfall as well as meltwater from ice and snow are providing the Indo-Gangetic river basins with indispensable freshwater resources (Pritchard, 2019; Viviroli et al., 2020) (see Chapter 4.2.2). Over 1.1 billion people are living in these river basins and in part heavily depend on the water resources supplied by these large river systems. In the context of amplified climate change, the transboundary river basins Indus, Ganges, Brahmaputra, and Meghna (IGBM) are experiencing increasing environmental and human pressure (Song et al., 2018; Wijngaard et al., 2018). In this context, investigations pointed towards declining terrestrial water storage in the Indo-Gangetic Plains which could be associated with unsustainable water withdrawal (MacDonald et al., 2016). In addition, with increasing surface air temperatures in high elevation areas, seasonal snow cover and glacier mass will be most likely negatively influenced (Miles et al., 2021; Pepin et al., 2015). Particularly in years with less rainfall, meltwater from glaciers and snow modulates the seasonal water availability in the investigated river basins (Biemans et al., 2019). In the long-term, decreasing amounts of meltwater from the mountains could endanger the availability of seasonal water resources which are fundamental for many sectors, including irrigated agriculture. Additionally, future climate projections are suggesting an increase in the occurrence of extreme events, including drought, heatwave (Dangar and Mishra, 2021; Mishra et al., 2020), and flooding (Nie et al., 2021). In this regard, a detailed analysis of land surface dynamics and respective driving mechanisms at seasonal and annual scales is required to improve the understanding of interactions between multiple spheres in the Indo-Gangetic river basins.

*Parts of this chapter have been submitted at Uereyen et al. (2022b)

This chapter aims at enhancing the understanding of seasonal land surface dynamics and investigating climatic, hydrological, and anthropogenic influences in the Indo-Gangetic river basins. As outlined in the previous chapter, the time series will be aggregated at a finer temporal granularity to enhance the intra-annual trend analyses and the detection of causal links. Specifically, time series with a biweekly temporal resolution will be processed for the period December 2002 to November 2020. In detail, the specific objectives include (1) the estimation of seasonal and annual trends at grid and river basin scale, (2) the investigation of direct and indirect influences on land surface variables at seasonal temporal scale, (3) the assessment of human influence on the land surface, and (4) the exploration of patterns in the spatial distribution of seasonal trends and driving variables.

In the following, the used time series (Chapter 6.1) and the applied methods (Chapter 6.2) will be briefly introduced. Next, the results of the seasonal trend analysis at different spatial scales as well as the estimation of drivers at seasonal temporal and various spatial scales will be presented in detail (Chapter 6.3). Chapter 6.4 provides a comprehensive discussion on the identified trends and environmental as well as anthropogenic drivers. Ultimately, Chapter 6.5 summarizes the findings and conclusions of this chapter.

6.1 Input Data

This chapter presents the used remote sensing-based datasets to characterize vegetation, surface water area, and snow cover area. Additionally, environmental and human controls are evaluated by means of climatic, hydrological, and anthropogenic variables.

6.1.1 Remote Sensing-Based Land Surface Variables

In contrast to the previous chapter, the full archive of daily Terra and Aqua MODIS (M*D09GA.006) surface reflectance products at 500 m spatial resolution were used (Verote and Wolfe, 2015) to characterize vegetation areas and enable the processing of NDVI composites at a finer temporal granularity. These images were acquired for the period between December 2002 and November 2020. In this regard, more than 100,000 MODIS images were processed to generate the NDVI composites (approx. 52,000 images for Terra and Aqua MODIS, respectively).

Moreover, the analysis of surface water area was conducted based on the previously introduced DLR Global WaterPack. In Chapter 5.5.3, the identified underestimations in this data set were discussed. To alleviate these shortcomings, particularly in the Indus river basin, the DLR Global WaterPack was complemented with the Global Surface Water Layer (GSWL) version 1.3 (Pekel et al., 2016). The GSWL data is computed on the

Google Earth Engine (GEE) (Gorelick et al., 2017) by means of the full Landsat archive and was developed at the Joint Research Center (JRC). Fusing both time series allows for the exploitation of their respective advantages being on the one hand, the daily temporal resolution (DLR Global WaterPack) and, on the other hand, the comparatively high spatial resolution (JRC Global Surface Water Layer). In addition, the DLR Global SnowPack (Dietz et al., 2015) was used as indicator for snow cover area. This data was already presented in Chapter 5.1.1.3.

6.1.2 Climatic and Hydrological Variables

To enable the analysis of climatic and hydrological controls on the land surface at a finer temporal granularity, the respective variables were extracted from time series based on the hourly ERA5-Land reanalyses data of the ECMWF (Muñoz-Sabater, 2019). Compared to the ERA5 reanalysis products (Hersbach et al., 2020), the ERA5-Land reanalysis represents the land component including hourly atmospheric and land variables at an enhanced spatial resolution of 0.1° (approx. 9 km) since 1950 (Muñoz-Sabater, 2019). In compliance with the aim to generate time series at biweekly intervals, the ERA5-Land reanalysis is of particular value due the hourly temporal resolution. Here, the variables total precipitation, surface solar radiation downwards, 2-m air temperature, soil moisture (7–28 cm), and 2-m dewpoint temperature were used.

Recently, studies investigating the Indo-Gangetic Plain and the Himalayan-Karakoram region widely employed the ERA5-Land reanalysis (e.g. Bhattacharya et al. 2021; Kolluru et al. 2020; Kraaijenbrink et al. 2021; Mishra et al. 2020; Nepal et al. 2021). In general, the trends and anomalies derived from ERA5-Land 2-m air temperature showed good agreement with in-situ measurements in India (Mishra et al., 2020) and in the Himalaya (Bhattacharya et al., 2021). For a subbasin in the upper Indus river basin, a comparison of ERA5-Land temperature and in-situ measurements indicated good agreement as well, despite a negative bias in the winter season (Nepal et al., 2021). In addition, studies point towards the improvements in the ERA5 and ERA5-Land reanalysis compared to the superseded ERA-Interim (Chen et al., 2021b) and their superiority compared to other reanalyses over India with respect to temperature and precipitation (Mahto and Mishra, 2019). Moreover, the performance of daily ERA5 precipitation was evaluated for selected river basins in India and showed better results compared to, e.g. the CHIRPS dataset (Kolluru et al., 2020). Chen et al. (2021b) particularly emphasized the improvement of the ERA5-Land for capturing the spatial patterns of precipitation over higher altitudes in the central Himalaya. Note that the validation of gridded reanalyses remains a difficult task, as in-situ stations in the Himalaya region are particularly sparse (Bhattacharya et al., 2021). Considering the

variable solar radiation, Urraca et al. (2018) stressed the improvements in ERA5 compared to ERA-Interim, in particular the reduction in the positive bias. Yang and Bright (2020) demonstrated a validation of several radiation products as well, where ERA5 outperformed the other reanalysis product Modern-Era Retrospective analysis for Research and Applications, version 2 (MERRA-2). Furthermore, the ERA5 and ERA5-Land soil moisture data were validated in several studies with in-situ measurements (e.g. Li et al. 2020; Muñoz-Sabater et al. 2021; Xing et al. 2021; Yang et al. 2020). Results in Muñoz-Sabater et al. (2021) showed that ERA5-Land soil moisture generally performs better than ERA5 and ERA5-Interim. Likewise, Li et al. (2020) reported that ERA5 outperforms its predecessor and four other reanalyses in capturing the temporal variations of soil moisture on the Tibetan Plateau. The utilized GloFAS-ERA5 daily river discharge version 3.1 data (Harrigan et al., 2020) was already introduced in Chapter 5.1.2. In addition, to quantify changes in terrestrial water storage, a daily time series based on the twin-satellite Gravity Recovery And Climate Experiment (GRACE) mission that characterizes the terrestrial water storage anomaly (TWSA) was used. This dataset is processed at the Institute of Geodesy at Graz University of Technology (ITSG) (Kvas et al., 2019; Mayer-Gürr et al., 2018). Note that the temporal availability of the TWSA data is limited to 2003–2016.

6.1.3 Anthropogenic Variables

To characterize human influence in the IGBM river basins, several geoscientific datasets were used as indicator. These data include the already introduced ESA CCI land cover at an annual temporal resolution covering the years 1992–2019 (European Space Agency, 2017) (see Chapter 4.2.3). Additionally, a globally available gridded population data at annual temporal and 1 km spatial resolution was used (Lloyd et al., 2019; WorldPop and CIESIN, 2018) (see Chapter 4.3). This dataset provides an estimation of the total population count per 1 km pixel. Moreover, a harmonized nighttime lights time series based on the instruments Defense Meteorological Satellite Program-Operational Linescan System (DMSP-OLS) and Visible Infrared Imaging Radiometer Suite (VIIRS) was utilized. This annual time series has a spatial resolution of 1 km and provides the intensity of night-lights as digital numbers. Ultimately, the DLR World Settlement Footprint (WSF) Evolution which is a binary classification of settlement areas between 1985 and 2015 was used as well (Marconcini et al., 2020, 2021) (see Chapter 4.3). The WSF Evolution was processed on the GEE by means of the full Landsat archive at an annual temporal resolution and a spatial resolution of 30 m. In combination, these datasets allow for the quantification of the spatio-temporal growth of the population and settlements which can be then used as proxy for the evaluation of the human influence in the IGBM river basins.

6.2 Methods

6.2.1 Time Series Preprocessing and Harmonization

All used daily time series were gathered for the period between December 2002 and November 2020. If available, the annual time series which include the anthropogenic variables were collocated for the period 2003 to 2020. Due to data gaps and interpolation purposes, the daily time series were temporally aggregated to biweekly composites, which is a finer temporal granularity than the monthly temporal resolution in the previous chapter.

Prior to the statistical analyses, the time series required further preprocessing. To compute high quality NDVI composites, Terra and Aqua MODIS imagery were first processed separately in accordance to the presented steps in Chapter 5.2.1. As the quality assurance layers have a spatial resolution of 1 km, the daily imagery were spatially aggregated from 500 m to 1 km. Next, the temporal aggregation was performed to compute biweekly composites. During the temporal aggregation, the median value of the input images was considered to minimize the influence of outliers. In a subsequent step, the biweekly NDVI composites of Terra and Aqua MODIS imagery were merged through the calculation of the mean value for the respective pixel and biweekly period. Still existing gaps in the time series were filled using linear interpolation. Ultimately, to mask non-vegetated areas, all pixels with a long-term NDVI value lower than 0.15 were excluded as suggested by Wittich and Hansing (1995).

Furthermore, to get a differentiated insight into the vegetation trends, the annual ESA CCI land cover (European Space Agency, 2017) time series were used to distinguish the NDVI for the classes forest, grassland, irrigated cropland, and rainfed cropland. For this purpose, as described in Chapter 4.2.3, the land cover time series were first reclassified and then stable pixels between 2002 and 2019 were computed for each of the aforementioned class. Next, the 300 m spatial resolution of the land cover data was aggregated to the spatial resolution of the NDVI (1 km). During the spatial aggregation, the land cover class occurring most frequently was assigned to the respective pixel. In a final step, the NDVI time series was intersected with the stable pixels of the respective land cover class. This resulted in NDVI time series for forest, grassland, irrigated cropland, and rainfed cropland areas.

In order to improve the regionally identified underestimations in the DLR Global WaterPack, the GSWL (Pekel et al., 2016) was incorporated into the time series of surface water area. The GSWL was downloaded from the GEE and aggregated to the spatial resolution of the Global WaterPack. Next, the daily Global WaterPack was temporally aggregated to biweekly composites. In a final step, both time series were conditionally merged. Pixels in

the Global WaterPack time series which were classified as “no-water”, were labeled with “water” if the GSWL had a valid value for the respective pixel and time step.

The preprocessing of DLR Global SnowPack (Dietz et al., 2015) data includes the same steps as described in Chapter 5.1.1.3 and Chapter 5.2.1. As stated before, the time series was used for the period December 2002 to November 2020. After preprocessing, the daily time series were aggregated to biweekly temporal intervals.

Moreover, the preprocessing of the hourly ERA5-Land time series included following steps. First, the variables total precipitation and surface solar radiation downwards were accumulated, whereas 2-m air temperature, soil moisture, and 2-m dewpoint temperature were averaged at daily temporal scale. Next, vapor pressure deficit was calculated based on 2-m air temperature and 2-m dewpoint temperature using the formula in Barkhordarian et al. (2019). Furthermore, during the preprocessing the physical unit of the variables were converted. Precipitation was converted from *m* to *mm*. The reanalysis on solar radiation was converted to daily energy fluxes in watts per square meter (Wm^{-2}) and the unit of temperature was changed from Kelvin (*K*) to degrees Celsius ($^{\circ}C$). Finally, all daily time series, including river discharge and terrestrial water storage anomaly (TWSA), were aggregated to biweekly temporal composites.

Afterwards, as presented in Chapter 5.2.2, all geoscientific time series were harmonized to a common spatial grid. In this chapter, a grid at a spatial resolution of 0.1° (approx. 9 km) and the geographical entities including the boundaries of the IGBM river basins and their respective subbasins, elevation-dependent zones, as well as regions stratified by land cover and land use classes were used (see Chapter 4.1 and Figure 4.1d).

6.2.2 Application of Statistical Time Series Analysis Techniques

The preparation and analysis of the multivariate time series was performed using the developed and implemented methodological framework (see Chapter 5.2). Figure 6.1 provides an overview of the applied workflow. In accordance to the defined objectives in the introduction of this chapter (see Chapter 6), the time series analyses included the computation of seasonal and annual trends, the estimation of direct and indirect influences on the remote sensing-based variables at seasonal scale, and the evaluation of anthropogenic influences.

6.2.2.1 Seasonal Trend Estimation

The employed non-parametric Mann-Kendall (MK) test in combination with the Theil-Sen (TS) slope estimator were introduced in Chapter 5.2.3.1. Here, the statistical significance of the trend was tested with the trend-free prewhitening after Wang and Swail

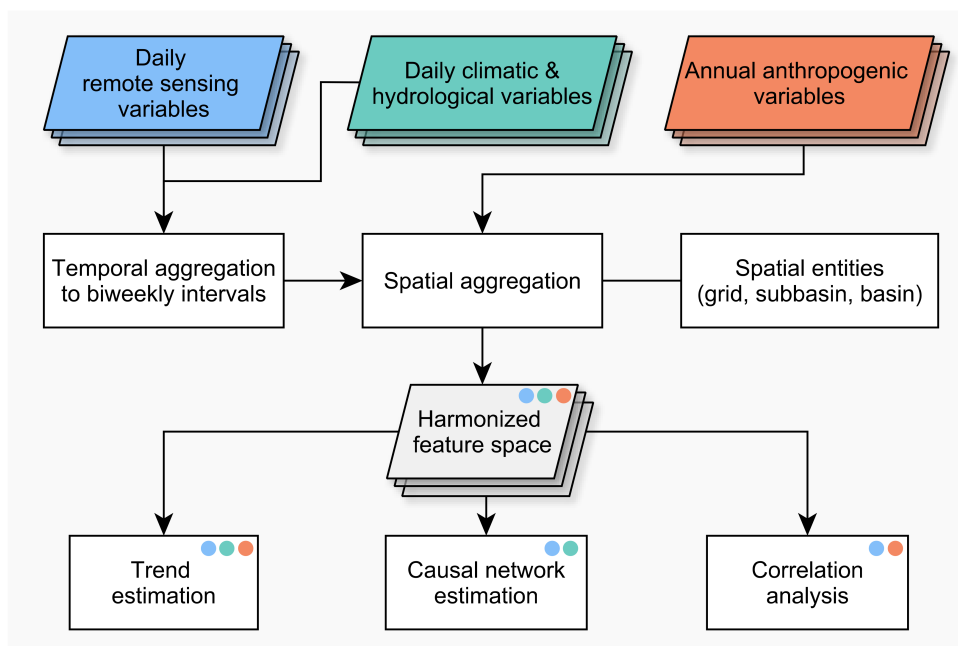


Figure 6.1: Simplified overview of the workflow as part of the developed and implemented framework. Modified after Ureyen et al. (2022b)

(TFPW-WS) approach (Wang and Swail, 2001), and the magnitude and direction based on the variance corrected prewhitening (VCPW) approach (Wang et al., 2015c). Following seasons were considered for the time series analyses in this chapter: winter (DJF), pre-monsoon (MAM), monsoon (JJAS), and post-monsoon (ON). First, the trend tests were performed at seasonal scale for the period December 2002 to November 2020. Based on the seasonal metrics, the annual trend was derived. During these calculations the time series were kept at biweekly temporal resolution, to obtain a larger number of data samples and, thus, improve the power of the trend test (Collaud Coen et al., 2020). As before, trends were considered as statistically significant at a confidence level of 95 %. Note that in the results and discussion section, non-significant trends are presented as tendencies.

6.2.2.2 Causal Networks at Seasonal Scale

Furthermore, a novel version of the PCMCi algorithm, specifically PCMCi⁺ (Runge et al., 2019b; Runge, 2020) was employed in this chapter. This version enables the full exploration of contemporaneous (lag 0) as well as lagged dependencies for a multivariate feature space. In this chapter, causal graphs were built using the PCMCi⁺ method. Here, the causal graphs are made up of nodes which are representing the respective time series variable and edges depicting the existence and direction of identified causal links within a feature space. A detailed description of the theory behind PCMCi was already provided in Chapter 5.2.3.3. As stated before, using the standard PCMCi algorithm, the direction of identified contemporaneous links is generally left undirected, because a temporal order is

not available in these cases. The direction of instantaneous links could only be assessed for a directed assessment, e.g. if investigating the influence of precipitation on NDVI, as was conducted in Chapter 5.2.3.3. The PCMCI⁺ version enables the assessment of contemporaneous links through the adaptation of the two-step procedure in PCMCI. These include the condition selection step, the skeleton phase, and additional orientation phases to identify the direction of contemporaneous links and are explained in detail in Runge (2020).

To use the harmonized feature space for PCMCI⁺, a detrending and computation of seasonal anomalies was performed to achieve stationarity in time series (see Chapter 5.2.3.3). Next, a maximum temporal lag of six time steps was defined which corresponds to three months at a biweekly temporal scale. In contrast to the previous chapter, the meteorological seasons were used as a temporal mask to fulfill the causal stationarity assumption. In addition, time steps with both NDVI values lower than 0.2 and temperature lower than 0 °C were removed as suggested by Wu et al. (2015). Further details on the used parameter settings are provided in Table 5.1.

Apart from the causal maps which were already presented in Chapter 5.3.3 and included the derived direct influences on the target variables (e.g. Figure 5.17), this chapter additionally visualizes causal graphs. These support the analysis of indirect influences on the land surface variables vegetation condition, surface water area, and snow cover area as well as the interdependencies among the entire feature space. Since the causal graphs were computed at subbasin and basin scale, only intersecting pixels of the NDVI, surface water area, and snow cover area with the respective driving variables were considered. The spatial intersection e.g., removes the influence of precipitation for non-vegetated areas.

6.2.2.3 Evaluation of Human Influence

To investigate anthropogenic controls on the land surface variables, the relation between vegetation condition and surface water area with the gathered anthropogenic variables were estimated. The anthropogenic variables involve the annual time series on gridded population counts, nighttime lights, and settlement area (see Chapter 6.1.3). Due to the annual temporal resolution, it was not possible to include these time series into the causal analysis. Instead, a Pearson's correlation analysis was performed to evaluate anthropogenic influences on vegetation as well as surface water area. The statistical significance of the correlation coefficients was evaluated at a confidence level of 95 %. Additionally, the NDVI trends were computed for multiple vegetation classes, including forest, grassland, irrigated agriculture, and rainfed agriculture (see Chapter 6.2.1). This provides a more detailed insight into the vegetation dynamics and supports the analysis of potential human influence on vegetated areas.

6.3 Results

In the following, the obtained results of the time series analysis for the Indus, Ganges, Brahmaputra, and Meghna river basins are presented. First, the trend analyses, which were performed at seasonal temporal scale and various spatial scales is presented in Chapter 6.3.1. Afterwards, Chapter 6.3.2 demonstrates the calculated results on environmental drivers on the vegetation condition, surface water area, and snow cover area at seasonal scale. In addition, the influence of anthropogenic influences is evaluated as well.

6.3.1 Seasonal Trends

Compared to the presented results on the trends at annual temporal scale in Chapter 5.3.1, this chapter focuses on seasonal and annual trends at river basin scale (see Chapter 6.3.1.1), grid scale (see Chapter 6.3.1.2), and for snow cover area additionally for elevation zones (see Chapter 6.3.1.3). All presented trends are representative for the period December 2002 to November 2020.

6.3.1.1 Trends at Basin Scale

Figure 6.2 illustrates all used biweekly time series aggregated at annual scale and differentiated by the respective river basin. In case of the NDVI, an increasing tendency in the respective time series is clearly visible. This increase is particularly pronounced since the year 2018 for the Indus and Ganges river basin as well as the Ganges-Brahmaputra-Meghna (GBM)-Delta. Moreover, the surface water area time series shows distinct anomalies and a partially a clear relationship with precipitation for the Meghna river basin and GBM-Delta (see Figure 6.2b,d). In case of the Indus river basin, several positive anomalies could be very likely associated with large flood events, e.g. in the year 2010, 2015, and 2020 (see Figure 6.2b). These positive anomalies are also reflected in the river discharge time series (Fig. 6.2g). This also applies to the Ganges river basin (e.g. 2013), and Brahmaputra as well as Meghna river basin (e.g. 2007). It is also likely that anomalies in precipitation and temperature are largely associated with snow cover area. For example, in the Indus river basin temperature and precipitation have a positive and negative anomaly in 2016, respectively (Fig. 6.2d,e). On the other hand, snow cover area reached the lowest point for the investigated period in 2016 (Fig. 6.2c). Particularly striking is the constant decline in the terrestrial water storage anomaly (TWSA) for all of the river basins (Fig. 6.2j). Note that this time series is only visualized for the period 2003 to 2015.

Considering seasonal and annual trends at river basin scale, Table 6.1 collocates all calculated trend metrics for the investigated geoscientific time series. For the NDVI, it is

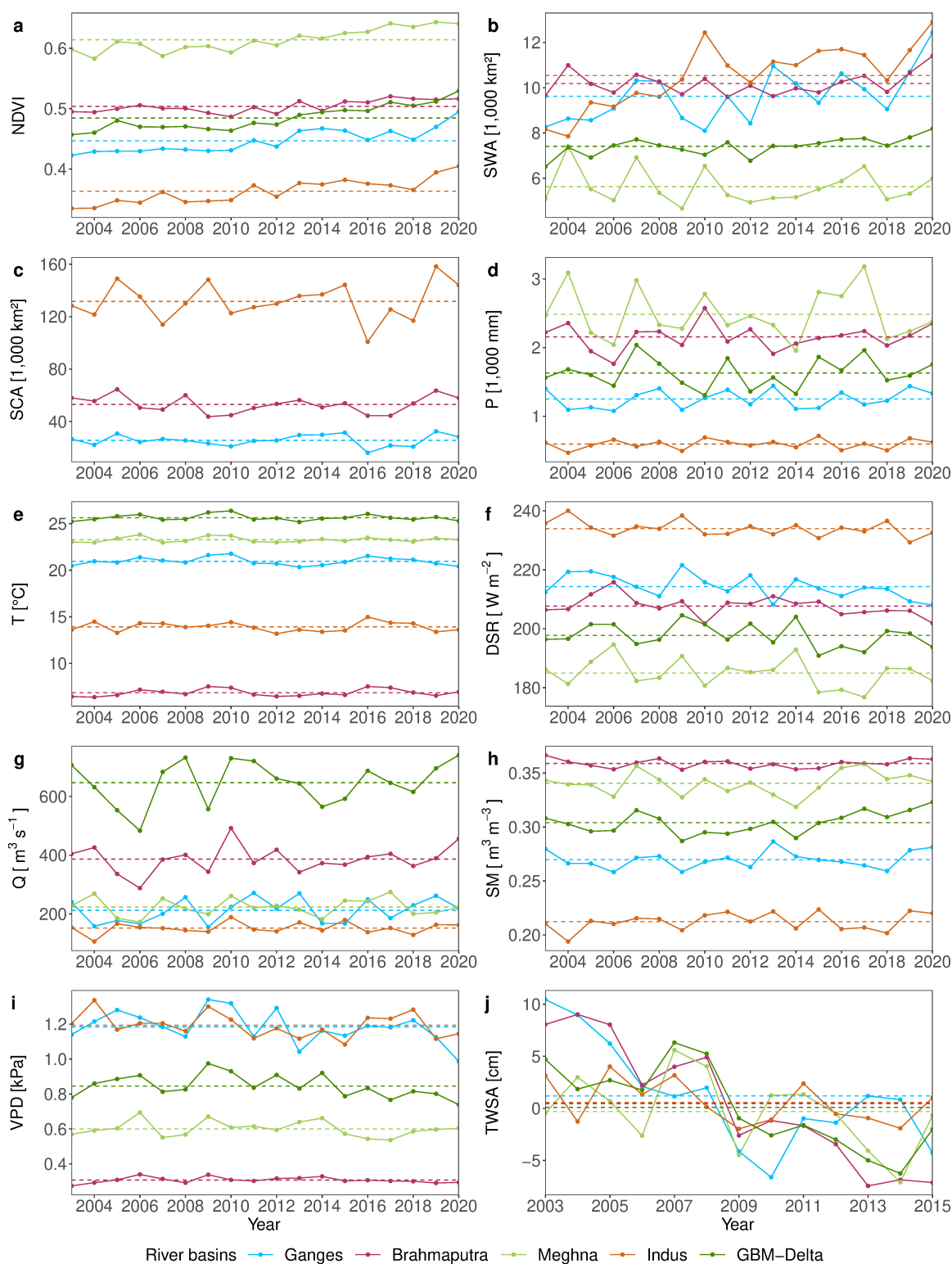


Figure 6.2: Time series variables for the river basins at annual temporal scale for the years between 2003 and 2020. Note that (j) terrestrial water storage anomaly (TWSA) only covers the years 2003–2015. The dashed line represents the respective average value of the time series. Abbreviations: (a) Normalized difference vegetation index (NDVI), (b) surface water area (SWA), (c) snow cover area (SCA), (d) precipitation (P), (e) temperature (T), (f) downward shortwave radiation (DSR), (g) river discharge (Q), (h) soil moisture (SM), (i) vapor pressure deficit (VPD). Modified after Ureyen et al. (2022b)

Table 6.1: Seasonal and annual trends at river basin scale for the period covering December 2002 and November 2020. Investigated time series include the normalized difference vegetation index (NDVI), surface water area (SWA), snow cover area (SCA), precipitation (P), terrestrial water storage anomaly (TWSA), temperature (T), surface solar radiation downward (DSR), river discharge (Q), soil moisture (SM), and vapor pressure deficit (VPD). All trend values are calculated at decadal scale and the trend values of SWA and SCA were divided by 1,000 km². Bold values denote statistically significant trends at a confidence level of 95 %. Source: Ureyen et al. (2022b)

Basin	Season	NDVI	SWA [1,000 km ²]	SCA [1,000 km ²]	P [mm]	TWSA [cm]	T [°C]	DSR [W m ⁻²]	Q [mm ⁻³ s ⁻¹]	SM [m ³ m ⁻³]	VPD [kPa]
Indus	DJF	0.048	-0.973	-0.679	-2.321	-4.181	-0.332	2.598	-0.586	-0.001	0.000
	MAM	0.040	1.041	0.848	3.934	3.292	-0.425	-7.101	13.909	0.009	-0.152
	JJAS	0.041	1.878	-2.997	-0.017	-2.530	0.293	-2.072	6.224	0.000	0.014
	ON	0.016	0.633	6.820	1.724	2.233	0.051	-3.914	-0.551	0.005	-0.043
	Annual	0.040	0.837	0.079	0.853	-0.149	-0.141	-2.993	2.836	0.002	-0.021
Ganges	DJF	0.055	0.324	2.223	2.608	-6.804	-0.333	-3.270	2.439	0.003	-0.058
	MAM	0.039	0.906	4.523	3.370	-1.532	-0.469	-5.761	3.009	0.005	-0.143
	JJAS	0.028	0.439	-2.080	7.235	-5.903	0.241	-6.524	48.436	0.002	-0.032
	ON	0.007	1.002	-3.435	-1.082	-4.684	0.443	-3.113	-0.626	-0.005	-0.006
	Annual	0.034	0.677	0.076	2.989	-5.293	-0.046	-4.516	2.724	0.002	-0.045
Brahmaputra	DJF	0.015	-0.065	-1.725	0.971	-7.467	0.027	-1.016	0.614	-0.003	-0.002
	MAM	0.021	-0.092	5.381	-2.030	-11.501	-0.272	-1.614	-12.928	0.001	-0.013
	JJAS	0.008	0.622	-1.633	11.523	-12.173	0.375	-9.165	45.747	0.003	-0.003
	ON	0.014	0.270	-7.301	1.009	-11.025	0.748	0.293	11.032	-0.002	0.012
	Annual	0.014	0.103	-1.676	0.990	-11.263	-0.046	-1.315	5.823	0.000	-0.003
Meghna	DJF	0.025	0.513	-	1.196	-1.115	-0.149	-4.776	1.247	0.003	-0.053
	MAM	0.043	0.289	-	4.839	-3.497	-0.231	-3.110	4.918	0.007	-0.024
	JJAS	0.027	-0.603	-	-6.022	-3.036	0.353	-2.507	0.577	-0.003	0.024
	ON	0.015	-0.132	-	1.332	-3.375	0.154	-3.930	2.559	0.006	-0.019
	Annual	0.026	0.078	-	1.264	-3.206	0.003	-3.520	1.903	0.005	-0.022
GBM-Delta	DJF	0.034	0.389	-	1.110	-4.959	-0.125	-8.465	3.023	0.004	-0.068
	MAM	0.050	-0.045	-	8.919	-6.338	-0.529	-7.694	0.720	0.012	-0.096
	JJAS	0.035	0.321	-	-0.342	-6.692	0.368	5.019	61.325	-0.003	0.031
	ON	0.019	0.359	-	1.298	-4.622	0.201	-2.389	14.483	0.004	-0.012
	Annual	0.034	0.340	-	1.204	-5.648	0.038	-5.041	8.753	0.004	-0.040

striking that all the reported statistically significant trend values, were positive at seasonal and annual temporal scale. The obtained magnitude of the significant trends was highest in the winter season for the Indus and Ganges river basin and in the pre-monsoon season for the Brahmaputra, Meghna, and GBM-Delta. Non-significant trends were only derived for the post-monsoon season in the Indus and Ganges river basin as well as for the GBM-Delta.

Surface water area also exhibited positive directions for all statistically significant trends. Negative tendencies (non-significant trends) can be observed for a number of seasons in the Brahmaputra, Meghna, and Indus river basin. The highest magnitude for surface water area was obtained for the Indus river basin with 1,878 km² decade⁻¹ in the monsoon season. At annual scale, the magnitude of the significant trend in the Indus river basin amounts to 837 km² decade⁻¹. In this regard, Table 6.2 shows the long-term average of surface water area in the respective river basins. For example, in the Indus river basin the long-term average in surface water area was 11,707 ±2,436 km² in the monsoon season and 10,535

Table 6.2: Long-term average of normalized difference vegetation index (NDVI), surface water area (SWA), and snow cover area (SCA) for the period between December 2002 and November 2020 at seasonal and annual temporal scale. SD: Standard deviation. Source: Ureyen et al. (2022b)

Basin	Season	NDVI		SWA [km ²]		SCA [km ²]	
		Mean	SD	Mean	SD	Mean	SD
Indus	DJF	0.387	±0.031	9,054	±1,230	215,979	±42,589
	MAM	0.331	±0.031	9,682	±1,315	184,597	±26,727
	JJAS	0.376	±0.030	11,707	±2,436	48,228	±13,719
	ON	0.349	±0.029	11,692	±1,891	91,841	±33,889
	Annual	0.363	±0.030	10,535	±1,763	131,527	±27,550
Ganges	DJF	0.487	±0.035	8,576	±1,058	37,095	±12,941
	MAM	0.347	±0.036	7,419	±1,242	37,957	±10,285
	JJAS	0.472	±0.032	10,000	±2,195	10,419	±2,760
	ON	0.482	±0.026	13,732	±1,884	20,342	±7,865
	Annual	0.446	±0.033	9,620	±1,621	25,626	±8,037
Brahmaputra	DJF	0.469	±0.021	8,450	±644	69,897	±23,889
	MAM	0.453	±0.022	8,422	±479	83,910	±15,798
	JJAS	0.540	±0.022	11,922	±1,313	22,620	±6,212
	ON	0.560	±0.024	11,964	±1,130	42,398	±18,407
	Annual	0.504	±0.022	10,186	±907	53,058	±15,060
Meghna	DJF	0.564	±0.029	3,958	±874	–	–
	MAM	0.587	±0.033	2,124	±1,204	–	–
	JJAS	0.628	±0.026	8,419	±1,657	–	–
	ON	0.701	±0.030	7,788	±1,416	–	–
	Annual	0.614	±0.029	5,625	±1,308	–	–
GBM-Delta	DJF	0.429	±0.025	7,791	±623	–	–
	MAM	0.449	±0.036	6,950	±342	–	–
	JJAS	0.507	±0.028	7,147	±670	–	–
	ON	0.576	±0.037	8,017	±744	–	–
	Annual	0.484	±0.031	7,404	±588	–	–

±1,763 km² at annual scale. On the contrary, despite one value, the resulting statistically significant trends have a negative direction in case of the TWSA. At annual scale, significant trends of TWSA point towards a declining groundwater level for all of the investigated river basins (see Table 6.1).

Regarding snow cover area, no statistically significant trend could be derived for any river basin at annual scale. Only the monsoon and post-monsoon season show a significant negative trend for the Ganges (−2,080 km² decade^{−1}) and Brahmaputra river basin (−7,301 km² decade^{−1}), respectively. In this context, Table 6.2 demonstrated that the long-term average of snow cover area was 10,419 ±2,760 km² in the monsoon season in the Ganges river basin and 42,398 ±18,407 km² in the post-monsoon season in the Brahmaputra river basin. Largest seasonal snow cover was found for the Indus river basin with 215,979 ±42,589 km² in the winter season (see Table 6.2). Overall, the climatic variables barely show any statistically significant trend.

To investigate changes in the direction and magnitude of the trends within the investigated period, additional analyses were conducted for the vegetation condition, surface water area, and snow cover area for two partially overlapping 11-year sub-periods. The results are

Table 6.3: Seasonal and annual trends at river basin scale for the period covering December 2002 and November 2020 denoted at decadal scale. The covered period is split into two periods. Bold values represent significant trends at a confidence level of 95 %. Source: Ureyen et al. (2022b)

Basin	Season	NDVI	2002–2012		2010–2020		
			SWA [1,000 km ²]	SCA [1,000 km ²]	NDVI	SWA [1,000 km ²]	SCA [1,000 km ²]
Indus	DJF	0.018	-0.534	0.505	0.063	-0.057	5.795
	MAM	0.020	-1.028	-9.571	0.030	2.099	-0.729
	JJAS	0.036	4.042	5.585	0.042	1.837	-6.022
	ON	0.038	1.176	-9.478	-0.016	-0.487	19.571
	Annual	0.028	0.321	-4.487	0.036	0.890	2.533
Ganges	DJF	0.044	0.336	-4.261	0.050	1.196	2.724
	MAM	0.010	0.775	-3.762	0.041	0.219	4.877
	JJAS	0.027	-0.208	-0.281	0.033	0.540	-3.740
	ON	0.007	-0.190	-6.459	0.004	1.217	2.073
	Annual	0.019	0.073	-4.011	0.037	0.868	2.398
Brahmaputra	DJF	-0.022	1.025	-20.472	0.040	-0.166	9.711
	MAM	-0.016	-0.282	-3.943	0.050	0.081	13.852
	JJAS	0.007	-0.452	2.385	-0.002	2.192	-5.192
	ON	0.016	-0.805	-11.212	0.003	1.356	-2.409
	Annual	-0.004	-0.367	-7.578	0.022	0.719	3.651
Meghna	DJF	-0.019	1.477	-	0.075	-0.295	-
	MAM	-0.002	-0.122	-	0.082	0.367	-
	JJAS	0.037	-0.761	-	0.002	0.640	-
	ON	0.021	-0.789	-	0.001	0.893	-
	Annual	0.010	-0.442	-	0.038	0.504	-
GBM-Delta	DJF	0.009	0.403	-	0.048	0.585	-
	MAM	0.001	-0.084	-	0.089	-0.106	-
	JJAS	0.027	0.156	-	0.036	0.606	-
	ON	0.011	-0.419	-	0.037	0.669	-
	Annual	0.010	0.036	-	0.043	0.595	-

listed in Table 6.3. In case of the NDVI, significant trends with a higher magnitude were obtained for the second sub-period between 2010–2020. In fact, for the winter season in the Brahmaputra and Meghna river basins, the results indicated even significant negative trends during the first sub-period. These turned positive during the second sub-period. On the other hand, surface water area revealed significant negative trends for the Meghna river basin at several temporal seasons during the first sub-period, whereas during the second sub-period the direction changed to positive trends. Considering snow cover area, the derived trends and tendencies at annual scale were all negative during the first sub-period. During the second sub-period they turned into positive tendencies at annual scale.

6.3.1.2 Trends at Grid Scale

Furthermore, Figure 6.3, Figure 6.4, and Figure 6.5 show the seasonal and annual trends of the land surface variables NDVI, surface water area, and snow cover area at grid scale, respectively. Trends obtained for the NDVI were significantly positive in the winter and pre-monsoon season for 68.4 % and 65.0 % of the grids, respectively (see Figure 6.3a,b). The magnitude of the significant positive trends was particularly high in the central Indus

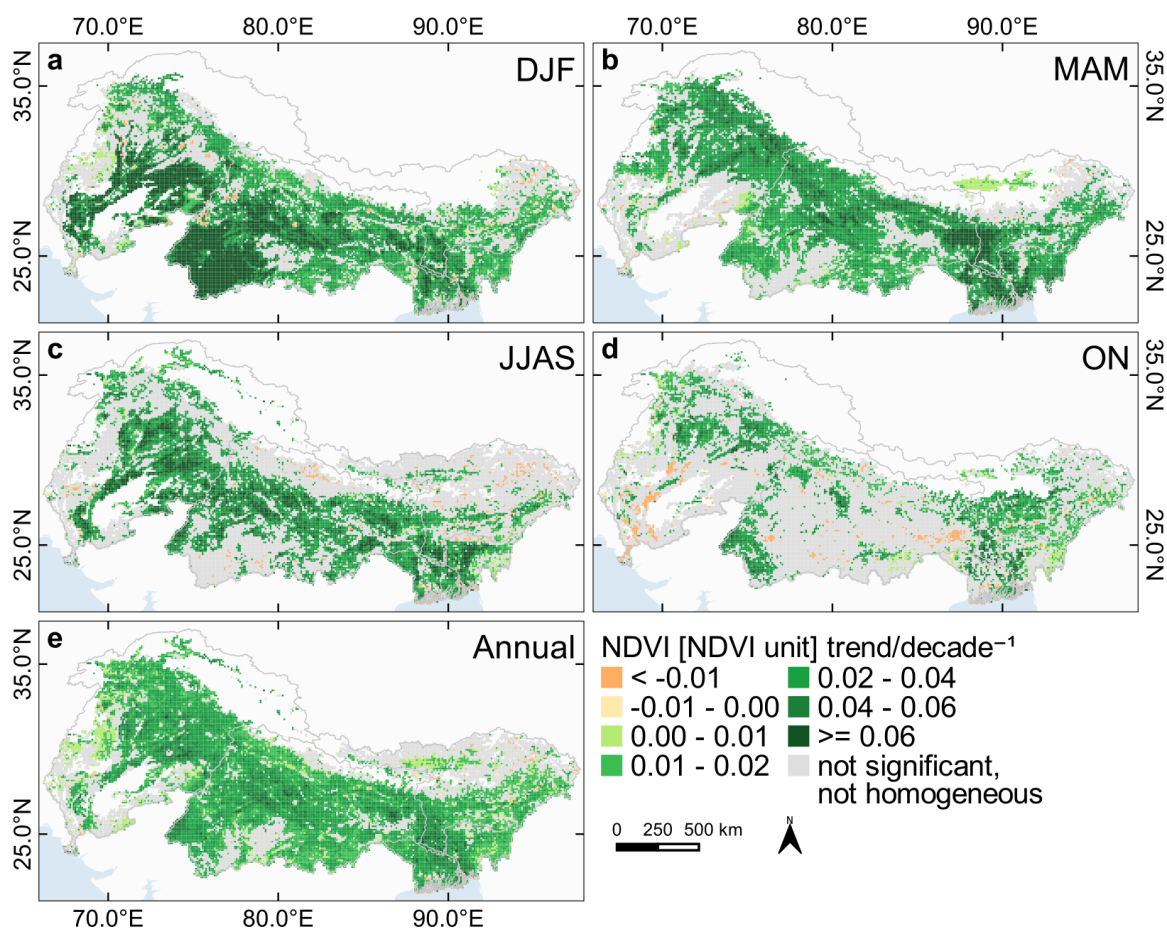


Figure 6.3: Magnitude of the significant trends (at a confidence level of 95 %) derived with the seasonal Mann-Kendall (MK) test in association with the Theil-Sen (TS) slope estimator for the normalized difference vegetation index (NDVI) at seasonal and annual temporal scale. The magnitude of the trend values is denoted at decadal scale and is representative for the period between December 2002 and November 2020. Trends are visualized for the seasons (a) winter, (b) pre-monsoon, (c) monsoon, and (d) post-monsoon. (e) Trends at annual scale are only colored if they are significant and homogeneous over the seasons. Modified after Ureyen et al. (2022b).

and southwest of the Ganges river basin (see Figure 6.3a) as well as in the north of the Bay of Bengal and east of the Ganges river basin (see Figure 6.3b). In the monsoon season, the number of non-significant trends was remarkably higher with 50.7 % of the grids, but highest in the post-monsoon season with 67.5 % of the grids (see Figure 6.3c,d). The post-monsoon season additionally featured the highest share of significant negative trends for the NDVI with 2.8 % of the grids.

Next, seasonal trends for surface water area were mostly significantly positive (see Figure 6.4). For example, 40.5 % of the grids indicated significant positive trends and 7.0 % negative trends in the pre-monsoons season (see Figure 6.4b). The percentages of significant positive trends were also high in the monsoon and post-monsoon season with 43.8 % and 40.7 %, respectively (see Figure 6.4c,d). Significant negative trends mostly occurred

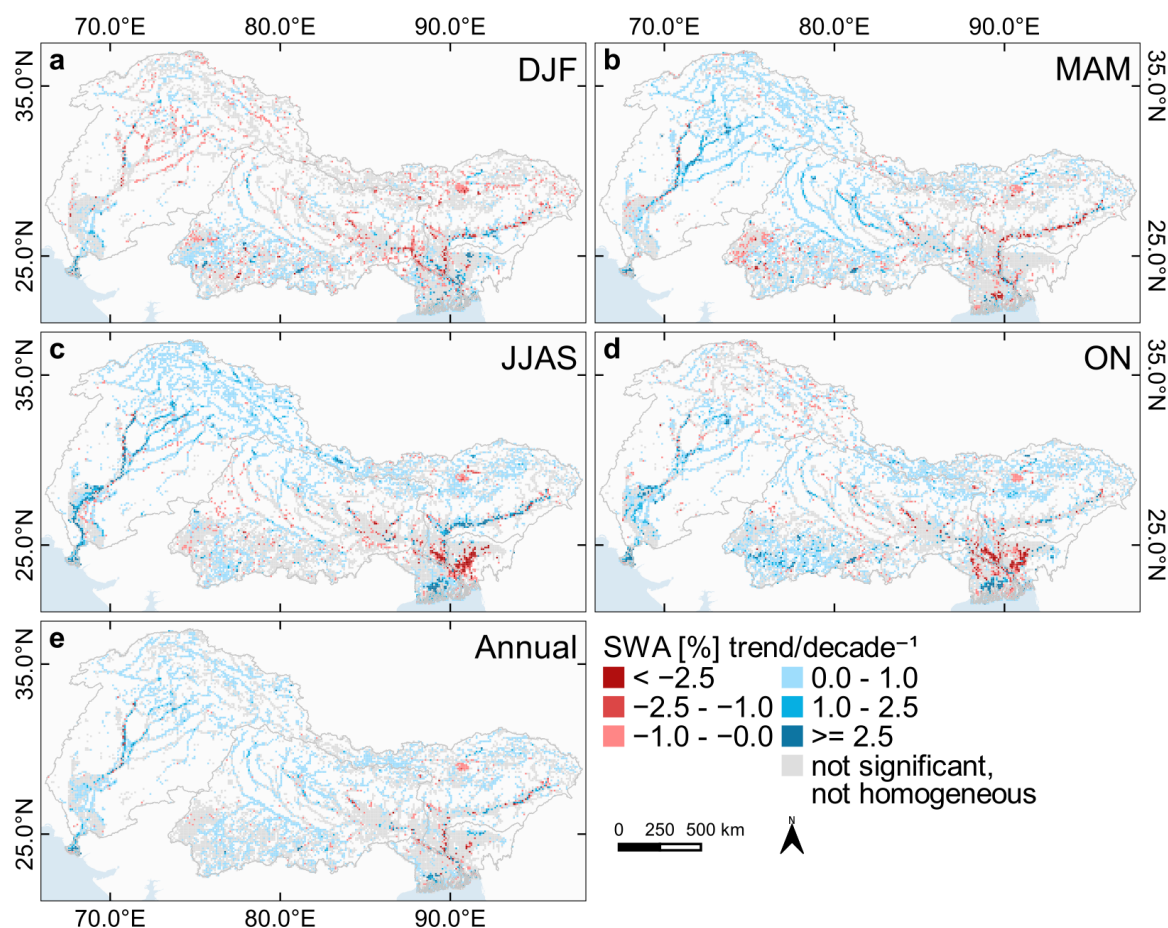


Figure 6.4: Same as Figure 6.3, but for surface water area (SWA). Modified after Uereyen et al. (2022b).

in the winter season with a share of 11.1 % of the grids (see Figure 6.4a). In this regard, negative trends were prevalent in the downstream area of the Himalaya, particularly along the Brahmaputra river (see Figure 6.4a,b), in the wetlands south of the Shillong Plateau in the Meghna river basin (see Figure 6.4c,d), and in the confluence region of the Ganges and Brahmaputra rivers (see Figure 6.4c,d). In comparison, dominant clusters with significant positive trends were striking in the GBM-Delta region (see Figure 6.4c,d) and along the Indus river in the downstream area (see Figure 6.4b,c,d). The seasonal trend analysis of snow cover area indicated mostly stable observations in case of the upper Indus river basin (see Figure 6.5). In the pre-monsoon season, significant positive trends were obtained regionally for the upper Ganges and Brahmaputra river basin (see Figure 6.5b). On the contrary, in the winter, monsoon, and post-monsoon season significant negative trends were dominant in the upper Ganges and Brahmaputra river basin (see Figure 6.5a,c,d).

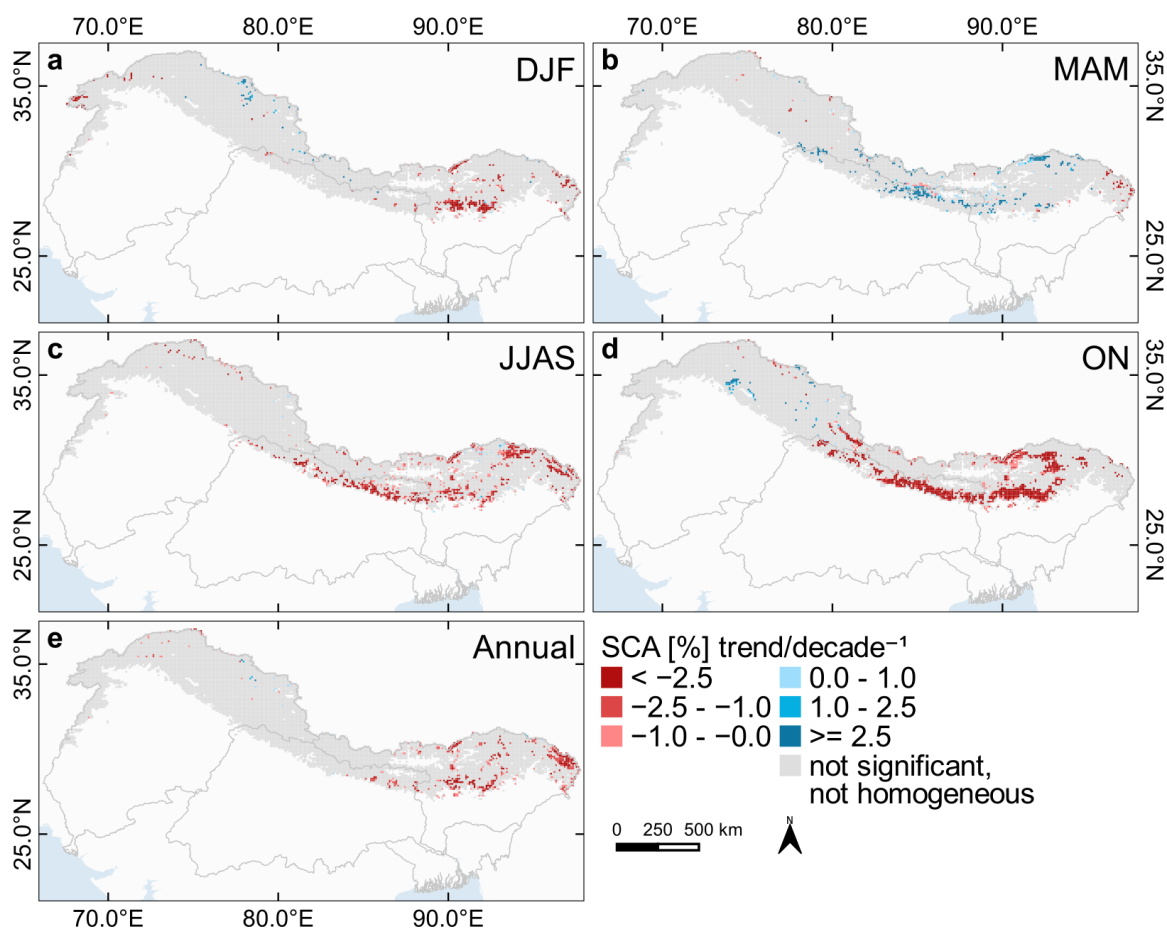


Figure 6.5: Same as Figure 6.3, but for snow cover area (SCA). Modified after Uereyen et al. (2022b).

6.3.1.3 Elevation-Dependent Trends

To analyze patterns in trends in dependence on elevation between December 2002 and November 2020, the NDVI and snow cover area time series were intersected with elevation zones and differentiated by the respective river basin (see Figure 6.6). Considering significant trends in NDVI, these were mostly positive as already outlined in the previous results. In addition, Figure 6.6a revealed that significant positive trends were particularly present at very low altitudes throughout all river basins and temporal scales. It was also striking, that during the monsoon season a significant negative trend was present in the Ganges river basins between 3,000 and 3,500 m. Also, the Indus river basin exhibited the highest magnitude in significant positive trends during the monsoon season (see Figure 6.6a).

Results for surface water area showed significant positive trends at low altitudes (see Figure 6.6b). Additional significant positive trends with comparatively low magnitudes were also present at higher altitudes during the monsoon and post-monsoon season. Regarding snow cover area, the obtained results were largely non-significant. However, available significant trends were mostly present at high altitudes. As already visualized in Figure 6.5,

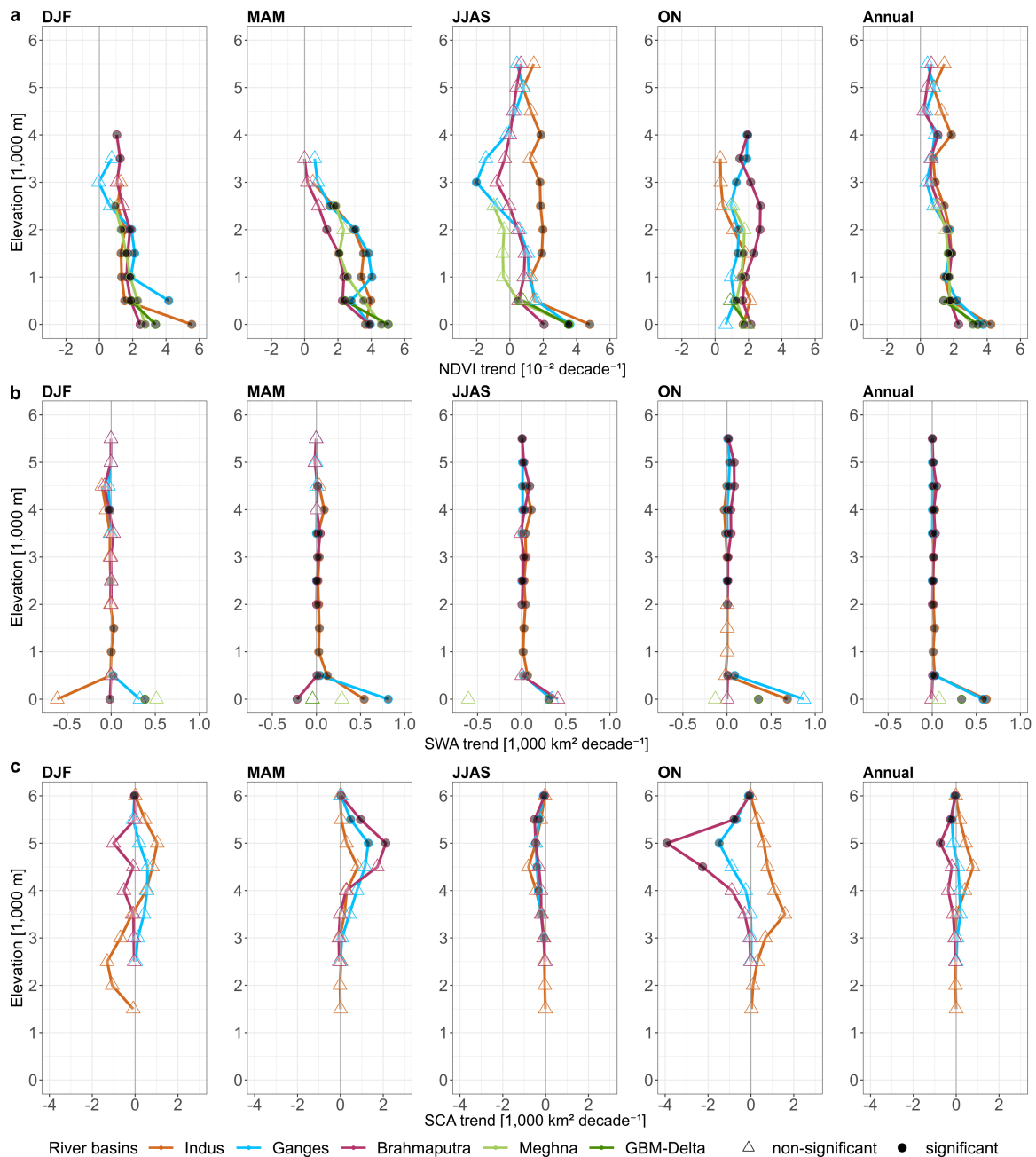


Figure 6.6: Seasonal and annual trends of the (a) normalized difference vegetation index (NDVI), (b) surface water area (SWA), and (c) snow cover area (SCA) in dependence of elevation zones, which are classified in 500 m intervals and differentiated by the respective river basin. The first class covers altitudes between 0 and 500 meters. The last class covers altitudes higher than 6,000 meters and only includes trends for SCA. Note that the NDVI trend values were multiplied with 100 and in case of SCA and SWA divided by 1,000. Modified after Ureyen et al. (2022b).

significant negative trends were pronounced during the post-monsoon season. This is also reflected in Figure 6.6c, where the snow cover area appears to be characterized by significant declines at altitudes above 4,500 m. On the other hand, trends during the pre-monsoon

season in snow cover area, pointed towards significant increases in the Ganges and Brahmaputra river basin above 5,000 m.

6.3.2 Analysis of Driving Variables

In comparison to the results in Chapter 5.3.3, the analyses of driving variables on NDVI, surface water area, and snow cover area were conducted at grid and seasonal scale (Chapter 6.3.2.1). Additionally, causal graphs were computed to evaluate indirect influences on the three land surface variables, but also the interdependencies among all time series variables (Chapter 6.3.2.2). Finally, human influences on vegetation condition and surface water area were analyzed (Chapter 6.3.2.3).

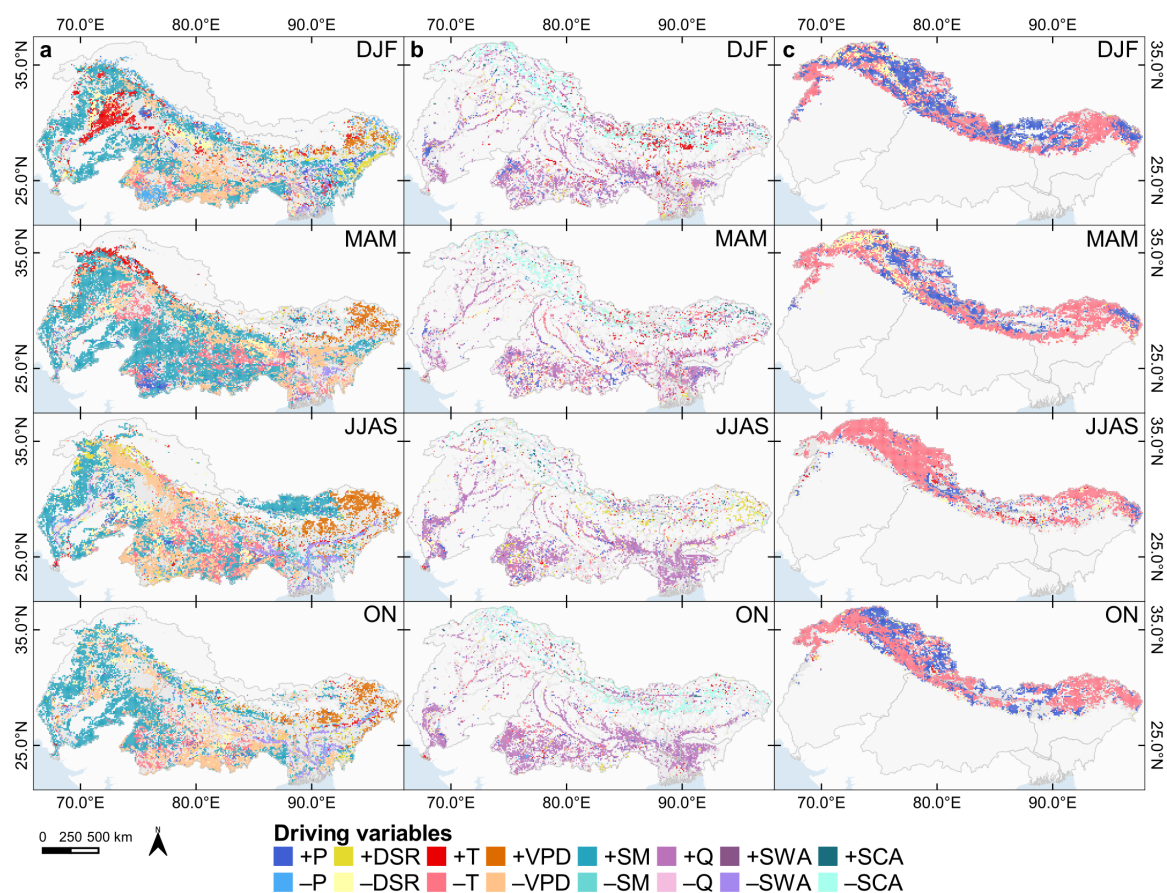


Figure 6.7: The spatial distribution of the dominant driving variables for the (a) normalized difference vegetation index (NDVI), (b) surface water area (SWA), and (c) snow cover area (SCA) at seasonal scale. The driving variables include precipitation (P), surface solar radiation downward (DSR), temperature (T), vapor pressure deficit (VPD), soil moisture (SM), river discharge (Q), SWA, and SCA. Gray colored grids have no significant causal link. The respective feature spaces include (a) NDVI: P, DSR, T, VPD, SM, SWA; (b) SWA: P, DSR, T, Q, SCA; (c) SCA: P, DSR, T. Modified after Uereyen et al. (2022b).

6.3.2.1 Direct Controls on Land Surface Variables at Grid Scale

Figure 6.7 illustrates the driving variables having the largest influence on the three land surface variables NDVI, surface water area, and snow cover area at grid and seasonal scale. The effect size of the causal links is denoted as the MCI cross-dependence value. As stated before, the partial correlation coefficient was used during the MCI step of PCMCI (see Chapter 5.2.3.3). Considering the controls on vegetation condition, soil moisture was found to have the largest influence throughout all seasons (see Figure 6.7a). This positive coupling between vegetation condition and soil moisture was most pronounced in the pre-monsoon season accounting for 34 % of all grids. The identified temporal lag for this coupling occurred largely at lag 1 and 2 (see Figure 6.8a). Over the seasons, the influence of further driving variables varied regionally. For example, in the winter season, vegetation condition was found to be positively coupled with temperature in the northern Indus plain (see Figure 6.7a) at a temporal lag of 1 (see Figure 6.8a). In areas of the Indus river basin, where grassland and sparse vegetation was the dominant land cover, soil moisture was the prevalent driver. A negative coupling between the NDVI and surface water area was most

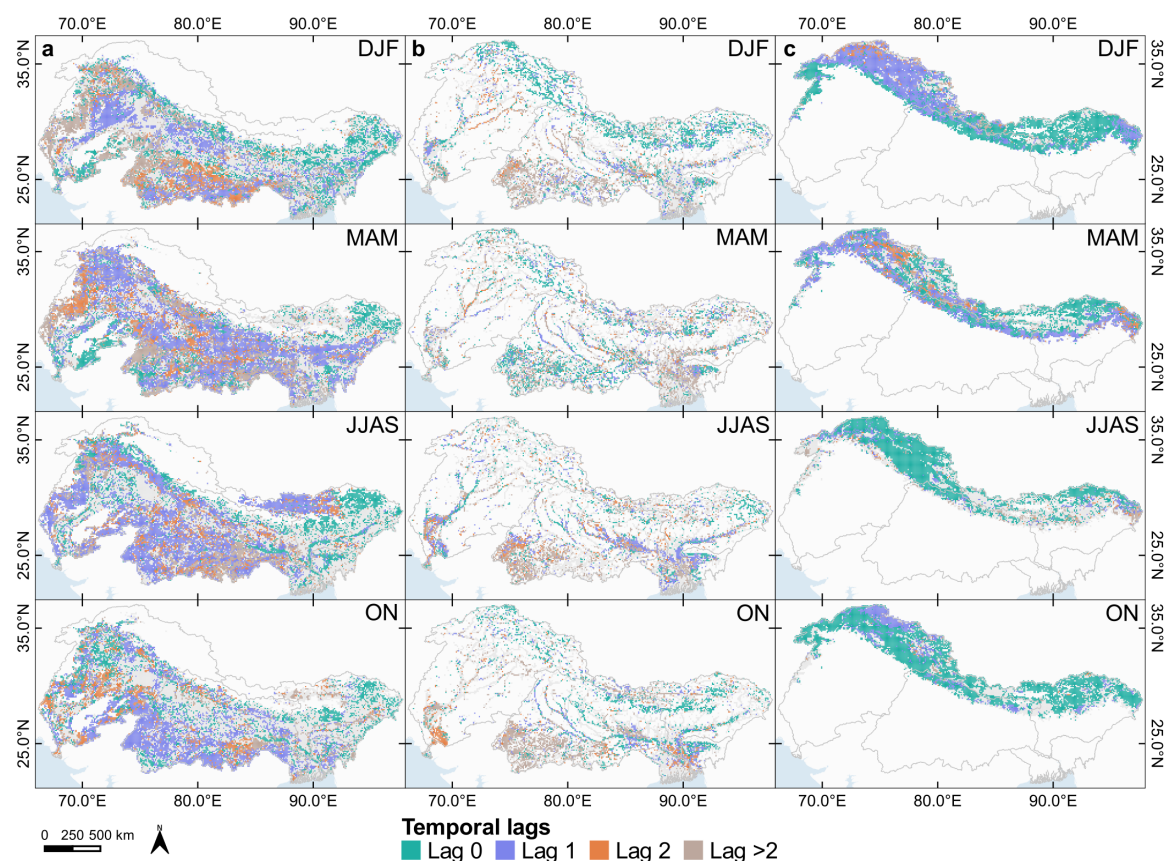


Figure 6.8: The temporal lags of the identified causal links between the target and the respective dominant driving variable at seasonal scale in Figure 6.7. The considered maximum temporal lag was 6 time steps, corresponding to 3 months. One lag corresponds to a biweekly timestep. Modified after Uereyen et al. (2022b).

notably present during the monsoon and post-monsoon season, particularly in the downstream areas close to the outlets as well as the confluences of the Ganges and Brahmaputra (see Figure 6.7a). This coupling was found to be instantaneous (see Figure 6.8a). Moreover, vapor pressure deficit appeared to be strongly linked positively with vegetation condition in the northeast of the Brahmaputra river basin in the pre-monsoon and monsoon season as well as negatively in parts of the Indo-Gangetic Plain in the winter and monsoon season. Here, the negative coupling occurred mostly at lags 1 and 2, whereas the positive links were contemporaneous (see Figure 6.8a). Moreover, vegetation availability is temporally limited by temperature at high altitudes of the Brahmaputra river basin. In the monsoon season, vegetation in the upper Brahmaputra river basin was found to be largely influenced by water availability through soil moisture at lag 1. Also, it was not possible to identify a causal link for a part of the grids. These grids were mostly located in the Indo-Gangetic Plain.

Surface water area was found to be largely controlled positively by river discharge throughout all seasons (see Figure 6.7b). This link mostly occurred at lag 0 and 1, while lag 0 was prevalent. Only in the monsoon season, links occurring at lag 1 were dominant. A negative coupling was detected between surface water area and snow cover area at high altitudes. This link was present during the winter, pre-monsoon, and post-monsoon season at lag 0. Precipitation only had the highest influence on surface water area for a small fraction of the grids.

On the other hand, driving variables having the largest influence on snow cover area are visualized in Figure 6.7c. Temperature was found to be negatively influencing snow cover area for large parts of the upper river basins. This link was most pronounced during the monsoon season. It is also noticeable that snow cover area and temperature were mostly contemporaneously linked. A positive coupling between snow cover area and precipitation was found to be eminent, particularly during the winter season and regionally in the pre-monsoon and post-monsoon season as well. During winter, this link was prevailing in the upper Indus river basin and in part also in the Ganges and Brahmaputra river basin. This coupling was found to be dominant at a lag of 1 (see Figure 6.8c).

6.3.2.2 Interdependencies Among Time Series Variables at Basin Scale

Apart from the quantification of the driving variable having the largest influence on one of the target variable NDVI, surface water area, and snow cover area, PCMCI computes causal graphs enabling the analysis of interdependencies among all included time series variables. A causal graph is represented by nodes which are describing the respective time series and its autocorrelation as well as edges demonstrating the presence of causal links, their direction, and their strength (see Chapter 5.2.3.3 and Chapter 6.2.2.2). In this regard,

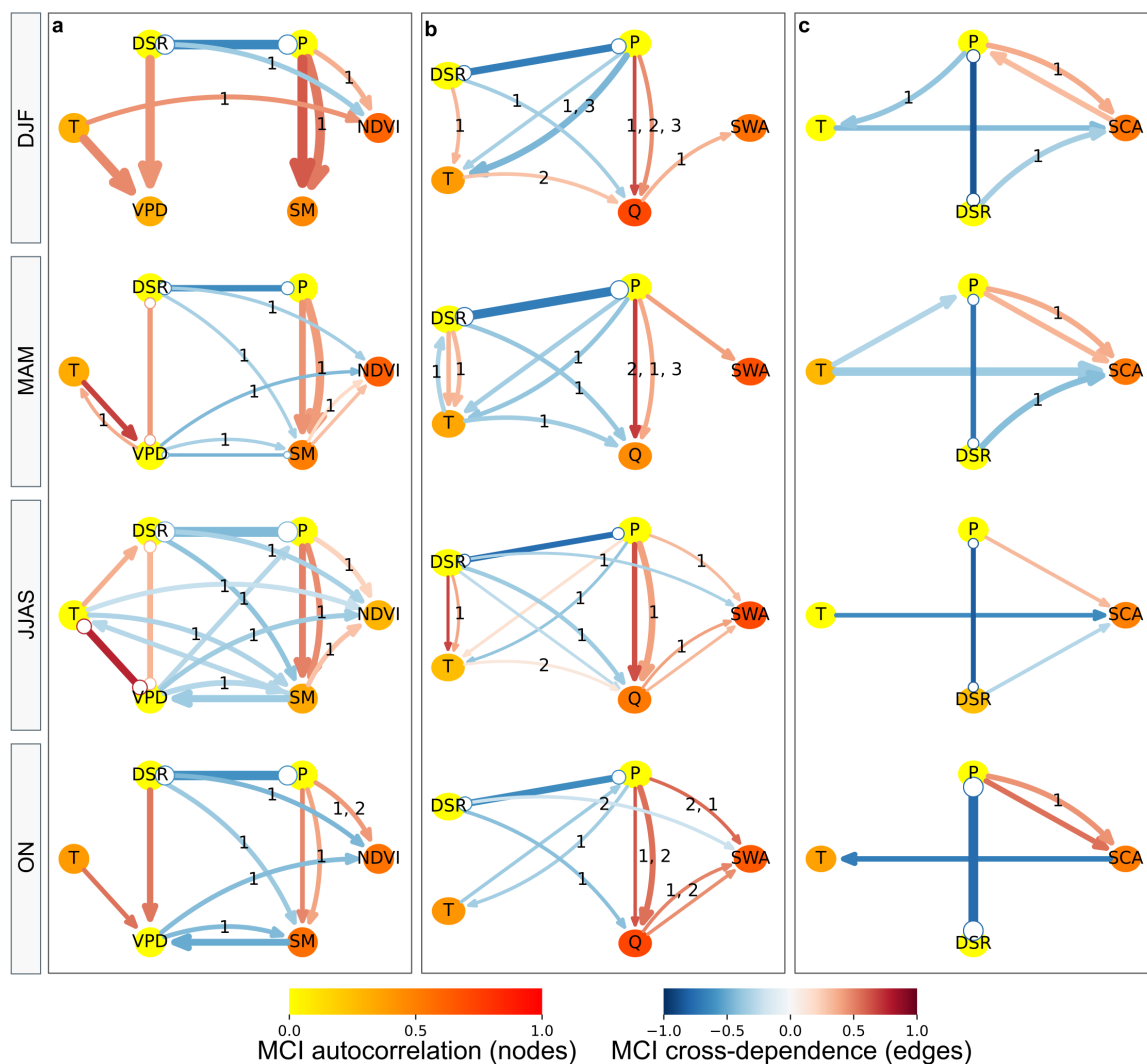


Figure 6.9: Causal graphs visualizing the interactions between the geoscientific time series, including the (a) normalized difference vegetation index (NDVI), (b) surface water area (SWA), and (c) snow cover area (SCA). The graphs are calculated for each subbasin and then aggregated for the IGBM river basins at seasonal scale. At this, a maximum temporal lag of 3 time steps was used. Thin edges express low occurrence of the link at basin scale and vice versa. Straight edges denote contemporaneous and curved edges lagged links. The temporal lag is indicated by the number on the curved edges. Links where the direction could not be resolved are indicated by circle ends. Following variables were considered: precipitation (P), soil moisture (SM), temperature (T), surface solar radiation downward (DSR), vapor pressure deficit (VPD), river discharge (Q), NDVI, SWA, and SCA. Source: Ureyen et al. (2022b).

Figure 6.9 illustrates the derived causal process graphs for three feature spaces involving one of the remote sensing-based land surface variable at seasonal temporal scale. These graphs were processed by means of biweekly time series variables for both, each season and one of the 117 subbasins separately (see Figure 4.1d). Next, all resulting causal graphs (up to 117 per season and feature space) were aggregated into one graph per season and feature space. Considering the causal process graphs in Figure 6.9, the frequency of the

occurrence of a causal link between two variables is represented by the width of the edges. In detail, it can be seen that the identified causal links point towards changing relationships over the seasons. For example, the causal graphs in Figure 6.9a include the NDVI and it is noticeable that the positive relation between precipitation and soil moisture prevailed over all seasons at a lag of 0 and 1. As depicted in the causal maps in Figure 6.7, the positive coupling between NDVI and soil moisture was prevalent. Using the causal graph, it can be concluded that the causal link between NDVI and soil moisture in the pre-monsoon and monsoon season was indirectly controlled by precipitation. But, NDVI was directly positively influenced by precipitation in almost all seasons with a temporal lag of 1 as well. Also, it was found that vapor pressure deficit is negatively influencing NDVI directly and via an indirect path over soil moisture during the pre-monsoon and monsoon season. Radiation appears to control vegetation condition negatively through a direct and multiple indirect paths, e.g. via soil moisture in the monsoon season. The adverse coupling between radiation and precipitation was also dominant in almost all causal graphs. Furthermore, temperature was directly controlling NDVI positively in the winter season, whereas this relation was found to turn negative during the other seasons through indirect pathways. A negative influence of soil moisture on temperature was also identified in the monsoon season (Figure 6.9a).

Moreover, the causal graph in Figure 6.9b involves surface water area. The causal maps in Figure 6.7b emphasized the largely existing positive coupling between surface water area and river discharge. In comparison, the causal graphs at seasonal scale, indicated that precipitation controls surface water area directly in the pre-monsoon, monsoon, and post-monsoon season. In the winter season, it was found that precipitation indirectly controls surface water through river discharge. This indirect path was also found in the monsoon and post-monsoon seasons at a temporal lag of 0 and 1. A direct negative control of radiation on surface water area could be detected during the monsoon and post-monsoon season at a temporal lag of 1 and 2, respectively. This negative coupling was also found via an indirect path through river discharge with a temporal lag of 1.

Considering the environmental controls on snow cover area in Figure 6.9c, it was found that many connections appear to be occurring contemporaneously. The previously identified negative control of temperature on snow cover area was also persistent in the causal graphs. Here, it has to be noted that during the post-monsoon season, the direction of influence changed from snow cover area towards temperature. In accordance with the causal maps in Figure 6.7, a positive coupling between snow cover area and precipitation could be identified in the causal graphs as well. This positive connection was found in every season.

Moreover, radiation was negatively coupled to snow cover area in most of the seasons and in the winter season, precipitation was found to influence temperature negatively.

6.3.2.3 Analysis of Anthropogenic Influences

A further detailed analysis of NDVI trends stratified by land cover and land use data was conducted and the results are listed in Table 6.4. This table includes seasonal and annual trends being differentiated by the classes rainfed cropland, irrigated cropland, forest, and grassland. The left panel covers trend values for the entire study period, whereas the right panel includes the difference between the trends of the second and first period. The obtained significant trends covering the entire study period at annual scale indicated that the magnitude was highest for irrigated croplands. In terms of seasonal trends, the magnitude of significant trends for irrigated croplands is comparatively high as well. Significant trends of rainfed croplands also resulted in relatively high magnitudes. At seasonal scale, the trend values for rainfed and irrigated croplands were particularly pronounced in the winter, pre-monsoon, and monsoon season. Considering the difference between the two periods on the

Table 6.4: Annual and seasonal trends of normalized difference vegetation index (NDVI) stratified by vegetation classes for the period between December 2002 and November 2020. The right panel includes the difference of trend values between the second (2010–2020) and first (2002–2012) period. All trend values are computed at decadal scale. Bold values represent statistically significant trends at a confidence level of 95 %. Bold values on the right panel denote significant trends in both periods. Basins: Indus (I), Ganges (G), Brahmaputra (B), Meghna (M), GBM-Delta (GBMD). Source: Ureyen et al. (2022b).

Basin	Class	DJF	MAM	JJAS	ON	Annual	Trend 2010–2020 – Trend 2002–2012				
							DJF	MAM	JJAS	ON	Annual
I	Cropland	0.031	0.029	0.030	0.010	0.029	⁽²⁾ 0.029	⁽²⁾ 0.017	–0.019	–0.017	⁽²⁾ 0.010
	Irrigation	0.051	0.038	0.046	0.019	0.042	⁽²⁾ 0.080	–0.002	0.002	–0.055	0.004
	Forest	0.025	0.036	0.017	0.013	0.021	⁽²⁾ 0.030	⁽²⁾ 0.035	⁽²⁾ 0.012	–0.038	0.017
	Grassland	0.013	0.018	0.011	0.006	0.012	⁽²⁾ 0.008	⁽²⁾ 0.010	–0.010	–0.030	–0.003
G	Cropland	0.060	0.033	0.033	0.008	0.033	–0.023	0.015	0.009	0.002	0.012
	Irrigation	0.062	0.041	0.036	0.004	0.038	0.011	0.024	0.000	0.000	0.012
	Forest	0.022	0.027	0.009	0.013	0.017	0.027	0.061	⁽²⁾ 0.009	0.001	⁽²⁾ 0.018
	Grassland	0.027	0.021	0.008	0.019	0.020	0.005	0.018	0.016	0.001	0.009
B	Cropland	0.021	0.028	0.021	0.016	0.021	0.099	⁽²⁾ 0.124	⁽¹⁾ –0.055	0.000	⁽²⁾ 0.049
	Irrigation	0.043	0.065	0.030	0.035	0.039	⁽²⁾ 0.081	⁽²⁾ 0.094	⁽¹⁾ –0.094	–0.010	0.028
	Forest	0.014	0.016	0.002	0.020	0.015	0.067	⁽²⁾ 0.064	⁽²⁾ 0.009	–0.034	⁽²⁾ 0.035
	Grassland	0.010	0.005	0.004	0.015	0.008	0.012	⁽²⁾ 0.001	0.011	0.006	0.007
M	Cropland	0.025	0.043	0.031	0.009	0.028	⁽²⁾ 0.109	⁽²⁾ 0.106	–0.028	–0.001	⁽²⁾ 0.045
	Irrigation	0.038	0.046	0.056	0.028	0.042	⁽²⁾ 0.103	⁽²⁾ 0.046	–0.053	–0.038	0.011
	Forest	0.022	0.034	0.004	0.011	0.017	0.096	⁽²⁾ 0.110	–0.016	–0.007	⁽²⁾ 0.040
	Grassland	0.017	0.014	0.001	0.019	0.015	0.055	⁽²⁾ 0.072	⁽²⁾ –0.008	–0.007	⁽²⁾ 0.034
GBMD	Cropland	0.019	0.036	0.039	0.011	0.028	⁽²⁾ 0.032	0.144	⁽²⁾ 0.032	0.029	⁽²⁾ 0.043
	Irrigation	0.043	0.061	0.037	0.026	0.040	0.028	⁽²⁾ 0.065	–0.003	⁽²⁾ 0.030	0.024
	Forest	0.023	0.024	0.006	0.016	0.019	⁽²⁾ 0.092	⁽²⁾ 0.055	⁽²⁾ 0.023	⁽²⁾ 0.025	⁽²⁾ 0.049
	Grassland	0.016	0.097	0.045	0.008	0.031	0.123	0.161	⁽²⁾ 0.067	⁽²⁾ 0.022	⁽²⁾ 0.085

⁽¹⁾ Significant trend during first period.

⁽²⁾ Significant trend during second period.

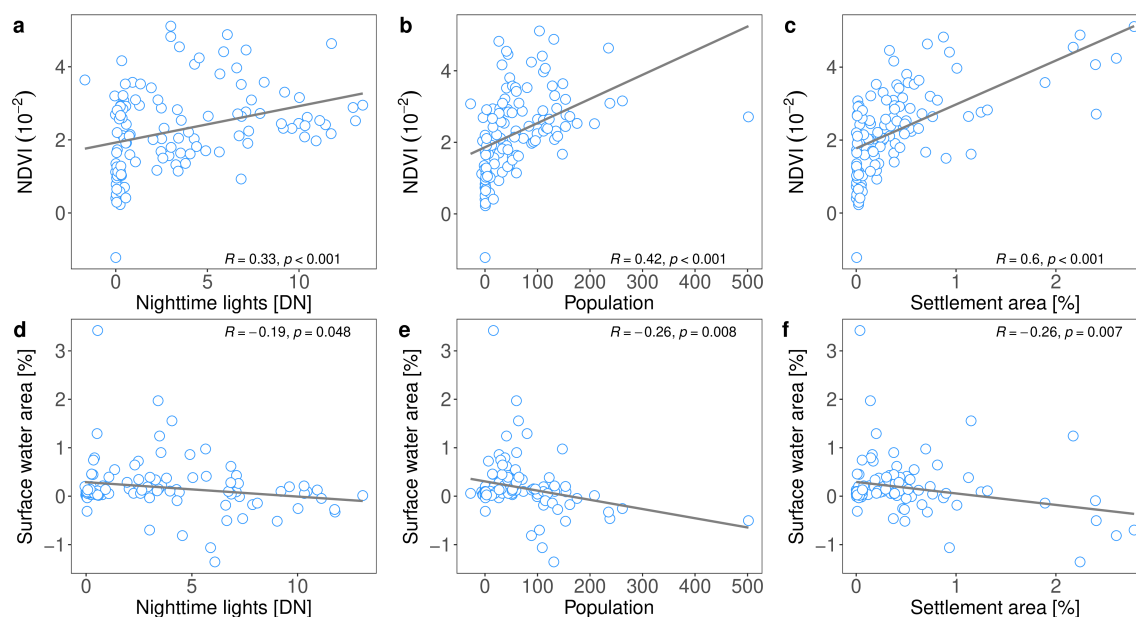


Figure 6.10: Relation between the trends of the land surface variables (a–c) normalized difference vegetation index (NDVI) and (d–f) surface water area (SWA) with trends derived from annual anthropogenic time series. First, the trends were calculated for each subbasin at annual scale and then correlated with each other. Each dot represents a subbasin. Modified after Uereyen et al. (2022b).

right panel of Table 6.4, the results indicated increasing magnitudes of the significant trends for most of the river basins and vegetation classes.

To evaluate the potential influence of anthropogenic factors on vegetation condition as well as surface water area, the computed annual trends of the respective time series were correlated at subbasins scale. The subbasins are illustrated in Figure 4.1d. In this regard, the results of the correlation analysis are illustrated in Figure 6.10. A linear positive relation could be identified between the NDVI trends and trends of nighttime lights, population counts, and relative settlement area (see Figure 6.10a,b,c). As an example, Figure 6.10c indicates that high NDVI trends in subbasins were found to be associated with relative settlement growth. On the other hand, the obtained correlation coefficients were negative for the trends in surface water area and anthropogenic variables (see Figure 6.10d,e,f). For example, the linear relations indicated that surface water area increased in subbasins with comparatively low trends in population counts and relative settlement growth (see Figure 6.10e,f).

6.4 Discussion

The presented results on seasonal trends revealed changes in the investigated land surface variables vegetation condition, surface water area, and snow cover area. For the first time, analyses on direct as well as indirect links within a multivariate feature space, in-

cluding multiple remote sensing-based land surface variables unveiled interdependencies in consideration of temporal lags for the transboundary river basins in South Asia using PCMCI. Additional trend and correlation analyses were performed to investigate anthropogenic influences on the land surface in the highly populated river basins.

6.4.1 Seasonal Trends and Drivers of Land Surface Dynamics

6.4.1.1 Vegetation Condition

The results of the monotonic trend analyses revealed significant positive trends for the NDVI being largely consistent at seasonal temporal scale and spatially at basin as well as grid scale. Comparable significant increasing trends in vegetation condition and leaf area index were reported in previous studies in parts of the investigated IGBM river basins at annual scale (e.g. Chen et al. 2019; Lamchin et al. 2018; Mishra and Mainali 2017; Sarmah et al. 2018). Here, the trend analyses provided detailed insights in the spatial distribution of seasonal trends. Additionally, seasonal trend analyses were performed for spatially stratified regions by land cover and land use classes as well as elevation zones until the end of 2020. Based on these detailed assessments, it was possible to demonstrate the significant contribution of irrigated and rainfed croplands to the increasing trends in vegetation condition (see Figure 6.3 and Table 6.4). Moreover, human influence was evaluated based on the correlation of trends in annual time series of anthropogenic indicators and trends of annually aggregated NDVI values at subbasin scale. The derived significant positive correlation was found to support the assumption that greening vegetation might be strongly controlled by human activities and land use management. Similar findings were also reported by Mishra and Mainali (2017). Also, the elevation-dependent trend analysis pointed towards increasing vegetation greening at very high altitudes as well (see Figure 6.6a). The expansion of vegetation cover in the Himalaya region at altitudes up to 6,000 meters was also investigated by Anderson et al. (2020). Likewise, the authors identified significant positive trends for green vegetation cover at high altitudes. Furthermore, the results of the additional trend analysis over the two study periods emphasized that the vegetation greening is ongoing and significantly higher in the last part of the investigated period (2010–2020) compared to the first (see Table 6.3). These increases could be favored by intensified land use and other human interventions such as irrigation or fertilization (Mishra and Mainali, 2017). This was also supported by the findings with respect to the calculated differences in NDVI trends being stratified by land cover and land use classes (see Table 6.4).

Regarding the evaluation of climatic and hydrological drivers using a causal discovery algorithm, the delineated causal maps and graphs pointed towards the importance of water

availability for vegetation condition (see Figure 6.7a and Figure 6.9a). The dominance of soil moisture and precipitation, which were largely positively coupled with vegetation condition, was particularly pronounced in the arid and semi-arid regions of the lower Indus and Ganges river basins. Despite this coupling being present throughout all seasons, it appeared to be most important in the dry pre-monsoon period (see Figure 6.7a and Figure 6.9a). For example, in the pre-monsoon season soil moisture and NDVI were both decreasing in the northern Ganges river basin. With the onset of the monsoon in June, both the NDVI and soil moisture started to increase. These decreases in NDVI at the end of the winter season or in the pre-monsoon season could be very likely related with the harvest of winter crops (Bokhari et al., 2017; Nageswararao et al., 2016).

As already noted, warming temperatures appear to favor vegetation expansion at high altitudes (Anderson et al., 2020; Kumar et al., 2022). However, the most influential environmental control at high elevation areas was found to be soil moisture with a temporal lag of 1 (see Figure 6.7a and Figure 6.8a). Moreover, another important factor influencing the vegetation condition could be vapor pressure deficit. Vapor pressure deficit is a crucial variable with respect to the atmospheric water demand for plants. Increases in vapor pressure deficit can limit the photosynthetic activity of vegetation (Konings et al., 2017; Yuan et al., 2019). Particularly in the dry pre-monsoon season vapor pressure deficit increases considerably in parts of the Indo-Gangetic Plain, hence, resulting in a negative coupling with NDVI (see Figure 6.7a). Together with a late onset of monsoon rainfall and reduced soil moisture, changes in vapor pressure deficit could likely exacerbate plant growth (Yuan et al., 2019).

Considering missing causal links, it was noticeable that these were mostly prevalent in the Indo-Gangetic Plain, particularly in the winter and post-monsoon season as well as in the monsoon season in the central Indus river basin (see Figure 6.7a). Groundwater abstraction is widespread in this region and is used for irrigation of agricultural areas (Biemans et al., 2019; MacDonald et al., 2016). Therefore, it could be very likely considered as an important factor in influencing vegetation greenness. Yet, the time series on terrestrial water storage anomaly was not included in the causal analysis, because of the very low spatial resolution and the limited temporal availability compared to the other time series (see Chapter 6.1). On the other hand, the detected negative coupling of NDVI and surface water area could be explained by seasonal changes, i.e. increases in surface water area, and accompanied decreases in the NDVI. Spatially, this causal link was particularly dominant along the large river streams of the Ganges and Brahmaputra and their confluence region, in parts of the southern Indus river, and in the wetlands of the Meghna river basin. Temporally, this connection was most prevalent during the monsoon and post-monsoon season (see Fig-

ure 6.7a) and could be annually exacerbated by severe flooding events, e.g. in the Indus river basin (Atif et al., 2021) or the Brahmaputra and Meghna river basin (Gouweleeuw et al., 2018).

6.4.1.2 Surface Water Area

Moreover, the seasonal trend analysis of surface water area, which was generated by merging the DLR Global WaterPack and the JRC Global Surface Water Layer, indicated mostly significant positive trends at grid (see Figure 6.4) and basin scale (see Table 6.1). For example, at grid scale, significant positive trends appeared to be dominant along the lower Indus river, particularly, in the pre-monsoon and monsoon season. These significant trends were also reflected at basin scale for the pre-monsoon and monsoon season (see Table 6.1). As already noted in Chapter 4.2.2, the river discharge of the Indus river is primarily depending on meltwater from glaciers and snow. In this context, Lutz et al. (2014) reported modeling results projecting an increase in river discharge in the Indus river basin until 2050. Similar findings, were reported by Pritchard (2019) as well. Here, the increasing trends in the Indus river basin might be also linked to the lately occurring flood events (Atif et al., 2021), which led to above-average surface water area extent in the last years of the investigated period (see Figure 6.2).

However, it was also found that terrestrial water storage anomaly reveals significant negative trends for all of the investigated river basins (see Figure 6.2 and Table 6.1). These negative trends were significant at seasonal as well as annual scale. Groundwater in the IGBM river basin appears to be largely withdrawn for crop irrigation in areas with arid and semi-arid climate (Rodell et al., 2018). In addition, the decline in terrestrial water storage could worsen in years with precipitation deficits and droughts (Dangar and Mishra, 2021; Rodell et al., 2018). Likewise, Zhu et al. (2021) reported similar findings on the identified negative trends in terrestrial water storage in the Indus river basin. Apart from irrigation purposes, water use and supply is also pressured by growing population, hydropower, and further domestic needs (Biemans et al., 2019; Viviroli et al., 2020). In this regard, the detected mismatch between the significant trends in surface water area and terrestrial water storage might be explained by the dependence of surface water area on precipitation as well as meltwater from glaciers and snow. The contributions of precipitation and meltwater to the river discharge could have potentially prevented a decline in surface water area in the studied period. In this context, it was also shown that surface water area was largely driven by river discharge in the downstream areas of the river basins (see Figure 6.7b). Although, it was also revealed that the analysis of direct influences on a variable might not be sufficient using causal maps, since the additional causal graphs highlighted that river discharge was

largely influenced by precipitation. Thus, precipitation was also important for the variable surface water area through an indirect path ($P \xrightarrow{+} Q \xrightarrow{+} SWA$). Additional correlation analyses were performed to evaluate the human influence on surface water area and showed a weak negative relation (see Figure 6.10d,e,f). This correlation analysis suggests e.g., that an increase in surface water area was more likely taking place in areas with a comparatively low population and settlement growth.

6.4.1.3 Snow Cover Area

As outlined previously, meltwater from glaciers and snow in the Himalaya-Karakoram region greatly contribute to the freshwater resources in South Asian river basins. Therefore, the assessment of changes in seasonal snow cover area is of great importance to quantify the impacts of climate change and to understand potential consequences for freshwater supply in the future (Kraaijenbrink et al., 2021; Miles et al., 2021). In this regard, seasonal snow cover in the Himalaya-Karakoram cumulates between the post-monsoon and winter season (see Figure 4.8). The maximum extent is generally reached in February or March and ablation starts in the pre-monsoon season.

So far, the detailed analyses of seasonal trends in snow cover area in the Himalaya-Karakoram remained understudied for the period December 2002 to November 2020. Recent investigations mostly focused on annual trends and a study period until 2017 (Ackroyd et al., 2021; Desinayak et al., 2022) and 2018 (Notarnicola, 2020). The obtained significant trends were mostly significantly negative during the winter, monsoon, and post-monsoon season for the upper Ganges and Brahmaputra river basins. In the pre-monsoon season significant positive trends were found in parts for the upper Indus, Ganges, and Brahmaputra river basins (see Figure 6.5). In this context, it has to be noted that most of the grids resulted in non-significant trend metrics indicating stable snow cover area for the IGBM river basins. At basin scale, significant negative trends were only obtained for the Ganges river basin in the monsoon and the Brahmaputra river basin in the post-monsoon season (see Table 6.1). Likewise, this significant negative trend in the Brahmaputra river basin was also reflected in the elevation-dependent trend analysis, particularly in the post-monsoon season and at altitudes higher than 4,500 m (see Figure 6.6). Considering the identified decreases in snow cover area, similar findings were reported for the Brahmaputra river basin, specifically at higher altitudes (Ackroyd et al., 2021). Also, the additional trend analyses for the two periods resulted in non-significant trends, but generally in negative tendencies (see Table 6.3). These findings were in agreement with a study investigating snow cover area between 2003–2012 for subbasins covering in parts the IGBM river basins (Gurung et al., 2017).

In regards of the determined direct controls on snow cover area at seasonal and grid scale, the previously reported negative coupling with temperature (see Chapter 5.3.3) was also persistent at seasonal scale. Yet, the temporally more detailed analyses at seasonal temporal scale revealed the particular positive coupling with precipitation in the winter and in parts in the pre-monsoon and post-monsoon season as well. This strong coupling, particularly in the upper Indus river basin, can be explained by the westerly disturbances (see Figure 4.3) (Cannon et al., 2015; Das and Meher, 2019; Farinotti et al., 2020). Next, the identified negative coupling with temperature was mostly instantaneous (see Figure 6.8). This negative link was also existing in the computed causal graphs (see Figure 6.9). However, with emerging snowfall in the pre-monsoon season, the direction of the detected negative coupling turned from snow cover area towards temperature. This finding might be explained by the snow-albedo feedback, potentially leading to cooler air temperatures through extended snow cover area. In addition, studies pointed towards elevation-dependent warming, where snow cover appears to prevent warming at altitudes higher than 5,000 m (Gao et al., 2018; Zhang et al., 2021).

6.4.2 Potential Future Implications for the Indo-Gangetic River Basins

In times of amplified climate change, warming temperatures will largely control land surface dynamics in the Indo-Gangetic river basins. Future projections indicated an above-average increase in temperatures, e.g. a global average increase of 1.5°C would imply a mean increase of 2.1°C in the IGBM river basins, being identified as a climate change hotspot (Lutz et al., 2018). In the past, particularly regions at high altitudes were affected by increasing temperatures (Pepin et al., 2015), however, being limited to areas below 5,000 m (Gao et al., 2018). Future projections pointed towards ongoing temperature increase over high mountain areas (Mondal et al., 2021; Palazzi et al., 2016). Changes in glacier mass and seasonal snow cover will be a consequence of ongoing warming temperatures. As presented before, the trend analyses revealed significant declines in snow cover area seasonally and regionally, specifically in the upper Ganges and Brahmaputra river basins. On the other hand, snow cover area in the upper Indus river basin was found to remain stable, which appears to be linked to the Karakoram anomaly (Dimri, 2021). Over the past two decades, glacier mass budgets were even found to be positive in the Karakoram, but in view of global warming it is not likely that the positive glacier mass budgets and the Karakoram anomaly will continue (Farinotti et al., 2020). In this regard, future projections indicated considerable decreases in snow cover area in the Himalaya as well as Karakoram mountains with decreases in the Himalayas being more pronounced (Provenzale et al., 2014). Additional future projections showed similar findings with respect to decreasing snow depth (Wei and Dong, 2015) and shorter snow cover duration (Ji and Kang, 2012).

Among other sectors, the population and food production in the Indo-Gangetic Plain was shown to heavily depend on freshwater resources from monsoon rainfall as well as glaciers and snow. The dependence on water resources from mountains is particularly high in the arid and semi-arid regions, including the Indus and in parts the Ganges river basin (Biemans et al., 2019; Pritchard, 2019; Kraaijenbrink et al., 2021; Viviroli et al., 2020). In this regard, changes in precipitation patterns and seasonal snow cover could threaten the freshwater supply and agricultural productivity. With warming temperatures, precipitation over the IGBM river basins will very likely increase (IPCC, 2021; Lutz et al., 2018; Mondal et al., 2021). For example, the northern parts of the Indus river basin will be wetter, but the southern parts will be hotter with more intense drought events (Mondal et al., 2021). In addition, Lutz et al. (2018) reported that the length of dry periods will likely increase in the Ganges river basin. In this connection, investigations outlined that heat stress in the Indo-Gangetic Plain appears to be counteracted by agricultural irrigation and increased soil moisture (Ambika and Mishra, 2021; Mishra et al., 2020). On the contrary, Lutz et al. (2018) also stated that monsoon precipitation and extreme precipitation events will very likely increase, particularly in the Ganges river basin. Accordingly, flood risk appears to enhance considerably in the future (Lutz et al., 2018; Uhe et al., 2019). Flooding events in these river basins cause high economic damage due to crop and infrastructure loss, but also high death cases such as in the monsoon flooding in 2017, where over 1,200 people died (Atif et al., 2021; Uhe et al., 2019). Even though an increase in precipitation might lead to a potentially higher water availability, it might be of disadvantage considering the previously mentioned flooding events.

As noted, heat stress and drought events appear to increase in the future. Apart from negative influences on the human well-being, agricultural production is also vulnerable to climate variability due to its dependency on weather conditions and water availability (BIRTHAL et al., 2021; Priyadarshini and Abhilash, 2020). The vulnerability of this sector is also amplified by the intensification and extensification of agricultural land use in parts of the IGBM river basins (Song et al., 2018). In this regard, Priyadarshini and Abhilash (2020) allude on the transition towards sustainable agriculture, which includes efficient resource management and usage of enhanced seed varieties. Overall, with climate change and human influences shaping the Earth's surface, the investigation and quantification of land surface dynamics remains an important task.

6.5 Summary

In this chapter, new insights were provided with respect to land surface dynamics in the Indus, Ganges, Brahmaputra, Meghna river basins by means of the multi-faceted seasonal

trend analyses and the evaluation of direct and indirect interdependencies in a multivariate feature space. Through the exploitation of the full Terra and Aqua MODIS archives, gap-free composites were generated for the Normalized Difference Vegetation Index (NDVI) being an indicator for vegetation condition. In addition, surface water area was characterized by merging both the DLR Global WaterPack at high temporal resolution and the JRC Global Surface Water Layer at relatively high spatial resolution. Snow cover area was investigated using the DLR Global SnowPack. In combination with further climatic and hydrological variables, a harmonized multivariate feature space was generated with all time series having a biweekly temporal resolution covering the period between December 2002 and November 2020. Additional annual time series on anthropogenic variables were used to analyze the human influence. Considering the trend analyses, the results can be summarized as follows:

- Significant trends in vegetation condition were largely positive. At basin scale, the magnitude of significant trends was highest during the winter (Indus and Ganges river basin) and in the pre-monsoon season (Brahmaputra and Meghna river basin and the GBM-Delta). For example, in the Indus river basin, the magnitude of the annual trend was $0.040 \text{ NDVI decade}^{-1}$. Additional analyses showed that irrigated and rainfed croplands in the Indus river basin contributed most to the observed trend magnitudes, with values of 0.042 and $0.029 \text{ NDVI decade}^{-1}$, respectively. In addition, it was found that the magnitude of trends increased in the second part of the studied period. The elevation-dependent trends indicated largely significant positive trends as well.
- At annual and basin scale, trends of surface water area were found to be significant positive in the Indus ($837 \text{ km}^2 \text{ decade}^{-1}$) and Ganges river basins ($677 \text{ km}^2 \text{ decade}^{-1}$) as well as in the GBM-Delta ($340 \text{ km}^2 \text{ decade}^{-1}$). To provide some context, in the Indus river basin, the long-term average in surface water area was $9,054 \pm 1,230 \text{ km}^2$ in the winter and $11,707 \pm 2,436 \text{ km}^2$ in the monsoon season. The largest variations in surface water area between the seasons were found in the Ganges (pre-monsoon season: $7,419 \pm 1,242 \text{ km}^2$, post-monsoon season: $13,732 \pm 1,884 \text{ km}^2$) and Meghna river basin (pre-monsoon season: $2,124 \pm 1,204 \text{ km}^2$, monsoon season: $8,419 \pm 1,657 \text{ km}^2$). Furthermore, the annually aggregated time series indicated above-normal surface water area extent since 2010 in the Indus river basin, which could potentially be linked to flooding events. At grid and seasonal scale, regions with significant negative trends were striking in the Meghna river basin and the GBM-Delta. A mismatch between trends in terrestrial water storage anomaly and surface water area was identified as well.

- Considering snow cover area, the derived trends were non-significant at annual and basin scale, but significant negative trends resulted for the Ganges river basin in the monsoon season ($-2,080 \text{ km}^2 \text{ decade}^{-1}$) as well as for the Brahmaputra river basin in the post-monsoon season ($-7,301 \text{ km}^2 \text{ decade}^{-1}$). In this context, the long-term average of snow cover area in the monsoon season was $10,419 \pm 2,760 \text{ km}^2$ in the Ganges and $42,398 \pm 18,407 \text{ km}^2$ in the Brahmaputra river basin during the post-monsoon season. The significant negative trends were also reflected in the elevation-dependent trend analysis. In the Indus river basin, snow cover area was found to be largest among the investigated river basins and remained stable with a long-term average of $215,979 \pm 42,589 \text{ km}^2$ in the winter season.

Furthermore, direct and indirect seasonal controls on the land surface variables were investigated using causal graphs. Water availability through the soil and atmosphere was found to influence the NDVI at grid scale. Seasonally and regionally, positive and negative couplings with NDVI were found to be dominant for temperature and surface water area, respectively. On the other hand, surface water area was largely positively coupled to river discharge in the lower river basins. In the upper river basins, snow cover area and temperature were linked negatively and positively with surface water area, respectively. Moreover, with variations in their spatial distribution over the seasons, temperature and precipitation were strongly coupled with snow cover area. As expected, the influence of precipitation was particularly high during the winter. At basin scale, the causal graphs revealed known mechanisms including the snow-albedo feedback or the cooling effect of soil moisture on surface air temperature. In this regard, the potential of causal graphs in detecting indirect links was highlighted in comparison to causal maps. Moreover, the analysis of anthropogenic influences on vegetation greenness resulted in significant positive correlations most likely suggesting an impact of land use management.

Here, the exploration of the interdependencies across spheres provided new and valuable insights into the interpretation of land surface dynamics and driving variables. Overall, the presented findings in this chapter are of great importance for the understanding and interpretation of seasonal trends and drivers of land surface variables for the Indo-Gangetic river basins and beyond. The Indo-Gangetic river basins are considered as hotspots of climate change with future projections indicating above-average warming, particularly at higher elevations. With amplified climate and environmental change, longer Earth observation-based time series on land surface variables will further enhance our understanding of the interdependencies with climatic, hydrological, and anthropogenic variables.

Chapter 7

Synthesis and Outlook

This final chapter provides a synthesis of the conclusive findings of this dissertation. More specifically, Chapter 7.1 summarizes and discusses the results with respect to the defined research questions in Chapter 1.3. Afterwards, Chapter 7.2 focuses on future challenges and opportunities of Earth observation-based multivariate time series analyses across spheres.

7.1 Summary and Conclusive Findings

In the introduction of this dissertation, impacts of climate change on the Earth's land surface covering diverse spheres of the Earth system were summarized, including anticipated changes of the cryosphere and biosphere as well as the importance of the anthroposphere. At the same time, it was emphasized that the quantification and evaluation of interdependencies within the components of the Earth system remain a challenging task due to its complexity. Accordingly, the importance and need for multivariate time series analyses as well as the relevance and suitability of river basins as a geographical entity involving the major components of the Earth system were stressed. In this regard, Earth observation (EO) provides long-term measurements encompassing a multitude of variables being representative for the components of the Earth system and enables large-scale analyses to quantify, analyze, and attribute land surface dynamics.

This dissertation addressed the exploration of multivariate time series, primarily using EO time series on land surface variables, with the aim of jointly characterizing land surface dynamics across spheres over the last two decades. Here, the main focus was on the remote sensing-based land surface variables vegetation condition, surface water area, and snow cover area. Additional climatic, hydrological, and anthropogenic time series were used to generate a multivariate feature space allowing for the assessment of their influence on the three land surface variables as well as the interdependencies between all investigated time

series variables. Apart from the influencing factors, detailed analyses on trends and phenological metrics were conducted to quantify land surface change for the investigated period. To this aim, the implementation of a methodological framework for both the harmonization of the multi-source time series and the application of statistical time series analyses was required. In this context, several research questions were defined as part of the primary research objectives in Chapter 1.3. Throughout this thesis, Chapters 2–6 dealt with answering the defined research questions. In addition, the following paragraphs provide a short summary thereof.

Research Questions 1

- *What is the potential of Earth observation time series for the analysis of land surface dynamics?*
- *Which Earth observation and further geoscientific time series are available?*
- *What is the geographical relevance of large river basins for multivariate time series analyses?*
- *How many studies investigated large river basins and what was their spatio-temporal coverage and resolution?*
- *Which spheres were most frequently analyzed in the context of large river basins and which spaceborne remote sensing instruments were most frequently utilized?*
- *Which research gaps exist with respect to remote sensing-based river basin analyses and how can they be addressed?*

In Chapter 2, general background information on time series was provided. In this context, EO data provide the great potential to quantify and analyze land surface dynamics over already multiple decades up to a spatial resolution of 30 m. Using EO time series, an abundance of land surface features across spheres can be characterized and analyzed. However, one has to keep in mind that remote sensing time series with comparatively high spatial resolution come at the cost of a reduced temporal resolution and vice versa. This needs to be considered to assess the suitability of EO time series for long-term and large-scale analyses. In this regard, available remote sensing time series as well as subsequently generated value-added data products were presented in detail, including the Terra and Aqua MODIS sensors that provide up to daily imagery with global coverage since 2000 and 2002, respectively. MODIS imagery has a spatial resolution of up to 250 m. Additional time series characterizing, e.g. the state of climatic and hydrological variables were presented and their importance with regards to performing multivariate time series analyses was highlighted. Overall, the lack and importance of multivariate time series analyses incorporating the joint consideration of diverse remote sensing-based land surface features in combination with further driving variables was outlined.

Furthermore, the geographical entity of river basins was introduced in Chapter 1.1.2 and Chapter 3. River basins are functional units dividing the Earth's land surface into distinct catchments based on their topographical characteristics irrespective of administrative boundaries. Therefore, as natural parts of the Earth system, river basins are particularly suitable for multivariate time series analyses to quantify and evaluate land surface dynamics including diverse spheres. In this context, a comprehensive literature review was performed to investigate the availability of EO-based analyses of the worldwide 28 largest river basins. In this review, studies focusing on the primary application of remote sensing data to analyze land surface characteristics within the spatial entity of river basins were considered. In total, 287 relevant research articles were identified. It was found that around 86 % of the studies were conducted at regional and subbasin scale. At the same time, ~14 % of the studies performed investigations including the entire area of a respective river basin. The most investigated river basins were found to be located in South America, Southeast Asia, and East Asia. In the advent of open data policies as well as the granted free access to cloud computing services such as the Google Earth Engine, remote sensing time series applications were found to be increasing, particularly since 2011. In general, the average investigation period of all studies was 10 years with an increasing tendency since 2009. However, only few studies focused on the remote sensing-based application of multivariate time series analyses to characterize land surface features across spheres. Overall, most studies were found to investigate single EO-based land surface variables such as vegetation greenness or surface water area in consideration of relevant environmental drivers. In this context, the most frequently investigated land surface variables included vegetation parameters, surface water area and inundation dynamics, as well as land cover and land use classifications. In this connection, optical (i.e. Landsat, MODIS, NOAA-AVHRR) and synthetic aperture radar (i.e. Sentinel-1, ALOS-PALSAR) remote sensing imagery were found to be mostly used.

In compliance with the findings of the literature review, several research gaps were identified with respect to EO-based river basin analyses. To start with, applications using remote sensing data were rarely performed at the entire scale of a respective river basin. In this regard, the investigation of transboundary river basins was found to be particularly limited due to the insufficient spatial coverage of the investigations with respect to the geographical entity of the respective river basins. In many cases, studies rather focused on selected riparian countries only. Furthermore, the joint analysis of remote sensing-based multivariate time series involving multiple land surface features was found to be understudied as well. Hence, the primal conclusions of the review were that future research should (1) exploit the potential of spaceborne remote sensing providing a multitude of observations and data products representative for various components of the Earth system, (2) focus on large

river basins irrespective of administrative boundaries, and (3) develop a methodological framework that is transferable in space and time for multivariate time series analyses.

To address these gaps, the transboundary river basins Indus, Ganges, Brahmaputra, and Meghna (IGBM) were selected as study area to develop and test the methodological framework. The geographical features of these transboundary river basins were described in Chapter 4. Overall, the selected study area is considered as a climate change hotspot and has a size of approximately 2.8 million km², corresponding to an area eight times the size of Germany. Also, over 1.1 billion people live in these river basins accounting for around 14 % of the world's population. In accordance with the defined research objectives of this thesis (see Chapter 1.3), the investigated river basins were particularly suitable for multivariate time series analyses and, thus, enabled a multi-faceted investigation of land surface dynamics. In this regard, the upper Indus, Ganges, and Brahmaputra river basins include parts of High Mountain Asia, holding the largest ice mass outside of the polar regions, being representative for the cryosphere. On the other hand, the lower river basins cover the Indo-Gangetic Plain where human pressure on the environment is high, with urban and intensive agricultural land use being dominant. Altogether, this geographical setting enables a detailed evaluation of the interplays between multiple spheres, including the anthroposphere, biosphere, cryosphere, hydrosphere, lithosphere, and atmosphere.

Research Questions 2

- *What are the challenges in using multi-source time series for joint analyses to characterize land surface dynamics and how can they be addressed?*
- *Which novel methods can be integrated in the methodological framework to analyze land surface dynamics and interdependencies across spheres?*
- *What needs to be considered to ensure the transferability of the developed methodological framework to any spatial entity or time series data?*
- *Are the results of the quantitative analyses of land surface dynamics consistent with existing literature?*

Next, as outlined in Chapter 5, a methodological framework was developed and implemented on an internal high-performance computing (HPC) environment at the German Aerospace Center (DLR). In this regard, a particular challenge was the joint use of multi-source time series coming with different data properties, e.g., concerning their data format, data quality, as well as spatial and temporal resolution. To enable a synergistic analysis of all time series variables, the feature space needs to be harmonized in terms of the spatial and temporal resolution of the input variables. In order to accomplish these requirements, a respective methodological framework was required. With more detail, a methodological framework that is easy-to-implement, time efficient with respect to data processing and sta-

tistical analyses, and flexible in consideration of the integration of data analyses modules and the use of respective programming languages was envisioned. The developed framework was implemented by means of the setup of corresponding docker containers, which were then deployed on the HPC environment. Ultimately, the framework combines (1) the ingestion of the time series on the HPC infrastructure, (2) the preprocessing of the univariate time series in consideration of their specific requirements, (3) the preparation of a harmonized feature space, and (4) the application of statistical time series analysis techniques to characterize land surface dynamics and assess driving variables.

In this thesis, land surface dynamics were characterized using remote sensing-based time series on vegetation condition, surface water area, and snow cover area over the last two decades for the transboundary Indus, Ganges, Brahmaputra, and Meghna river basins. The time series on vegetation condition was based on MODIS normalized difference vegetation index (NDVI) data. Surface water area was characterized by using the DLR Global WaterPack. Likewise, the DLR Global SnowPack was used for representation of snow cover area. To quantitatively assess land surface dynamics, several statistical analysis methods, which were integrated as modules into the framework, were utilized. First, the Mann-Kendall trend test was applied in combination with the Theil-Sen slope estimator to investigate the existence of significant trends and their magnitude, respectively. In this context, the necessity to consider autocorrelation and seasonality of the time series was elaborated in detail. To this end, the application of respective prewhitening algorithms was tested. Second, the Timesat tool was employed to derive phenological metrics and to assess changes in seasonal characteristics between two investigated decades. Third, the causal discovery algorithm Peter and Clark Momentary Conditional Independence (PCMCI) was used to analyze the influence of relevant climatic and hydrological time series on vegetation condition, surface water area, and snow cover area. An important objective regarding the methodological framework was its transferability. In fact, due to the implementation of this framework with globally applicable parameter settings, the transferability is ensured in space and time to any other river basin, geographical, or spatial entity. Depending on the used time series variables, it might yet be necessary to include adjusted modules on the respective preprocessing steps. The used statistical time series analysis techniques are working independent of the used time series variables.

In Chapter 5, the functionality of the framework was tested using monthly time series for all three remote sensing-based land surface variables in combination with climatic and hydrological variables. The resulting significant trends for vegetation condition, surface water area, and snow cover area were compared with findings in available literature. In this regard, it was noted that a direct comparison of trend test results might be hampered by several

facts that need to be considered. These include variations in the data source, the conducted preprocessing steps, the investigated period, the design of the trend test, the application of prewhitening methods, and the defined confidence level. Nonetheless, comparisons of the trend tests and the phenological metrics with available reference studies indicated a good alignment of the general direction of trends and changes as well as directions of the assessed phenological metrics. Likewise, the evaluation of the retrieved couplings between the three land surface variables and climatic as well as hydrological controls were found to be congruent with existing literature proving the functionality of the framework and used causal discovery algorithm. In this regard, limitations and further requirements were discussed. For example, causal links can disappear at a coarse temporal resolution, due to the temporal aggregation. Here, a finer temporal granularity could enable the detection of more significant causal links. Additional constraints and challenges with respect to the used time series were elaborated as well, including the MODIS data products.

Research Questions 3

- *What are the seasonal patterns of trends with respect to vegetation condition, surface water area, and snow cover area between December 2002 and November 2020? Are there any changes in phenological characteristics?*
- *What are the dominant controls on vegetation condition, surface water area, and snow cover area dynamics? Are there differences in the prevalent environmental controls with respect to the investigated river basins?*
- *What are the interdependencies among the respective feature spaces?*
- *What are future implications of climate change for the investigated Indo-Gangetic river basins in South Asia?*

In order to obtain a finer temporal granularity and a higher sample size, the temporal resolution of the time series was increased. This modification enabled a more detailed analysis with respect to seasonal patterns of trends and environmental controls. Additional constraints with respect to the used time series were alleviated, e.g. through the combination of two time series on surface water area. For this purpose, the advantages of the DLR Global WaterPack coming at daily temporal resolution and of the JRC Global Surface Water Layer coming at comparatively high spatial resolution were exploited. Furthermore, another aim was to consider anthropogenic influences on the land surface variables in the investigated Indo-Gangetic river basins.

In this context, the developed framework was utilized to prepare a harmonized multi-variate feature space involving biweekly time series on vegetation condition, surface water area, snow cover area, and climatic as well hydrological variables covering the period December 2002 to November 2020. To generate time series at biweekly temporal scale, daily,

and in case of the climatic features, hourly data were gathered. For example, the NDVI was calculated by means of the full archive of daily Terra and Aqua MODIS surface reflectance imagery to obtain high quality and gap-free time series. Moreover, the anthropogenic time series, characterizing land cover and land use, settlement area, population count, and night-time lights were available at an annual resolution and were used to investigate their relation with NDVI and surface water area. The considered seasons included the winter (DJF), pre-monsoon (MAM), monsoon (JJAS), and post-monsoon (ON) season.

The multi-faceted seasonal trend analyses uncovered detailed patterns with respect to the significance, direction, and magnitude of trends at grid scale and for diverse geographically stratified regions, including river basins, land cover and land use classes, and elevation-dependent zones. In combination with the analysis of phenological metrics, both results enabled a comprehensive characterization of land surface dynamics. The primary findings are summarized in the following:

- The IGBM river basins largely experienced significant positive trends in vegetation greenness throughout all seasons. At river basin scale, the magnitude of the significant positive trends was highest during the winter (Indus and Ganges river basin) and the pre-monsoon season (Brahmaputra and Meghna river basin and the GBM-Delta). In the winter season, the trends were found to be particularly high in the arid and semi-arid parts of the river basins. At annual and basin scale, the magnitude of the trend was at 0.040 and 0.034 NDVI decade⁻¹ for the Indus and Ganges river basin, respectively. At basin scale, it was also found that the magnitude of trends accelerated in the second part of the studied period. Irrigated and rainfed agricultural areas in the Indus river basin were found to contribute most to significant positive trends, e.g. with values of 0.042 and 0.029 NDVI decade⁻¹, respectively. Elevation-dependent areas up to 5,500 m above sea level showed largely significant positive trends, with highest magnitudes at lower altitudes. In alignment with the trend analyses, the amplitude of the NDVI was mostly decreasing, but the seasonal peak values remained stable or even increased between the two investigated decades.
- Surface water area in the IGBM river basins showed significant positive trends in the Indus (837 km² decade⁻¹) and Ganges river basins (677 km² decade⁻¹) as well as in the GBM-Delta (340 km² decade⁻¹) at annual scale. To provide some context, the long-term average in surface water area in the Indus river basin amounts to 10,535 ± 1,763 km² at annual scale. Large variations between the seasons were found in the Ganges and Meghna river basin. At annual scale, above-normal surface water area extent was detected for the Indus river basin in most of the years since 2010, which were most likely associated with flood events. Furthermore, at grid and sea-

sonal scale, clusters with significant negative trends were identified in parts of the Meghna river basin and the GBM-Delta.

- Analyses for snow cover area in the upper Indus, Ganges, and Brahmaputra largely indicated non-significant trends at annual and basin scale. At basin scale, significant negative trends were obtained seasonally for the Ganges river basin in the monsoon season ($-2,080 \text{ km}^2 \text{ decade}^{-1}$) and for the Brahmaputra river basin in the post-monsoon season ($-7,301 \text{ km}^2 \text{ decade}^{-1}$). To provide some context, snow cover area had a long-term average of $10,419 \pm 2,760 \text{ km}^2$ in the Ganges river basin during the monsoon season and of $42,398 \pm 18,407 \text{ km}^2$ in the Brahmaputra river basin during the post-monsoon season. Significant negative trends were found in the elevation-dependent analysis as well, being most prominent in the post-monsoon season at high altitudes. On the other hand, significant positive trends were obtained for the pre-monsoon season in the Ganges and Brahmaputra river basins at altitudes higher than 5,000 m. The largest extent of snow cover area was observed in the Indus river basin with $215,979 \pm 42,589 \text{ km}^2$ during the winter season. Here, the trend analysis suggested that the snow cover area remained stable for the investigated period. Matching patterns were identified for the resulting changes in the phenological metrics, e.g., a decreasing seasonal duration of snow cover area in the upper Ganges and Brahmaputra river basin.

Moreover, for the first time, the evaluation of direct and indirect links for a multivariate feature space, involving multiple remote sensing-based land surface variables across spheres was conducted for the transboundary river basins in South Asia using the causal discovery algorithm PCMCI. In this regard, the findings are briefly summarized as follows:

- In the IGBM river basins, at grid and seasonal scale, NDVI was largely found to be influenced by water availability through the soil and the atmosphere. During the winter season, a regional cluster showing a positive coupling between the NDVI and temperature was particularly striking in the lower Indus river basin. Here, the phenology of the NDVI and temperature were largely aligning, with decreasing NDVI due to crop harvests towards the end of the post-monsoon season and increases in NDVI during the winter season after the sowing of winter crops. Moreover, a negative coupling between NDVI and surface water area was prevalent along the large river streams in the lower river basins during the monsoon and the post-monsoon season. This coupling can be explained with the advance of surface water area during the monsoon rainfall. The analysis of interplays between all variables in the feature space at basin scale expectably uncovered a direct and indirect path of precipitation towards NDVI via soil moisture.

- Surface water area was mostly positively influenced by river discharge in the lower river basins over all seasons at grid scale. In contrast, in the upper river basins, snow cover area and temperature were found to be coupled negatively and positively to surface water area, respectively. The analysis of causal graphs at basin scale provided further insights into the interplays of the investigated time series variables. As expected, it was found that river discharge was largely coupled to precipitation. Thus, surface water area was found to be indirectly controlled by precipitation via river discharge. These links prove the functionality of the causal discovery algorithm.
- In the upper Indus, Ganges, and Brahmaputra river basins, snow cover area was largely negatively coupled with temperature and positively with precipitation. However, these influences had variations in their spatial distribution during the respective seasons. Precipitation was found to control snow cover area mostly during the winter season. This coupling was particularly prominent in the Indus river basin. On the other hand, influences of temperature were most dominant during the monsoon season. Besides these couplings, the causal graphs additionally showed seasonal variations in the interplays between the time series variables at basin scale. For example, the changing direction of influence between snow cover area and temperature. In particular, in the post-monsoon season, with advancing snow cover area, the direction of influence turned from snow cover area towards temperature, which could indicate the impacts of the snow-albedo feedback.
- Additional analyses were performed to evaluate the influence of human factors. These revealed that vegetation condition might be positively influenced in areas with a high human footprint, since large positive trends in NDVI coincided with large positive trends in relative settlement growth and population counts. On the contrary, the obtained correlation coefficient between surface water area and anthropogenic factors was weak negative. These relations suggested that surface water area increased in areas with relatively low trend values in population counts and relative settlement growth.

Overall, the presented results and findings of the previous chapters greatly contribute to an improved understanding and interpretation of seasonal trends and drivers of remote sensing-based land surface dynamics. In addition, the investigation of the interplays across spheres provided new and valuable insights into interactions between land surface, climatic, and hydrological variables. Besides the Indo-Gangetic river basins, these findings could be of great relevance and value also for other geographical regions and river basins. However, in regards of the river basins originating at the Himalaya-Karakoram, it was stressed

that these are considered to be hotspots of climate change. In particular, future projections indicate above-average warming being most pronounced at high altitudes.

7.2 Future Challenges and Opportunities

As a result of amplified climate and environmental change, the source and delta regions of river basins are particularly vulnerable to changing boundary conditions. In fact, the cryosphere experiences the most rapid and dramatic changes and the land surface in proximity to the river outlets is threatened by sea level rise and more frequent flood events. In this context, the monitoring of land surface dynamics using spaceborne remote sensing is of great importance to quantify and evaluate changes at the Earth's land surface as well as their spatio-temporal patterns and the influence of natural and anthropogenic drivers.

However, in consideration of the methodological framework and performed analyses, several aspects could be further investigated. For example, the abundance of available remote sensing and additional geoscientific time series, including land-atmosphere fluxes, snow water equivalent, gross primary production, or sea surface temperature could further enhance the understanding of land surface dynamics and cover further components of the Earth system. For example, the inclusion of sea surface temperature would enable the analysis of the influence of teleconnections and large-scale atmospheric modes on land surface dynamics. Another aspect requiring further improvements is the consideration and integration of anthropogenic controls on the land surface. This remains a challenging task as geoscientific data on anthropogenic features are mostly constrained by their spatial or temporal characteristics. Considering spatial constraints, time series on agricultural productivity or fertilization, which could enhance the attribution of vegetation trends, are only available for national or other administrative units. Additionally, the temporal resolution of such anthropogenic variables is mostly coarse making it difficult to integrate the data properly into the time series analyses. However, further methods, e.g. from machine learning, could be tested to improve the attribution and differentiation between natural and anthropogenic influences on the environment.

Furthermore, the application of causal graphs showed its potential with respect to the identification of direct and indirect influences in a high dimensional feature space. However, in this thesis, linear relationships were primarily focused on. As non-linear dependencies cannot be precluded, future research could also investigate the application of non-linear settings of the PCMCI algorithm. Additionally, the causal graphs could be computed for distinct river basins or other geographically stratified regions to provide more detailed insight into the interplays of the used time series variables within a particular system. Regarding the

performed monotonic trend tests, additional modules could be included to explore breakpoints in the time series. This could further improve the analysis of land surface dynamics and support the assessment of large-scale disturbances.

With increasing records of spaceborne remote sensing measurements over multiple decades, future results from statistical time series analyses on land surface dynamics will be even more reliable. This thesis primarily focused on remote sensing data products based on Terra and Aqua MODIS imagery. MODIS imagery are now available for over two decades and the continuity of this mission is already ensured by means of the Visible Infrared Imaging Radiometer Suite (VIIRS) and the Sentinel-3 mission of the European Copernicus Programme. Apart from these missions, future harmonized products from the Landsat and Sentinel-2 missions will certainly enhance the generation of dense and equidistant remote sensing time series at higher spatial resolution over long periods and, thus, enable the revelation of land surface dynamics at unprecedented levels. Overall, these developments will contribute to an improved understanding of the complex interplays between land surface variables and climatic, hydrological, and anthropogenic controls.

Altogether, this thesis provided valuable and detailed insights into past land surface dynamics, including multiple remote sensing-based land surface variables and climatic drivers. In addition, anthropogenic influences were investigated for consideration of impacts of the human footprint, e.g. on vegetation condition or surface water area. In this regard, the presented and implemented methodological framework provides useful tools to prepare, harmonize, and evaluate multi-source time series for the analysis of large-scale land surface dynamics in river basins and beyond. Data and knowledge about the past state and evolution of the land surface greatly enhance the understanding of interdependencies between the components of the Earth system and in particular the response of the investigated land surface variables to a changing climate. Correspondingly, the insights learned from multivariate time series analyses are of great importance and form a basis with respect to regional projections and forecasts of components of the Earth system. In combination with ever-increasing amounts of geoscientific data and further advances in multivariate data analysis through artificial intelligence, an enhanced understanding of the past and future state of the Earth's land surface will be fostered.

Bibliography

- Abatzoglou, J.T., Dobrowski, S.Z., Parks, S.A., Hegewisch, K.C., 2018. TerraClimate, a high-resolution global dataset of monthly climate and climatic water balance from 1958-2015. *Sci. Data* 5, 170191. doi:10.1038/sdata.2017.191.
- Abell, R., Lehner, B., Thieme, M., Linke, S., 2016. Looking Beyond the Fenceline: Assessing Protection Gaps for the World's Rivers. *Conserv. Lett.* 10, 384–394. doi:10.1111/conl.12312.
- Ackroyd, C., Skiles, S.M., Rittger, K., Meyer, J., 2021. Trends in Snow Cover Duration Across River Basins in High Mountain Asia From Daily Gap-Filled MODIS Fractional Snow Covered Area. *Front. Earth Sci.* 9, 713145. doi:10.3389/feart.2021.713145.
- Akyurek, Z., Surer, S., Beser, O., 2011. Investigation of the snow-cover dynamics in the Upper Euphrates Basin of Turkey using remotely sensed snow-cover products and hydrometeorological data. *Hydrol. Process.* 25, 3637–3648. doi:10.1002/hyp.8090.
- Ali, S., Cheema, M.J.M., Waqas, M.M., Waseem, M., Awan, U.K., Khaliq, T., 2020. Changes in Snow Cover Dynamics over the Indus Basin: Evidences from 2008 to 2018 MODIS NDSI Trends Analysis. *Remote Sens.* 12, 2782. doi:10.3390/rs12172782.
- Ambika, A.K., Mishra, V., 2021. Modulation of Compound Extremes of Low Soil Moisture and High Vapor Pressure Deficit by Irrigation in India. *J. Geophys. Res. Atmos.* 126, e2021JD034529. doi:10.1029/2021jd034529.
- Anderson, K., Fawcett, D., Cugulliere, A., Benford, S., Jones, D., Leng, R., 2020. Vegetation expansion in the subnival Hindu Kush Himalaya. *Glob. Chang. Biol.* 26, 1608–1625. doi:10.1111/gcb.14919.
- Anthony, E.J., Brunier, G., Besset, M., Goichot, M., Dussouillez, P., Nguyen, V.L., 2015. Linking rapid erosion of the Mekong River delta to human activities. *Sci. Rep.* 5, 14745. doi:10.1038/srep14745.
- Antonova, S., Duguay, C.R., Kaab, A., Heim, B., Langer, M., Westermann, S., Boike, J., 2016a. Monitoring Bedfast Ice and Ice Phenology in Lakes of the Lena River Delta Using TerraSAR-X Backscatter and Coherence Time Series. *Remote Sens.* 8, 23. doi:10.3390/rs8110903.
- Antonova, S., Kaab, A., Heim, B., Langer, M., Boike, J., 2016b. Spatio-temporal variability of X-band radar backscatter and coherence over the Lena River Delta, Siberia. *Remote Sens. Environ.* 182, 169–191. doi:10.1016/j.rse.2016.05.003.
- Arias, P., Bellouin, N., Coppola, E., Jones, R., Krinner, G., Marotzke, J., Naik, V., Palmer, M., Plattner, G.K., Rogelj, J., Rojas, M., Sillmann, J., Storelvmo, T., Thorne, P., Trewin, B., Achuta Rao, K., Adhikary, B., Allan, R., Armour, K., Bala, G., Barimalala, R., Berger, S., Canadell, J., Cassou, C., Cherchi, A., Collins, W., Collins, W., Connors, S., Corti, S., Cruz, F., Dentener, F., Dereczynski, C., Di Luca, A., Diongue Niang, A., Doblaser-Reyes, F., Dosio, A., Douville, H., Engelbrecht, F., Eyring, V., Fischer, E., Forster, P., Fox-Kemper, B., Fuglestedt, J., Fyfe, J., Gillett, N., Goldfarb, L., Gorodetskaya, I., Gutierrez, J., Hamdi, R., Hawkins, E., Hewitt, H., Hope, P., Islam, A., Jones, C., Kaufman, D., Kopp, R., Kosaka, Y., Kossin, J., Krakovska, S., Lee, J.Y., Li, J., Mauritsen, T., Maycock, T., Meinshausen, M., Min, S.K., Monteiro, P., Ngo-Duc, T., Otto, F., Pinto, I., Pirani, A., Raghavan, K., Ranasinghe, R., Ruane, A., Ruiz, L., Sallée, J.B., Samset, B., Sathyendranath, S., Seneviratne, S., Sörensson, A., Szopa, S., Takayabu, I., Tréguier,

- A.M., van den Hurk, B., Vautard, R., von Schuckmann, K., Zaehle, S., Zhang, X., Zickfeld, K., 2021. Technical Summary, in: Masson-Delmotte, V., Zhai, P., Pirani, A., Connors, S.L., Péan, C., Berger, S., Caud, N., Chen, Y., Goldfarb, L., Gomis, M.I., Huang, M., Leitzell, K., Lonnoy, E., Matthews, J., Maycock, T.K., Waterfield, T., Yelekci, O., Yu, R., Zhou, B. (Eds.), *Climate Change 2021: The Physical Science Basis. Contribution of Working Group I to the Sixth Assessment Report of the Intergovernmental Panel on Climate Change*, p. 150.
- Arnesen, A.S., Silva, T.S.F., Hess, L.L., Novo, E., Rudorff, C.M., Chapman, B.D., McDonald, K.C., 2013. Monitoring flood extent in the lower Amazon River floodplain using ALOS/PALSAR ScanSAR images. *Remote Sens. Environ.* 130, 51–61. doi:10.1016/j.rse.2012.10.035.
- Arneeth, A., Denton, F., Agus, F., Elbehri, A., Erb, K., Osman Elasha, B., Rahimi, M., Rounsevell, M., Spence, A., Valentini, R., 2019. Framing and Context, in: Shukla, P.R., Skea, J., Calvo Buendi, E., Masson-Delmotte, V., Pörtner, H.O., Roberts, D.C., Zhai, P., Slade, R., Connors, S., Diemen, R.v., Ferrat, M., Haughey, E., Luz, S., Neogi, S., Pathak, M., Petzold, J., Portugal Pereira, J., Vyas, P., Huntley, E., Kissick, K., Belkacemi, M., Malley, J. (Eds.), *Climate Change and Land: an IPCC special report on climate change, desertification, land degradation, sustainable land management, food security, and greenhouse gas fluxes in terrestrial ecosystems*, pp. 77–129.
- Arvor, D., Daher, F.R.G., Briand, D., Dufour, S., Rollet, A.J., Simoes, M., Ferraz, R.P.D., 2018. Monitoring thirty years of small water reservoirs proliferation in the southern Brazilian Amazon with Landsat time series. *ISPRS J. Photogramm. Remote Sens.* 145, 225–237. doi:10.1016/j.isprsjprs.2018.03.015.
- Asmaryan, S., Muradyan, V., Tepanosyan, G., Hovsepian, A., Saghatelyan, A., Astsatryan, H., Grigoryan, H., Abrahamyan, R., Guigoz, Y., Giuliani, G., 2019. Paving the Way towards an Armenian Data Cube. *Data* 4, 117. doi:10.3390/data4030117.
- Atif, S., Umar, M., Ullah, F., 2021. Investigating the flood damages in Lower Indus Basin since 2000: Spatiotemporal analyses of the major flood events. *Nat. Hazards* 108, 2357–2383. doi:10.1007/s11069-021-04783-w.
- Azam, M.F., Kargel, J.S., Shea, J.M., Nepal, S., Haritashya, U.K., Srivastava, S., Maussion, F., Qazi, N., Chevallier, P., Dimri, A.P., Kulkarni, A.V., Cogley, J.G., Bahuguna, I.M., 2021. Glaciohydrology of the Himalaya-Karakoram. *Science* 373, eabf3668. doi:10.1126/science.abf3668.
- Baki, A.B.M., Gan, T.Y., 2012. Riverbank migration and island dynamics of the braided Jamuna River of the Ganges–Brahmaputra basin using multi-temporal Landsat images. *Quat. Int.* 263, 148–161. doi:10.1016/j.quaint.2012.03.016.
- Banerjee, A., Chen, R., E. Meadows, M., Singh, R.B., Mal, S., Sengupta, D., 2020. An Analysis of Long-Term Rainfall Trends and Variability in the Uttarakhand Himalaya Using Google Earth Engine. *Remote Sens.* 12, 709. doi:10.3390/rs12040709.
- Barkhordarian, A., Saatchi, S.S., Behrangi, A., Loikith, P.C., Mechoso, C.R., 2019. A Recent Systematic Increase in Vapor Pressure Deficit over Tropical South America. *Sci. Rep.* 9, 15331. doi:10.1038/s41598-019-51857-8.
- Bartholomé, E., Belward, A.S., 2005. GLC2000: a new approach to global land cover mapping from Earth observation data. *Int. J. Remote Sens.* 26, 1959–1977. doi:10.1080/01431160412331291297.
- Baumann, P., Rossi, A.P., Bell, B., Clements, O., Evans, B., Hoenig, H., Hogan, P., Kakaletis, G., Koltsida, P., Mantovani, S., Marco Figuera, R., Merticariu, V., Misev, D., Pham, H.B., Siemen, S., Wagemann, J., 2018. Fostering Cross-Disciplinary Earth Science Through Datacube Analytics, in: *Earth Observation Open Science and Innovation*. Springer, Cham. book section Chapter 5, pp. 91–119. doi:10.1007/978-3-319-65633-5_5.

- Baumhoer, C.A., Dietz, A.J., Kneisel, C., Kuenzer, C., 2019. Automated Extraction of Antarctic Glacier and Ice Shelf Fronts from Sentinel-1 Imagery Using Deep Learning. *Remote Sens.* 11, 2529. doi:10.3390/rs11212529.
- Bayazit, M., Onoz, B., 2007. To prewhiten or not to prewhiten in trend analysis? *Hydrol. Sci. J.* 52, 611–624. doi:10.1623/hysj.52.4.611.
- Beck, H.E., Zimmermann, N.E., McVicar, T.R., Vergopolan, N., Berg, A., Wood, E.F., 2018. Present and future Koppen-Geiger climate classification maps at 1-km resolution. *Sci. Data* 5, 180214. doi:10.1038/sdata.2018.214.
- Becker, M., Papa, F., Karpytchev, M., Delebecque, C., Krien, Y., Khan, J.U., Ballu, V., Durand, F., Le Cozannet, G., Islam, A., Calmant, S., Shum, C.K., 2020. Water level changes, subsidence, and sea level rise in the Ganges-Brahmaputra-Meghna delta. *Proc. Natl. Acad. Sci. U.S.A.* 117, 1867–1876. doi:10.1073/pnas.1912921117.
- Becker, M., da Silva, J.S., Calmant, S., Robinet, V., Linguet, L., Seyler, F., 2014. Water Level Fluctuations in the Congo Basin Derived from ENVISAT Satellite Altimetry. *Remote Sens.* 6, 9340–9358. doi:10.3390/rs6109340.
- Berg, A., Sheffield, J., 2018. Climate Change and Drought: the Soil Moisture Perspective. *Curr. Clim. Chang. Rep.* 4, 180–191. doi:10.1007/s40641-018-0095-0.
- Best, J., 2018. Anthropogenic stresses on the world's big rivers. *Nat. Geosci.* 12, 7–21. doi:10.1038/s41561-018-0262-x.
- de Beurs, K.M., Henebry, G.M., Owsley, B.C., Sokolik, I., 2015. Using multiple remote sensing perspectives to identify and attribute land surface dynamics in Central Asia 2001–2013. *Remote Sens. Environ.* 170, 48–61. doi:10.1016/j.rse.2015.08.018.
- Bhattacharya, A., Bolch, T., Mukherjee, K., King, O., Menounos, B., Kapitsa, V., Neckel, N., Yang, W., Yao, T., 2021. High Mountain Asian glacier response to climate revealed by multi-temporal satellite observations since the 1960s. *Nat. Commun.* 12, 4133. doi:10.1038/s41467-021-24180-y.
- Biemans, H., Siderius, C., Lutz, A.F., Nepal, S., Ahmad, B., Hassan, T., von Bloh, W., Wijngaard, R.R., Wester, P., Shrestha, A.B., Immerzeel, W.W., 2019. Importance of snow and glacier meltwater for agriculture on the Indo-Gangetic Plain. *Nat. Sustain.* 2, 594–601. doi:10.1038/s41893-019-0305-3.
- Birthal, P.S., Hazrana, J., Negi, D.S., Pandey, G., 2021. Benefits of irrigation against heat stress in agriculture: Evidence from wheat crop in India. *Agric. Water Manag.* 255, 106950. doi:10.1016/j.agwat.2021.106950.
- Boergens, E., Dettmering, D., Schwatke, C., Seitz, F., 2016. Treating the Hooking Effect in Satellite Altimetry Data: A Case Study along the Mekong River and Its Tributaries. *Remote Sens.* 8, 22. doi:10.3390/rs8020091.
- Bokhari, S.A.A., Rasul, G., Ruane, A.C., Hoogenboom, G., Ahmad, A., 2017. The Past and Future Changes in Climate of the Rice-Wheat Cropping Zone in Punjab, Pakistan. *Pak. J. Meteorol.* 13, 14.
- Bolch, T., Kulkarni, A., Kaab, A., Huggel, C., Paul, F., Cogley, J.G., Frey, H., Kargel, J.S., Fujita, K., Scheel, M., Bajracharya, S., Stoffel, M., 2012. The state and fate of Himalayan glaciers. *Science* 336, 310–4. doi:10.1126/science.1215828.
- Broich, M., Tulbure, M.G., Verbesselt, J., Xin, Q.C., Wearne, J., 2018. Quantifying Australia's dryland vegetation response to flooding and drought at sub-continental scale. *Remote Sens. Environ.* 212, 60–78. doi:10.1016/j.rse.2018.04.032.
- Buono, A., Nunziata, F., Migliaccio, M., Yang, X., Li, X., 2017. Classification of the Yellow River delta area using fully polarimetric SAR measurements. *Int. J. Remote Sens.* 38, 6714–6734. doi:10.1080/01431161.2017.1363437.

- Calmant, S., da Silva, J.S., Moreira, D.M., Seyler, F., Shum, C.K., Crétaux, J.F., Gabalda, G., 2013. Detection of Envisat RA2/ICE-1 retracked radar altimetry bias over the Amazon basin rivers using GPS. *Adv. Space Res.* 51, 1551–1564. doi:10.1016/j.asr.2012.07.033.
- Cannon, F., Carvalho, L.M.V., Jones, C., Norris, J., 2015. Winter westerly disturbance dynamics and precipitation in the western Himalaya and Karakoram: a wave-tracking approach. *Theor. Appl. Climatol.* 125, 27–44. doi:10.1007/s00704-015-1489-8.
- Cao, N., Lee, H., Jung, H.C., Yu, H.W., 2018a. Estimation of Water Level Changes of Large-Scale Amazon Wetlands Using ALOS2 ScanSAR Differential Interferometry. *Remote Sens.* 10, 966. doi:10.3390/rs10060966.
- Cao, R., Chen, Y., Shen, M., Chen, J., Zhou, J., Wang, C., Yang, W., 2018b. A simple method to improve the quality of NDVI time-series data by integrating spatiotemporal information with the Savitzky-Golay filter. *Remote Sens. Environ.* 217, 244–257. doi:10.1016/j.rse.2018.08.022.
- Chan, D., Wu, Q., 2015. Significant anthropogenic-induced changes of climate classes since 1950. *Sci. Rep.* 5, 13487. doi:10.1038/srep13487.
- Chao, N., Luo, Z., Wang, Z., Jin, T., 2018. Retrieving Groundwater Depletion and Drought in the Tigris-Euphrates Basin Between 2003 and 2015. *Groundwater* 56, 770–782. doi:10.1111/gwat.12611.
- Chao, N.F., Wang, Z.T., Hwang, C., Jin, T.Y., Cheng, Y.S., 2017. Decline of Geladandong Glacier Elevation in Yangtze River's Source Region: Detection by ICESat and Assessment by Hydroclimatic Data. *Remote Sens.* 9, 75. doi:10.3390/rs9010075.
- Chapman, B., McDonald, K., Shimada, M., Rosenqvist, A., Schroeder, R., Hess, L., 2015. Mapping Regional Inundation with Spaceborne L-Band SAR. *Remote Sens.* 7, 5440–5470. doi:10.3390/rs70505440.
- Chatenoux, B., Richard, J.P., Small, D., Roeoesli, C., Wingate, V., Poussin, C., Rodila, D., Peduzzi, P., Steinmeier, C., Ginzler, C., Psomas, A., Schaepman, M.E., Giuliani, G., 2021. The Swiss data cube, analysis ready data archive using earth observations of Switzerland. *Sci. Data* 8, 295. doi:10.1038/s41597-021-01076-6.
- Chatfield, C., Xing, H., 2019. *The Analysis of Time Series : An Introduction with R*. CRC Press LLC, Milton, United Kingdom.
- Chen, C., Park, T., Wang, X., Piao, S., Xu, B., Chaturvedi, R.K., Fuchs, R., Brovkin, V., Ciais, P., Fensholt, R., Tommervik, H., Bala, G., Zhu, Z., Nemani, R.R., Myneni, R.B., 2019. China and India lead in greening of the world through land-use management. *Nat. Sustain.* 2, 122–129. doi:10.1038/s41893-019-0220-7.
- Chen, D., Chen, H.W., 2013. Using the Köppen classification to quantify climate variation and change: An example for 1901–2010. *Environ. Dev.* 6, 69–79. doi:10.1016/j.envdev.2013.03.007.
- Chen, D., Rojas, M., Samset, B.H., Cobb, K., Diongue Niang, A., Edwards, P., Emori, S., Faria, S.H., Hawkins, E., Hope, P., Huybrechts, P., Meinshausen, M., Mustafa, S.K., Plattner, G.K., Tréguier, A.M., 2021a. Framing, Context, and Methods, in: Masson-Delmotte, V., Zhai, P., Pirani, A., Connors, S.L., Péan, C., Berger, S., Caud, N., Chen, Y., Goldfarb, L., Gomis, M.I., Huang, M., Leitzell, K., Lonnoy, E., Matthews, J., Maycock, T.K., Waterfield, T., Yelekçi, O., Yu, R., Zhou, B. (Eds.), *Climate Change 2021: The Physical Science Basis. Contribution of Working Group I to the Sixth Assessment Report of the Intergovernmental Panel on Climate Change*, p. 215.
- Chen, X., Liang, S., Cao, Y., He, T., Wang, D., 2015. Observed contrast changes in snow cover phenology in northern middle and high latitudes from 2001-2014. *Sci. Rep.* 5, 16820. doi:10.1038/srep16820.

- Chen, Y., Sharma, S., Zhou, X., Yang, K., Li, X., Niu, X., Hu, X., Khadka, N., 2021b. Spatial performance of multiple reanalysis precipitation datasets on the southern slope of central Himalaya. *Atmos. Res.* 250, 105365. doi:10.1016/j.atmosres.2020.105365.
- Cheng, M., Jin, J., Zhang, J., Jiang, H., Wang, R., 2017. Effect of climate change on vegetation phenology of different land-cover types on the Tibetan Plateau. *Int. J. Remote Sens.* 39, 470–487. doi:10.1080/01431161.2017.1387308.
- Chowdhury, M.D.R., Ward, N., 2004. Hydro-meteorological variability in the greater Ganges-Brahmaputra-Meghna basins. *Int. J. Climatol.* 24, 1495–1508. doi:10.1002/joc.1076.
- Claverie, M., Matthews, J., Vermote, E., Justice, C., 2016. A 30+ Year AVHRR LAI and FAPAR Climate Data Record: Algorithm Description and Validation. *Remote Sens.* 8, 263. doi:10.3390/rs8030263.
- Collaud Coen, M., Andrews, E., Bigi, A., Martucci, G., Romanens, G., Vogt, F.P.A., Vuilleumier, L., 2020. Effects of the prewhitening method, the time granularity, and the time segmentation on the Mann–Kendall trend detection and the associated Sen's slope. *Atmos. Meas. Tech.* 13, 6945–6964. doi:10.5194/amt-13-6945-2020.
- Collins, J., Riegler, G., Schrader, H., Tinz, M., 2015. Applying Terrain and Hydrological Editing to Tandem-X Data to Create a Consumer-Ready WorldDEM Product. *Int. Arch. Photogramm. Remote Sens.* XL-7/W3, 1149–1154. doi:10.5194/isprsarchives-XL-7-W3-1149-2015.
- Cook, B.I., Mankin, J.S., Marvel, K., Williams, A.P., Smerdon, J.E., Anchukaitis, K.J., 2020. Twenty-First Century Drought Projections in the CMIP6 Forcing Scenarios. *Earth's Future* 8, e2019EF001461. doi:10.1029/2019ef001461.
- Cooley, S.W., Pavelsky, T.M., 2016. Spatial and temporal patterns in Arctic river ice breakup revealed by automated ice detection from MODIS imagery. *Remote Sens. Environ.* 175, 310–322. doi:10.1016/j.rse.2016.01.004.
- Costa, M.P.F., Niemann, O., Novo, E., Ahern, F., 2002. Biophysical properties and mapping of aquatic vegetation during the hydrological cycle of the Amazon floodplain using JERS-1 and Radarsat. *Int. J. Remote Sens.* 23, 1401–1426. doi:10.1080/01431160110092957.
- Crétaux, J.F., Jelinski, W., Calmant, S., Kouraev, A., Vuglinski, V., Bergé-Nguyen, M., Gennero, M.C., Nino, F., Abarca Del Rio, R., Cazenave, A., Maisongrande, P., 2011. SOLS: A lake database to monitor in the Near Real Time water level and storage variations from remote sensing data. *Adv. Space Res.* 47, 1497–1507. doi:10.1016/j.asr.2011.01.004.
- Dangar, S., Mishra, V., 2021. Natural and anthropogenic drivers of the lost groundwater from the Ganga River basin. *Environ. Res. Lett.* 16, 114009. doi:10.1088/1748-9326/ac2ceb.
- Das, L., Meher, J.K., 2019. Drivers of climate over the Western Himalayan region of India: A review. *Earth-Sci. Rev.* 198, 102935. doi:10.1016/j.earscirev.2019.102935.
- Davie, T., Quinn, N.W., 2019. *Fundamentals of Hydrology*. Taylor & Francis Group, Florence, United States.
- Deng, Y., Jiang, W., Tang, Z., Ling, Z., Wu, Z., 2019. Long-Term Changes of Open-Surface Water Bodies in the Yangtze River Basin Based on the Google Earth Engine Cloud Platform. *Remote Sens.* 11, 2213. doi:10.3390/rs11192213.
- Desinayak, N., Prasad, A.K., El-Askary, H., Kafatos, M., Asrar, G.R., 2022. Snow cover variability and trend over the Hindu Kush Himalayan region using MODIS and SRTM data. *Ann. Geophys.* 40, 67–82. doi:10.5194/angeo-40-67-2022.

- Detsch, F., Otte, I., Appelhans, T., Hemp, A., Nauss, T., 2016a. Seasonal and long-term vegetation dynamics from 1-km GIMMS-based NDVI time series at Mt. Kilimanjaro, Tanzania. *Remote Sens. Environ.* 178, 70–83. doi:10.1016/j.rse.2016.03.007.
- Detsch, F., Otte, I., Appelhans, T., Nauss, T., 2016b. A Comparative Study of Cross-Product NDVI Dynamics in the Kilimanjaro Region—A Matter of Sensor, Degradation Calibration, and Significance. *Remote Sens.* 8, 159. doi:10.3390/rs8020159.
- Di Capua, G., Kretschmer, M., Donner, R.V., van den Hurk, B., Vellore, R., Krishnan, R., Coumou, D., 2020a. Tropical and mid-latitude teleconnections interacting with the Indian summer monsoon rainfall: a theory-guided causal effect network approach. *Earth Syst. Dyn.* 11, 17–34. doi:10.5194/esd-11-17-2020.
- Di Capua, G., Runge, J., Donner, R.V., van den Hurk, B., Turner, A.G., Vellore, R., Krishnan, R., Coumou, D., 2020b. Dominant patterns of interaction between the tropics and mid-latitudes in boreal summer: causal relationships and the role of timescales. *Weather Clim. Dyn.* 1, 519–539. doi:10.5194/wcd-1-519-2020.
- Didan, K., Munoz, A.B., 2019. MODIS vegetation index user's guide (MOD13 series), Version 3.10. University of Arizona: Vegetation Index and Phenology Lab .
- Dietz, A.J., Kuenzer, C., Dech, S., 2015. Global SnowPack: a new set of snow cover parameters for studying status and dynamics of the planetary snow cover extent. *Remote Sens. Lett.* 6, 844–853. doi:10.1080/2150704X.2015.1084551.
- Dimri, A.P., 2021. Decoding the Karakoram Anomaly. *Sci. Total Environ.* 788, 147864. doi:10.1016/j.scitotenv.2021.147864.
- Dimri, A.P., Niyogi, D., Barros, A.P., Ridley, J., Mohanty, U.C., Yasunari, T., Sikka, D.R., 2015. Western Disturbances: A review. *Rev. Geophys.* 53, 225–246. doi:10.1002/2014rg000460.
- Dirscherl, M., Dietz, A.J., Kneisel, C., Kuenzer, C., 2021. A Novel Method for Automated Supraglacial Lake Mapping in Antarctica Using Sentinel-1 SAR Imagery and Deep Learning. *Remote Sens.* 13, 197. doi:10.3390/rs13020197.
- Domeneghetti, A., Tarpanelli, A., Brocca, L., Barbetta, S., Moramarco, T., Castellarin, A., Brath, A., 2014. The use of remote sensing-derived water surface data for hydraulic model calibration. *Remote Sens. Environ.* 149, 130–141. doi:10.1016/j.rse.2014.04.007.
- Donchyts, G., Schellekens, J., Winsemius, H., Eisemann, E., van de Giesen, N., 2016. A 30 m Resolution Surface Water Mask Including Estimation of Positional and Thematic Differences Using Landsat 8, SRTM and OpenStreetMap: A Case Study in the Murray-Darling Basin, Australia. *Remote Sens.* 8, 22. doi:10.3390/rs8050386.
- Dorigo, W., Wagner, W., Albergel, C., Albrecht, F., Balsamo, G., Brocca, L., Chung, D., Ertl, M., Forkel, M., Gruber, A., Haas, E., Hamer, P.D., Hirschi, M., Ikonen, J., de Jeu, R., Kidd, R., Lahoz, W., Liu, Y.Y., Miralles, D., Mistelbauer, T., Nicolai-Shaw, N., Parinussa, R., Pratola, C., Reimer, C., van der Schalie, R., Seneviratne, S.I., Smolander, T., Lecomte, P., 2017. ESA CCI Soil Moisture for improved Earth system understanding: State-of-the art and future directions. *Remote Sens. Environ.* 203, 185–215. doi:10.1016/j.rse.2017.07.001.
- Du, J.Y., Kimball, J.S., Jones, L.A., Watts, J.D., 2016. Implementation of satellite based fractional water cover indices in the pan-Arctic region using AMSR-E and MODIS. *Remote Sens. Environ.* 184, 469–481. doi:10.1016/j.rse.2016.07.029.
- Duan, S.B., Li, Z.L., Li, H., Göttsche, F.M., Wu, H., Zhao, W., Leng, P., Zhang, X., Coll, C., 2019. Validation of Collection 6 MODIS land surface temperature product using in situ measurements. *Remote Sens. Environ.* 225, 16–29. doi:10.1016/j.rse.2019.02.020.

- Duveiller, G., Defourny, P., Desclee, B., Mayaux, P., 2008. Deforestation in Central Africa: Estimates at regional, national and landscape levels by advanced processing of systematically-distributed Landsat extracts. *Remote Sens. Environ.* 112, 1969–1981. doi:10.1016/j.rse.2007.07.026.
- Eckert, S., Hüsler, F., Liniger, H., Hodel, E., 2015. Trend analysis of MODIS NDVI time series for detecting land degradation and regeneration in Mongolia. *J. Arid Environ.* 113, 16–28. doi:10.1016/j.jaridenv.2014.09.001.
- Eklundh, L., Jönsson, P., 2017. TIMESAT 3.3 with seasonal trend decomposition and parallel processing software manual. Lund Malmo University, Sweden.
- Erasmi, S., Schucknecht, A., Barbosa, M., Matschullat, J., 2014. Vegetation Greenness in Northeastern Brazil and Its Relation to ENSO Warm Events. *Remote Sens.* 6, 3041–3058. doi:10.3390/rs6043041.
- Estupinan-Suarez, L.M., Gans, F., Brenning, A., Gutierrez-Velez, V.H., Londono, M.C., Pabon-Moreno, D.E., Poveda, G., Reichstein, M., Reu, B., Sierra, C.A., Weber, U., Mahecha, M.D., 2021. A Regional Earth System Data Lab for Understanding Ecosystem Dynamics: An Example from Tropical South America. *Front. Earth Sci.* 9, 613395. doi:10.3389/feart.2021.613395.
- European Space Agency, 2017. Land Cover CCI Product User Guide Version 2. Tech. Rep. URL: maps.elie.ucl.ac.be/CCI/viewer/download/ESACCI-LC-Ph2-PUGv2_2.0.pdf.
- European Space Agency, Sinergise, 2021. Copernicus Global Digital Elevation Model. Distributed by OpenTopography. doi:10.5069/G9028PQB. (Last accessed on: 2022-02-01).
- Evenson, R.E., Gollin, D., 2003. Assessing the impact of the green revolution, 1960 to 2000. *Science* 300, 758–62. doi:10.1126/science.1078710.
- FAO, 2009. Hydrological basins in Southeast Asia. URL: <https://data.apps.fao.org/map/catalog/static/api/records/ee616dc4-3118-4d67-ba05-6e93dd3e962f>. (Last accessed on: 2022-02-01).
- Farinosi, F., Giupponi, C., Reynaud, A., Ceccherini, G., Carmona-Moreno, C., De Roo, A., Gonzalez-Sanchez, D., Bidoglio, G., 2018. An innovative approach to the assessment of hydro-political risk: A spatially explicit, data driven indicator of hydro-political issues. *Glob. Environ. Chang.* 52, 286–313. doi:10.1016/j.gloenvcha.2018.07.001.
- Farinotti, D., Huss, M., Fürst, J.J., Landmann, J., Machguth, H., Maussion, F., Pandit, A., 2019. A consensus estimate for the ice thickness distribution of all glaciers on Earth. *Nat. Geosci.* 12, 168–173. doi:10.1038/s41561-019-0300-3.
- Farinotti, D., Immerzeel, W.W., de Kok, R., Quincey, D.J., Dehecq, A., 2020. Manifestations and mechanisms of the Karakoram glacier Anomaly. *Nat. Geosci.* 13, 8–16. doi:10.1038/s41561-019-0513-5.
- Farr, T.G., Rosen, P.A., Caro, E., Crippen, R., Duren, R., Hensley, S., Kobrick, M., Paller, M., Rodriguez, E., Roth, L., Seal, D., Shaffer, S., Shimada, J., Umland, J., Werner, M., Oskin, M., Burbank, D., Alsdorf, D., 2007. The Shuttle Radar Topography Mission. *Rev. Geophys.* 45, 2005RG000183. doi:10.1029/2005RG000183.
- Fassoni-Andrade, A.C., de Paiva, R.C.D., 2019. Mapping spatial-temporal sediment dynamics of river-floodplains in the Amazon. *Remote Sens. Environ.* 221, 94–107. doi:10.1016/j.rse.2018.10.038.
- Fatras, C., Parrens, M., Peña Luque, S., Al Bitar, A., 2021. Hydrological Dynamics of the Congo Basin From Water Surfaces Based on L-Band Microwave. *Water Resour. Res.* 57, e2020WR027259. doi:10.1029/2020WR027259.

- Fensholt, R., Proud, S.R., 2012. Evaluation of Earth Observation based global long term vegetation trends — Comparing GIMMS and MODIS global NDVI time series. *Remote Sens. Environ.* 119, 131–147. doi:10.1016/j.rse.2011.12.015.
- Ferreira, K.R., Queiroz, G.R., Vinhas, L., Marujo, R.F.B., Simoes, R.E.O., Picoli, M.C.A., Camara, G., Cartaxo, R., Gomes, V.C.F., Santos, L.A., Sanchez, A.H., Arcanjo, J.S., Fronza, J.G., Noronha, C.A., Costa, R.W., Zaglia, M.C., Zioti, F., Korting, T.S., Soares, A.R., Chaves, M.E.D., Fonseca, L.M.G., 2020. Earth Observation Data Cubes for Brazil: Requirements, Methodology and Products. *Remote Sens.* 12, 4033. doi:10.3390/rs12244033.
- Fick, S.E., Hijmans, R.J., 2017. WorldClim 2: new 1-km spatial resolution climate surfaces for global land areas. *Int. J. Climatol.* 37, 4302–4315. doi:10.1002/joc.5086.
- Forkel, M., Carvalhais, N., Verbesselt, J., Mahecha, M., Neigh, C., Reichstein, M., 2013. Trend Change Detection in NDVI Time Series: Effects of Inter-Annual Variability and Methodology. *Remote Sens.* 5, 2113–2144. doi:10.3390/rs5052113.
- Formayer, H., Fritz, A., 2017. Temperature dependency of hourly precipitation intensities - surface versus cloud layer temperature. *Int. J. Climatol.* 37, 1–10. doi:10.1002/joc.4678.
- Frappart, F., Calmant, S., Cauhope, M., Seyler, F., Cazenave, A., 2006. Preliminary results of ENVISAT RA-2-derived water levels validation over the Amazon basin. *Remote Sens. Environ.* 100, 252–264. doi:10.1016/j.rse.2005.10.027.
- Friedl, M.A., McIver, D.K., Hodges, J.C., Zhang, X.Y., Muchoney, D., Strahler, A.H., Woodcock, C.E., Gopal, S., Schneider, A., Cooper, A., 2002. Global land cover mapping from MODIS: algorithms and early results. *Remote Sens. Environ.* 83, 287–302.
- Frolking, S., Milliman, T., Palace, M., Wisser, D., Lammers, R., Fahnestock, M., 2011. Tropical forest backscatter anomaly evident in Sea Winds scatterometer morning overpass data during 2005 drought in Amazonia. *Remote Sens. Environ.* 115, 897–907. doi:10.1016/j.rse.2010.11.017.
- Funk, C., Peterson, P., Landsfeld, M., Pedreros, D., Verdin, J., Shukla, S., Husak, G., Rowland, J., Harrison, L., Hoell, A., Michaelsen, J., 2015. The climate hazards infrared precipitation with stations—a new environmental record for monitoring extremes. *Sci. Data* 2, 150066. doi:10.1038/sdata.2015.66.
- Furtado, L.F.D., Silva, T.S.F., Novo, E., 2016. Dual-season and full-polarimetric C band SAR assessment for vegetation mapping in the Amazon varzea wetlands. *Remote Sens. Environ.* 174, 212–222. doi:10.1016/j.rse.2015.12.013.
- Fuster, B., Sánchez-Zapero, J., Camacho, F., García-Santos, V., Verger, A., Lacaze, R., Weiss, M., Baret, F., Smets, B., 2020. Quality Assessment of PROBA-V LAI, fAPAR and fCOVER Collection 300 m Products of Copernicus Global Land Service. *Remote Sens.* 12, 1017. doi:10.3390/rs12061017.
- Gain, A., Giupponi, C., 2014. Impact of the Farakka Dam on Thresholds of the Hydrologic Flow Regime in the Lower Ganges River Basin (Bangladesh). *Water* 6, 2501–2518. doi:10.3390/w6082501.
- Ganeshi, N.G., Mujumdar, M., Krishnan, R., Goswami, M., 2020. Understanding the linkage between soil moisture variability and temperature extremes over the Indian region. *J. Hydrol.* 589, 125183. doi:10.1016/j.jhydrol.2020.125183.
- Gao, J., Williams, M.W., Fu, X., Wang, G., Gong, T., 2012. Spatiotemporal distribution of snow in eastern Tibet and the response to climate change. *Remote Sens. Environ.* 121, 1–9. doi:10.1016/j.rse.2012.01.006.
- Gao, Y., Chen, F., Lettenmaier, D.P., Xu, J., Xiao, L., Li, X., 2018. Does elevation-dependent warming hold true above 5000 m elevation? Lessons from the Tibetan Plateau. *NPJ Clim. Atmos. Sci.* 1, 1–19. doi:10.1038/s41612-018-0030-z.

- Ge, J., Meng, B.P., Liang, T.G., Feng, Q.S., Gao, J.L., Yang, S.X., Huang, X.D., Xie, H.J., 2018. Modeling alpine grassland cover based on MODIS data and support vector machine regression in the headwater region of the Huanghe River, China. *Remote Sens. Environ.* 218, 162–173. doi:10.1016/j.rse.2018.09.019.
- Gessner, U., Naeimi, V., Klein, I., Kuenzer, C., Klein, D., Dech, S., 2013. The relationship between precipitation anomalies and satellite-derived vegetation activity in Central Asia. *Glob. Planet. Chang.* 110, 74–87. doi:10.1016/j.gloplacha.2012.09.007.
- Giuliani, G., Chatenoux, B., De Bono, A., Rodila, D., Richard, J.P., Allenbach, K., Dao, H., Peduzzi, P., 2017. Building an Earth Observations Data Cube: lessons learned from the Swiss Data Cube (SDC) on generating Analysis Ready Data (ARD). *Big Earth Data* 1, 100–117. doi:10.1080/20964471.2017.1398903.
- Gocic, M., Trajkovic, S., 2013. Analysis of changes in meteorological variables using Mann-Kendall and Sen's slope estimator statistical tests in Serbia. *Glob. Planet. Chang.* 100, 172–182. doi:10.1016/j.gloplacha.2012.10.014.
- Gorelick, N., Hancher, M., Dixon, M., Ilyushchenko, S., Thau, D., Moore, R., 2017. Google Earth Engine: Planetary-scale geospatial analysis for everyone. *Remote Sens. Environ.* 202, 18–27. doi:10.1016/j.rse.2017.06.031.
- Gouweleeuw, B.T., Kvas, A., Gruber, C., Gain, A.K., Mayer-Gürr, T., Flechtner, F., Güntner, A., 2018. Daily GRACE gravity field solutions track major flood events in the Ganges–Brahmaputra Delta. *Hydrol. Earth Syst. Sci.* 22, 2867–2880. doi:10.5194/hess-22-2867-2018.
- de Grandi, G.F., Mayaux, P., Malingreau, J.P., Rosenqvist, A., Saatchi, S., Simard, M., 2000. New perspectives on global ecosystems from wide-area radar mosaics: flooded forest mapping in the tropics. *Int. J. Remote Sens.* 21, 1235–1249. doi:10.1080/014311600210155.
- Granger, C.W.J., 1969. Investigating Causal Relations by Econometric Models and Cross-spectral Methods. *Econometrica* 37. doi:10.2307/1912791.
- GRDC, 2020. Major River Basins of the World / Global Runoff Data Centre, GRDC. 2nd, rev. ext. ed. Koblenz, Germany: Federal Institute of Hydrology (BfG). URL: https://www.bafg.de/GRDC/EN/02_srvcs/22_gslrs/221_MRB/riverbasins_node.html. (Last accessed on: 2022-02-01).
- Griffin, C.G., McClelland, J.W., Frey, K.E., Fiske, G., Holmes, R.M., 2018. Quantifying CDOM and DOC in major Arctic rivers during ice-free conditions using Landsat TM and ETM+ data. *Remote Sens. Environ.* 209, 395–409. doi:10.1016/j.rse.2018.02.060.
- Grill, G., Lehner, B., Thieme, M., Geenen, B., Tickner, D., Antonelli, F., Babu, S., Borrelli, P., Cheng, L., Crochetiere, H., Ehalt Macedo, H., Filgueiras, R., Goichot, M., Higgins, J., Hogan, Z., Lip, B., McClain, M.E., Meng, J., Mulligan, M., Nilsson, C., Olden, J.D., Opperman, J.J., Petry, P., Reidy Liermann, C., Sáenz, L., Salinas-Rodríguez, S., Schelle, P., Schmitt, R.J.P., Snider, J., Tan, F., Tockner, K., Valdujo, P.H., van Soesbergen, A., Zarfl, C., 2019. Mapping the world's free-flowing rivers. *Nature* 569, 215–221. doi:10.1038/s41586-019-1111-9.
- Grimaldi, S., Li, Y., Pauwels, V.R.N., Walker, J.P., 2016. Remote Sensing-Derived Water Extent and Level to Constrain Hydraulic Flood Forecasting Models: Opportunities and Challenges. *Surv. Geophys.* 37, 977–1034. doi:10.1007/s10712-016-9378-y.
- Grumbine, R.E., Pandit, M.K., 2013. Ecology. Threats from India's Himalaya dams. *Science* 339, 36–7. doi:10.1126/science.1227211.
- Gu, L., Chen, J., Yin, J., Sullivan, S.C., Wang, H.M., Guo, S., Zhang, L., Kim, J.S., 2020. Projected increases in magnitude and socioeconomic exposure of global droughts in 1.5 and 2°C warmer climates. *Hydrol. Earth Syst. Sci.* 24, 451–472. doi:10.5194/hess-24-451-2020.

- Guerreiro, S.B., Fowler, H.J., Barbero, R., Westra, S., Lenderink, G., Blenkinsop, S., Lewis, E., Li, X.F., 2018. Detection of continental-scale intensification of hourly rainfall extremes. *Nat. Clim. Chang.* 8, 803–807. doi:10.1038/s41558-018-0245-3.
- Guerschman, J.P., Warren, G., Byrne, G., Lymburner, L., Mueller, N., Van-Dijk, A., 2011. MODIS-based standing water detection for flood and large reservoir mapping: algorithm development and applications for the Australian continent. CSIRO: Water for a Healthy Country National Research Flagship Report, Canberra.
- Gumma, M.K., Thenkabail, P.S., Teluguntla, P., Whitbread, A.M., 2019. Chapter 9 - Indo-Ganges River Basin Land Use/Land Cover (LULC) and Irrigated Area Mapping, in: Khan, S.I., Adams, T.E. (Eds.), *Indus River Basin*. Elsevier, pp. 203–228. doi:10.1016/B978-0-12-812782-7.00010-2.
- Gupta, V., Jain, M.K., Singh, P.K., Singh, V., 2019. An assessment of global satellite-based precipitation datasets in capturing precipitation extremes: A comparison with observed precipitation dataset in India. *Int. J. Climatol.* 40, 3667–3688. doi:10.1002/joc.6419.
- Gurung, D.R., Maharjan, S.B., Shrestha, A.B., Shrestha, M.S., Bajracharya, S.R., Murthy, M.S.R., 2017. Climate and topographic controls on snow cover dynamics in the Hindu Kush Himalaya. *Int. J. Climatol.* 37, 3873–3882. doi:10.1002/joc.4961.
- Haddeland, I., Heinke, J., Biemans, H., Eisner, S., Flörke, M., Hanasaki, N., Konzmann, M., Ludwig, F., Masaki, Y., Schewe, J., Stacke, T., Tessler, Z.D., Wada, Y., Wisser, D., 2014. Global water resources affected by human interventions and climate change. *Proc. Natl. Acad. Sci. U.S.A.* 111, 3251. doi:10.1073/pnas.1222475110.
- Hall, D.K., Riggs, G.A., 2007. Accuracy assessment of the MODIS snow products. *Hydrol. Process.* 21, 1534–1547. doi:10.1002/hyp.6715.
- Hall, D.K., Riggs, G.A., Salomonson, V.V., DiGirolamo, N.E., Bayr, K.J., 2002. MODIS snow-cover products. *Remote Sens. Environ.* 83, 181–194. doi:10.1016/s0034-4257(02)00095-0.
- Hamed, K.H., Ramachandra Rao, A., 1998. A modified Mann-Kendall trend test for auto-correlated data. *J. Hydrol.* 204, 182–196. doi:10.1016/s0022-1694(97)00125-x.
- Hansen, M.C., Potapov, P.V., Moore, R., Hancher, M., Turubanova, S.A., Tyukavina, A., Thau, D., Stehman, S.V., Goetz, S.J., Loveland, T.R., Kommareddy, A., Egorov, A., Chini, L., Justice, C.O., Townshend, J.R.G., 2013. High-Resolution Global Maps of 21st-Century Forest Cover Change. *Science* 342, 850–853. doi:10.1126/science.1244693.
- Harrigan, S., Zsoter, E., Alfieri, L., Prudhomme, C., Salamon, P., Wetterhall, F., Barnard, C., Cloke, H., Pappenberger, F., 2020. GloFAS-ERA5 operational global river discharge reanalysis 1979–present. *Earth Syst. Sci. Data* 12, 2043–2060. doi:10.5194/essd-12-2043-2020.
- Harris, I., Osborn, T.J., Jones, P., Lister, D., 2020. Version 4 of the CRU TS monthly high-resolution gridded multivariate climate dataset. *Sci. Data* 7, 109. doi:10.1038/s41597-020-0453-3.
- Hecht, J.S., Lacombe, G., Arias, M.E., Dang, T.D., Piman, T., 2019. Hydropower dams of the Mekong River basin: A review of their hydrological impacts. *J. Hydrol.* 568, 285–300. doi:10.1016/j.jhydrol.2018.10.045.
- Heimhuber, V., Tulbure, M.G., Broich, M., 2016. Modeling 25 years of spatio-temporal surface water and inundation dynamics on large river basin scale using time series of Earth observation data. *Hydrol. Earth Syst. Sci.* 20, 2227–2250. doi:10.5194/hess-20-2227-2016.

- Heimhuber, V., Tulbure, M.G., Broich, M., 2017. Modeling multidecadal surface water inundation dynamics and key drivers on large river basin scale using multiple time series of Earth-observation and river flow data. *Water Resour. Res.* 53, 1251–1269. doi:10.1002/2016wr019858.
- Hersbach, H., Bell, B., Berrisford, P., Hirahara, S., Horányi, A., Muñoz-Sabater, J., Nicolas, J., Peubey, C., Radu, R., Schepers, D., Simmons, A., Soci, C., Abdalla, S., Abellan, X., Balsamo, G., Bechtold, P., Biavati, G., Bidlot, J., Bonavita, M., Chiara, G., Dahlgren, P., Dee, D., Diamantakis, M., Dragani, R., Flemming, J., Forbes, R., Fuentes, M., Geer, A., Haimberger, L., Healy, S., Hogan, R.J., Hólm, E., Janisková, M., Keeley, S., Laloyaux, P., Lopez, P., Lupu, C., Radnoti, G., Rosnay, P., Rozum, I., Vamborg, F., Villaume, S., Thépaut, J., 2020. The ERA5 global reanalysis. *Q. J. R. Meteorol. Soc.* doi:10.1002/qj.3803.
- Hilker, T., Lyapustin, A.I., Hall, F.G., Myneni, R., Knyazikhin, Y., Wang, Y.J., Tucker, C.J., Sellers, P.J., 2015. On the measurability of change in Amazon vegetation from MODIS. *Remote Sens. Environ.* 166, 233–242. doi:10.1016/j.rse.2015.05.020.
- Hock, R., Rasul, G., Adler, C., Cáceres, B., Gruber, S., Hirabayashi, Y., Jackson, M., Kääb, A., Kang, S., Kutuzov, S., Milner, A., Molau, U., Morin, S., Orlove, B., Steltzer, H., 2019. High Mountain Areas, in: Pörtner, H.O., Roberts, D.C., Masson-Delmotte, V., Zhai, P., Tignor, M., Poloczanska, E., Mintenbeck, K., Alegría, A., Nicolai, M., Okem, A., Petzold, J., Rama, B., Weyer, N. (Eds.), *IPCC Special Report on the Ocean and Cryosphere in a Changing Climate*, pp. 131–202.
- Hu, Z., Dietz, A., Zhao, A., Uereyen, S., Zhang, H., Wang, M., Mederer, P., Kuenzer, C., 2020. Snow Moving to Higher Elevations: Analyzing Three Decades of Snowline Dynamics in the Alps. *Geophys. Res. Lett.* 47, e2019GL085742. doi:10.1029/2019gl085742.
- Huang, C., Chen, Y., Wu, J.P., 2014. Mapping spatio-temporal flood inundation dynamics at large river basin scale using time-series flow data and MODIS imagery. *Int. J. Appl. Earth Obs. Geoinf.* 26, 350–362. doi:10.1016/j.jag.2013.09.002.
- Huang, C., Chen, Y., Zhang, S., Wu, J., 2018a. Detecting, Extracting, and Monitoring Surface Water From Space Using Optical Sensors: A Review. *Rev. Geophys.* 56, 333–360. doi:10.1029/2018rg000598.
- Huang, Q., Long, D., Du, M.D., Zeng, C., Li, X.D., Hou, A.Z., Hong, Y., 2018b. An improved approach to monitoring Brahmaputra River water levels using retracked altimetry data. *Remote Sens. Environ.* 211, 112–128. doi:10.1016/j.rse.2018.04.018.
- Huang, S.L., Jin, S.M., Dahal, D., Chen, X.X., Young, C., Liu, H.P., Liu, S.G., 2013. Reconstructing satellite images to quantify spatially explicit land surface change caused by fires and succession: A demonstration in the Yukon River Basin of interior Alaska. *ISPRS J. Photogramm. Remote Sens.* 79, 94–105. doi:10.1016/j.isprsjprs.2013.02.010.
- Huang, X., Deng, J., Wang, W., Feng, Q., Liang, T., 2017. Impact of climate and elevation on snow cover using integrated remote sensing snow products in Tibetan Plateau. *Remote Sens. Environ.* 190, 274–288. doi:10.1016/j.rse.2016.12.028.
- Iftekhhar, M.S., Saenger, P., 2007. Vegetation dynamics in the Bangladesh Sundarbans mangroves: a review of forest inventories. *Wetl. Ecol. Manag.* 16, 291–312. doi:10.1007/s11273-007-9063-5.
- IMF, 2021. World Economic and Financial Surveys. World Economic Outlook Database. April 2021 Edition. URL: <https://www.imf.org/en/Publications/WEO/weo-database/2021/April/>.
- IPCC, 2013. *Climate Change 2013: The Physical Science Basis. Contribution of Working Group I to the Fifth Assessment Report of the Intergovernmental Panel on Climate Change*. Cambridge University Press, Cambridge, United Kingdom and New York, NY, USA. doi:10.1017/cbo9781107415324.004.

- IPCC, 2019a. Summary for Policymakers, in: Shukla, P.R., Skea, J., Calvo Buendi, E., Masson-Delmotte, V., Pörtner, H.O., Roberts, D.C., Zhai, P., Slade, R., Connors, S., Diemen, R.v., Ferrat, M., Haughey, E., Luz, S., Neogi, S., Pathak, M., Petzold, J., Portugal Pereira, J., Vyas, P., Huntley, E., Kissick, K., Belkacemi, M., Malley, J. (Eds.), *Climate Change and Land: an IPCC special report on climate change, desertification, land degradation, sustainable land management, food security, and greenhouse gas fluxes in terrestrial ecosystems*, pp. 1–36.
- IPCC, 2019b. Summary for Policymakers, in: Pörtner, H.O., Roberts, D.C., Masson-Delmotte, V., Zhai, P., Tignor, M., Poloczanska, E., Mintenbeck, K., Alegría, A., Nicolai, M., Okem, A., Petzold, J., Rama, B., Weyer, N. (Eds.), *IPCC Special Report on the Ocean and Cryosphere in a Changing Climate*, pp. 1–35.
- IPCC, 2019c. Technical Summary, in: Pörtner, H.O., Roberts, D.C., Masson-Delmotte, V., Zhai, P., Tignor, M., Poloczanska, E., Mintenbeck, K., Alegría, A., Nicolai, M., Okem, A., Petzold, J., Rama, B., Weyer, N.M. (Eds.), *IPCC Special Report on the Ocean and Cryosphere in a Changing Climate*, pp. 37–69.
- IPCC, 2021. Summary for Policymakers, in: Masson-Delmotte, V., Zhai, P., Pirani, A., Connors, S.L., Péan, C., Berger, S., Caud, N., Chen, Y., Goldfarb, L., Gomis, M.I., Huang, M., Leitzell, K., Lonnoy, E., Matthews, J., Maycock, T.K., Waterfield, T., Yelekçi, O., Yu, R., Zhou, B. (Eds.), *Climate Change 2021: The Physical Science Basis. Contribution of Working Group I to the Sixth Assessment Report of the Intergovernmental Panel on Climate Change*. Cambridge University Press, pp. 1–31.
- Islam, M.A., Cartwright, N., 2020. Evaluation of climate reanalysis and space-borne precipitation products over Bangladesh. *Hydrol. Sci. J.* 65, 1112–1128. doi:10.1080/02626667.2020.1730845.
- Janes, T., McGrath, F., Macadam, I., Jones, R., 2019. High-resolution climate projections for South Asia to inform climate impacts and adaptation studies in the Ganges-Brahmaputra-Meghna and Mahanadi deltas. *Sci. Total Environ.* 650, 1499–1520. doi:10.1016/j.scitotenv.2018.08.376.
- Ji, Q., Liang, W., Fu, B., Zhang, W., Yan, J., Lü, Y., Yue, C., Jin, Z., Lan, Z., Li, S., Yang, P., 2021. Mapping Land Use/Cover Dynamics of the Yellow River Basin from 1986 to 2018 Supported by Google Earth Engine. *Remote Sens.* 13, 1299. doi:10.3390/rs13071299.
- Ji, Z., Kang, S., 2012. Projection of snow cover changes over China under RCP scenarios. *Clim. Dyn.* 41, 589–600. doi:10.1007/s00382-012-1473-2.
- Jia, G., Shevliakova, E., Artaxo, P., Noblet-Ducoudré, D., Houghton, R., House, J., Kitajima, K., Lennard, C., Popp, A., Sirin, A., 2019. Land-climate interactions, in: Shukla, P.R., Skea, J., Calvo Buendi, E., Masson-Delmotte, V., Pörtner, H.O., Roberts, D.C., Zhai, P., Slade, R., Connors, S., Diemen, R.v., Ferrat, M., Haughey, E., Luz, S., Neogi, S., Pathak, M., Petzold, J., Portugal Pereira, J., Vyas, P., Huntley, E., Kissick, K., Belkacemi, M., Malley, J. (Eds.), *Climate Change and Land: an IPCC special report on climate change, desertification, land degradation, sustainable land management, food security, and greenhouse gas fluxes in terrestrial ecosystems*. Cambridge University Press, pp. 131–247.
- Jin, Q., Wang, C., 2017. A revival of Indian summer monsoon rainfall since 2002. *Nat. Clim. Chang.* 7, 587–594. doi:10.1038/nclimate3348.
- John, R., Chen, J., Giannico, V., Park, H., Xiao, J., Shirkey, G., Ouyang, Z., Shao, C., Laforteza, R., Qi, J., 2018. Grassland canopy cover and aboveground biomass in Mongolia and Inner Mongolia: Spatiotemporal estimates and controlling factors. *Remote Sens. Environ.* 213, 34–48. doi:10.1016/j.rse.2018.05.002.
- de Jong, R., de Bruin, S., de Wit, A., Schaepman, M.E., Dent, D.L., 2011. Analysis of monotonic greening and browning trends from global NDVI time-series. *Remote Sens. Environ.* 115, 692–702. doi:10.1016/j.rse.2010.10.011.

- Justice, C.O., Townshend, J.R.G., Vermote, E.F., Masuoka, E., Wolfe, R.E., Saleous, N., Roy, D.P., Morisette, J.T., 2002. An overview of MODIS Land data processing and product status. *Remote Sens. Environ.* 83, 3–15. doi:10.1016/S0034-4257(02)00084-6.
- Jönsson, P., Eklundh, L., 2002. Seasonality extraction by function fitting to time-series of satellite sensor data. *IEEE Trans. Geosci. Remote Sens.* 40, 1824–1832.
- Jönsson, P., Eklundh, L., 2004. TIMESAT—a program for analyzing time-series of satellite sensor data. *Comput. Geosci.* 30, 833–845. doi:10.1016/j.cageo.2004.05.006.
- Kath, J., Byrareddy, V.M., Craparo, A., Nguyen-Huy, T., Mushtaq, S., Cao, L., Bossolasco, L., 2020. Not so robust: Robusta coffee production is highly sensitive to temperature. *Glob. Chang. Biol.* 26, 3677–3688. doi:10.1111/gcb.15097.
- Kathayat, G., Cheng, H., Sinha, A., Yi, L., Li, X., Zhang, H., Li, H., Ning, Y., Edwards, R.L., 2017. The Indian monsoon variability and civilization changes in the Indian sub-continent. *Sci. Adv.* 3, e1701296. doi:10.1126/sciadv.1701296.
- Kendall, M.G., 1975. *Rank Correlation Methods*. Oxford University Press, New York.
- Kennedy, R.E., Yang, Z., Cohen, W.B., 2010. Detecting trends in forest disturbance and recovery using yearly Landsat time series: 1. LandTrendr — Temporal segmentation algorithms. *Remote Sens. Environ.* 114, 2897–2910. doi:10.1016/j.rse.2010.07.008.
- Khan, S.I., Hong, Y., Gourley, J.J., Khattak, M.U., De Groeve, T., 2014. Multi-Sensor Imaging and Space-Ground Cross-Validation for 2010 Flood along Indus River, Pakistan. *Remote Sens.* 6, 2393–2407. doi:10.3390/rs6032393.
- Killough, B., 2019. The Impact of Analysis Ready Data in the Africa Regional Data Cube, in: *Int. Geosci. Remote Sens. Symp. (IGARSS)*, pp. 5646–5649. doi:10.1109/IGARSS.2019.8898321.
- Kim, D., Lee, H., Laraque, A., Tshimanga, R.M., Yuan, T., Jung, H.C., Beighley, E., Chang, C.H., 2017. Mapping spatio-temporal water level variations over the central Congo River using PALSAR ScanSAR and Envisat altimetry data. *Int. J. Remote Sens.* 38, 7021–7040. doi:10.1080/01431161.2017.1371867.
- Klein, I., Gessner, U., Dietz, A.J., Kuenzer, C., 2017. Global WaterPack – A 250m resolution dataset revealing the daily dynamics of global inland water bodies. *Remote Sens. Environ.* 198, 345–362. doi:10.1016/j.rse.2017.06.045.
- Klein, I., Mayr, S., Gessner, U., Hirner, A., Kuenzer, C., 2021. Water and hydropower reservoirs: High temporal resolution time series derived from MODIS data to characterize seasonality and variability. *Remote Sens. Environ.* 253, 112207. doi:10.1016/j.rse.2020.112207.
- Koehler, J., Kuenzer, C., 2020. Forecasting Spatio-Temporal Dynamics on the Land Surface Using Earth Observation Data—A Review. *Remote Sens.* 12, 3513. doi:10.3390/rs12213513.
- Kolluru, V., Kolluru, S., Konkathi, P., 2020. Evaluation and integration of reanalysis rainfall products under contrasting climatic conditions in India. *Atmos. Res.* 246, 105121. doi:10.1016/j.atmosres.2020.105121.
- Konings, A.G., Williams, A.P., Gentine, P., 2017. Sensitivity of grassland productivity to aridity controlled by stomatal and xylem regulation. *Nat. Geosci.* 10, 284–288. doi:10.1038/ngeo2903.
- Kontgis, C., Schneider, A., Ozdogan, M., 2015. Mapping rice paddy extent and intensification in the Vietnamese Mekong River Delta with dense time stacks of Landsat data. *Remote Sens. Environ.* 169, 255–269. doi:10.1016/j.rse.2015.08.004.

- Kraaijenbrink, P.D.A., Stigter, E.E., Yao, T., Immerzeel, W.W., 2021. Climate change decisive for Asia's snow meltwater supply. *Nat. Clim. Chang.* 11, 591–597. doi:10.1038/s41558-021-01074-x.
- Kretschmer, M., Coumou, D., Donges, J.F., Runge, J., 2016. Using Causal Effect Networks to Analyze Different Arctic Drivers of Midlatitude Winter Circulation. *J. Clim.* 29, 4069–4081. doi:10.1175/jcli-d-15-0654.1.
- Krich, C., Runge, J., Miralles, D.G., Migliavacca, M., Perez-Priego, O., El-Madany, T., Carrara, A., Mahecha, M.D., 2020. Estimating causal networks in biosphere–atmosphere interaction with the PCMCI approach. *Biogeosciences* 17, 1033–1061. doi:10.5194/bg-17-1033-2020.
- Krispin, R., 2019. *Hands-On Time Series Analysis with R : Perform Time Series Analysis and Forecasting Using R*. Packt Publishing, Limited, Birmingham, United Kingdom.
- Kuenzer, C., Dech, S., Wagner, W., 2015a. Remote Sensing Time Series Revealing Land Surface Dynamics: Status Quo and the Pathway Ahead, in: *Remote Sensing Time Series*. Springer, Cham. Remote Sensing and Digital Image Processing. book section Chapter 1, pp. 1–24. doi:10.1007/978-3-319-15967-6_1.
- Kuenzer, C., Klein, I., Ullmann, T., Georgiou, E.F., Baumhauer, R., Dech, S., 2015b. Remote Sensing of River Delta Inundation: Exploiting the Potential of Coarse Spatial Resolution, Temporally-Dense MODIS Time Series. *Remote Sens.* 7, 8516–8542. doi:10.3390/rs70708516.
- Kuhn, C., Valerio, A.D., Ward, N., Loken, L., Sawakuchi, H.O., Karnpel, M., Richey, J., Stadler, P., Crawford, J., Striegl, R., Vermote, E., Pahlevan, N., Butman, D., 2019. Performance of Landsat-8 and Sentinel-2 surface reflectance products for river remote sensing retrievals of chlorophyll-a and turbidity. *Remote Sens. Environ.* 224, 104–118. doi:10.1016/j.rse.2019.01.023.
- Kumar, R., Nath, A.J., Nath, A., Sahu, N., Pandey, R., 2022. Landsat-based multi-decadal spatio-temporal assessment of the vegetation greening and browning trend in the Eastern Indian Himalayan Region. *Remote Sens. Appl.: Soc. Environ.* 25, 100695. doi:10.1016/j.rsase.2022.100695.
- Kummu, M., Taka, M., Guillaume, J.H.A., 2018. Gridded global datasets for Gross Domestic Product and Human Development Index over 1990–2015. *Sci. Data* 5, 180004. doi:10.1038/sdata.2018.4.
- Kvas, A., Behzadpour, S., Ellmer, M., Klinger, B., Strasser, S., Zehentner, N., Mayer-Gürr, T., 2019. ITSG-Grace2018: Overview and Evaluation of a New GRACE-Only Gravity Field Time Series. *J. Geophys. Res. Solid Earth* 124, 9332–9344. doi:10.1029/2019jb017415.
- Kwak, Y., Park, J., Fukami, K., 2014. Near Real-Time Flood Volume Estimation From MODIS Time-Series Imagery in the Indus River Basin. *IEEE J. Sel. Top. Appl. Earth. Obs. Remote Sens.* 7, 578–586. doi:10.1109/jstars.2013.2284607.
- Lam, N.S.N., Cheng, W.J., Zou, L., Cai, H., 2018. Effects of landscape fragmentation on land loss. *Remote Sens. Environ.* 209, 253–262. doi:10.1016/j.rse.2017.12.034.
- Lamchin, M., Lee, W.K., Jeon, S.W., Wang, S.W., Lim, C.H., Song, C., Sung, M., 2018. Long-term trend and correlation between vegetation greenness and climate variables in Asia based on satellite data. *Sci. Total Environ.* 618, 1089–1095. doi:10.1016/j.scitotenv.2017.09.145.
- Lehner, B., Verdin, K., Jarvis, A., 2008. New global hydrography derived from spaceborne elevation data. *Eos, Transactions American Geophysical Union* 89, 93–94.

- Leinenkugel, P., Kuenzer, C., Oppelt, N., Dech, S., 2013. Characterisation of land surface phenology and land cover based on moderate resolution satellite data in cloud prone areas - A novel product for the Mekong Basin. *Remote Sens. Environ.* 136, 180–198. doi:10.1016/j.rse.2013.05.004.
- Lewis, A., Oliver, S., Lymburner, L., Evans, B., Wyborn, L., Mueller, N., Raevksi, G., Hooke, J., Woodcock, R., Sixsmith, J., Wu, W., Tan, P., Li, F., Killough, B., Minchin, S., Roberts, D., Ayers, D., Bala, B., Dwyer, J., Dekker, A., Dhu, T., Hicks, A., Ip, A., Purss, M., Richards, C., Sagar, S., Trenham, C., Wang, P., Wang, L.W., 2017. The Australian Geoscience Data Cube — Foundations and lessons learned. *Remote Sens. Environ.* 202, 276–292. doi:10.1016/j.rse.2017.03.015.
- Li, L., Zhang, Y., Liu, L., Wu, J., Wang, Z., Li, S., Zhang, H., Zu, J., Ding, M., Paudel, B., 2018. Spatiotemporal Patterns of Vegetation Greenness Change and Associated Climatic and Anthropogenic Drivers on the Tibetan Plateau during 2000–2015. *Remote Sens.* 10, 1525. doi:10.3390/rs10101525.
- Li, M., Wu, P., Ma, Z., 2020. A comprehensive evaluation of soil moisture and soil temperature from third-generation atmospheric and land reanalysis data sets. *Int. J. Climatol.* 40, 5744–5766. doi:10.1002/joc.6549.
- Li, X., Zhou, Y., 2017. A Stepwise Calibration of Global DMSP/OLS Stable Nighttime Light Data (1992–2013). *Remote Sens.* 9, 637. doi:10.3390/rs9060637.
- Li, Z., Wang, S., Song, S., Wang, Y., Musakwa, W., 2021. Detecting land degradation in Southern Africa using Time Series Segment and Residual Trend (TSS-RESTREND). *J. Arid Environ.* 184, 104314. doi:10.1016/j.jaridenv.2020.104314.
- Linke, S., Lehner, B., Ouellet Dallaire, C., Ariwi, J., Grill, G., Anand, M., Beames, P., Burchard-Levine, V., Maxwell, S., Moidu, H., Tan, F., Thieme, M., 2019. Global hydro-environmental sub-basin and river reach characteristics at high spatial resolution. *Sci. Data* 6, 283. doi:10.1038/s41597-019-0300-6.
- Liu, J.T., Feng, Q.L., Gong, J.H., Zhou, J.P., Li, Y., 2016. Land-cover classification of the Yellow River Delta wetland based on multiple end-member spectral mixture analysis and a Random Forest classifier. *Int. J. Remote Sens.* 37, 1845–1867. doi:10.1080/01431161.2016.1165888.
- Liu, Y., Li, Y., Li, S., Motesharrei, S., 2015. Spatial and Temporal Patterns of Global NDVI Trends: Correlations with Climate and Human Factors. *Remote Sens.* 7, 13233–13250. doi:10.3390/rs71013233.
- Lloyd, C.T., Chamberlain, H., Kerr, D., Yetman, G., Pistolesi, L., Stevens, F.R., Gaughan, A.E., Nieves, J.J., Hornby, G., MacManus, K., Sinha, P., Bondarenko, M., Sorichetta, A., Tatem, A.J., 2019. Global spatio-temporally harmonised datasets for producing high-resolution gridded population distribution datasets. *Big Earth Data* 3, 108–139. doi:10.1080/20964471.2019.1625151.
- Lobo, F.L., Costa, M.P.F., Novo, E., 2015. Time-series analysis of Landsat-MSS/TM/OLI images over Amazonian waters impacted by gold mining activities. *Remote Sens. Environ.* 157, 170–184. doi:10.1016/j.rse.2014.04.030.
- Lu, Q., Zhao, D., Wu, S., 2017. Simulated responses of permafrost distribution to climate change on the Qinghai-Tibet Plateau. *Sci. Rep.* 7, 3845. doi:10.1038/s41598-017-04140-7.
- Luojus, K., Moisander, M., Pulliainen, J., Takala, M., Lemmetyinen, J., Derksen, C., Mortimer, C., Schwaizer, G., Nagler, T., 2020. ESA Snow Climate Change Initiative (Snow_cci): Snow Water Equivalent (SWE) level 3C daily global climate research data package (CRDP) (1979 - 2018), version 1.0. doi:10.5285/fa20aaa2060e40cabf5fedce7a9716d0.

- Lutz, A.F., Immerzeel, W.W., Shrestha, A.B., Bierkens, M.F.P., 2014. Consistent increase in High Asia's runoff due to increasing glacier melt and precipitation. *Nat. Clim. Chang.* 4, 587–592. doi:10.1038/nclimate2237.
- Lutz, A.F., ter Maat, H.W., Wijngaard, R.R., Biemans, H., Syed, A., Shrestha, A.B., Wester, P., Immerzeel, W.W., 2018. South Asian river basins in a 1.5 °C warmer world. *Reg. Environ. Change* 19, 833–847. doi:10.1007/s10113-018-1433-4.
- MacDonald, A.M., Bonsor, H.C., Ahmed, K.M., Burgess, W.G., Basharat, M., Calow, R.C., Dixit, A., Foster, S.S.D., Gopal, K., Lapworth, D.J., Lark, R.M., Moench, M., Mukherjee, A., Rao, M.S., Shamsudduha, M., Smith, L., Taylor, R.G., Tucker, J., van Steenbergen, F., Yadav, S.K., 2016. Groundwater quality and depletion in the Indo-Gangetic Basin mapped from in situ observations. *Nat. Geosci.* 9, 762–766. doi:10.1038/ngeo2791.
- Macklin, M.G., Lewin, J., 2015. The rivers of civilization. *Quat. Sci. Rev.* 114, 228–244. doi:10.1016/j.quascirev.2015.02.004.
- Mahecha, M.D., Gans, F., Brandt, G., Christiansen, R., Cornell, S.E., Fomferra, N., Kraemer, G., Peters, J., Bodesheim, P., Camps-Valls, G., Donges, J.F., Dorigo, W., Estupinan-Suarez, L.M., Gutierrez-Velez, V.H., Gutwin, M., Jung, M., Londoño, M.C., Miralles, D.G., Papastefanou, P., Reichstein, M., 2020. Earth system data cubes unravel global multivariate dynamics. *Earth Syst. Dyn.* 11, 201–234. doi:10.5194/esd-11-201-2020.
- Mahto, S.S., Mishra, V., 2019. Does ERA-5 Outperform Other Reanalysis Products for Hydrologic Applications in India? *J. Geophys. Res. Atmos.* 124, 9423–9441. doi:10.1029/2019jd031155.
- Mann, H.B., 1945. Nonparametric tests against trend. *Econometrica: Journal of the econometric society* , 245–259.
- Marconcini, M., Metz-Marconcini, A., Esch, T., Gorelick, N., 2021. Understanding Current Trends in Global Urbanisation - The World Settlement Footprint Suite. *GI_Forum* 1, 33–38. doi:10.1553/giscience2021_01_s33.
- Marconcini, M., Metz-Marconcini, A., Ureyen, S., Palacios-Lopez, D., Hanke, W., Bachofer, F., Zeidler, J., Esch, T., Gorelick, N., Kakarla, A., Paganini, M., Strano, E., 2020. Outlining where humans live, the World Settlement Footprint 2015. *Sci. Data* 7, 242. doi:10.1038/s41597-020-00580-5.
- Martens, B., Miralles, D.G., Lievens, H., van der Schalie, R., de Jeu, R.A.M., Fernández-Prieto, D., Beck, H.E., Dorigo, W.A., Verhoest, N.E.C., 2017. GLEAM v3: satellite-based land evaporation and root-zone soil moisture. *Geosci. Model Dev.* 10, 1903–1925. doi:10.5194/gmd-10-1903-2017.
- Masson, T., Dumont, M., Mura, M., Sirguey, P., Gascoin, S., Dedieu, J.P., Chanussot, J., 2018. An Assessment of Existing Methodologies to Retrieve Snow Cover Fraction from MODIS Data. *Remote Sens.* 10, 619. doi:10.3390/rs10040619.
- Mathur, R., AchutaRao, K., 2019. A modelling exploration of the sensitivity of the India's climate to irrigation. *Clim. Dyn.* 54, 1851–1872. doi:10.1007/s00382-019-05090-8.
- Matsuoka, M., Hayasaka, T., Fukushima, Y., Honda, Y., 2007. Land cover in East Asia classified using Terra MODIS and DMSP OLS products. *Int. J. Remote Sens.* 28, 221–248. doi:10.1080/01431160600675911.
- Mayer-Gürr, T., Behzadpur, S., Ellmer, M., Kvas, A., Klinger, B., Strasser, S., Zehentner, N., 2018. ITSG-Grace2018–Monthly, Daily and Static Gravity Field Solutions from GRACE, GFZ Data Services. doi:10.5880/ICGEM.2018.003.
- Mekonnen, M.M., Hoekstra, A.Y., 2016. Four billion people facing severe water scarcity. *Sci. Adv.* 2, e1500323. doi:10.1126/sciadv.1500323.

- Mermoz, S., Allain-Bailhache, S., Bernier, M., Pottier, E., Van der Sanden, J.J., Chokmani, K., 2014. Retrieval of River Ice Thickness From C-Band PolSAR Data. *IEEE Trans. Geosci. Remote Sens.* 52, 3052–3062. doi:10.1109/tgrs.2013.2269014.
- Miles, E., McCarthy, M., Dehecq, A., Kneib, M., Fugger, S., Pellicciotti, F., 2021. Health and sustainability of glaciers in High Mountain Asia. *Nat. Commun.* 12, 2868. doi:10.1038/s41467-021-23073-4.
- Militino, A.F., Moradi, M., Ugarte, M.D., 2020. On the Performances of Trend and Change-Point Detection Methods for Remote Sensing Data. *Remote Sens.* 12, 1008. doi:10.3390/rs12061008.
- Miralles, D.G., Holmes, T.R.H., De Jeu, R.A.M., Gash, J.H., Meesters, A.G.C.A., Dolman, A.J., 2011. Global land-surface evaporation estimated from satellite-based observations. *Hydrol. Earth Syst. Sci.* 15, 453–469. doi:10.5194/hess-15-453-2011.
- Mishra, N.B., Mainali, K.P., 2017. Greening and browning of the Himalaya: Spatial patterns and the role of climatic change and human drivers. *Sci. Total Environ.* 587-588, 326–339. doi:10.1016/j.scitotenv.2017.02.156.
- Mishra, V., 2020. Long-term (1870–2018) drought reconstruction in context of surface water security in India. *J. Hydrol.* 580, 124228. doi:10.1016/j.jhydrol.2019.124228.
- Mishra, V., Ambika, A.K., Asoka, A., Aadhar, S., Buzan, J., Kumar, R., Huber, M., 2020. Moist heat stress extremes in India enhanced by irrigation. *Nat. Geosci.* 13, 722–728. doi:10.1038/s41561-020-00650-8.
- Mishra, V., Smoliak, B.V., Lettenmaier, D.P., Wallace, J.M., 2012. A prominent pattern of year-to-year variability in Indian Summer Monsoon Rainfall. *Proc. Natl. Acad. Sci. U.S.A.* 109, 7213–7. doi:10.1073/pnas.1119150109.
- Mondal, S.K., Tao, H., Huang, J., Wang, Y., Su, B., Zhai, J., Jing, C., Wen, S., Jiang, S., Chen, Z., Jiang, T., 2021. Projected changes in temperature, precipitation and potential evapotranspiration across Indus River Basin at 1.5-3.0 degrees C warming levels using CMIP6-GCMs. *Sci. Total Environ.* 789, 147867. doi:10.1016/j.scitotenv.2021.147867.
- Montgomery, D.C., Jennings, C.L., Kulahci, M., 2015. *Introduction to Time Series Analysis and Forecasting*. John Wiley & Sons, Incorporated, Somerset, United States.
- Morice, C.P., Kennedy, J.J., Rayner, N.A., Winn, J.P., Hogan, E., Killick, R.E., Dunn, R.J.H., Osborn, T.J., Jones, P.D., Simpson, I.R., 2021. An Updated Assessment of Near-Surface Temperature Change From 1850: The HadCRUT5 Data Set. *J. Geophys. Res. Atmos.* 126, e2019JD032361. doi:10.1029/2019JD032361.
- de Moura, Y.M., Hilker, T., Lyapustin, A.I., Galva, L.S., Dos Santos, J.R., Anderson, L.O., de Sousa, C.H.R., Arai, E., 2015. Seasonality and drought effects of Amazonian forests observed from multi-angle satellite data. *Remote Sens. Environ.* 171, 278–290. doi:10.1016/j.rse.2015.10.015.
- Mousivand, A., Arsanjani, J.J., 2019. Insights on the historical and emerging global land cover changes: The case of ESA-CCI-LC datasets. *Appl. Geogr.* 106, 82–92. doi:10.1016/j.apgeog.2019.03.010.
- Mudryk, L., Santolaria-Otín, M., Krinner, G., Ménégos, M., Derksen, C., Brutel-Vuilmet, C., Brady, M., Essery, R., 2020. Historical Northern Hemisphere snow cover trends and projected changes in the CMIP6 multi-model ensemble. *The Cryosphere* 14, 2495–2514. doi:10.5194/tc-14-2495-2020.
- Mujumdar, M., Bhaskar, P., Ramarao, M.V.S., Uppara, U., Goswami, M., Borgaonkar, H., Chakraborty, S., Ram, S., Mishra, V., Rajeevan, M., Niyogi, D., 2020. Droughts and Floods, in: Krishnan, R., Sanjay, J., Gnanaseelan, C., Mujumdar, M., Kulkarni, A., Chakraborty, S. (Eds.), *Assessment of Climate Change over the Indian Region*. Springer, Singapore. book section Chapter 6, pp. 117–141. doi:10.1007/978-981-15-4327-2_6.

- Muñoz-Sabater, J., 2019. ERA5-Land hourly data from 1981 to present. Copernicus Climate Change Service (C3S) Climate Data Store (CDS). doi:10.24381/cds.e2161bac. accessed on 01 June 2021.
- Muñoz-Sabater, J., Dutra, E., Agustí-Panareda, A., Albergel, C., Arduini, G., Balsamo, G., Boussetta, S., Choulga, M., Harrigan, S., Hersbach, H., Martens, B., Miralles, D.G., Piles, M., Rodríguez-Fernández, N.J., Zsoter, E., Buontempo, C., Thépaut, J.N., 2021. ERA5-Land: a state-of-the-art global reanalysis dataset for land applications. *Earth Syst. Sci. Data* 13, 4349–4383. doi:10.5194/essd-13-4349-2021.
- Naegeli, K., Neuhaus, C., Salberg, A.B., Schwaizer, G., Wiesmann, A., Wunderle, S., Nagler, T., 2021a. ESA Snow Climate Change Initiative (Snow_cci): Daily global Snow Cover Fraction - snow on ground (SCFG) from AVHRR (1982–2019), version 1.0. doi:10.5285/5484dc1392bc43c1ace73ba38a22ac56.
- Naegeli, K., Neuhaus, C., Salberg, A.B., Schwaizer, G., Wiesmann, A., Wunderle, S., Nagler, T., 2021b. ESA Snow Climate Change Initiative (Snow_cci): Daily global Snow Cover Fraction - viewable (SCFV) from AVHRR (1982–2019), version 1.0. doi:10.5285/d9df331e346f4a50b18bcf41a64b98c7.
- Nageswararao, M.M., Dhekale, B.S., Mohanty, U.C., 2016. Impact of climate variability on various Rabi crops over Northwest India. *Theor. Appl. Climatol.* 131, 503–521. doi:10.1007/s00704-016-1991-7.
- Nagler, T., Schwaizer, G., Keuris, L., Hetzenecker, M., Metsämäki, S., 2021. ESA Snow Climate Change Initiative (Snow_cci): Daily global Snow Cover Fraction - viewable snow (SCFV) from MODIS (2000–2019), version 1.0. doi:10.5285/ef8eb5ff84994f2ca416dbb2df7f72c7.
- Nepal, S., Khatiwada, K.R., Pradhananga, S., Kralisch, S., Samyn, D., Bromand, M.T., Jamal, N., Dildar, M., Durrani, F., Rassouly, F., Azizi, F., Salehi, W., Malikzooi, R., Krause, P., Koirala, S., Chevallier, P., 2021. Future snow projections in a small basin of the Western Himalaya. *Sci. Total Environ.* 795, 148587. doi:10.1016/j.scitotenv.2021.148587.
- Nguyen, P., Shearer, E.J., Tran, H., Ombadi, M., Hayatbini, N., Palacios, T., Huynh, P., Braithwaite, D., Updegraff, G., Hsu, K., Kuligowski, B., Logan, W.S., Sorooshian, S., 2019. The CHRS Data Portal, an easily accessible public repository for PERSIANN global satellite precipitation data. *Sci. Data* 6, 180296. doi:10.1038/sdata.2018.296.
- Niculescu, S., Lardeux, C., Grigoras, I., Hanganu, J., David, L., 2016. Synergy Between LiDAR, RADARSAT-2, and Spot-5 Images for the Detection and Mapping of Wetland Vegetation in the Danube Delta. *IEEE J. Sel. Top. Appl. Earth. Obs. Remote Sens.* 9, 3651–3666. doi:10.1109/jstars.2016.2545242.
- Nie, Y., Pritchard, H.D., Liu, Q., Hennig, T., Wang, W., Wang, X., Liu, S., Nepal, S., Samyn, D., Hewitt, K., Chen, X., 2021. Glacial change and hydrological implications in the Himalaya and Karakoram. *Nat. Rev. Earth Environ.* 2, 91–106. doi:10.1038/s43017-020-00124-w.
- Nitze, I., Grosse, G., Jones, B.M., Arp, C.D., Ulrich, M., Fedorov, A., Veremeeva, A., 2017. Landsat-Based Trend Analysis of Lake Dynamics across Northern Permafrost Regions. *Remote Sens.* 9, 28. doi:10.3390/rs9070640.
- Notarnicola, C., 2020. Hotspots of snow cover changes in global mountain regions over 2000–2018. *Remote Sens. Environ.* 243, 111781. doi:10.1016/j.rse.2020.111781.
- Nyland, K.E., Gunn, G.E., Shiklomanov, N.I., Engstrom, R.N., Streletskiy, D.A., 2018. Land Cover Change in the Lower Yenisei River Using Dense Stacking of Landsat Imagery in Google Earth Engine. *Remote Sens.* 10, 20. doi:10.3390/rs10081226.
- Onoz, B., Bayazit, M., 2003. The power of statistical tests for trend detection. *Turkish J. Eng. Env. Sci.* 27, 247–251.

- Osborn, T.J., Jones, P.D., Lister, D.H., Morice, C.P., Simpson, I.R., Winn, J.P., Hogan, E., Harris, I.C., 2021. Land Surface Air Temperature Variations Across the Globe Updated to 2019: The CRUTEM5 Data Set. *J. Geophys. Res. Atmos.* 126, e2019JD032352. doi:10.1029/2019JD032352.
- Ouyang, W., Wan, X., Xu, Y., Wang, X., Lin, C., 2020. Vertical difference of climate change impacts on vegetation at temporal-spatial scales in the upper stream of the Mekong River Basin. *Sci. Total Environ.* 701, 134782. doi:10.1016/j.scitotenv.2019.134782.
- Palacios-Lopez, D., Bachofer, F., Esch, T., Heldens, W., Hirner, A., Marconcini, M., Sorichetta, A., Zeidler, J., Kuenzer, C., Dech, S., Tatem, A.J., Reinartz, P., 2019. New Perspectives for Mapping Global Population Distribution Using World Settlement Footprint Products. *Sustainability* 11, 6056. doi:10.3390/su11216056.
- Palazzi, E., Filippi, L., von Hardenberg, J., 2016. Insights into elevation-dependent warming in the Tibetan Plateau-Himalayas from CMIP5 model simulations. *Clim. Dyn.* 48, 3991–4008. doi:10.1007/s00382-016-3316-z.
- Pan, C.G., Kirchner, P.B., Kimball, J.S., Du, J., Rawlins, M.A., 2021. Snow Phenology and Hydrologic Timing in the Yukon River Basin, AK, USA. *Remote Sens.* 13, 2284. doi:10.3390/rs13122284.
- Pandey, R.K., Cretaux, J.F., Berge-Nguyen, M., Tiwari, V.M., Drolon, V., Papa, F., Calmant, S., 2014. Water level estimation by remote sensing for the 2008 flooding of the Kosi River. *Int. J. Remote Sens.* 35, 424–440. doi:10.1080/01431161.2013.870678.
- Papagiannopoulou, C., Miralles, D.G., Dorigo, W.A., Verhoest, N.E.C., Depoorter, M., Waegeman, W., 2017. Vegetation anomalies caused by antecedent precipitation in most of the world. *Environ. Res. Lett.* 12, 074016. doi:10.1088/1748-9326/aa7145.
- Park, H., Jeong, S., Penuelas, J., 2020. Accelerated rate of vegetation green-up related to warming at northern high latitudes. *Glob. Chang. Biol.* 26, 6190–6202. doi:10.1111/gcb.15322.
- Patakamuri, S.K., Muthiah, K., Sridhar, V., 2020. Long-Term Homogeneity, Trend, and Change-Point Analysis of Rainfall in the Arid District of Ananthapuramu, Andhra Pradesh State, India. *Water* 12, 211. doi:10.3390/w12010211.
- Patel, A., Goswami, A., Dharpure, J.K., Thamban, M., 2020. Rainfall variability over the Indus, Ganga, and Brahmaputra river basins: A spatio-temporal characterisation. *Quat. Int.* 575–576, 280–294. doi:10.1016/j.quaint.2020.06.010.
- Pavelsky, T.M., Smith, L.C., 2004. Spatial and temporal patterns in Arctic river ice breakup observed with MODIS and AVHRR time series. *Remote Sens. Environ.* 93, 328–338. doi:10.1016/j.rse.2004.07.018.
- Pekel, J.F., Cottam, A., Gorelick, N., Belward, A.S., 2016. High-resolution mapping of global surface water and its long-term changes. *Nature* 540, 418. doi:10.1038/nature20584.
- Peng, S., Piao, S., Ciais, P., Myneni, R.B., Chen, A., Chevallier, F., Dolman, A.J., Janssens, I.A., Penuelas, J., Zhang, G., Vicca, S., Wan, S., Wang, S., Zeng, H., 2013. Asymmetric effects of daytime and night-time warming on Northern Hemisphere vegetation. *Nature* 501, 88–92. doi:10.1038/nature12434.
- Pepin, N., Bradley, R.S., Diaz, H.F., Baraer, M., Caceres, E.B., Forsythe, N., Fowler, H., Greenwood, G., Hashmi, M.Z., Liu, X.D., Miller, J.R., Ning, L., Ohmura, A., Palazzi, E., Rangwala, I., Schöner, W., Severskiy, I., Shahgedanova, M., Wang, M.B., Williamson, S.N., Yang, D.Q., 2015. Elevation-dependent warming in mountain regions of the world. *Nat. Clim. Chang.* 5, 424–430. doi:10.1038/nclimate2563.

- Pereira, V.F.G., Congalton, R.G., Zarin, D.J., 2002. Spatial and temporal analysis of a tidal floodplain landscape - Arnapi, Brazil - Using geographic information systems and remote sensing. *Photogramm. Eng. Remote Sens.* 68, 463–472.
- Pesaresi, M., Huadong, G., Blaes, X., Ehrlich, D., Ferri, S., Gueguen, L., Halkia, M., Kauffmann, M., Kemper, T., Lu, L., 2013. A global human settlement layer from optical HR/VHR RS data: concept and first results. *IEEE J. Sel. Top. Appl. Earth. Obs. Remote Sens.* 6, 2102–2131. doi:10.1109/JSTARS.2013.2271445.
- Pham, H.T., Marshall, L., Johnson, F., Sharma, A., 2018. Deriving daily water levels from satellite altimetry and land surface temperature for sparsely gauged catchments: A case study for the Mekong River. *Remote Sens. Environ.* 212, 31–46. doi:10.1016/j.rse.2018.04.034.
- Piao, S., Wang, X., Park, T., Chen, C., Lian, X., He, Y., Bjerke, J.W., Chen, A., Ciais, P., Tømmervik, H., Nemani, R.R., Myneni, R.B., 2020. Characteristics, drivers and feedbacks of global greening. *Nat. Rev. Earth Environ.* 1, 14–27. doi:10.1038/s43017-019-0001-x.
- Pinzon, J., Tucker, C., 2014. A Non-Stationary 1981–2012 AVHRR NDVI3g Time Series. *Remote Sens.* 6, 6929–6960. doi:10.3390/rs6086929.
- Platnick, S., Meyer, K.G., King, M.D., Wind, G., Amarasinghe, N., Marchant, B., Arnold, G.T., Zhang, Z., Hubanks, P.A., Holz, R.E., Yang, P., Ridgway, W.L., Riedi, J., 2017. The MODIS Cloud Optical and Microphysical Products: Collection 6 Updates and Examples From Terra and Aqua. *IEEE Trans. Geosci. Remote Sens.* 55, 502–525. doi:10.1109/TGRS.2016.2610522.
- Plummer, S., Lecomte, P., Doherty, M., 2017. The ESA Climate Change Initiative (CCI): A European contribution to the generation of the Global Climate Observing System. *Remote Sens. Environ.* 203, 2–8. doi:10.1016/j.rse.2017.07.014.
- Prakash, S., 2019. Performance assessment of CHIRPS, MSWEP, SM2RAIN-CCI, and TMPA precipitation products across India. *J. Hydrol.* 571, 50–59. doi:10.1016/j.jhydrol.2019.01.036.
- Praveen, B., Talukdar, S., Shahfahad, Mahato, S., Mondal, J., Sharma, P., Islam, A., Rahman, A., 2020. Analyzing trend and forecasting of rainfall changes in India using non-parametrical and machine learning approaches. *Sci. Rep.* 10, 10342. doi:10.1038/s41598-020-67228-7.
- Pritchard, H.D., 2019. Asia's shrinking glaciers protect large populations from drought stress. *Nature* 569, 649–654. doi:10.1038/s41586-019-1240-1.
- Priyadarshini, P., Abhilash, P.C., 2020. Policy recommendations for enabling transition towards sustainable agriculture in India. *Land Use Policy* 96, 104718. doi:10.1016/j.landusepol.2020.104718.
- Provenzale, A., Palazzi, E., von Hardenberg, J., Terzago, S., 2014. Snowpack Changes in the Hindu Kush–Karakoram–Himalaya from CMIP5 Global Climate Models. *J. Hydrometeorol.* 15, 2293–2313. doi:10.1175/jhm-d-13-0196.1.
- Rahman, M., Dustegir, M., Karim, R., Haque, A., Nicholls, R.J., Darby, S.E., Nakagawa, H., Hossain, M., Dunn, F.E., Akter, M., 2018. Recent sediment flux to the Ganges-Brahmaputra-Meghna delta system. *Sci. Total Environ.* 643, 1054–1064. doi:10.1016/j.scitotenv.2018.06.147.
- Ramarao, M.V.S., Sanjay, J., Krishnan, R., Mujumdar, M., Bazaz, A., Revi, A., 2018. On observed aridity changes over the semiarid regions of India in a warming climate. *Theor. Appl. Climatol.* 136, 693–702. doi:10.1007/s00704-018-2513-6.

- Rao, P.Z., Jiang, W.G., Hou, Y.K., Chen, Z., Jia, K., 2018. Dynamic Change Analysis of Surface Water in the Yangtze River Basin Based on MODIS Products. *Remote Sens.* 10, 20. doi:10.3390/rs10071025.
- Rateb, A., Scanlon, B.R., Kuo, C.Y., 2021. Multi-decadal assessment of water budget and hydrological extremes in the Tigris-Euphrates Basin using satellites, modeling, and in-situ data. *Sci. Total Environ.* 766, 144337. doi:10.1016/j.scitotenv.2020.144337.
- Reichstein, M., Camps-Valls, G., Stevens, B., Jung, M., Denzler, J., Carvalhais, N., Prabhat, 2019. Deep learning and process understanding for data-driven Earth system science. *Nature* 566, 195–204. doi:10.1038/s41586-019-0912-1.
- Reygadas, Y., Jensen, J.L.R., Moisen, G.G., Currit, N., Chow, E.T., 2020. Assessing the relationship between vegetation greenness and surface temperature through Granger causality and Impulse-Response coefficients: a case study in Mexico. *Int. J. Remote Sens.* 41, 3761–3783. doi:10.1080/01431161.2019.1711241.
- Rodell, M., Famiglietti, J.S., Wiese, D.N., Reager, J.T., Beaudoin, H.K., Landerer, F.W., Lo, M.H., 2018. Emerging trends in global freshwater availability. *Nature* 557, 651–659. doi:10.1038/s41586-018-0123-1.
- Rosenqvist, A., Birkett, C.M., 2002. Evaluation of JERS-1 SAR mosaics for hydrological applications in the Congo river basin. *Int. J. Remote Sens.* 23, 1283–1302. doi:10.1080/01431160110092902.
- Runge, J., 2018. Causal network reconstruction from time series: From theoretical assumptions to practical estimation. *Chaos* 28, 075310. doi:10.1063/1.5025050.
- Runge, J., 2020. Discovering contemporaneous and lagged causal relations in autocorrelated nonlinear time series datasets. URL: <http://proceedings.mlr.press/v124/runge20a.html>.
- Runge, J., Bathiany, S., Bollt, E., Camps-Valls, G., Coumou, D., Deyle, E., Glymour, C., Kretschmer, M., Mahecha, M.D., Munoz-Mari, J., van Nes, E.H., Peters, J., Quax, R., Reichstein, M., Scheffer, M., Scholkopf, B., Spirtes, P., Sugihara, G., Sun, J., Zhang, K., Zscheischler, J., 2019a. Inferring causation from time series in Earth system sciences. *Nat. Commun.* 10, 2553. doi:10.1038/s41467-019-10105-3.
- Runge, J., Nowack, P., Kretschmer, M., Flaxman, S., Sejdinovic, D., 2019b. Detecting and quantifying causal associations in large nonlinear time series datasets. *Sci. Adv.* 5, eaau4996. doi:10.1126/sciadv.aau4996.
- Running, S., Mu, Q., Zhao, M., 2015a. MOD17A2H MODIS/Terra Gross Primary Productivity 8-Day L4 Global 500m SIN Grid V006. doi:10.5067/MODIS/MOD17A2H.006.
- Running, S., Mu, Q., Zhao, M., 2015b. MOD17A3H MODIS/Terra Net Primary Production Yearly L4 Global 500m SIN Grid V006. doi:10.5067/MODIS/MOD17A3H.006.
- Rößler, S., Witt, M.S., Ikonen, J., Brown, I.A., Dietz, A.J., 2021. Remote Sensing of Snow Cover Variability and Its Influence on the Runoff of Sápmi's Rivers. *Geosciences* 11, 130. doi:10.3390/geosciences11030130.
- Saatchi, S.S., Nelson, B., Podest, E., Holt, J., 2000. Mapping land cover types in the Amazon Basin using 1 km JERS-1 mosaic. *Int. J. Remote Sens.* 21, 1201–1234. doi:10.1080/014311600210146.
- Sakai, T., Hatta, S., Okumura, M., Hiyama, T., Yamaguchi, Y., Inoue, G., 2015. Use of Landsat TM/ETM plus to monitor the spatial and temporal extent of spring breakup floods in the Lena River, Siberia. *Int. J. Remote Sens.* 36, 719–733. doi:10.1080/01431161.2014.995271.

- Sakamoto, T., Van Nguyen, N., Ohno, H., Ishitsuka, N., Yokozawa, M., 2006. Spatio-temporal distribution of rice phenology and cropping systems in the Mekong Delta with special reference to the seasonal water flow of the Mekong and Bassac rivers. *Remote Sens. Environ.* 100, 1–16. doi:10.1016/j.rse.2005.09.007.
- Salcedo-Sanz, S., Ghamisi, P., Piles, M., Werner, M., Cuadra, L., Moreno-Martínez, A., Izquierdo-Verdiguier, E., Muñoz-Marí, J., Mosavi, A., Camps-Valls, G., 2020. Machine learning information fusion in Earth observation: A comprehensive review of methods, applications and data sources. *Inf. Fusion* 63, 256–272. doi:10.1016/j.inffus.2020.07.004.
- Sarker, M.H., Huque, I., Alam, M., Koudstaal, R., 2003. Rivers, chars and char dwellers of Bangladesh. *Int. J. River Basin Manag.* 1, 61–80. doi:10.1080/15715124.2003.9635193.
- Sarmah, S., Jia, G., Zhang, A., 2018. Satellite view of seasonal greenness trends and controls in South Asia. *Environ. Res. Lett.* 13, 034026. doi:10.1088/1748-9326/aaa866.
- Schneider, R., Godiksen, P.N., Villadsen, H., Madsen, H., Bauer-Gottwein, P., 2017. Application of CryoSat-2 altimetry data for river analysis and modelling. *Hydrol. Earth Syst. Sci.* 21, 651–664. doi:10.5194/hess-21-751-2017.
- Sen, P.K., 1968. Estimates of the regression coefficient based on Kendall's tau. *J. Am. Stat. Assoc.* 63, 1379–1389.
- Sheffield, J., Wood, E.F., Pan, M., Beck, H., Coccia, G., Serrat-Capdevila, A., Verbist, K., 2018. Satellite Remote Sensing for Water Resources Management: Potential for Supporting Sustainable Development in Data-Poor Regions. *Water Resour. Res.* 54, 9724–9758. doi:10.1029/2017wr022437.
- Shukla, A.K., Ojha, C.S.P., Mijic, A., Buytaert, W., Pathak, S., Garg, R.D., Shukla, S., 2018. Population growth, land use and land cover transformations, and water quality nexus in the Upper Ganga River basin. *Hydrol. Earth Syst. Sci.* 22, 4745–4770. doi:10.5194/hess-22-4745-2018.
- Shukla, P.R., Skea, J., Slade, R., Diemen, R.v., Haughey, E., Malley, J., Pathak, M., Portugal Pereira, J., 2019. Technical Summary, in: Shukla, P.R., Skea, J., Calvo Buendi, E., Masson-Delmotte, V., Pörtner, H.O., Roberts, D.C., Zhai, P., Slade, R., Connors, S., Diemen, R.v., Ferrat, M., Haughey, E., Luz, S., Neogi, S., Pathak, M., Petzold, J., Portugal Pereira, J., Vyas, P., Huntley, E., Kissick, K., Belkacemi, M., Malley, J. (Eds.), *Climate Change and Land: an IPCC special report on climate change, desertification, land degradation, sustainable land management, food security, and greenhouse gas fluxes in terrestrial ecosystems*, pp. 35–74.
- Shumway, R.H., Stoffer, D.S., 2017. *Time Series Analysis and Its Applications*. Springer, Cham.
- Siddique-E-Akbor, A.H.M., Hossain, F., Lee, H., Shum, C.K., 2011. Inter-comparison study of water level estimates derived from hydrodynamic-hydrologic model and satellite altimetry for a complex deltaic environment. *Remote Sens. Environ.* 115, 1522–1531. doi:10.1016/j.rse.2011.02.011.
- da Silva, J.S., Calmant, S., Seyler, F., Rotunno, O.C., Cochonneau, G., Mansur, W.J., 2010. Water levels in the Amazon basin derived from the ERS 2 and ENVISAT radar altimetry missions. *Remote Sens. Environ.* 114, 2160–2181. doi:10.1016/j.rse.2010.04.020.
- da Silva, J.S., Seyler, F., Calmant, S., Rotunno, O.C., Roux, E., Araujo, A.A.M., Guyot, J.L., 2012. Water level dynamics of Amazon wetlands at the watershed scale by satellite altimetry. *Int. J. Remote Sens.* 33, 3323–3353. doi:10.1080/01431161.2010.531914.
- Simoës, R., Camara, G., Queiroz, G., Souza, F., Andrade, P.R., Santos, L., Carvalho, A., Ferreira, K., 2021. Satellite Image Time Series Analysis for Big Earth Observation Data. *Remote Sens.* 13, 2428. doi:10.3390/rs13132428.

- Singh, D., Tsiang, M., Rajaratnam, B., Diffenbaugh, N.S., 2014. Observed changes in extreme wet and dry spells during the South Asian summer monsoon season. *Nat. Clim. Chang.* 4, 456–461. doi:10.1038/nclimate2208.
- Song, X.P., Hansen, M.C., Stehman, S.V., Potapov, P.V., Tyukavina, A., Vermote, E.F., Townshend, J.R., 2018. Global land change from 1982 to 2016. *Nature* 560, 639–643. doi:10.1038/s41586-018-0411-9.
- Southworth, J., Muir, C., 2021. Specialty Grand Challenge: Remote Sensing Time Series Analysis. *Front. Remote Sens.* 2, 770431. doi:10.3389/frsen.2021.770431.
- Spinoni, J., Vogt, J., Naumann, G., Carrao, H., Barbosa, P., 2015. Towards identifying areas at climatological risk of desertification using the Köppen-Geiger classification and FAO aridity index. *Int. J. Climatol.* 35, 2210–2222. doi:10.1002/joc.4124.
- de Stefano, L., Petersen-Perlman, J.D., Sproles, E.A., Eynard, J., Wolf, A.T., 2017. Assessment of transboundary river basins for potential hydro-political tensions. *Glob. Environ. Chang.* 45, 35–46. doi:10.1016/j.gloenvcha.2017.04.008.
- Steffen, W., Richardson, K., Rockström, J., Schellnhuber, H.J., Dube, O.P., Dutreuil, S., Lenton, T.M., Lubchenco, J., 2020. The emergence and evolution of Earth System Science. *Nat. Rev. Earth Environ.* 1, 54–63. doi:10.1038/s43017-019-0005-6.
- Stettner, S., Beamish, A.L., Bartsch, A., Heim, B., Grosse, G., Roth, A., Lantuit, H., 2018. Monitoring Inter- and Intra-Seasonal Dynamics of Rapidly Degrading Ice-Rich Permafrost Riverbanks in the Lena Delta with TerraSAR-X Time Series. *Remote Sens.* 10, 20. doi:10.3390/rs10010051.
- Strahler, A.H., 2013. *Introducing Physical Geography*. Wiley Textbooks, New York, United States.
- Strozzi, T., Antonova, S., Gunther, F., Matzler, E., Vieira, G., Wegmuller, U., Westermann, S., Bartsch, A., 2018. Sentinel-1 SAR Interferometry for Surface Deformation Monitoring in Low-Land Permafrost Areas. *Remote Sens.* 10, 20. doi:10.3390/rs10091360.
- Sudmanns, M., Tiede, D., Lang, S., Bergstedt, H., Trost, G., Augustin, H., Baraldi, A., Blaschke, T., 2019. Big Earth data: disruptive changes in Earth observation data management and analysis? *Int. J. Digit Earth* 13, 832–850. doi:10.1080/17538947.2019.1585976.
- Tan, J., Piao, S., Chen, A., Zeng, Z., Ciais, P., Janssens, I.A., Mao, J., Myneni, R.B., Peng, S., Penuelas, J., Shi, X., Vicca, S., 2015. Seasonally different response of photosynthetic activity to daytime and night-time warming in the Northern Hemisphere. *Glob. Chang. Biol.* 21, 377–87. doi:10.1111/gcb.12724.
- Tang, X., Woodcock, C.E., Olofsson, P., Hutyrá, L.R., 2021. Spatiotemporal assessment of land use/land cover change and associated carbon emissions and uptake in the Mekong River Basin. *Remote Sens. Environ.* 256, 112336. doi:10.1016/j.rse.2021.112336.
- Tekeli, A.E., Akyurek, Z., Sorman, A.A., Sensoy, A., Sorman, A.U., 2005. Using MODIS snow cover maps in modeling snowmelt runoff process in the eastern part of Turkey. *Remote Sens. Environ.* 97, 216–230. doi:10.1016/j.rse.2005.03.013.
- Thapa, S., Zhang, F., Zhang, H., Zeng, C., Wang, L., Xu, C.Y., Thapa, A., Nepal, S., 2021. Assessing the snow cover dynamics and its relationship with different hydro-climatic characteristics in Upper Ganges river basin and its sub-basins. *Sci. Total Environ.* 793, 148648. doi:10.1016/j.scitotenv.2021.148648.
- Theil, H., 1950. A rank-invariant method of linear and polynomial regression analysis. *Indag. Math.* 12, 173.

- Thenkabail, P.S., Schull, M., Turrall, H., 2005. Ganges and Indus river basin land use/land cover (LULC) and irrigated area mapping using continuous streams of MODIS data. *Remote Sens. Environ.* 95, 317–341. doi:10.1016/j.rse.2004.12.018.
- Tomaszewska, M.A., Nguyen, L.H., Henebry, G.M., 2020. Land surface phenology in the highland pastures of montane Central Asia: Interactions with snow cover seasonality and terrain characteristics. *Remote Sens. Environ.* 240, 111675. doi:10.1016/j.rse.2020.111675.
- Troitskaya, Y., Rybushkina, G., Soustova, I., Lebedev, S., 2014. Adaptive Retracking of Jason-1, 2 Satellite Altimetry Data for the Volga River Reservoirs. *IEEE J. Sel. Top. Appl. Earth. Obs. Remote Sens.* 7, 1603–1608. doi:10.1109/jstars.2013.2267092.
- Tsarouchi, G.M., Mijic, A., Moulds, S., Buytaert, W., 2014. Historical and future land-cover changes in the Upper Ganges basin of India. *Int. J. Remote Sens.* 35, 3150–3176. doi:10.1080/01431161.2014.903352.
- Tulbure, M.G., Broich, M., 2019. Spatiotemporal patterns and effects of climate and land use on surface water extent dynamics in a dryland region with three decades of Landsat satellite data. *Sci. Total Environ.* 658, 1574–1585. doi:10.1016/j.scitotenv.2018.11.390.
- Tulbure, M.G., Broich, M., Stehman, S.V., Kommareddy, A., 2016. Surface water extent dynamics from three decades of seasonally continuous Landsat time series at subcontinental scale in a semi-arid region. *Remote Sens. Environ.* 178, 142–157. doi:10.1016/j.rse.2016.02.034.
- Uereyen, S., Bachofer, F., Kuenzer, C., 2022a. A Framework for Multivariate Analysis of Land Surface Dynamics and Driving Variable—A Case Study for Indo-Gangetic River Basins. *Remote Sens.* 14, 197. doi:10.3390/rs14010197.
- Uereyen, S., Bachofer, F., Klein, I., Kuenzer, C., 2022b. Multi-faceted analyses of seasonal trends and drivers of land surface variables in Indo-Gangetic river basins. *Sci. Total Environ.* 847, 157515. doi:10.1016/j.scitotenv.2022.157515.
- Uereyen, S., Kuenzer, C., 2019. A Review of Earth Observation-Based Analyses for Major River Basins. *Remote Sens.* 11, 2951. doi:10.3390/rs11242951.
- Uhe, P.F., Mitchell, D.M., Bates, P.D., Sampson, C.C., Smith, A.M., Islam, A.S., 2019. Enhanced flood risk with 1.5 °C global warming in the Ganges–Brahmaputra–Meghna basin. *Environ. Res. Lett.* 14, 074031. doi:10.1088/1748-9326/ab10ee.
- UN-Water, 2021. Summary Progress Update 2021 – SDG 6 – water and sanitation for all. Version: July 2021. Geneva, Switzerland. URL: https://www.unwater.org/app/uploads/2021/12/SDG-6-Summary-Progress-Update-2021_Version-July-2021a.pdf.
- Urraca, R., Huld, T., Gracia-Amillo, A., Martinez-de Pison, F.J., Kaspar, F., Sanz-Garcia, A., 2018. Evaluation of global horizontal irradiance estimates from ERA5 and COSMO-REA6 reanalyses using ground and satellite-based data. *Sol. Energy* 164, 339–354. doi:10.1016/j.solener.2018.02.059.
- Vanham, D., Hoekstra, A.Y., Wada, Y., Bouraoui, F., de Roo, A., Mekonnen, M.M., van de Bund, W.J., Batelaan, O., Pavelic, P., Bastiaanssen, W.G.M., Kummu, M., Rockstrom, J., Liu, J., Bisselink, B., Ronco, P., Pistocchi, A., Bidoglio, G., 2018. Physical water scarcity metrics for monitoring progress towards SDG target 6.4: An evaluation of indicator 6.4.2 "Level of water stress". *Sci. Total Environ.* 613-614, 218–232. doi:10.1016/j.scitotenv.2017.09.056.
- Verbesselt, J., Hyndman, R., Newnham, G., Culvenor, D., 2010. Detecting trend and seasonal changes in satellite image time series. *Remote Sens. Environ.* 114, 106–115. doi:10.1016/j.rse.2009.08.014.
- Vermote, E., Wolfe, R., 2015. MOD09GA MODIS/Terra Surface Reflectance Daily L2G Global 1km and 500m SIN Grid V006. doi:10.5067/MODIS/MOD09GA.006.

- Vicente-Serrano, S.M., Domínguez-Castro, F., McVicar, T.R., Tomas-Burguera, M., Peña-Gallardo, M., Noguera, I., López-Moreno, J.I., Peña, D., El Kenawy, A., 2020. Global characterization of hydrological and meteorological droughts under future climate change: The importance of timescales, vegetation-CO₂ feedbacks and changes to distribution functions. *Int. J. Climatol.* 40, 2557–2567. doi:10.1002/joc.6350.
- Viers, J., Dupre, B., Gaillardet, J., 2009. Chemical composition of suspended sediments in World Rivers: New insights from a new database. *Sci. Total Environ.* 407, 853–68. doi:10.1016/j.scitotenv.2008.09.053.
- Villadsen, H., Andersen, O.B., Stenseng, L., Nielsen, K., Knudsen, P., 2015. CryoSat-2 altimetry for river level monitoring - Evaluation in the Ganges-Brahmaputra River basin. *Remote Sens. Environ.* 168, 80–89. doi:10.1016/j.rse.2015.05.025.
- Viviroli, D., Kummu, M., Meybeck, M., Kallio, M., Wada, Y., 2020. Increasing dependence of lowland populations on mountain water resources. *Nat. Sustain.* 3, 917–928. doi:10.1038/s41893-020-0559-9.
- Vörösmarty, C.J., McIntyre, P.B., Gessner, M.O., Dudgeon, D., Prusevich, A., Green, P., Glidden, S., Bunn, S.E., Sullivan, C.A., Liermann, C.R., Davies, P.M., 2010. Global threats to human water security and river biodiversity. *Nature* 467, 555. doi:10.1038/nature09440.
- Wan, Z., Hook, S., Hulley, G., 2015. MOD11C3 MODIS/Terra Land Surface Temperature/Emissivity Monthly L3 Global 0.05Deg CMG V006. doi:10.5067/MODIS/MOD11C3.006.
- Wang, C., Jia, M.M., Chen, N.C., Wang, W., 2018a. Long-Term Surface Water Dynamics Analysis Based on Landsat Imagery and the Google Earth Engine Platform: A Case Study in the Middle Yangtze River Basin. *Remote Sens.* 10, 18. doi:10.3390/rs10101635.
- Wang, D., Liang, S., He, T., Yu, Y., Schaaf, C., Wang, Z., 2015a. Estimating daily mean land surface albedo from MODIS data. *J. Geophys. Res. Atmos.* 120, 4825–4841. doi:10.1002/2015jd023178.
- Wang, F., Shao, W., Yu, H., Kan, G., He, X., Zhang, D., Ren, M., Wang, G., 2020. Re-evaluation of the Power of the Mann-Kendall Test for Detecting Monotonic Trends in Hydrometeorological Time Series. *Front. Earth Sci.* 8, 14. doi:10.3389/feart.2020.00014.
- Wang, F., Wang, Z.M., Yang, H.B., Zhao, Y., Li, Z.H., Wu, J.P., 2018b. Capability of Remotely Sensed Drought Indices for Representing the Spatio-Temporal Variations of the Meteorological Droughts in the Yellow River Basin. *Remote Sens.* 10, 18. doi:10.3390/rs10111834.
- Wang, L., Tian, F., Wang, Y., Wu, Z., Schurgers, G., Fensholt, R., 2018c. Acceleration of global vegetation greenup from combined effects of climate change and human land management. *Glob. Chang. Biol.* 24, 5484–5499. doi:10.1111/gcb.14369.
- Wang, R., Yao, Z.J., Liu, Z.F., Wu, S.S., Jiang, L.G., Wang, L., 2015b. Snow cover variability and snowmelt in a high-altitude ungauged catchment. *Hydrol. Process.* 29, 3665–3676. doi:10.1002/hyp.10472.
- Wang, R., Yao, Z.J., Wu, S.S., Liu, Z.F., 2017a. Glacier retreat and its impact on summer-time run-off in a high-altitude ungauged catchment. *Hydrol. Process.* 31, 3672–3681. doi:10.1002/hyp.11287.
- Wang, S.Y., Ding, C.B., Liu, J.S., 2009. Landscape evolution in the Yellow River Basin using satellite remote sensing and GIS during the past decade. *Int. J. Remote Sens.* 30, 5573–5591. doi:10.1080/01431160802687482.
- Wang, W., Chen, Y., Becker, S., Liu, B., 2015c. Variance Correction Prewhitening Method for Trend Detection in Autocorrelated Data. *J. Hydrol. Eng.* 20, 04015033. doi:10.1061/(ASCE)HE.1943-5584.0001234.

- Wang, X., Wu, C., Wang, H., Gonsamo, A., Liu, Z., 2017b. No evidence of widespread decline of snow cover on the Tibetan Plateau over 2000-2015. *Sci. Rep.* 7, 14645. doi:10.1038/s41598-017-15208-9.
- Wang, X.L., Swail, V.R., 2001. Changes of Extreme Wave Heights in Northern Hemisphere Oceans and Related Atmospheric Circulation Regimes. *J. Clim.* 14, 2204–2221. doi:10.1175/1520-0442(2001)014<2204:Coewhi>2.0.Co;2.
- Wei, Z., Dong, W., 2015. Assessment of Simulations of Snow Depth in the Qinghai-Tibetan Plateau Using CMIP5 Multi-Models. *Arct. Antarct. Alp. Res.* 47, 611–625. doi:10.1657/aaar0014-050.
- Wessel, B., Huber, M., Wohlfart, C., Marschalk, U., Kosmann, D., Roth, A., 2018. Accuracy assessment of the global TanDEM-X Digital Elevation Model with GPS data. *ISPRS J. Photogramm. Remote Sens.* 139, 171–182. doi:10.1016/j.isprsjprs.2018.02.017.
- Whitley, M.A., Frost, G.V., Jorgenson, M.T., Macander, M.J., Maio, C.V., Winder, S.G., 2018. Assessment of LiDAR and Spectral Techniques for High-Resolution Mapping of Sporadic Permafrost on the Yukon-Kuskokwim Delta, Alaska. *Remote Sens.* 10, 20. doi:10.3390/rs10020258.
- Wijngaard, R.R., Biemans, H., Lutz, A.F., Shrestha, A.B., Wester, P., Immerzeel, W.W., 2018. Climate change vs. socio-economic development: understanding the future South Asian water gap. *Hydrol. Earth Syst. Sci.* 22, 6297–6321. doi:10.5194/hess-22-6297-2018.
- Winkler, K., Fuchs, R., Rounsevell, M., Herold, M., 2021. Global land use changes are four times greater than previously estimated. *Nat. Commun.* 12, 2501. doi:10.1038/s41467-021-22702-2.
- Wittich, K.P., Hansing, O., 1995. Area-averaged vegetative cover fraction estimated from satellite data. *Int. J. Biometeorol.* 38, 209–215. doi:10.1007/BF01245391.
- Wißkirchen, K., Tum, M., Günther, K.P., Niklaus, M., Eisfelder, C., Knorr, W., 2013. Quantifying the carbon uptake by vegetation for Europe on a 1 km² resolution using a remote sensing driven vegetation model. *Geosci. Model Dev.* 6, 1623–1640. doi:10.5194/gmd-6-1623-2013.
- Wohl, E.E., 2007. Hydrology and Discharge, in: Gupta, A. (Ed.), *Large Rivers*. John Wiley & Sons, pp. 29–44. doi:10.1002/9780470723722.ch3.
- Wohlfart, C., Liu, G.H., Huang, C., Kuenzer, C., 2016. A River Basin over the Course of Time: Multi-Temporal Analyses of Land Surface Dynamics in the Yellow River Basin (China) Based on Medium Resolution Remote Sensing Data. *Remote Sens.* 8, 25. doi:10.3390/rs8030186.
- Wolf, A.T., Natharius, J.A., Danielson, J.J., Ward, B.S., Pender, J.K., 1999. International River Basins of the World. *Int. J. Water Resour. Dev.* 15, 387–427. doi:10.1080/07900629948682.
- Woodcock, C.E., Loveland, T.R., Herold, M., Bauer, M.E., 2020. Transitioning from change detection to monitoring with remote sensing: A paradigm shift. *Remote Sens. Environ.* 238, 111558. doi:10.1016/j.rse.2019.111558.
- WorldPop, CIESIN, 2018. WorldPop (www.worldpop.org - School of Geography and Environmental Science, University of Southampton; Department of Geography and Geosciences, University of Louisville; Departement de Geographie, Université de Namur) and Center for International Earth Science Information Network (CIESIN), Columbia University (2018). Global High Resolution Population Denominators Project - Funded by The Bill and Melinda Gates Foundation (OPP1134076). doi:10.5258/SOTON/WP00647. (Last accessed on: 2022-02-01).

- Wu, D., Zhao, X., Liang, S., Zhou, T., Huang, K., Tang, B., Zhao, W., 2015. Time-lag effects of global vegetation responses to climate change. *Glob. Chang. Biol.* 21, 3520–31. doi:10.1111/gcb.12945.
- Wulder, M.A., Masek, J.G., Cohen, W.B., Loveland, T.R., Woodcock, C.E., 2012. Opening the archive: How free data has enabled the science and monitoring promise of Landsat. *Remote Sens. Environ.* 122, 2–10. doi:10.1016/j.rse.2012.01.010.
- Xie, X., He, B., Guo, L., Miao, C., Zhang, Y., 2019. Detecting hotspots of interactions between vegetation greenness and terrestrial water storage using satellite observations. *Remote Sens. Environ.* 231, 111259. doi:10.1016/j.rse.2019.111259.
- Xing, Z., Fan, L., Zhao, L., De Lannoy, G., Frappart, F., Peng, J., Li, X., Zeng, J., Al-Yaari, A., Yang, K., Zhao, T., Shi, J., Wang, M., Liu, X., Hu, G., Xiao, Y., Du, E., Li, R., Qiao, Y., Shi, J., Wen, J., Ma, M., Wigneron, J.P., 2021. A first assessment of satellite and reanalysis estimates of surface and root-zone soil moisture over the permafrost region of Qinghai-Tibet Plateau. *Remote Sens. Environ.* 265, 112666. doi:10.1016/j.rse.2021.112666.
- Xu, Z., Cao, L., Zhong, S., Liu, G., Yang, Y., Zhu, S., Luo, X., Di, L., 2020. Trends in Global Vegetative Drought From Long-Term Satellite Remote Sensing Data. *IEEE J. Sel. Top. Appl. Earth. Obs. Remote Sens.* 13, 815–826. doi:10.1109/jstars.2020.2972574.
- Yan, D., Zhang, X.Y., Yu, Y.Y., Guo, W., 2016. A Comparison of Tropical Rainforest Phenology Retrieved From Geostationary (SEVIRI) and Polar-Orbiting (MODIS) Sensors Across the Congo Basin. *IEEE Trans. Geosci. Remote Sens.* 54, 4867–4881. doi:10.1109/tgrs.2016.2552462.
- Yan, D., Zhang, X.Y., Yu, Y.Y., Guo, W., 2017. Characterizing Land Cover Impacts on the Responses of Land Surface Phenology to the Rainy Season in the Congo Basin. *Remote Sens.* 9, 17. doi:10.3390/rs9050461.
- Yang, D., Bright, J.M., 2020. Worldwide validation of 8 satellite-derived and reanalysis solar radiation products: A preliminary evaluation and overall metrics for hourly data over 27 years. *Sol. Energy* 210, 3–19. doi:10.1016/j.solener.2020.04.016.
- Yang, S., Li, R., Wu, T., Hu, G., Xiao, Y., Du, Y., Zhu, X., Ni, J., Ma, J., Zhang, Y., Shi, J., Qiao, Y., 2020. Evaluation of reanalysis soil temperature and soil moisture products in permafrost regions on the Qinghai-Tibetan Plateau. *Geoderma* 377, 114583. doi:10.1016/j.geoderma.2020.114583.
- You, G., Liu, B., Zou, C., Li, H., McKenzie, S., He, Y., Gao, J., Jia, X., Altaf Arain, M., Wang, S., Wang, Z., Xia, X., Xu, W., 2021. Sensitivity of vegetation dynamics to climate variability in a forest-steppe transition ecozone, north-eastern Inner Mongolia, China. *Ecol. Ind.* 120, 106833. doi:10.1016/j.ecolind.2020.106833.
- Yuan, W., Zheng, Y., Piao, S., Ciais, P., Lombardozzi, D., Wang, Y., Ryu, Y., Chen, G., Dong, W., Hu, Z., Jain, A.K., Jiang, C., Kato, E., Li, S., Lienert, S., Liu, S., Nabel, J., Qin, Z., Quine, T., Sitch, S., Smith, W.K., Wang, F., Wu, C., Xiao, Z., Yang, S., 2019. Increased atmospheric vapor pressure deficit reduces global vegetation growth. *Sci. Adv.* 5, eaax1396. doi:10.1126/sciadv.aax1396.
- Yue, S., Pilon, P., Phinney, B., Cavadias, G., 2002. The influence of autocorrelation on the ability to detect trend in hydrological series. *Hydrol. Process.* 16, 1807–1829. doi:10.1002/hyp.1095.
- Zhang, H., Immerzeel, W.W., Zhang, F., de Kok, R.J., Chen, D., Yan, W., 2021. Snow cover persistence reverses the altitudinal patterns of warming above and below 5000 m on the Tibetan Plateau. *Sci. Total Environ.* 803, 149889. doi:10.1016/j.scitotenv.2021.149889.

- Zhang, M., Wang, B., Cleverly, J., Liu, D.L., Feng, P., Zhang, H., Huete, A., Yang, X., Yu, Q., 2020a. Creating New Near-Surface Air Temperature Datasets to Understand Elevation-Dependent Warming in the Tibetan Plateau. *Remote Sens.* 12, 1722. doi:10.3390/rs12111722.
- Zhang, W., Wang, L., Xiang, F., Qin, W., Jiang, W., 2020b. Vegetation dynamics and the relations with climate change at multiple time scales in the Yangtze River and Yellow River Basin, China. *Ecol. Ind.* 110, 105892. doi:10.1016/j.ecolind.2019.105892.
- Zhang, W., Zhou, T., Zhang, L., Zou, L., 2019. Future Intensification of the Water Cycle with an Enhanced Annual Cycle over Global Land Monsoon Regions. *J. Clim.* 32, 5437–5452. doi:10.1175/jcli-d-18-0628.1.
- Zhao, K., Wulder, M.A., Hu, T., Bright, R., Wu, Q., Qin, H., Li, Y., Toman, E., Mallick, B., Zhang, X., Brown, M., 2019a. Detecting change-point, trend, and seasonality in satellite time series data to track abrupt changes and nonlinear dynamics: A Bayesian ensemble algorithm. *Remote Sens. Environ.* 232, 111181. doi:10.1016/j.rse.2019.04.034.
- Zhao, M., Heinsch, F.A., Nemani, R.R., Running, S.W., 2005. Improvements of the MODIS terrestrial gross and net primary production global data set. *Remote Sens. Environ.* 95, 164–176. doi:10.1016/j.rse.2004.12.011.
- Zhao, S., Zhang, S., Cheng, W., Zhou, C., 2019b. Model Simulation and Prediction of Decadal Mountain Permafrost Distribution Based on Remote Sensing Data in the Qilian Mountains from the 1990s to the 2040s. *Remote Sens.* 11, 183. doi:10.3390/rs11020183.
- Zhou, S., Zhang, W., Wang, S., Zhang, B., Xu, Q., 2021. Spatial–Temporal Vegetation Dynamics and Their Relationships with Climatic, Anthropogenic, and Hydrological Factors in the Amur River Basin. *Remote Sens.* 13, 684. doi:10.3390/rs13040684.
- Zhu, W.N., Tian, Y.Q., Yu, Q., Becker, B.L., 2013. Using Hyperion imagery to monitor the spatial and temporal distribution of colored dissolved organic matter in estuarine and coastal regions. *Remote Sens. Environ.* 134, 342–354. doi:10.1016/j.rse.2013.03.009.
- Zhu, Y., Liu, S., Yi, Y., Xie, F., Grunwald, R., Miao, W., Wu, K., Qi, M., Gao, Y., Singh, D., 2021. Overview of terrestrial water storage changes over the Indus River Basin based on GRACE/GRACE-FO solutions. *Sci. Total Environ.* 799, 149366. doi:10.1016/j.scitotenv.2021.149366.
- Zhu, Z., Piao, S., Myneni, R.B., Huang, M., Zeng, Z., Canadell, J.G., Ciais, P., Sitch, S., Friedlingstein, P., Arneth, A., Cao, C., Cheng, L., Kato, E., Koven, C., Li, Y., Lian, X., Liu, Y., Liu, R., Mao, J., Pan, Y., Peng, S., Peñuelas, J., Poulter, B., Pugh, T.A.M., Stocker, B.D., Viovy, N., Wang, X., Wang, Y., Xiao, Z., Yang, H., Zaehle, S., Zeng, N., 2016. Greening of the Earth and its drivers. *Nat. Clim. Chang.* 6, 791–795. doi:10.1038/nclimate3004.

Eidesstattliche Erklärung

Versicherung an Eides Statt

Ich, Soner Üreyen, wohnhaft in München mit der Matrikelnummer X versichere an Eides Statt durch meine Unterschrift, dass ich die Dissertation “Multivariate Time Series for the Analysis of Land Surface Dynamics - Evaluating Trends and Drivers of Land Surface Variables for the Indo-Gangetic River Basins” selbständig und ohne fremde Hilfe angefertigt, alle Stellen, die ich wörtlich oder dem Sinne nach aus Veröffentlichungen entnommen habe, als solche kenntlich gemacht und ich auch keine anderen als die von mir angegebenen Quellen und Hilfsmittel benutzt habe. Ich versichere an Eides Statt durch meine Unterschrift, dass ich die Regeln der Universität Würzburg über gute wissenschaftliche Praxis eingehalten habe, insbesondere, dass ich die Gelegenheit zum Promotionsvorhaben nicht kommerziell vermittelt bekommen und insbesondere nicht eine Person oder Organisation eingeschaltet habe, die gegen Entgelt Betreuer bzw. Betreuerinnen für die Anfertigung von Dissertationen sucht.

Ich versichere an Eides Statt, dass ich die vorgenannten Angaben nach bestem Wissen und Gewissen gemacht habe und dass die Angaben der Wahrheit entsprechen und ich nichts verschwiegen habe. Die Strafbarkeit einer falschen eidesstattlichen Versicherung ist mir bekannt, namentlich die Strafandrohung gemäß § 156 StGB bis zu drei Jahren Freiheitsstrafe oder Geldstrafe bei vorsätzlicher Begehung der Tat bzw. gemäß § 161 Abs.1 StGB bis zu einem Jahr Freiheitsstrafe oder Geldstrafe bei fahrlässiger Begehung.

München, 23.03.2022

Unterschrift